Green Energy and Technology

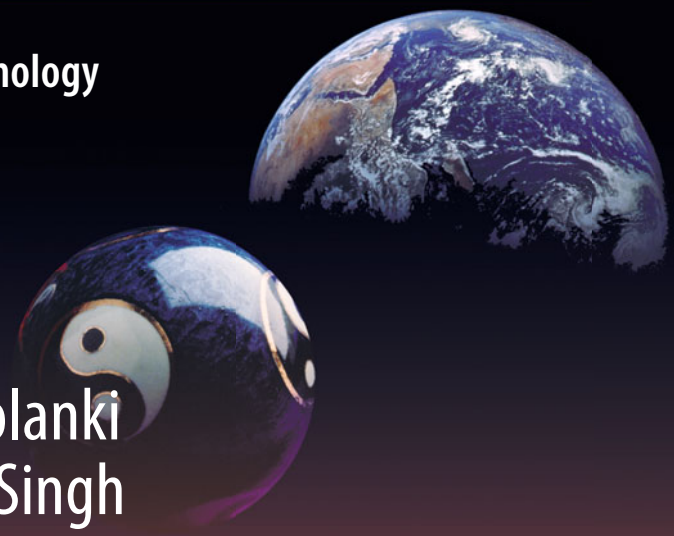

Chetan Singh Solanki
Hemant Kumar Singh

Anti-reflection and Light Trapping in c-Si Solar Cells

Springer

Green Energy and Technology

More information about this series at http://www.springer.com/series/8059

Chetan Singh Solanki · Hemant Kumar Singh

Anti-reflection and Light Trapping in c-Si Solar Cells

Springer

Chetan Singh Solanki
Department of Energy Science
and Engineering
Indian Institute of Technology Bombay
Mumbai, Maharashtra
India

Hemant Kumar Singh
Department of Energy Science
and Engineering
Indian Institute of Technology Bombay
Mumbai, Maharashtra
India

ISSN 1865-3529 ISSN 1865-3537 (electronic)
Green Energy and Technology
ISBN 978-981-10-4770-1 ISBN 978-981-10-4771-8 (eBook)
DOI 10.1007/978-981-10-4771-8

Library of Congress Control Number: 2017940816

© Springer Nature Singapore Pte Ltd. 2017
This work is subject to copyright. All rights are reserved by the Publisher, whether the whole or part of the material is concerned, specifically the rights of translation, reprinting, reuse of illustrations, recitation, broadcasting, reproduction on microfilms or in any other physical way, and transmission or information storage and retrieval, electronic adaptation, computer software, or by similar or dissimilar methodology now known or hereafter developed.
The use of general descriptive names, registered names, trademarks, service marks, etc. in this publication does not imply, even in the absence of a specific statement, that such names are exempt from the relevant protective laws and regulations and therefore free for general use.
The publisher, the authors and the editors are safe to assume that the advice and information in this book are believed to be true and accurate at the date of publication. Neither the publisher nor the authors or the editors give a warranty, express or implied, with respect to the material contained herein or for any errors or omissions that may have been made. The publisher remains neutral with regard to jurisdictional claims in published maps and institutional affiliations.

Printed on acid-free paper

This Springer imprint is published by Springer Nature
The registered company is Springer Nature Singapore Pte Ltd.
The registered company address is: 152 Beach Road, #21-01/04 Gateway East, Singapore 189721, Singapore

Preface

Solar photovoltaic technologies have been growing with over 35% CAGR annually, with annual production now crossing 77,000 MW. This is extremely impressive high production volume by any measure. About 90% of this production is done using crystalline Si wafers. Despite the competition from the other materials and technologies, strong growth in the crystalline Si cell technology and improvement in efficiency has led to strong position of this technology in current market.

There is further scope for improvement in technology which will lead to cost reduction. International technology roadmap on crystalline Si cell technology has identified several areas of improvements in crystalline Si cell like front metal contact, front and back surface passivation, bulk material, reduction in wafer thickness, and alternative anti-reflection techniques. It is anticipated that the future crystalline Si solar cells will be much thinner than the current standard of 180 microns. In this scenario efficient light harvesting becomes key to growth of the technology and cost reduction. Anti-reflection and light trapping techniques will play a key role in efficient light trapping by future solar cells. In this context, this book brings an insight into various aspects related to reflection, refraction, and light trappings in c-Si cell technologies. Basic physics and technology for light trapping in c-Si-based solar cell has been covered starting from traditional light trapping structure to advanced light trapping structures based on nanostructures.

Chapter 1 gives an overview of solar cell technology. In this chapter, different types of solar cell technologies have been discussed in brief and the importance of c-Si-based solar cell technology has been described along with the importance of light trapping technology.

Chapter 2 covers the main stream technology of c-Si solar cells. It explores development in design and technology of the c-Si solar cells from traditional to advanced device architecture. It highlights the historical development in cell design and technology along with the technological approach, which is being researched for next-generation c-Si solar cells. Some basics on solar cell performance and corresponding cell performance tracking parameters like open circuit voltage, short circuit current, maximum power point, FF, Efficiency, EQE and IQE, and their

interdependence has also been discussed. Toward the end of the chapter, International Technology Roadmap for Photovoltaic (ITRPV) has been introduced.

Chapter 3 focuses on the interference based anti-reflection and light trapping methodologies for solar cell applications. Detailed analysis of interference based anti-reflection and principle behind the observed phenomenon has been covered. Correlation with reflectance minima with wavelength and dielectric layer parameters has been presented. Experimental measurements of reflectance for various suitable anti-reflection coatings has also been presented and compared with the theoretical results. At the end, benefits and limitations of dielectric based reflectance have been discussed in the context of c-Si solar cells.

Chapter 4 presents an exploration on methodologies of texturization for light trapping. Starting from impact of surface morphology on light trapping, detailed analysis, and principle behind the observed phenomenon from textured surfaces has been discussed. Analytical analysis on current generation potential based on optical path length enhancement capability for different light trapping structures appropriate for c-Si solar cells has been covered.

Chapter 5 covers process technology for making textured surfaces in c-Si solar cells. Starting with c-Si crystal structure and role of crystal planes, wafer type and orientation in deciding the chemical process chemistry for texturing have been covered. Also, chemical processes used for achieving different shape of textures on surface in mono as well as multi c-Si wafers have been discussed along with the principle behind the process, which makes texturization possible. Toward end, practical implications involved in chemical texturing based technology has been discussed in the context of manufacturing of the c-Si solar cells.

Chapter 6 presents a comparative study on dielectric layer based light trapping, texture-based light trapping, and combination of the both light trapping structures on the solar cell performances. Also, implications and solutions have been discussed in context of next-generation c-Si solar cells.

Chapter 7 gives latest developments in traditional light trapping structures. In this chapter, discussion is made mainly on the advancement in traditional light trapping, e.g., development and techniques for nano-sized textures, back reflectors together with the cell designs incorporating the latest developments.

Chapter 8 introduces principles and technologies of plasmonics for an alternate light trapping method. Historical developments in the area of plasmonics and the review on applicability of plasmonics based light trapping technology in solar cells have been discussed. Relevant light trapping techniques such as scattering, local field enhancement, and surface plasmon polariton (SPP) has been discussed along with the associated mechanism involved for efficient light trapping. Mie scattering theory and the mathematical solutions to calculate Mie efficiencies for different size, shape, dielectric medium based nanostructures have also been covered.

Chapter 9 focuses on exploration of plasmonic-based technology for light trapping applications in c-Si solar cells. It presents updates on plasmonic-based light trapping structure research and developments for c-Si solar cells. Need and applicability of such emerging plasmonic-based light trapping structures in the

context of c-Si solar cells has been discussed. Also, a broad overview of limitations of plasmonic-based techniques and their probable solutions have been presented.

Chapter 10 discusses the future scope and requirements of research for different light trapping technologies in context of future development of c-Si solar cells. Discussion made in this chapter is focused mainly on the future advancement needed in light trapping structure development and a brief projection for certain areas which can be of immediate interest to research community.

Mumbai, India

Chetan Singh Solanki
Hemant Kumar Singh

Acknowledgements

Writing a book and bringing it to conclusion is always a humongous task. It goes without saying that such a task cannot be completed alone and requires valuable help of several people. In this case as well, we have taken help from several people and it is our great pleasure to acknowledge their contribution in writing of this book.

The help in the form of discussion and support from Seema, Amruta, Bandana, Vishnu, Mehul, Som, and many other students and staff members from IIT Bombay at various stages of writing of this book is invaluable. We would like to take this opportunity to thank them. We would like to acknowledge the help from Prof. Juzer Vasi, Prof. Anil K, Prof. B.M. Arora, Prof. K.L. Narasimhan, Prof. Pratibha, and many others in evolution and learning of the subject knowledge. Their encouragement for the work has always been a catalyst in doing better.

We would also like to acknowledge Ministry of New and Renewable Energy (MNRE), Government of India for setting up National Center for Photovoltaic Research and Education (NCPRE) at IIT Bombay which provided much needed research facilities for a better understanding of solar photovoltaic technologies.

Last but not least, Dr. Singh would like to express his gratitude toward his family members and his wife Priyanka for their co-operation and encouragement which helped in completion of this book. Dr. Solanki would like express his gratitude to his wife Rajni and love for his cute daughters, Suhani and Mahak, for their constant support and co-operation without which this book would not have been completed.

Chetan Singh Solanki
Hemant Kumar Singh

Contents

About the Authors

Dr. Chetan Singh Solanki is currently Professor at the Department of Energy Science and Engineering at the Indian Institute of Technology Bombay (IITB), India. He is an expert in crystalline Si technology, Si-nanostructures (including quantum dots), thin film Si solar cells, PV concentrator systems, and carbon nanotubes. He received his Ph.D. from the specialist silicon laboratory, IMEC (Inter-university Micro-electronics Center, Catholic University of Leuven, Belgium). He has worked on several state-sponsored and private sector projects exploring crystalline Si solar cells, both wafer-based and thin film nanomaterial based variants. The Ministry of New and Renewable Energy has sponsored a project titled "National Center for Photovoltaic Research and Education (NCPRE)", in which he is one of the principal investigators. He is also one of the principal investigators of "Localization of Solar Energy through Local Assembly, Sale and Usage of 1 Million Solar Urja Lamps (SoUL)". He has been the recipient of many awards as an investigator, has authored several books on solar PV and more than 100 international and national publications, and holds 11 patents.

Dr. Hemant Kumar Singh has more than 6 years of experience in the research and development of solar photovoltaic technologies. He also has industry experience of in-line 6 inch multi c-Si wafer based solar cell manufacturing. Dr. Singh worked toward his Ph.D. thesis at the Department of Energy Science and Engineering (DESE) under the MNRE, Government of India funded project "National Center for Photovoltaic Research and Education (NCPRE)" at the IIT Bombay, India. His R&D work was in fabrication and characterization of solar cells. His Ph.D. thesis focused on plasmonic-based advanced light trapping structures for next-generation thin c-Si solar cell applications. Prior to his Ph.D., he completed his M.Tech in Solid State Technology from IIT Kharagpur, West Bengal, India. During his M.Tech course, his research focus was on CIGS-CdS based hetero-junction for solar applications. He also holds an M.Sc. degree in Physics with a specialization in Electronics from D.D.U. Gorakhpur University, Gorakhpur, Uttar Pradesh, India.

List of Figures

Chapter 1
Solar Cells Overview and Perspective to Light-Trapping Schemes

In this chapter, overview of solar cell technology in general and its importance has been covered. Different types of solar cell technologies have been discussed in brief and the importance of c-Si based solar cell technology has been debated. Also the importance of light trapping technology in solar cells has been discussed.

1.1 Place of Solar PV Technology in World Energy Mix

Energy is primary requirement for any kind of living creature. Since the beginning of civilization, we are using energy resources for different types of needs whether it is for food cooking, lighting our houses, running our vehicles, and many other activities. Different sources for energy are used like biomass, oil, gas, etc., to fulfill our needs of energy. Together with social and economic advancement of civilization, consumption of energy has also increased. Many energy resources of different kinds are explored over the years which include nuclear energy, geothermal energy, solar thermal energy, etc. Though there are many sources for energy, primary source is mostly Sun. The sources of energy that we use, e.g., biomass, oil, gas, nuclear energy, etc., are the result of energy conversion from one form to other via different natural processes. In other words, Sun is the ultimate source of energy.

The two parameters that are driving the energy consumption across the globe are due to growth of population and growth of economic activities. The worldwide population is increasing day by day. In 1800, the world population was estimated around 1 billion and by 2011, it became 7 billion (see Fig. 1.1a). The twentieth century has seen most drastic increment in human population and hence the increment in energy consumption. In 2012, the global primary energy need was estimated around 12000 million ton oil equivalent (Mtoe) which is equivalent to about 140000 terawatt hour (TWh). It is expected that this primary need would further increase, and the primary energy requirement would be about 16800 Mtoe, i.e., about 196000 TWh by 2030.

© Springer Nature Singapore Pte Ltd. 2017

C.S. Solanki and H.K. Singh, *Anti-reflection and Light Trapping in c-Si Solar Cells*, Green Energy and Technology,
DOI 10.1007/978-981-10-4771-8_1

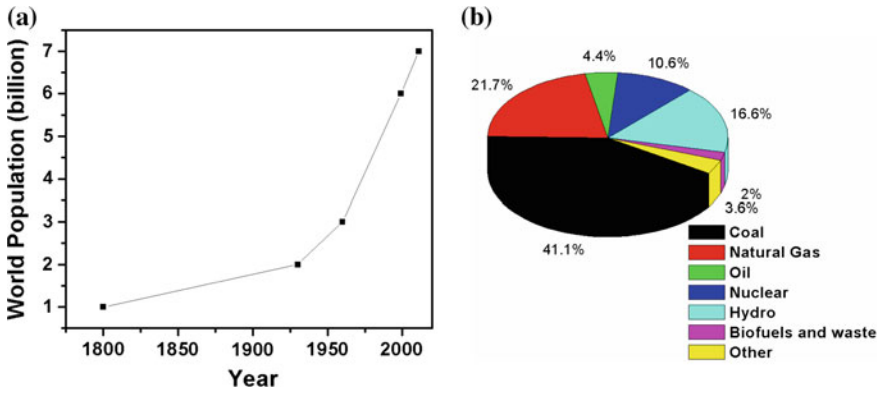

Fig. 1.1 **a** World population over the years; **b** contribution of different resources in electricity production in year 2013

Electricity is one of the most convenient form of energy and has become integral part of our lives. The consumption of electricity indicates the development status of a country and supposedly more developed countries use more electricity. In 2013, the estimated worldwide electricity production was around 23391 TWh (International Energy Agency 2015). Fossil fuels contributed major proportion in electricity production, which was about 67.2% (Coal: 41.1%, Oil: 4.4%, and Natural gas: 21.7%). The next major contributor was hydroelectricity with the contribution of 16.6%, followed by nuclear electricity with contribution of 10.6%. Biofuels and waste contributed about 2% in total energy production. A complete contribution for electricity production in the form of pie chart can be seen in Fig. 1.1b. It can be seen that electricity based on fossil fuel dominates electricity production. By now it is globally clear that there are downside of using electricity produced from fossil fuels. Fossil fuels are available in finite quantity and their excessive use leads to emission of greenhouse gases causing environmental damage. Greenhouse effect is referred to the trapping of some of the energy from the Sun in Earth's atmosphere. When the solar energy is radiated back from the Earth's surface to space, it is absorbed by atmospheric gases such as water vapor (H_2O), carbon dioxide (CO_2), methane (CH_4), nitrous oxide (N_2O), fluorinated gases, etc., and re-emitted in all directions. Out of these gases, CO_2 is a major threat. The concentration of CO_2 in earth atmosphere is increasing due to excessive use of fossil fuels. In 1965, the CO_2 concentration in earth atmosphere was less than 300 parts per million (ppm) which has increased to about 400 ppm by 2015. Increased CO_2 concentration is having serious impact on climate change, mainly resulting in global warming. In the last 100 years, the average temperature of the Earth's surface has increased by about 0.85 °C (BBC News 2016). The major increment in temperature/global warming has happened in the last three decades which is about 0.6 °C, an alarming number. The Intergovernmental Panel on Climate Change (IPCC) (http://www.ipcc.ch) forecasted that earth surface temperature change may exceed 1.5 °C by the end of the twenty-first century relative to 1850. A 2 °C change is generally threshold and

regarded as dangerous warming as it would impact the earth climate heavily and may result in natural disasters. All the countries in the world are trying to make policies to tackle the global warming effect and devising policies to mitigate it.

Renewable energy sources are being given due importance and being encouraged as an alternative to fossil fuels. Renewable sources that are being considered include hydro plant, wind, solar thermal, solar photovoltaics, biomass, tidal energy, wave energy, ocean thermal energy, etc. These renewable energy resources are technically having unlimited availability. Out of various renewable sources, currently biomass and hydro are major contributors in energy production. Due to huge energy demands and different process/conditions required for extracting energy from different renewable sources and limitation imposed by the nature of renewable energy source, all the energy needs cannot be met by exploring a single source and there is requirement of energy mix from different renewable resources.

Solar photovoltaic (solar PV) or solar cells-based energy generation have important role in exploring renewable energy technology in cleaner and greener way. Though solar photovoltaic/solar cell technology presently contributes less than 0.1% in energy production, it has huge potential. Having based on nonmoving semiconductors for electricity generation, the solar PV technology offers several benefits which include environment friendliness, noise-free operation, minimal maintenance requirements, and long working life. One of the core strength of the solar PV technology is its ability to provide modular electricity solutions as per the need of consumers. The technology can provide solution for very low power requirements like in Watt and at the same time it can also provide solution to high-power requirements in megawatts. The initial cost of solar cell-based electricity generation is holding point for its mass scale use and continuous efforts are being put to make it cheaper and affordable.

International energy agency (IEA) predicts that 11% of total worldwide electricity need would be supplied from solar cell-based technology by 2050 (Tanaka 2010), and it would result in reduction of 2.3 gigatons CO_2 emissions. The annual PV power generation in 2010 was 37 TWh and it is expected that by 2030 it would become 1247 TWh and would touch 4600 TWh mark by 2050. Similarly, the cumulative installed PV-based electricity generation capacity reached 178 GW by the end of 2014 from 27 GW in 2010 and is expected to rise to 872 GW by 2030 and 3155 GW by 2050. This will lead to an obvious increase in annual global PV market from 7 GW/year in 2010 to 105 GW/year by 2030 and expected to touch the 150 GW/year mark by 2050.

1.2 Historical Development of Solar Cells

When a solar cell is subjected to light or electromagnetic radiation, it generates electricity. This effect is known as photovoltaic effect. The beginning of solar cell history starts from discovery of photovoltaic effect in 1839 by Bequerel. He

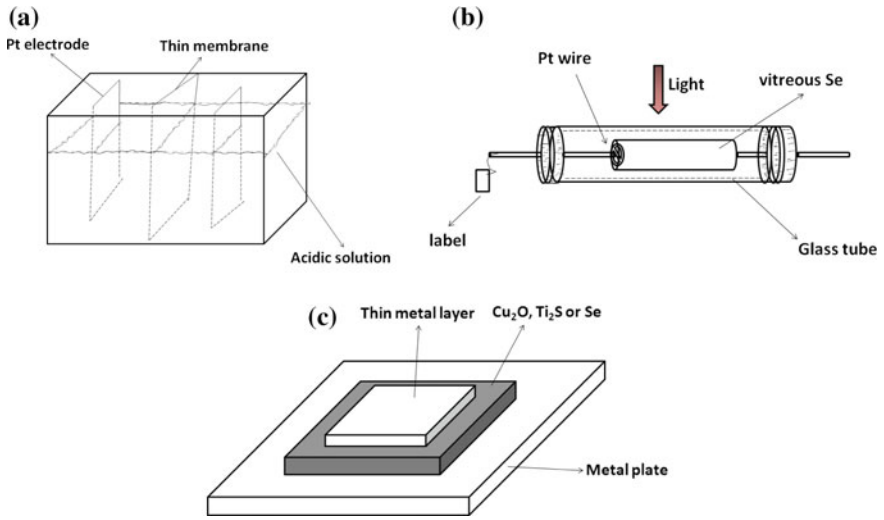

Fig. 1.2 **a** Schematic of Bequerel experimental setup; **b** Adams and Day experimental setup for photovoltaic effect study in Selenium (Se); **c** Most efficient solar cell structure developed till 1930s (after Ref. Green 2002a)

observed the photovoltaic effect, i.e., generation of electricity under the influence of light by illuminating silver bromide (AgBr) and silver chloride (AgCl) coated Pt electrodes submerged into AgBr and AgCl acidic solution respectively (see Fig. 1.2a) (Green 2002a).

After Bequerel's experiment in 1839, Adam and Day, while investigating photoconductive effect in selenium (Se) in 1876, observed that when Platinum (Pt) comes into contact with Se bar (see Fig. 1.2b), it result in current flow under the influence of light. This observation led to the development of first thin film Se-based solar cell by Fritt in 1883 (Green 2002a). Until 1940, the Se-based thin film solar cell-like structure as shown in Fig. 1.2c remained the most efficient solar cell where copper dioxide (CuO_2) or thallium sulfide (Tl_2S) or Se used as active absorbing material with suitable metal contacts. These early year solar cells were based on Schottky contacts in which semitransparent metal layer were deposited on top of active absorbing layer and metal–semiconductor contact resulted in asymmetric electronic junction. In 1941, the first p/n junction solar cell came into existence at Bell Labs by Russel Ohl where he showed photovoltaic effect in "grown-in" junction which was formed by impurity segregation in slowly recrystallized silicon melts (Treble 1998). Most of the solar cells produced today are based on p/n junction. In 1954, Chapin, Fuller, and Pearson reported the first diffused p-n junction-based c-Si solar cell with efficiency of 4.5%. Since then there has been revolution in photovoltaic research and development and different types of solar cells along with c-Si solar cell technology were developed over the years, e.g., III-V (GaAs, InP) based solar cells and II-VI (CdS, CdTe), I-III-VI semiconductor

(CuInGaSe) based thin film cells. Most of the cells were single junction cell, however, the band gap tunability in III-V based semiconductors also led to multi-junction solar cells development which resulted in reduced optical and electrical losses and efficiencies higher than single junction solar cells.

1.3 Different Solar Cell Technologies

Fundamental objective of research in solar cell technology is to drive the cost down and increase the efficiency up, both of these measures would be helpful in reducing the per unit cost of electricity generated. It is challenging to keep the cost of the solar cell fabrication low and at the same time expect for best efficiency. In this endeavor, scientists all around the world have been researching several material possibilities in order to find the best compromise between optical and electrical performance of the cell material and its cost of production.

Typically, more efficient cell means more complex design and hence more cost. The research and development in solar cell technology were aimed by considering either the cost aspect as first priority or the efficiency aspect depending upon the application. For terrestrial applications, cost aspect is more important and the efficiency is secondary if it is to be made affordable to masses. However, there are applications where efficiency aspect matter much more than cost aspect, e.g., space applications.

In the last 70–80 years, there have been many types of cell development and the cell types are generally identified with the active absorbing material used. The solar cells can categorize into three different categories as shown in Fig. 1.3. First category is c-Si/III-V semiconductors-based cells which are also known as first generation solar cells. The cells falling into this category have active absorbing material either c-Si or III-V semiconductors like gallium arsenide (GaAs)/Indium phosphide (InP), etc. These first generation solar cells can be further categorized as single junction or multi-junction solar cells. In single junction solar cell, there is only one p/n junction and one type of active absorbing material like mono c-Si/ multi c-Si or GaAs or InP is used. The p/n junction usually has a p-type and a n-type layer of same material (homojunction). In multi-junction solar cells, more than one p/n junction is used with the help of more than one active absorbing material with active absorbing material band gap in decreasing order from top to bottom. Some examples of single junction first generation solar cells are mono c-Si, multi c-Si, GaAs, InP-based solar cells. Examples of multi-junction solar cells are GaInP/GaAs (double junction), GaInAsP/GaIn (double junction), GaInP/GaAs/InGaAs (triple junction), GaInP/GaAs/GaInAs/GaInAs (four junctions), etc., where GaInP represents gallium indium phosphide, GaInAsP represents gallium indium arsenide phosphide, GaInAs represents gallium arsenide, and GaIn represents gallium–indium compound semiconductor.

The second category solar cells are referred as thin film solar cells. In this type, the active absorbing material thickness is few microns and these cells may have p/n

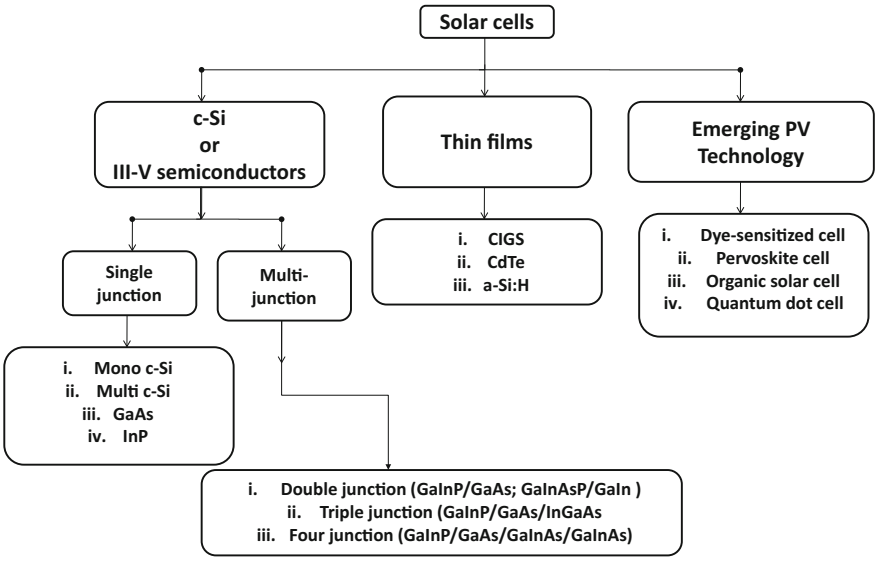

Fig. 1.3 Classification of different types of solar cells

junction with p-type and n-type layer of same material (homojunction) or of two different materials (heterojunction). Some examples are Copper Indium Gallium Selenide (CIGS), Cadmium Telluride (CdTe), and hydrogenated amorphous silicon (a-Si:H) based cells.

The third category of cells is grouped in emerging PV technologies as these technologies have been recently realized and the used active absorbing material's characteristics are still being explored. Some examples of emerging PV technologies are organic solar cells, quantum dot solar cells, dye-sensitized solar cells, perovskite-based cells, etc. In organic solar cells, organic compounds, like PTB7, PCBM, are used as active absorbing material (Liu et al. 2014). In quantum dot solar cells, nanoscale sizes of material (quantum dots), like PbS, CdTe, etc. (Shen et al. 2015; Ko et al. 2016), are used as active absorbing material. In dye-sensitized solar cells, dye, e.g., ruthenium polypyridine (Pellegrin et al. 2011) are used. And in perovskite-based cells, materials having perovskite structure (ABX_3), e.g., methylammonium lead trihalide ($CH_3NH_3PbX_3$), X can be iodine (I), bromine (Br) or chlorine (Cl), are used (Dualeh et al. 2014; Liu et al. 2015).

1.4 Current Status of Solar Cell Technologies

There are different types of solar cells which have been developed over the time and continuous efforts are being put to make them more and more cost-effective and efficient. New material and cell technology are also being explored which have

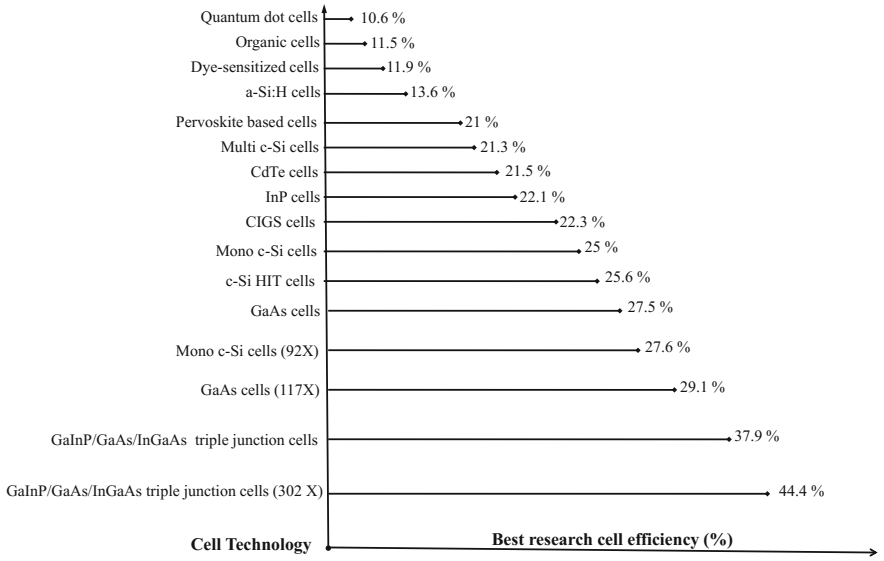

Fig. 1.4 Best research cell efficiencies till date of some well-known solar cell technologies. (data based on Ref. Green et al. 2015; NREL 2016)

given new insights and direction in solar cell technology development. Figure 1.4 shows different notable solar cell technologies which have achieved big milestone and their best research cell world record efficiency reported till date (Green et al. 2015; NREL 2016).

Mono c-Si solar cells have achieved world record efficiency of 25% on large device area. Mono c-Si solar cell with HIT (heterojunction with intrinsic thin layer) technology has also reached 25.6% efficiency mark which is world record on large device area with c-Si wafer-based solar cell technology. Multi c-Si-based solar cells have achieved 21.3% mark on large device area. All these cells have been measured under standard test condition (STC) in 1 sun intensity. With light concentration technology, mono c-Si solar cells have been reported to give efficiency as high as 27.6% in concentrated light equivalent to 92 suns (92X) on device designated illumination area of 1 cm^2. Concentrator PV technology-based cells generally have small area and light is concentrated on the cell with the help of concentration optics (using less and mirror) which can be externally arranged or integrated with the device itself. The concentrator solar cells are well designed such that it can sustain high temperature when functioning under large intensity.

Further, GaAs-based technology have been reported to show efficiency as high as 27.5% under 1 sun intensity, and using light concentration technology with light intensity equivalent to 117 suns (117X), it have been reported to show 29.1% efficiency. Another III-V semiconductor-based cell, i.e. InP, has been reported with 22.1% efficiency having total device area of 4 cm^2 (Green et al. 2015; NREL 2016).

In multi-junction-based solar technology, GaInP/GaAs/InGaAs-based triple junction solar cell with device aperture area of 1 cm^2 have been reported with 37.9% efficiency under 1 sun and with 44.4% efficiency for concentrator PV-based technology with 302 suns (302X) on designated illumination area of about 0.17 cm^2.

In thin film technology, CIGS solar cell technology has been reported to give highest efficiency of 22.3% followed by CdTe thin film technology which has shown 21.5% efficiency at research level. a-Si: H-based solar cells have been reported with best stabilized efficiency of 13.6% (Green et al. 2015; NREL 2016).

Under Emerging PV technology category, Dye-sensitized solar cell technology, which was first reported in 1991(O'Regan and Grätzel 1991), has reached 11.9% world record efficiency mark on designated illumination area of 1 cm^2. Organic solar cell technology has achieved 11.5% efficiency mark which is more than twice when compared to reported world record efficiency mark in 2001. Quantum dot-based solar cells have been reported with recent best research cell efficiency of 10.6%. A noble perovskite based solar cell which was first reported in 2009 (Kojima et al. 2009) with efficiency of 3.8% have reached 21% mark but shown to have unstabilized performance. Stability of perovskite-based solar cell is currently a big challenge as its performance degrade very rapidly in presence of moisture (Sivaram et al. 2015; Bryant et al. 2016).

1.5 Basic Working Principle of Solar Cells

The basic requirement for a solar cell is to have an active absorbing material which absorbs light and generates free electrons (e). And, there should be appropriate contacts to collect the electrons from the device. Figure 1.5a shows the most general design for a solar cell. For an efficient solar cell, there are three important processes, i.e., light absorption or light trapping, charge carrier generation, and charge carrier collection. All these processes have to be efficient (Fig. 1.5b). The first important requirement is efficient light absorption. To get better output in terms of photon energy to electrical energy conversions, the input energy must be delivered efficiently to the active absorbing material which absorbs the light and produces electron–hole (e-h) pairs. Efficient light trapping in solar cell would mean minimization of reflection from front surface, maximization of light absorption in active material, and minimization of transmission across the active absorbing material. The next important requirement for efficient solar cell is an effective charge carrier generation. It requires high-quality active absorbing material (defectless and contaminant-free material). The third important requirement of an efficient solar cell is effective charge carrier collection. It makes the passivation layers and metal contacts as important parts of operation. To maximize the solar cell performance of any type of solar cell, all the three operations should be executed efficiently by solar cells. The design of solar cells and choice of various materials used in solar cell fabrication should be done keeping above points in mind.

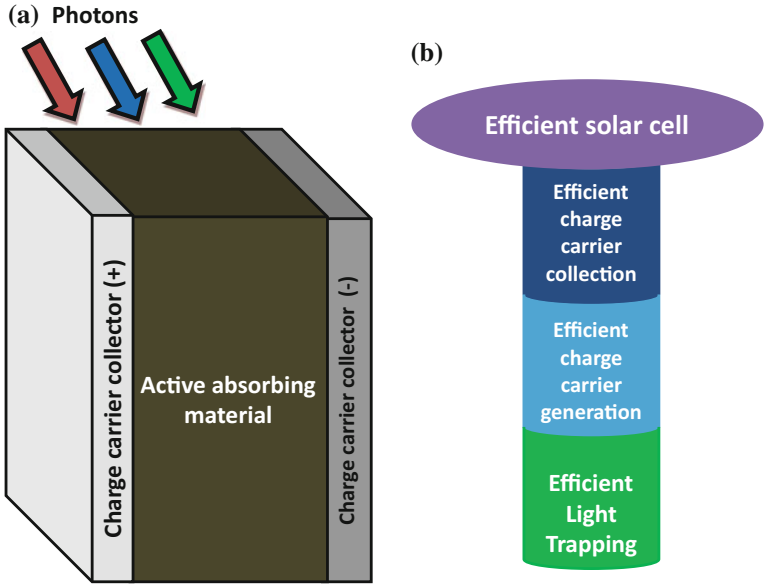

Fig. 1.5 **a** Most general design for solar cell; **b** three important processes to be optimized for making efficient solar cell

Further, different types of solar cells may have different arrangements for efficient light trapping. For example, in c-Si solar cell, the surface of the active absorbing material (c-Si wafer) is made rough to randomize the incident light which increases the optical path length in c-Si material (the active absorbing material) and helps in reflection minimization, overall it results in maximization of the light absorption. In thin film technology, glass substrates, through which light enters into the thin film active absorbing material, are made rough. Rough glass surface randomize the incident light and increases the optical path length into the active absorbing material. It helps in minimization of the reflection and maximization of the light absorption.

Now let us discuss about the generation of charge carriers in active absorbing material. The main and essential requirement for generation of charge carriers is that the photons should be absorbed in the active absorbing material and it should excite electrons directly from low energy state to high energy state. These excited electrons then should travel to the charge collectors (contacts). The photon absorption, excitation of electron from ground state to excited state, and transport to contacts in active absorbing material may vary in different types of solar cell technology. For example, in p/n junction-based c-Si solar cell (more detail about p/n junction solar cell has been discussed in Chap. 2), the photon absorption occur throughout the active absorbing material (c-Si) and electron is excited from valance band (V.B) to conduction band (C.B). During the photovoltaic operation, electrons flow from p-type region to n-type region (see Fig. 1.6a). Also, excitation of electron from V.B to C.B results in a deficiency of electron in V.B which is imagined as hole

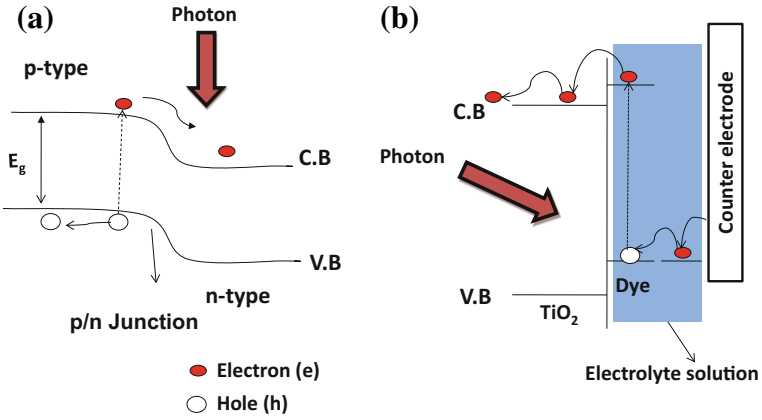

Fig. 1.6 Photon absorption and electron (e) and hole (h) generation and transport **a** in p/n junction based c-Si solar cell; **b** in Dye-sensitized solar cell

(absence of electron). The motion of hole happens in opposite direction of the electron motion (see Fig. 1.6a). However, in case of dye-sensitized solar cell technology, the photon absorption does not occur throughout the volume as in p/n junction solar cell, rather, it is absorbed at dye molecules attached to the porous titanium medium. This results in excitation of electron from ground state to high energy state within the dye molecule (Green 2002b). The excited electron is then transferred to the conduction band of the adjacent titania (TiO_2) (see Fig. 1.6b) and transported to the contact from where it is to be collected. The dye in which the electron was excited and transferred to titania is again recharged by electron from counter electrode though liquid medium (electrolyte) (see Fig. 1.6b).

Further, the e-h pair generated within the active absorbing material may behave differently in different active absorbing materials. For example, in c-Si solar cells at room temperature, the e-h pairs are bound with each other which form exciton and move as a pair within the material until broken by internal field. However, in case of perovskite, it has been reported that at room temperature, the electrons and holes are present in free form rather than exciton due to low e-h pair binding energy (D'Innocenzo et al. 2014).

In summary, different materials used as active absorbing material in solar cells behave differently to perform various basic operations of solar cells, i.e., light trapping, charge carrier generation and collection. Therefore, the optimized conditions for making efficient solar cell cannot be generalized.

1.6 Why c-Si Solar Cell?

Why c-Si solar cells accounts for 85–90% solar photovoltaic market today and is the most preferred technology than any other solar cell technology? There are many reasons for it. The evolution of c-Si cell technologies has benefited from the

development of microelectronics industry. Many processes that are developed for microelectronics industry were directly adopted by c-Si cell industry, which resulted in continuous improvement of cell efficiencies. C-Si cells are made of abundant material and the material is nontoxic, which is not the case for other competitive solar cell technologies. But more importantly, the performance of c-Si cell technology at industry scale is best compared to any other technology, with similar investment. As described in Sect. 1.4, there are many technologies like GaAs-based multi-junction solar cells, GaAs single junction cells which offer better cell efficiency but these technologies are more costly than the c-Si-based technology and economically not viable for terrestrial applications. The c-Si solar cells are very stable and have lifetime of about 25 years. The only drawback of c-Si solar cell technology was poor absorption of light for which use of more c-Si material and hence thicker wafers are necessary. The need of relative thicker material as compared to other solar cell technologies results in significant cost of the active material itself. However, with time there has been significant development in process technologies to enhance the light absorption and collection of photogenerated carriers in c-Si solar cells. The introduction of surface texturization for light trapping in 1954 and introduction of silicon nitride as passivation layer and screen printing for contacts in 1980s along with the reduction in cost of c-Si wafers took the c-Si solar cell technology to new height with enhancement in efficiency and performance which resulted in further reduction in cost of the cell from about $76 per Watt in 1977 to $10–12 per Watt in 2012(Economist.com 2012) (see Fig. 1.7). Presently, the c-Si solar cell average cost is $0.33 per Watt (Energytrend 2016) which is competitive with any other technology.

There are efforts worldwide to reduce the cost of c-Si cell further. One of the way to reduce the cost of c-Si cell is by reducing the material used, which is achieved by making c-Si wafer thinner. The standard thickness of wafer currently

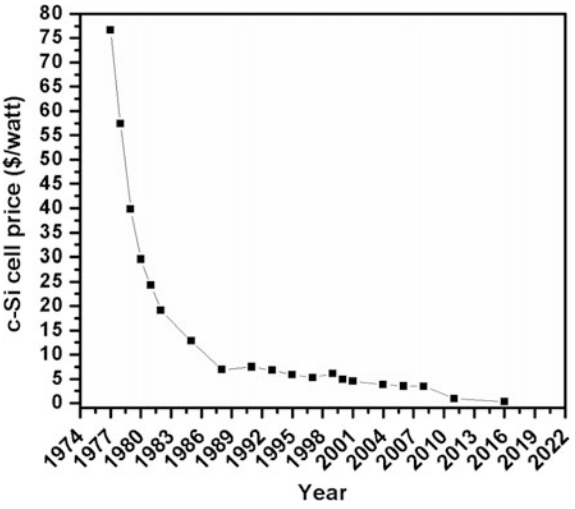

Fig. 1.7 c-Si solar cell price over the years (after Ref. Economist.com 2012; Energytrend 2016)

used is 180 μm, which accounts for more than 50% of the solar cell manufacturing cost (ITRPV 2015). Making solar cells using thinner wafers raises many challenge schemes and implementing light trappings in thinner wafers is one of the important challenges to overcome.

1.7 Importance of Light-Trapping Structure

Every solar cell has an active absorbing material volume which is an essential requirement of a solar cell where light is absorbed and charge carriers are generated which contributes to the electrical output. When light passes through the active absorbing material of the cell, some light is reflected from the front surface, some gets transmitted and some gets absorbed. As per Beer–Lambert law, if the incident light intensity of wavelength λ is $I_o(\lambda)$ and transmitted light intensity of wavelength λ is I(λ) (see Fig. 1.8), the absorption in the active absorbing material can be given by following Eq. (1.1):

$$A = \frac{I_0 - I}{I_0} = 1 - \frac{I}{I_o} = 1 - \exp(-\alpha t), \tag{1.1}$$

where'α' is absorption coefficient of the material and is a wavelength dependent parameter. 't' is the thickness of the active absorbing material.

Equation (1.1) suggests that the absorption in the active absorbing material depend on the absorption coefficient of the material and thickness of the material. Higher value of 'α' leads to more light absorption in the material and would result in more charge carrier generation. Larger thickness of material also absorbs more light and hence more charge carrier generation. 'α' is considered as characteristic property of a material. Since 'α' is different for different wavelengths, it is important that the active absorbing material selection should be such that it absorbs maximum available photons in the solar spectrum reaching on the earth surface. Figure 1.9a shows the spectral photon irradiance falling on earth surface per unit square meters per second per unit wavelength. Maximum photon density is in 300–2000 nm wavelength range with peak at around 550–600 nm. Now let's consider the case of

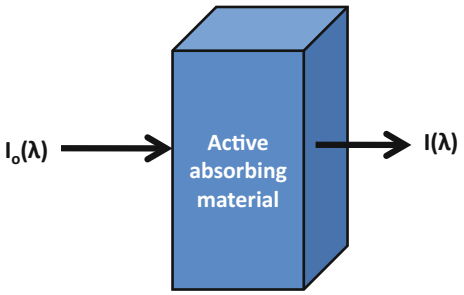

Fig. 1.8 Schematic of light of wavelength λ and intensity I_o passing through an active absorbing material volume

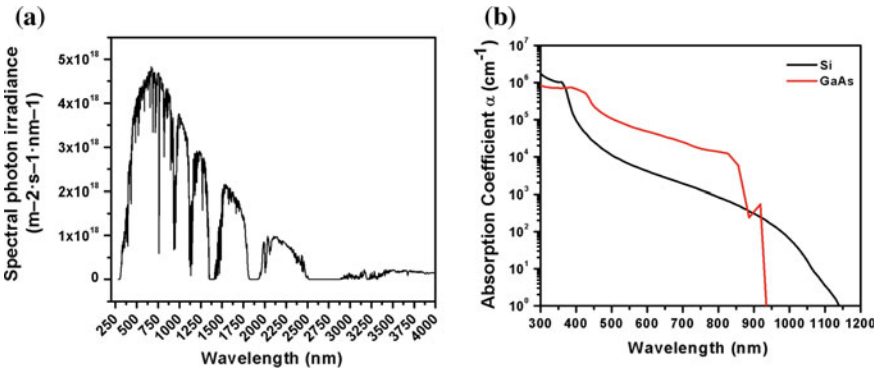

Fig. 1.9 **a** Spectral photon irradiation of different wavelengths falling on earth surface (AM 1.5G) (after Ref. Standard IEC 60904-3 2008); **b** wavelength dependent absorption coefficient of silicon (Si) and gallium arsenide (GaAs) (after Ref. Aspnes and Studna 1983; Green and Keevers 1995)

Si, which is indirect band gap semiconductor, and GaAs, which is direct band gap semiconductor, as solar cell active absorbing material. The band gap of Si is 1.12 eV and for GaAs is around 1.39 eV. It means Si can absorb light having energy above 1.12 eV, i.e., all the photons of wavelength between 300 and 1120 nm can be absorbed. Similarly, GaAs can absorb light having energy above 1.39 eV, i.e., all the photons of wavelength between 300 and 900 nm can be absorbed. Also, the absorption coefficient of Si and GaAs is shown in Fig. 1.9b, indicates much better absorption probability in direct band gap material like GaAs than the indirect band gap like Si.

Further, let's compare Si and GaAs as an active absorbing material targeting the radiations in 300–1200 nm wavelength range. Accounting the wavelength dependent absorption coefficient of these two materials, the maximum current that can be generated from c-Si and GaAs based cells having different thickness can be seen in Fig. 1.10a, b. In a solar cell when there is no light-trapping structure, optical thickness of the cell would be equivalent to the geometrical thickness as the light will not go through multiple bounce within the active absorbing material. In such case, the maximum current which can be expected from a 200 μm c-Si-based cell would be 38.9 mA/cm^2 and from GaAs solar cell of same thickness would be 35.1 mA/cm^2.

Despite being direct band gap semiconductor, GaAs-based cell would be able to generate lower current than Si which is due to its larger band gap compared to Si. However, the important aspect to consider here is the current generation potential in c-Si-based solar cell which is very much dependent of the cell thickness and it decreases as the thickness of the cell decreases (see Fig. 1.10a). In case of GaAs, after 100 μm material thickness, the variation in current generation is not significant (see Fig. 1.10b) which is due to high absorption coefficient of GaAs making it to absorb most of the light in thinner material. For very low thickness of GaAs material, some gain in current generation can be achieved with the help of

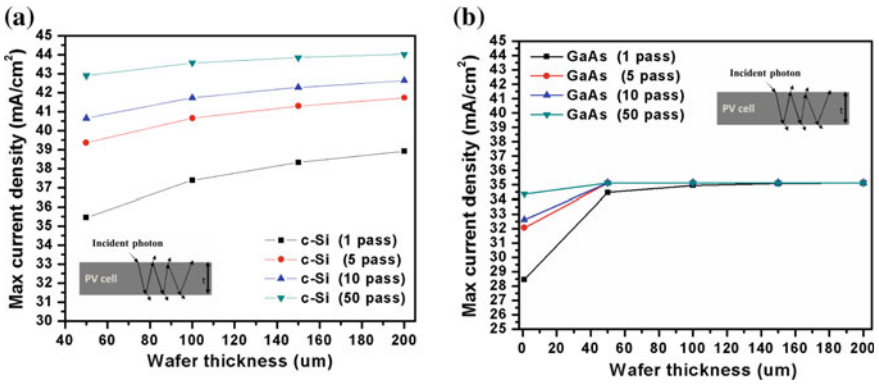

Fig. 1.10 Maximum current that can be generated under single and multiple light bouncing in **a** c-Si-based solar cell of different thickness; **b**. GaAs-based solar cell of different thickness

light-trapping structure where the optical thickness is increased by making light to take multiple bounce or holding the light for longer time within the active absorbing material. In general, the c-Si-based cell would be much more benefited by use of light-trapping structure than GaAs-based cell as the impact on current generation potential in GaAs-based cell would be very less influenced with multiple bounce of light until it is sufficiently thin (see Fig. 1.10a, b).

To harvest wide range of wavelengths (300–2000 nm) for light to electricity conversion, multi-junction approach, where multi-junction of different active absorbing materials are used with decreasing band gap from top to bottom as in GaInP/GaAs/InGaAs based triple junction solar cells, would be more appropriate. However, for single junction c-Si solar cells where the wavelengths of interest are 300–1200 nm, much more gain in current can be targeted with suitable light-trapping structure. The expected maximum current density from a 200 μm c-Si solar cell without any light-trapping structure would be 38.9 mA/cm^2 and it would decrease further when the thickness of the cell would decrease (see Fig. 1.10a). However, the solar current density for 300–1200 nm range is about 46.6 mA/cm^2 under AM 1.5G spectrum considering that each photon generate one electron–hole pair which contribute to the current. It means that there are many opportunities for improvement in c-Si solar cell performance using appropriate light-trapping structure. Thus the need and importance of the light-trapping structure to make light stay longer within the active absorbing material in case of indirect band gap materials like c-Si can be understood. And when reduction in c-Si wafer thickness are being aimed to save the c-Si material and hence to reduce the cell manufacturing cost, role of light-trapping structure become much more important. There are many different techniques for enhancement of light trapping within c-Si solar cell has been explored and many other new concepts and designs are being

explored worldwide. In this book, traditional as well as advanced light-trapping structures in context of c-Si solar cells has been covered in subsequent chapters with their future prospects. Such light-trapping structures can be useful for other solar cell technologies too where whole idea of having light-trapping structure is to get optical path length enhancement or holding the light for longer time so that light absorption in the cell active absorbing material can be better. In c-Si solar cell technology, the trend is to reduce the cell manufacturing cost by reducing the wafer thickness. In such scenario, development of appropriate light-trapping structure becomes essential considering the indirect band gap nature of c-Si materials.

Different techniques like surface texturing, plasmonics-based forward and backward light scattering, surface plasmon polariton (SSP) based light coupling, etc., are being explored for achieving better and efficient light trapping by enhancing the optical path length or holding the light for longer time in c-Si solar cells.

1.8 Questions and Problems

1. What do you understand by global warming? How solar cells can contribute toward mitigation of global warming?
2. Put some light on historical development of solar cell technology?
3. How many types of solar cells do you know? How are they different from each other?
4. Discuss on current status of different technology-based solar cells?
5. What are the basic requirements of a solar cell? What all aspects are to be considered to fabricate an efficient solar cell?
6. Why c-Si solar cell is most preferred technology for terrestrial application?
7. Discuss on the role of light-trapping structure and its necessity for a solar cell of your interest?
8. What do you understand by solar current density? Calculate solar current density for 300-2000 nm wavelength range?
9. Why multi-junction solar cell perform better than single junction solar cell in terms of output current and efficiency?
10. Calculate maximum current that can be generated from a c-Si solar cell having thickness of 50 μm, 100 μm, 180 μm, 400 μm? Assume that all the photons absorbed contribute to the electrical current.

References

Aspnes DE, Studna AA (1983) Dielectric functions and optical parameters of Si, Ge, GaP, GaAs, GaSb, InP, InAs, and InSb from 1.5 to 6.0 eV. Phys Rev B 27:985–1009. doi:10.1103/PhysRevB.27.985

BBC News (2016) What is climate change? In: BBC News. http://www.bbc.com/news/science-environment-24021772. Accessed 20 Nov 2016

Bryant D, Aristidou N, Pont S et al (2016) Light and oxygen induced degradation limits the operational stability of methylammonium lead triiodide perovskite solar cells. Energy Environ Sci 9:1655–1660. doi:10.1039/C6EE00409A

D'Innocenzo V, Grancini G, Alcocer MJP et al (2014) Excitons versus free charges in organo-lead tri-halide perovskites. Nat Commun 5:3586. doi:10.1038/ncomms4586

Dualeh A, Gao P, Seok S Il et al (2014) Thermal behavior of methylammonium lead-trihalide perovskite photovoltaic light harvesters. Chem Mater 26:6160–6164. doi:10.1021/cm502468k

Economist.com (2012) Sunny uplands. http://www.economist.com/news/21566414-alternative-energy-will-no-longer-be-alternative-sunny-uplands. Accessed 11 Mar 2016

Energytrend (2016) PV Energy trend. http://www.energytrend.com/. Accessed 11 Mar 2016

Green MA (2002a) Photovoltaic principles. Phys E Low-dimensional Syst Nanostruct 14:11–17. doi:10.1016/S1386-9477(02)00354-5

Green MA (2002b) Photovoltaic principles. Phys E Low-dimensional Syst Nanostruct 14:11–17. doi:10.1016/S1386-9477(02)00354-5

Green MA, Emery K, Hishikawa Y et al (2015) Solar cell efficiency tables (version 46). Prog Photovoltaics Res Appl 23:805–812. doi:10.1002/pip.2637

Green MA, Keevers MJ (1995) Optical properties of intrinsic silicon at 300 K. Prog Photovoltaics Res Appl 3:189–192. doi:10.1002/pip.4670030303

Intergovernmental Panel on Climate Change (IPCC). http://www.ipcc.ch

International Energy Agency (2015) IEA statistics: electricity information

ITRPV (2015) International technology roadmap for photovoltaic (ITRPV) 2014 results

Ko D-K, Maurano A, Suh SK et al (2016) Photovoltaic performance of PbS quantum dots treated with metal salts. ACS Nano 10:3382–3388. doi:10.1021/acsnano.5b07186

Kojima A, Teshima K, Shirai Y, Miyasaka T (2009) Organometal halide perovskites as visible-light sensitizers for photovoltaic cells. J Am Chem Soc 131:6050–6051. doi:10.1021/ja809598r

Liu F, Zhao W, Tumbleston JR et al (2014) Understanding the Morphology of PTB7:PCBM Blends in Organic Photovoltaics. Adv Energy Mater 4:1301377. doi:10.1002/aenm.201301377

Liu L, McLeod JA, Wang R et al (2015) Tracking the formation of methylammonium lead triiodide perovskite. Appl Phys Lett 107:61904. doi:10.1063/1.4928662

NREL (2016) Best research cell efficiencies. http://www.nrel.gov/ncpv/images/efficiency_chart.jpg

O'Regan B, Grätzel M (1991) A low-cost, high-efficiency solar cell based on dye-sensitized colloidal TiO2 films. Nature 353:737–740. doi:10.1038/353737a0

Pellegrin Y, Le Pleux L, Blart E et al (2011) Ruthenium polypyridine complexes as sensitizers in NiO based p-type dye-sensitized solar cells: effects of the anchoring groups. J Photochem Photobiol A Chem 219:235–242. doi:10.1016/j.jphotochem.2011.02.025

Shen X, Jia J, Lin Y, Zhou X (2015) Enhanced performance of CdTe quantum dot sensitized solar cell via anion exchanges. J Power Sources 277:215–221. doi:10.1016/j.jpowsour.2014.12.022

Sivaram V, Stranks SD, Snaith HJ (2015) Outshining silicon. Sci Am 313:54–59. doi:10.1038/scientificamerican0715-54

Standard IEC 60904-3 (2008) Measurement principles for terrestrial PV solar devices with reference spectral irradiance data

Tanaka N (2010) Technology roadmap: solar photovoltaic energy. OECD publishing

Treble F (1998) Milestones in the development of crystalline silicon solar cells. Renew Energy 15:473–478. doi:10.1016/S0960-1481(98)00207-9

Chapter 2
c-Si Solar Cells: Physics and Technology

This chapter presents the main stream technology of c-Si solar cells. It explores development in design and technology of the c-Si solar cells from traditional to advanced device architecture. It highlights the historical development in cell design and technology along with the technological approach which are being researched for next generation c-Si solar cells. Starting from most general cell architecture to complex architecture design, like HIT and PERL cells, has been covered. In this chapter, both mono- as well as multi c-Si wafer-based cells and their development have been discussed along with the manufacturing process sequence which is widely followed. Some basics on solar cell performance and corresponding cell performance tracking parameters like open circuit voltage, short circuit current, maximum power point, FF, Efficiency, EQE and IQE, etc., and their interdependence has also been discussed. Toward the end of the chapter, International Technology Roadmap for Photovoltaic (ITRPV) has been introduced. Also, discussion on next-generation c-Si wafer-based solar cells technology has been done highlighting the complications and importance of study on advanced light trapping in such structures.

2.1 Overview of c-Si Solar Cells

First c-Si solar cell was made in 1941. Back then the c-Si solar cell was merely 1% efficient (Green 2009). The c-Si-based solar cell technology has now reached 25% efficiency mark and even crossed this mark (Green et al. 2015). This development has come due to continuous efforts to make solar cell design, material quality, passivation technologies, and light tapping architectures better and better. The cost reduction with better efficiency has been the focus of the c-Si-based solar cell technology development to make solar cells more cost-effective and affordable to the masses. Today, c-Si solar cell-based modules; mainly mono c-Si and multi c-Si, shares 85–90% global market (Tanaka 2010). The first solar cell was fabricated

© Springer Nature Singapore Pte Ltd. 2017

C.S. Solanki and H.K. Singh, *Anti-reflection and Light Trapping in c-Si Solar Cells*, Green Energy and Technology,
DOI 10.1007/978-981-10-4771-8_2

using mono c-Si wafers, however, multi c-Si-based solar cell technology, as the cheaper and available alternative, came into existence in 1974 (Treble 1998). Improvement in slicing technology and reduced kerf loss leads to manufacturing of solar cell on 180 μm wafers compared to 400 μm thickness wafers used in early years. The cost of c-Si-based cells has been declining over the years as the technology becoming more mature (see Fig. 2.1). This is also in sync with reduction in wafer prices. The processing cost of cell manufacturing was further reduced after introduction of screen printing technology for contacts in 1975. The cell size also played a role in reduction in cell prices. In the beginning (around 1970s), the industrial cell size used to be mono c-Si wafer-based 50 mm circular cells (Treble 1998). These days, 125 and 156 mm pseudosquare cells are available in the market. Even up to 300 mm multi c-Si-based cells has also been produced by some manufactures(Treble 1998).

Figure 2.1 shows the trend of annual fall in prices of multi c-Si based solar cells and wafer in the recent years in USD/W_p.

Note that the multi c-Si-based solar cells are relatively less efficient than the mono c-Si-based cell, however, the lower processing cost of multi c-Si-based cells makes it more preferable. In 1985, the best multi c-Si cell efficiency was in the range of 15–16%, whereas mono c-Si-based cell were shown to have efficiency about 19%. As per recent reports, best multi c-Si-based cell have reached 21.3% efficiency mark and mono c-Si-based cell at 25% mark having large area (Green et al. 2015; NREL 2016). Figure 2.2 shows research cell or laboratory cell efficiency improvements of mono- and multi c-Si-based cells over the years.

Though the best efficiency in labs has crossed the 25% mark, the industrial cells are in 21–22% efficiency range (Green et al. 2015). Continuous efforts are being given to make this technology more efficient and affordable by researching and implementing the noble technologies for wafer manufacturing and cell processing.

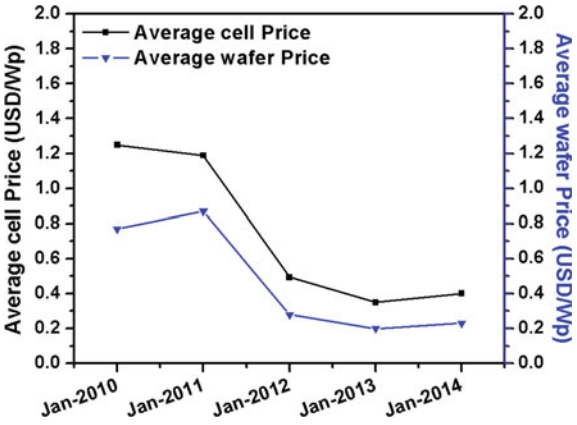

Fig. 2.1 Price trend of multi c-Si wafer and cells in recent years (after Ref. (www.itrpv.net/Reports/Downloads/2014/2014))

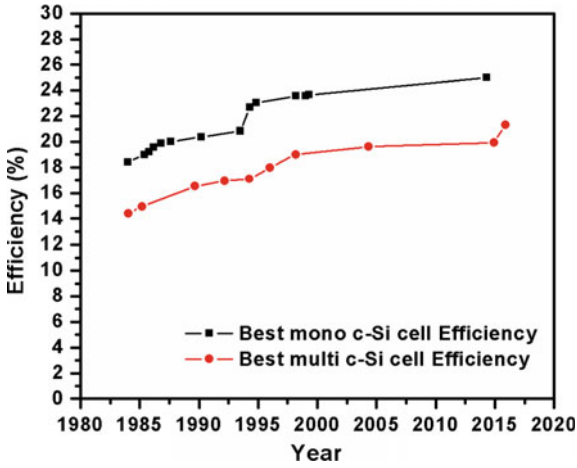

Fig. 2.2 Improvement trend in research cell efficiency of mono- and multi c-Si-based cells over the years (after Ref. (NREL 2016))

2.2 c-Si Solar Cell: Design and Technology

2.2.1 Classification of c-Si-Based Solar Cells

c-Si solar cells are mainly divided into two categories, e.g., mono c-Si solar cell and multi-crystalline Si solar cells. This classification is based on the type of wafer used in fabrication of the cell.

i. **Mono c-Si solar cell**:

In mono c-Si solar cells, mono-crystalline wafers are used. These wafers have well-arranged atoms in crystallographic structure which is free from any grain boundaries. Figure 2.3a shows the plain view of a typical mono c-Si wafer and Fig. 2.3b shows symbolic microscopic view of wafer where atoms of Si are arranged in periodic manner and connected with each with covalent bond. Czochralski (Cz) technique and float zone (FZ) techniques are most commonly used for manufacturing mono c-Si ingots from high-purity polycrystalline Si. The typical manufactured mono c-Si wafers have circular shape due to technicality involved in manufacturing of ingots which comes out in cylindrical shape (see Fig. 2.4a). But for economic benefits in making PV modules, the wafers are cut from ingots such that it gets pseudosquare shape, as much as possible. While making the mono c-Si ingots, dopants are added to make it either p-type (mainly B (Boron) is used as dopants) of n-type (mainly P (Phosphorus) is used as dopant). Both p-type and n-type mono c-Si wafers are used for making solar cells.

ii. **Multi-/poly-crystalline solar cells:**

In multi/poly c-Si solar cells, multi-crystalline wafers are used. These wafers have many well-arranged atoms in crystallographic structure; crystal size typically varies in the range from mm to cm, separated by grain boundaries. Figure 2.3c shows the

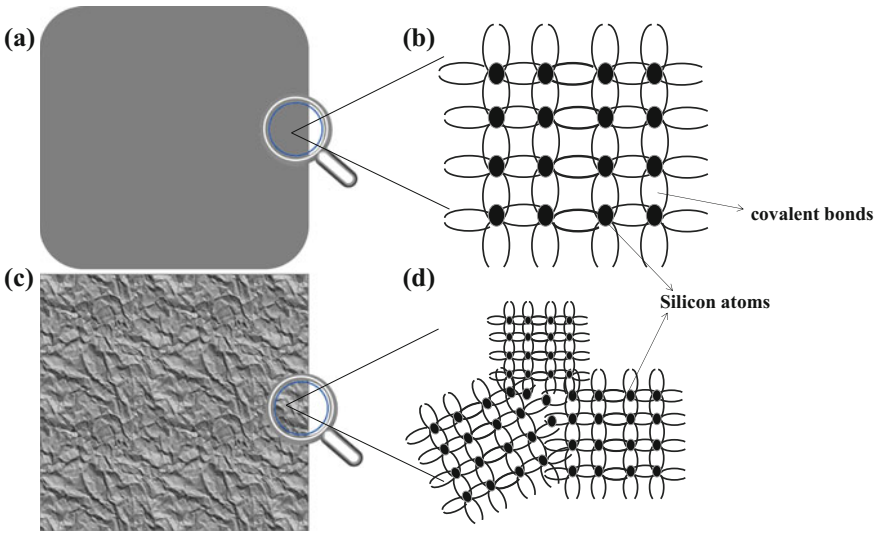

Fig. 2.3 **a** Plain view of a mono c-Si wafer; **b** symbolic microscope view for atomic arrangements in mono c-Si wafer; **c** plain view of a multi/poly c-Si wafer; **d** symbolic microscope view for atomic arrangements in multi c-Si wafer

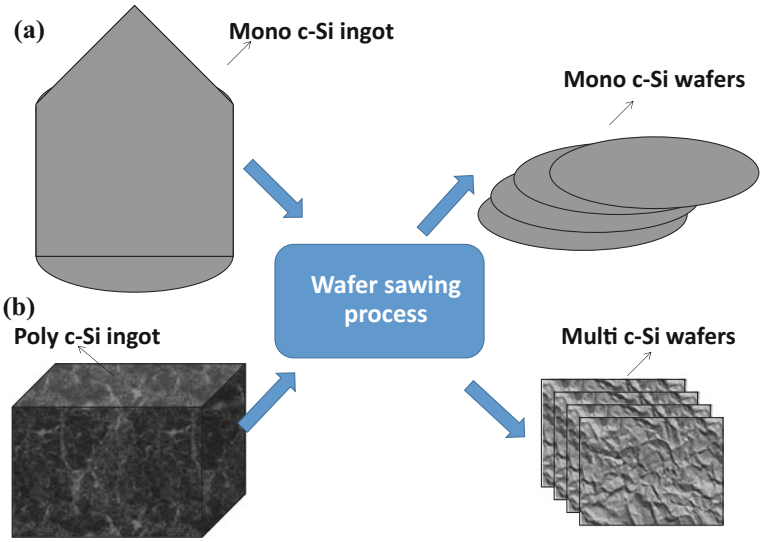

Fig. 2.4 Schematic of **a** Mono c-Si ingots and circular wafers after sawing process; **b** multi c-Si ingots and rectangular wafers after sawing process

pain view of a typical multi/poly c-Si wafer and Fig. 2.3d shows symbolic microscopic view of wafer where atoms of Si are arranged in periodic manner in small grain sizes separated by grains of different sizes. Due to presence of grains, the wafer looks nonuniform in color across the wafer and grain boundaries can be easily distinguished. The method for making purified poly-Si for multi c-Si wafers is the same as that of mono c-Si wafers; however, conversion of poly-Si into crystalline Si is done by directional solidification method. In this method, it is possible to make square-shaped ingots and hence square and rectangular wafers (see Fig. 2.4b) which are beneficial when manufacturing PV modules. Just like mono c-Si wafers, the multi c-Si wafers can also be p-type and n-type. The process used for manufacturing the poly/multi c-Si wafers are simpler and cost-effective, however, the efficiency achieved in these types of wafer-based cells are typically 1–2% lower than that of mono c-Si wafer-based cells produced with the same process.

Figure 2.5a shows a typical 5-inch mono c-Si solar cell and Fig. 2.5b shows a typical 5-inch multi c-Si solar cells. Clear difference can be seen from surface and edges, mainly corners.

2.2.2 *Architecture of c-Si Solar Cells*

A typical c-Si solar cell has a p-type or n-type base which is also known as base or substrate and is moderately doped with impurity (B or P respectively) doping concentration of $\sim 10^{15}$–$10^{16}/cm^3$. The junction (also called Emitter) is formed by highly doped region (impurity concentration $\sim 10^{20}/cm^3$). The Emitter is of n-type for p-type base and p-type for n-type base. In order to reduce the reflection from the surface there is textured surface with anti-reflection coating, which also acts as

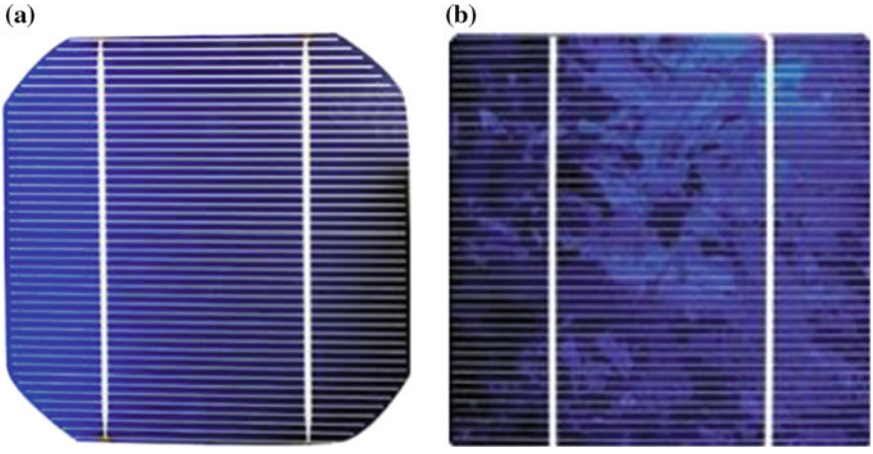

Fig. 2.5 Front view camera image of a typical **a** mono c-Si solar cell; **b** multi c-Si solar cell

surface passivation layer. And, then there are metal contacts at the front and at the rear side.

Figure 2.6a shows schematic of a typical p-type c-Si solar cell and Fig. 2.6b shows schematic of a typical n-type c-Si solar cell. In p-type c-Si solar cell as in Fig. 2.6a, base is p-type and emitter is made by heavy doping of pentavalent dopant usually phosphorus which form n^+ region and makes p-n junction. The p-n junction helps to separate the charge carriers (electrons (e) and holes (h)) which are generated when light is absorbed in the base. Cell surface is textured to enhance the light absorption in solar cell. Dielectric coating is done to passivate the dangling bond present at the surface of Si. If the surface is not passivated, the dangling bonds would act as recombination centers for photogenerated charge carriers and would reduce the electrical performance of the cell. The dielectric, usually silicon nitride (SiN_x) or silicon oxide (SiO_x)/silicon nitride (SiN_x) stack, also act as anti-reflection coating. For back contact usually Aluminum (Al) is used. When cell is annealed to form proper contact, Al reacts with Si and form p^+ region at based which serves the purpose of passivation at back surface, known as back surface field passivation (BSF). For front contact, usually silver (Ag) is used to make fingers and bus bars (see Fig. 2.5).

Similarly in n-type cells (Fig. 2.6b), base is n-type and emitter is made by doping trivalent dopant usually boron which form p^+ region. In this case also surface is textured to enhance the light absorption and dielectric coating (SiN_x or SiO_x/SiN_x or aluminum oxide (Al_2O_3)) is done to passivate the dangling bond present at the surface which also acts as anti-reflection coating. For back contact, usually Aluminum (Al) is used here also. However, for BSF in this case, phosphorus doping is preferred to form n^+ region which acts as BSF. For front contact, usually Al or Ag is used to make fingers and bus bars. Please note that the architecture shown here for n-type solar cell is more generic. There are many other possible architectures which are followed.

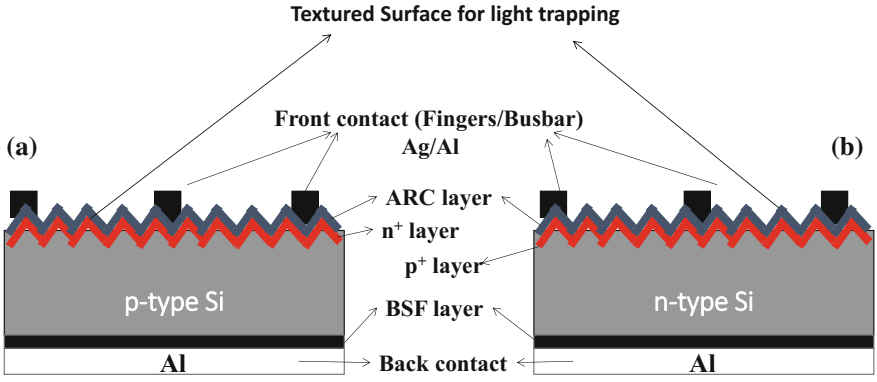

Fig. 2.6 Schematic of a typical **a** p-type c-Si solar cell; **b** n-type c-Si solar cell

2.2.3 Historical Development

The early c-Si-based p-n junction solar cell came into existence in 1941 at Bell Laboratory by Russel Ohl (Green 2002). The reported solar cell has "grown-in" junction which is formed by impurity segregation in slowly recrystallized silicon melts. Figure 2.7 shows schematic of a typical "grown-in" p-n junction solar cell reported in 1941. The efficiency of such cell was less than 1% (Green 2009).

The history of modern c-Si solar cell starts from 1954, when Fuller, Pearson, and Chaplin found that a diffuse p-n junction generated current when it is exposed to light (Treble 1998). The cell analysis then indicated 4.5% efficiency (Treble 1998). In 1956, a team led by Dr. Morton Prince at Hoffman Electronics of Evanston started commercial production of p/n junction cell which was 7% efficient (Treble 1998). The cell size was 1 cm $\times$ 2 cm and had single positive strip contact. The schematic of the cell is shown in Fig. 2.8. The cell also had silicon oxide (SiO_x) coating at the top.

In the beginning, the cell cost was very high and use for terrestrial application was not practically encouraging. After first public trail of silicon solar cell in 1956 in Bell rural carrier system, the next application is found in Vanguard I (first solar-powered satellite launched in 1958) to power 5 mW back-up transmitter (Treble 1998). By 1961, the production level cell efficiency reached 11% with improvement in series resistance and fabrication processes. For space application, it was a necessity to use solar power and the issue of cell price was secondary. However, for terrestrial application, solar cell cost was driving force for its further development. After 1972, solar cells started getting attention as an alternate energy source for terrestrial applications when oil prices increased significantly.

In 1972, the concept of back surface field passivation is introduced by NASA Lewis Research Center. In BSF, p^+ impurity (e.g., aluminum) is driven into the back of the silicon wafer which results in impurity concentration gradient and helps to accelerate minority carriers generated in the base of the cell toward the junction and also improves the red response of the cell. With the help of BSF, it became possible to make thinner cells of thicknesses from 100 to 200 μm (Treble 1998).

In 1974, a major improvement came from COMSAT Laboratories where they introduced surface texturing concept (Green et al. 1999). For surface texturing, the

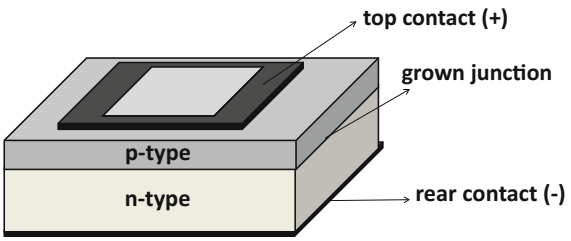

Fig. 2.7 Si solar cell based on "grown-in" junction due to segregation of impurities in slow recrystallization of silicon melt reported in 1941 (after Ref. (Green 2002))

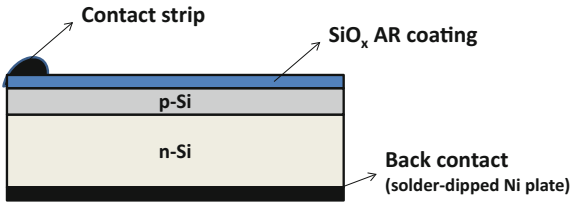

Fig. 2.8 Early p/n junction cell (1956) by Hoffman Electronics of Evanston (after Ref. (Treble 1998))

surface was selectively etched to form pyramids to eliminate the reflection losses from the cell surface. The combination of BSF and surface texturing along with introduction of junction depth reduction concept resulted in solar cell efficiency up to 15% in air mass (AM) zero condition (AM0) which is meant for space applications. These types of cells shown 16–17% efficiency in air mass 1.5 global (AM1.5G) radiation, i.e., for terrestrial applications (Green et al. 1999).

In the direction of manufacturing cheaper cells, multi-crystalline silicon (c-Si) wafers were introduced in 1974 as an alternative to mono c-Si wafers for producing cells (Treble 1998). Also, improvement in wafer cutting technique led to manufacture thinner wafers (400–250 μm). Dramatic reduction in cell manufacturing cost was seen after introduction of screen printing technology for contacts which replaced the costly photolithographic masking and vacuum deposition process requirements. By 1980s, screen printing technology had become well adapted for contact fabrication in cells. The multi c-Si wafer-based cell with screen printed contact made the cells commercially viable for terrestrial applications. In 1975, the terrestrial c-Si solar cells had achieved 10% efficiency (under AM 1.5 conditions) for mono c-Si- and 8% multi c-Si-based materials.

In 1982, Passivated Emitter Solar Cell (PESC) was reported by Dr. M.A. Green research group from UNSW. It had 2–3 nm thin SiO_2 insulator on the front surface (see Fig. 2.9a). The thin SiO_2 insulator was used to reduce the recombination of generated carriers at front. This design modification resulted in improvement in open circuit voltage enhancement from 614 to 690 mV under standard test conditions (STC) which resulted in achieving the 16% efficiency mark (Treble 1998).

Further design modifications were done in PESC cell structure, e.g., reduction in front contact metallization (see Fig. 2.9b) and process refinement, which helped to achieve the 19.1% efficiency mark under AM1.5 condition by 1985. Incorporation of microgrooved surface further raises the efficiency to 20.9%. These cells were fabricated using float zone wafers and contacts were made using photolithographic mask and vacuum deposition technique. Though the techniques used in these cell fabrications were costly, but it showed the way and the potential to achieve high efficiency. In 1985, Dr. M.A. Green research group from UNSW came up with cheaper process option to fabricate high-efficiency cells. These cells were called buried contact cell (see Fig. 2.9c) made from mono c-Si p-type Czochralski (CZ) Si wafers which were much cheaper than float zone wafers. These cells have textured surface, an oxide layer, BSF layer, plated Ni/Cu contact buried in laser scribed slots

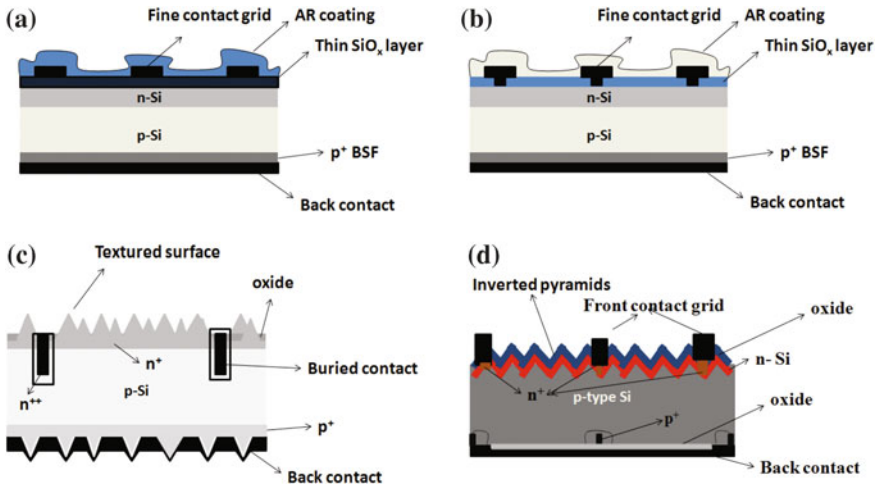

Fig. 2.9 Schematic of **a** Passivated Emitter Solar Cell (PESC); **b** Modified Passivated Emitter Solar Cell; **c** buried contact cell; **d** PERL (passivated emitter and rear locally diffused) cells (after Ref. (Treble 1998)) (images not to scale)

(Treble 1998; Green et al. 1999). This cell design was shown to give 19.6% efficiency and was adopted by BP solar for industry scale production.

M.A. Green's group in 1991 made PERL (passivated emitter and rear locally diffused; see Fig. 2.9d) cells having efficiency of 23.3% (Blakers et al. 1990; Treble 1998). It was fabricated using float zone mono c-Si wafer and had inverted pyramids for reflection reduction and thin oxide layer on front as well as back for surface passivation (Green et al. 1999). It also had small contact area with highly doped p^+ and n^+ regions. Further process modification and use of double layer antireflection (DLAR) coating in PERL cell resulted in 24–25% efficiency (Zhao et al. 1996; Green 2009). Today, best multi c-Si-based cells have reached 21.3% efficiency mark and mono c-Si-based cells at 25% mark having large area (NREL 2016).

c-Si-based solar cell with new cell design having heterojunction, known as HIT (heterojunction with intrinsic thin layer) cell, was also reported by Panasonic. It has marked world record efficiency of 25.6% (Green et al. 2015) which had been first announced in 2013 with record efficiency of 24.7%. In HIT cell, an intrinsic (i-type) a-Si layer and a p-type a-Si layer deposited on a randomly textured n-type CZ c-Si wafer to form a p/n heterojunction as shown in Fig. 2.10 (Taguchi et al. 2014).

The i-type and n-type a-Si layers deposited on the opposite side of the wafer resulted in a back surface field structure (see Fig. 2.10). On both sides of the doped a-Si layers, transparent conductive oxide (TCO) layers and metal grid electrodes were used (Taguchi et al. 2014).

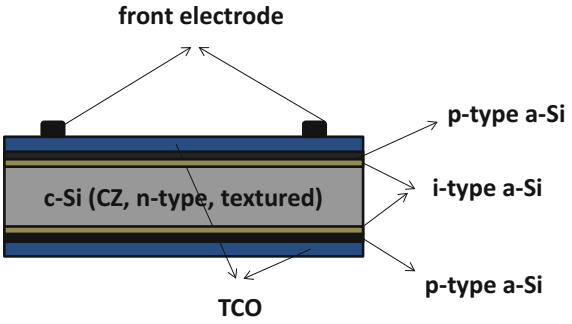

Fig. 2.10 Schematic of a HIT cell (after Ref. (Taguchi et al. 2014))

2.3 Manufacturing Process of c-Si Solar Cells

c-Si solar cell was the first among various types of solar cells which came into existence and became widely used solar cell technology. The main reason behind becoming most preferred technology and its fast development was:

a. Presence of well-established microelectronic industry.
b. Simple processing requirement.
c. Well understood physics behind its operation and performance impacting parameters.
d. Stability and reliability of the device.

The manufacturing of a c-Si solar cell has many unit processes depending upon the planned device structure. However, it is much lesser than the unit processes involved in many microelectronics device fabrications. For better and efficient solar cell, each unit processes requires proper optimization. Here, we will discuss in brief the process steps involved in fabricating a typical solar cell to have a basic understanding of c-Si solar cell device fabrication.

For fabricating c-Si wafer-based solar cell, start with c-Si wafer. It can be mono c-Si wafer or multi c-Si wafer. For manufacturing wafer, silica (SiO_2), also known as sand, is used as raw material which is made from second most earth abundant element available on earth, i.e., silicon (Si). Silica is molten at high temperature and reduction with carbon gives metallurgical grade silicon which is about 97% pure. Further purification process is done to reduce the elemental impurities and electronic grade Si is achieved when the impurity present is less than parts per billion (ppb). Hydrogen chloride (HCl) is used to make trichlorosilane ($SiHCl_3$) which is an intermediate compound of polysilicon manufacturing. $SiHCl_3$ is further vaporized and diluted with hydrogen (H_2) while passing it through deposition reactor, which transforms the material into elemental silicon which has impurity level less than 0.001 ppb. After this, the electronic grade poly silicon is used for fabricating mono- or multi c-Si ingots. For mono c-Si ingot manufacturing, the most widely used techniques are Czochralski (CZ) technique or Float Zone (FZ) technique. For multi c-Si ingot manufacturing the most widely used technique is Siemens

technique. The details of these techniques are not being discussed here as it is beyond the scope of the book. After manufacturing the ingots, the wafers are produced by wire sawing. Technological advancement in wafer cutting is important to make wafers thinner and with low kerf loss. Kerf loss is the loss of material (usually indicated in width) while cutting the wafers from ingots. Many techniques like wire electrical discharge machining and other kerf loss less processes are being explored (Dongre et al. 2015). Manufacturing of the wafers constitute a complete industry which supplies the wafers of desired quality and quantity to solar cell manufactures.

Once the wafer is available, further process of manufacturing solar cell begins. Figure 2.11 shows the steps involved in manufacturing of a typical cell having geometry as shown in Fig. 2.12.

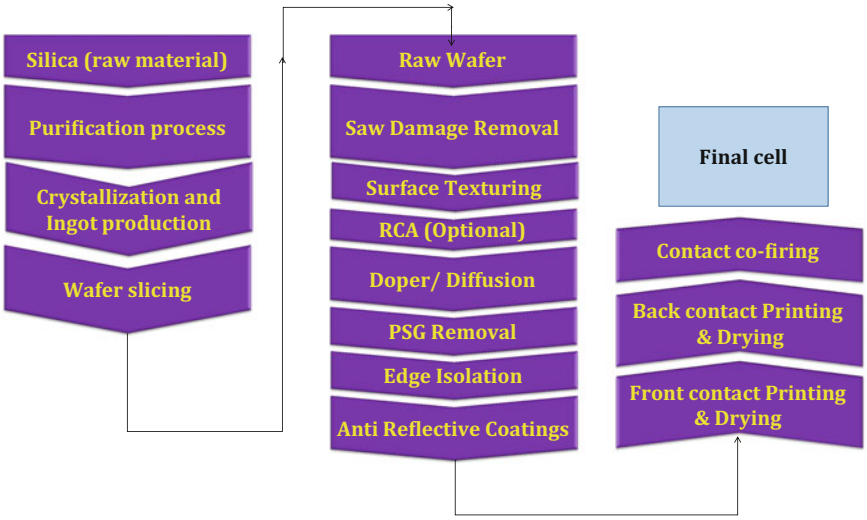

Fig. 2.11 Process flow/steps involved in manufacturing of a typical c-Si based solar cell

Fig. 2.12 Schematic of a typical cell structure under consideration

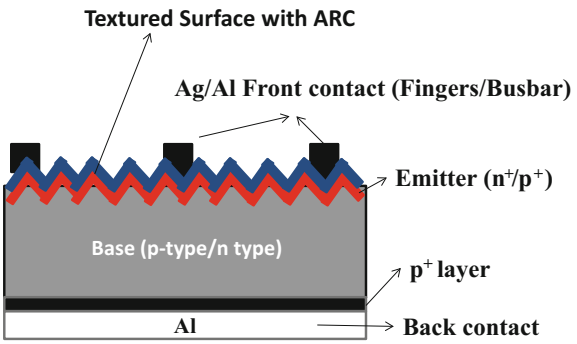

First, the wafer received as per desired base doping/resistivity, usually in as-cut form, is subjected to chemical process for saw damage removal. For saw damage removal, usually sodium hydroxide (NaOH) or potassium hydroxide (KOH) solution in deionized (DI) water is used at temperature of 70–80 °C.

After saw damage removal, surface roughening/texturing process is done to reduce the reflection from the surface. In case of mono c-Si wafers, directional etching using chemical solution usually NaOH/KOH in DI water in the presence of isopropyl alcohol (IPA) is used. In case of multi c-Si wafers, acidic solution for texturing is used to form honeycomb-like structure on surface. In this case chemical solutions like hydrofluoric acid (HF) and nitric acid (HNO_3) are widely used.

After surface texturing, RCA cleaning step can be used. RCA process was first developed at Radio Corporation of America and that is why the name RCA. RCA processes have two types. One is called RCA-1 which is a combination of DI water, ammonium hydroxide (NH_4OH), and hydrogen peroxide (H_2O_2). This process helps to remove residue of organic solvents from the surface of Si wafer. The other type is RCA-2 which is a combination of DI water, hydrogen chloride (HCl), and H_2O_2. It helps to remove crucial contaminant like gold (Au) which can introduce mid-gap trap states, which can severely impact the solar cell performance. This step is usually optional in industry process as it adds up to the cost of the cell.

The next step is dopant diffusion for p/n junction formation. Phosphorous-based dopant (usually liquid source like phosphoryl trichloride ($POCl_3$)) is used for p-type cells and boron-based dopant (usually liquid source like boron tribromide (BBr_3)) for n-type cells. Diffusion process is done at high temperature usually 800–900 °C. Diffusion process optimization is done depending upon the requirement of the concentration of doping in the emitter of the cell.

After diffusion process, glass removal (phosphorus silicate glass (PSG) in case of phosphorous-based dopant/borosilicate glass (BSG) in case of boron-based dopant) process is done. Usually, dilute HF solution is used for PSG/BSG removal.

After glass removal step, edge isolation is done which helps to remove the conduction path from top and bottom layers which may have resulted in shunt. This step basically results in electrical isolation between emitter and rear base of the cell. Usually, laser/plasma etching-based techniques are used for edge isolation. In laser technique, edges of the cell are finely cut. In plasma technique, reactive ion etchant are used for etching the edges.

After edge isolation, anti-reflection coating layer is used. The thickness and the refractive index is optimized such that it suits with the texture surface and result in minimum reflection from the surface. It also serves the purpose of passivation which is important for better performance of the cell. Depending upon the type (p-type/n-type), dielectric material is chosen. Usually, thermal oxide (SiO_2), silicon nitride (SiN_x), aluminum oxide (Al_2O_3), titanium dioxide (TiO_2) are used. Also, combination of the dielectric layers of different thicknesses has been used for better cell performance. Most widely used technique for dielectric deposition is chemical vapor deposition (CVD).

After dielectric layer deposition, contact printing is done. The most widely used technique for contact printing is screen printing. In cell contact printing, the back

surface is fully covered with metal and the front surface has fingers and bus bars with optimized thickness and width so that it offers minimum series resistance and minimum metal shading to allow maximum light to reach the cell. For screen printing, usually aluminum (Al) and silver (Ag) paste is used which contain an organic binder, solvent, glass frit, and Ag/Al nanoparticle. Screen which used to print the contact on cell surface has wire netting usually stainless steel coated with emulsion. After printing, drying is done at 200–250 °C to remove the solvent.

After contact printing and drying, contact co-firing is done to ensure the ohmic contact of metal contacts with semiconductor. Usually, belt furnace is used which has different temperature zones ranging from 400 to 900 °C. The cell move through the furnace on belt and passes through different temperature zones. In this process, the metal contacts get through dielectric layer at front surface and make contact with Si. And at the same time, Al at the back side, reacts with Si and forms BSF. Cell is ready now for measurement.

2.4 Photovoltaic Effect in c-Si Solar Cells and Important Parameters

2.4.1 Photovoltaic Effect in c-Si Solar Cells

When light shines on a c-Si solar cell, the photons are absorbed in Si material and results in generation of electron–hole (e-h) pairs. These e-h pairs move within the material until it sees a potential gradient, i.e., electric field which is sufficient to break the e-h paring. This phenomenon happens at p/n junction where there is potential gradient. In a p-type cell, the holes moves toward the back electrode and the electron are collected at front electrode as shown in Fig. 2.13a. Figure 2.13b

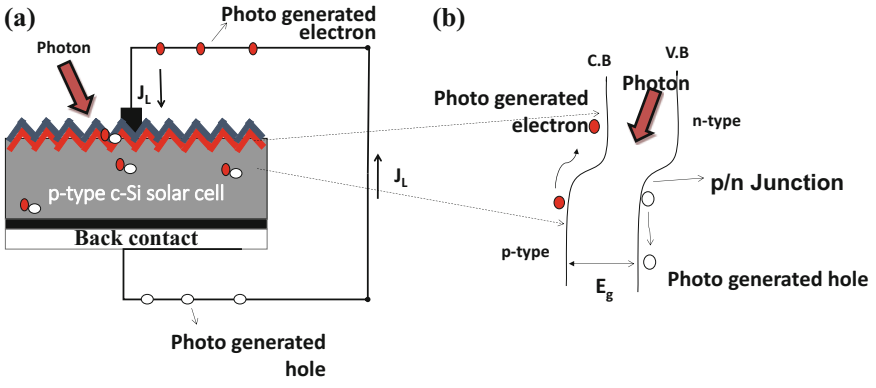

Fig. 2.13 **a** Schematic of a e–h pair generation and collection in typical p-type c-Si solar cell; **b** energy band diagram of a photovoltaic operation. C.B indicates conduction band and V.B indicates valance band. (Images not to scale)

shows the energy band diagram of a typical p-type c-Si solar cell photovoltaic operation. When light falls on solar cell, e-h pair is generated. The e-h pair moves toward the junction where it gets separated and is collected from electrodes. Here to note that only photons having energy larger than or equal to the band gap of Si (≥ 1.12 eV) are absorbed (neglecting phonon-assisted absorption) and contribute to the e-h pair generation and photogenerated current (J_L).

2.4.2 Current–Voltage Characteristics

In solar cell, the photogenerated current is maximum when there is no connected load. When the load is connected to the cell, the photogenerated current (J_L) due to cell illumination results in voltage drop (V) across the load which biases the p/n junction in forward direction. The equivalent circuit diagram of a solar cell is shown in Fig. 2.14a in ideal case, where solar cell is combination of constant current source and a p/n junction diode in parallel as shown with load resistance (R_L).

The forward-biased p/n junction results in forward bias diode current (J_D). But the photogenerated current (J_L) is much larger than the forward bias diode current (J_D) and it is in opposite direction to J_D. Therefore, the net solar cell current under illuminated condition is in reverse direction of generated forward bias voltage. The solar cell operation is given by Eq. (2.1) where J_o is reverse saturation current density of the diode, q is electron charge, k is Boltzmann constant and T is temperature.

$$J = J_D - J_L = J_0[\exp(\frac{qV}{kT}) - 1] - J_L. \tag{2.1}$$

The net current shown in Eq. (2.1) is in ideal case. But in realistic case, series and shunt resistance comes into picture which impacts the cell performance. A realistic case solar cell equivalent circuit diagram is shown in Fig. 2.14b. Here a shunt resistance (R_{sh}) is considered in parallel to the p/n junction diode which accounts for the various leakage currents in the solar cell due to different recombination effects. The series resistance (R_s) in series accounts for the various ohmic

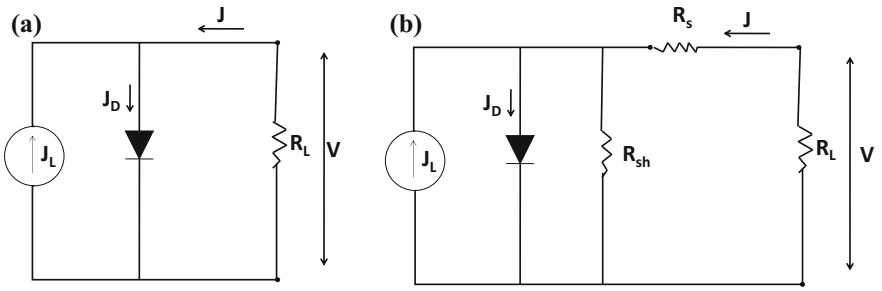

Fig. 2.14 Solar cell equivalent circuit diagram in **a** ideal case; **b** realistic case

losses in the bulk material, at metal–semiconductor interface and contacts during current collection. In light of series and shunt resistance presence, the current–voltage equation under illuminated condition is modified as given in Eq. (2.2) where the new variable n (ideality factor) is introduced which accounts for the nonideal p/n junction diode and $R_{s;}$ R_{sh} are series and shunt resistance respectively.

$$J = J_0[\exp(\frac{q(V - J.R_s)}{nkT}) - 1] + \frac{V - J.R_s}{R_{sh}} - J_L. \tag{2.2}$$

Above Eq. (2.2) is based on single diode model, however multi diode models are also considered in order to account the various recombination phenomenon in the solar cell and the Eq. (2.2) is further modified and is given by Eq. (2.3) where each term of J_{0k} and n_k represent a particular recombination mechanism (Altermatt et al. 1996).

$$J = \sum_{k=1}^{m} J_{0k}[\exp(\frac{q(V - J.R_s)}{n_k kT}) - 1] + \frac{V - J.R_s}{R_{sh}} - J_L. \tag{2.3}$$

In typical solar cell, the widely used model is two diode model which was first introduced in 1963 by Wolf and Raushenbach (1963). The two diode model-based equivalent circuit is shown in Fig. 2.15a. And for illuminated condition, the current–voltage characteristic is given in Eq. (2.4).

$$J = J_{01}[\exp(\frac{q(V - J.R_s)}{n_1 kT}) - 1] + J_{02}[\exp(\frac{q(V - J.R_s)}{n_2 kT}) - 1] + \frac{V - J.R_s}{R_{sh}} - J_L. \tag{2.4}$$

Here J_{01} and J_{02} are the saturation current densities through the two modeled diodes which separately represent recombination current densities of emitter/base, which dominates at high forward bias, and space charge region, which dominates at low forward bias, respectively (Pysch et al. 2007). Also, n_1 and n_2 are the ideality

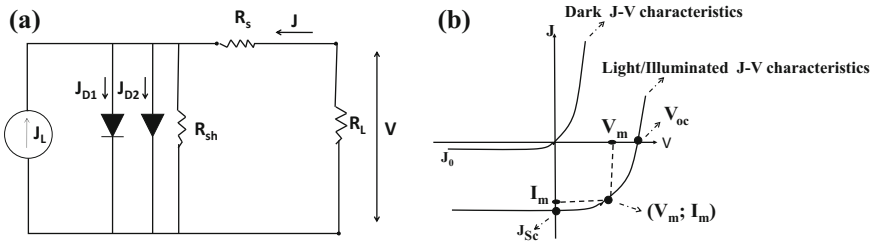

Fig. 2.15 **a** A typical solar cell equivalent circuit diagram with two diode model; **b** Current–voltage characteristics of a typical cell in dark and illuminated condition

factors representing for the two modeled diodes of the solar cell. A typical current–voltage (J-V) characteristic for a solar cell can be seen in Fig. 2.15b for both light/illuminated and dark measurement conditions. In dark condition, the photo-generated current (J_L) would be zero.

2.4.3 Important Solar Cell Parameters

2.4.3.1 Open Circuit Voltage (V_{oc})

When cell is illuminated and no current is drawn from the cell, the voltage obtained from the cell is called open circuit voltage (V_{oc}) (at J = 0 in Fig. 2.15b).V_{oc} is function of photogenerated current (J_L), reverse saturation current (J_0), ideality factor (n), and cell temperature (T). It is expressed in mathematical form as in Eq. (2.5).

$$V_{oc} = \frac{nkT}{q} \ln\left(\frac{J_L}{J_0} + 1\right). \tag{2.5}$$

Here V_{oc} dependence on J_0 makes it dependent on recombination effect in the cell. For better V_{oc} from the cell, the recombination in the cell should be avoided. V_{oc} is also influenced by temperature. Per degree centigrade increase in temperature of the cell results in about 1.7 mV reduction in V_{oc} in case of c-Si-based solar cells (Goetzberger et al. 1998).

2.4.3.2 Short Circuit Current (J_{sc})

When cell is illuminated and short circuited, the current obtained from the cell is called short circuit current (J_{sc}) (at V = 0 in Fig. 2.15b). It is the maximum current that can be drawn from the cell. For Si-based cell, if all the photons are absorbed, about 46.6 mA/cm^2 current can be expected (neglecting all electrical and optical losses) in AM 1.5G radiation (radiation falling on earth surface is 100 mW/cm^2 in AM 1.5G condition).

2.4.3.3 Maximum Power (P_{max})

Maximum power (P_{max}) indicates the maximum achievable power from the solar cell when it is illuminated. It is the product of voltage (V_m) and current (J_m) at optimal operating point (see Fig. 2.15b). At P_{max}, d(J.V)/dV = 0 and P_{max} can be also be expressed in terms of V_{oc} as given in Eq. (2.6).

$$P_{max} = V_m.J_m = \frac{nkT}{q}\ln\left[\frac{\left(\frac{J_L}{J_o}\right)+1}{1+\left(\frac{nkT}{q}\right)V_m}\right].\ J_m \approx \left[V_{oc} - \frac{nkT}{q}\ln\left(1 + \frac{V_m}{\left(\frac{nkT}{q}\right)}\right)\right].\ J_m. \tag{2.6}$$

2.4.3.4 Fill Factor (FF)

Fill factor is defined as the ratio of maximum achievable power (P_{max}, i.e., $V_m.J_m$) from the device to the maximum power generation capacity of the device (i.e., $V_{oc}.J_{sc}$). It is expressed as Eq. (2.7).

$$FF = \frac{V_m.J_m}{V_{oc}.J_{sc}}. \tag{2.7}$$

FF of the cell is influenced by resistive losses and nonideal recombination in solar cells. It is also a measure of the p/n junction quality and series resistance (R_s) of the cell. Also, significant shunt effect ($R_{sh} < 1000\ \Omega\text{-cm}^2$) in the cell would impact FF of the cell. In practical c-Si solar cells, FF mostly observed between 0.78 and 0.80 depending upon the quality of contact on the cell fabricated and the cell manufacturing process. Note that the poor contact quality may result in much lesser FF.

2.4.3.5 Efficiency (η)

Quantitatively, efficiency is defined as the ratio of output from a device to the input and is important parameter to quantify the device performance. In solar cell, the efficiency is defined as ratio of maximum achievable power to the input power. It depends on the incident light intensity and spectrum as well as temperature of the cell. Terrestrial cells are measured under standard test conditions (STC) with simulated AM1.5G radiation. The cell temperature is kept at 25 °C. For AM 1.5G spectrum, incident power (P_{in}) is 100 mW/cm^2 and maximum achievable power from a device is P_{max} (=$V_m.J_m$).

Mathematically, Efficiency(η) is expressed as Eq. (2.8):

$$\eta = \frac{P_{max}}{P_{in}} = \frac{V_m.J_m}{P_{in}} = \frac{FF.V_{oc}.J_{sc}}{P_{in}}. \tag{2.8}$$

2.4.3.6 Quantum Efficiency (QE)

Quantum efficiency (QE) is used as a diagnostic tool to evaluate the solar cell performance. It helps in analyzing the cell performance quantitatively as well as

qualitatively. Solar cell responds to different wavelengths differently. Photon of particular wavelength absorbed in solar cell generate e-h pair and depending upon the number of photons in spectrum for a particular wavelength, number of e-h pairs are generated. Percentage of photons of particular wavelength converted into e-h pairs which contribute to electrical current (collected from device) when the cell is short circuited is called quantum efficiency (QE). QE is further divided into two categories known as external quantum efficiency (EQE) and internal quantum efficiency (IQE).

(i) **External Quantum Efficiency (EQE):** EQE is defined as the ratio of number of electrons collected from solar cell under short circuit condition to the number of photons of particular wavelength incident on the cell. It is also known as Incident Photon to Current Efficiency (IPCE). EQE (in %) can be mathematically expressed as Eq. (2.9):

$$EQE(\lambda) = \frac{1240 \times J_L}{\lambda \times P_{in}} \times 100, \tag{2.9}$$

where λ is incident photon wavelength in nm, J_L is photogenerated current from the incident photon (in mA/cm^2) and P_{in} is incident photon power (W/m^2).

(ii) **Internal Quantum Efficiency (IQE):** IQE is defined as the ratio of number of electrons collected from solar cell under short circuit condition to the number of photons of particular wavelength absorbed by the cell. Note that IQE does not include the reflected or transmitted photons in account. IQE (in %) can be mathematically expressed as Eq. (2.10):

$$IQE(\lambda) = \frac{EQE(\lambda)}{(1 - R - T)} \times 100, \tag{2.10}$$

where R is reflectance from the cell and T is transmittance through the cell. In case of c-Si solar cell, back surface is fully covered with metal contact which makes T = 0% and the IQE is generally expressed as Eq. (2.11):

$$IQE(\lambda) = \frac{EQE(\lambda)}{(1 - R)} \times 100. \tag{2.11}$$

Here to note that IQE is corrected form of EQE which does not account for reflection losses in the cell and it is considered as better indicator of solar cell bulk material, the p-n junction, front and back surface passivation quality, etc. Since high-energy photons are absorbed near front surface of the cell, IQE at high-energy wavelengths indicates the junction and front surface passivation quality. Also, low-energy photons travel deep into the cell, IQE at lower energy wavelength

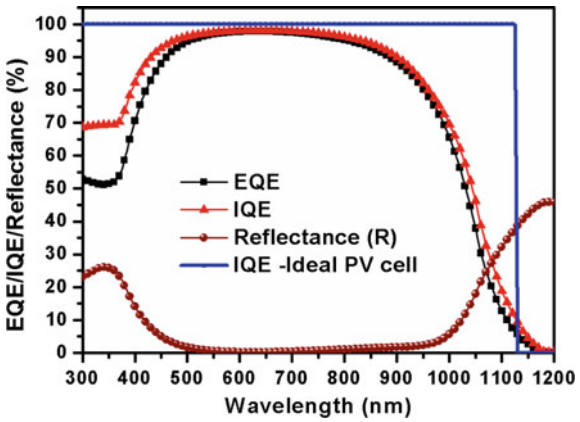

Fig. 2.16 EQE, IQE and reflectance graph plot of a typical c-Si solar cell and IQE of a ideal c-Si PV cell

indicates the bulk property of the cell as well as the back surface passivation quality. In ideal case, IQE should be 100%, however, in realistic case; it is always less than 100% reflecting the loss of generated e-h in recombination. To get maximum performance from the cell, the cell should be designed such that the IQE be maximum for the wavelengths which are in abundance in the incident light spectrum. QE curve of a typical c-Si-based solar cell is shown in Fig. 2.16.

One can see that for high-energy photons, IQE is less and this loss can be attributed to front surface recombination. Also, nonactive absorbing layer, e.g. ARC layers, may result in parasitic absorption leading to IQE loss. Also, at low-energy wavelengths, IQE loss can be seen which can be attributed to low absorption, low minority carrier lifetime, back surface recombination, etc.

2.5 Role of Light-Trapping Structures

c-Si wafers are made up of silicon (Si) which is an indirect band gap semiconductor. Light absorption and corresponding excitation of an electron from valance band to conduction band is week in indirect band gap semiconductor as it does not satisfy the requirement of momentum conservation since top of the valence band and bottom of the conduction band does not occur on same momentum (k) in energy (E)–momentum (k) diagram as shown in Fig. 2.17. To conserve the momentum, the optical absorption is assisted by phonon which is quantized lattice vibration. A phonon is either emitted or absorbed during the process of photon absorption (Pankove 1971) and result in electron transition from valance band to conduction band. Due to involvement of phonons in optical absorption, the absorption coefficient of an indirect band gap semiconductor is proportional to energy band gap (E_g) and phonon energy (E_p) as per relation as given in Eq. 2.12 where E is photon energy (Sze and Ng 2006).

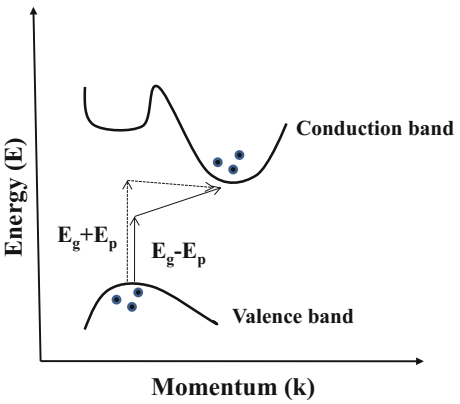

Fig. 2.17 E-k diagram of a typical indirect band semiconductor (after Ref. (Pankove 1971))

$$\alpha(E) \propto (E - E_g \pm E_p)^2. \tag{2.12}$$

Due to indirect band gap nature of Si, it weekly absorbs light especially at longer wavelength near its band gap where the absorption coefficient is very small (Fig. 2.18a). Figure 2.18a shows the absorption coefficient (α) of Si in cm^{-1} along with absorption length (1/α), a length required to absorb light completely for a particular wavelength. It can be noticed that a 100-μm-thick c-Si wafer would be sufficient to absorb light up to 950 nm wavelength. However, above 950 nm till band gap of Si (1.12 eV), much thicker material is required. For 1150 nm wavelength, the required thickness of material is about 10 mm. Using such thick material is infeasible, particularly from the perspective of cost.

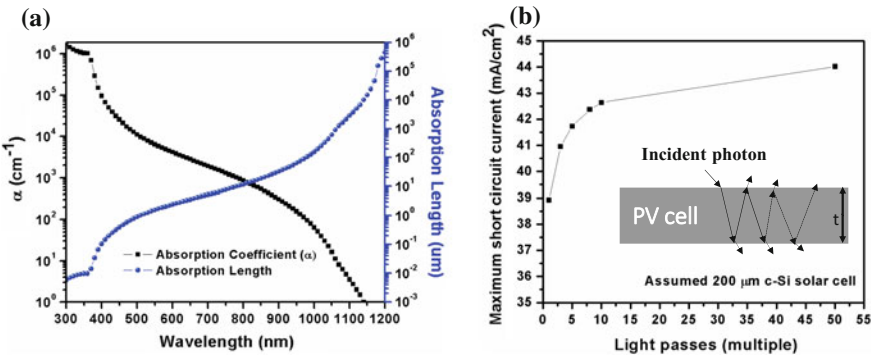

Fig. 2.18 **a** Wavelength dependence of absorption coefficient (α) of Si in cm^{-1} (after Ref. (Green and Keevers 1995)) along with absorption length; **b** Maximum short circuit current that can be generated after multiple light passing through active absorbing material of c-Si solar cell of 200 μm thickness

When targeting cell using c-Si wafer, the wavelengths in solar spectrum which are of interest are 300–1200 nm. In order to absorb this entire wavelength range, large thickness of wafer would be required. However, if light is made to travel back-and-forth in the solar cell (in active absorbing material), the optical thickness of the solar cell can be increased while keeping the geometrical thickness same. This can be used useful in reducing the thickness of the wafer required, which can be obtained by suitably optimized light-trapping structure. Figure 2.18b shows the maximum short circuit current that can be generated after multiple light passes through active absorbing material of c-Si solar cell of 200 μm thickness. For single pass, the maximum expected short circuit current is 38.9 mA/cm^2 which is increased to 42.4 mA/cm^2 for 8 passes and 44.0 mA/cm^2 for 50 passes. It can be noticed that how an efficient light-trapping structure can result in optical thickness increment of the cell keeping the same geometrical thickness (200 μm in present case), and hence increase in current generation capacity. This indicates the necessity of a suitable light-trapping structure in Si-based cell where cost-effectiveness and efficiency both are desired.

The Si flat surface results in reflection in the range of 35–50%. In order to reduce reflection from Si surface, surface texturization is done where Si surface is intentionally made rough. In 1974, Haynos reported the first evidence of reflection reduction in Si solar cell using Si surface texturing (Haynos et al. 1974). The cells were made using (100) Si wafer and anisotropic etching. These texturing-based cells resulted in efficiency of 15.0–15.5% under AM0 radiation which would be equivalent to 16.7–17.2% under AM1.5G radiation (Green et al. 1999). Yablonovitch and Cody (1982), Yablonovitch (1982) theoretically showed using statistical ray optics approach that light-trapping absorption can be enhanced maximum up to $4n^2$, where n is the refractive index, for weekly absorbing wavelengths by surface roughening of a semiconductor surface.

2.6 ITRPV Roadmap for c-Si Solar Cell Development

Global leaders in manufacturing of c-Si products, e.g., wafers, cells and modules, came together and created International Technology Roadmap for Photovoltaic (ITRPV). The first ITRPV report result was published in 2010. The aim of ITRPV was to ensure constant efficiency increase along with the cost reduction with the help of technology advancements. ITRPV provides a common platform to discuss the sustainable PV market; guideline for whole c-Si PV technology supply chain (includes silicon, c-Si wafer, c-Si module, inverter, and PV system, etc.); ground for cooperation among the supply chain; guideline for material and equipment suppliers; target for R&D centers and PV standardization source; which are regularly updated.

The topics presented in the ITRPV report are divided into three main areas, i.e., materials, process, and products. In this section we would discuss some of the proposed improvements in near further at cell level only.

The recent 2014 ITRPV reports (ITRPV 2015) indicate that poly silicon price has been reduced from 67 USD/kg in 2010 to 16.6 USD/kg in 2014, i.e., about 75% reduction in price in just 4 years and even further reduction in prices is indicated. In wafer sawing technology, slurry-based wafer sawing is dominating. However, diamond wire sawing is expected to gain market in near future with targeted kerf loss of less than 20 μm. Further, as per latest poly Si prices and wafer manufacturing technology, wafer still accounts for 51% of the cost in cell price and need for technology to reduce the thickness of the wafer has been envisioned. Wafer thickness of 100–120 μm range would possibly be in mass production made by 2025.

Improvements in process technology have been aimed to reduce recombination losses in solar cells. Reduction in bulk recombination current ($J_{o,bulk}$) of the solar cell has been targeted from 350 to 100 fA/cm^2 for p-type multi c-Si solar cell and from 250 to 50 fA/cm^2 for p-type mono c-Si solar cells. Emphasis to improve rear side passivation of the cell has been given to improve the cell performance. Silicon oxynitride ($SiON_x$)/Aluminum oxide (Al_2O_3) has been indicated as potential dielectric for back surface passivation.

Also, reduction in silver mass by reducing contact finger width for contacts has been proposed along with introduction of copper (Cu) plating technology for contact fabrication as an alternative to Ag to make solar cell even more cheaper.

2.7 Next Generation c-Si Solar Cells

For making solar cell cheaper, thinner wafer is being targeted for solar cell manufacturing and it is expected to be available in mass production by 2025. Top-down as well as bottom-up approaches are being actively researched for fabricating thin wafer-based c-Si solar cells. In bottom-up approach, epitaxial grown c-Si layer on substrates using porous layer transfer method are being explored. Layer transfer techniques consist of three important steps which are (Petermann et al. 2012):

i. HF acid-based electrochemical pores etching into a silicon substrate wafer.
ii. Epitaxial growth of mono c-Si layer on the porous silicon.
iii. Separation of the epitaxial layer from the growth wafer.

Recently, a 16.8% efficient 18-μm silicon solar cell on steel substrate was demonstrated using such method where the 18 μm n-type silicon as active absorbing layer was expitaxially grown with 2 μm front surface n^+ layer and 1 μm rear p^+ layer with shallow texturing on the top (front surface) (Wang et al. 2014). The cell was having architecture more like PERL cells where the front contact was made using Ni-Cu plating through dielectric opening at front. Also, in another effort to make thin c-Si wafer-based cells, similar technique of porous layer transfer was followed to fabricate 43 μm thin c-Si solar cell which resulted in 19% efficiency. The schematic of the solar cell device structure is shown in Fig. 2.19a.

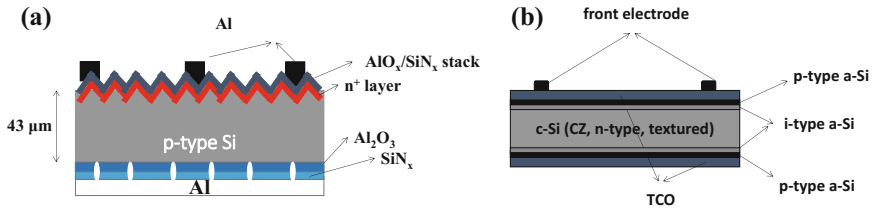

Fig. 2.19 **a** Schematic of porous layer transfer based 43 µm thin c-Si solar cell (after Ref. (Petermann et al. 2012)); **b** schematic of HIT cell using less than 100 µm thin c-Si wafer (after Ref. (Taguchi et al. 2014))

The cell has rear surface passivation using dielectric which is necessity for efficient thin wafers-based solar cells. The back contact was made using local opening in dielectric and subsequent Al evaporation. Also, the front surface was textured and had about 4 µm random pyramids for light trapping.

In top-down approach, different wafers cutting techniques are being explored to manufacture thin wafers with minimum kerf loss and ITRPV projects to have 100–120 µm thin wafers in mass production by 2025. Up to 25% efficiency cell on less than 100 µm thin c-Si wafer has been demonstrated recently (Taguchi et al. 2014). The solar cell is known as heterojunction with intrinsic thin layer (HIT) cell. The typical schematic of the HIT cell is shown in Fig. 2.19b. In HIT solar cell, p/n heterojunction is formed using intrinsic (i-type) amorphous silicon (a-Si) layer and a p-type a-Si layer deposited on a randomly textured n-type CZ c-Si wafer. The a-Si (n-type and i-type) deposited on the opposite side of the wafer provide back surface field passivation. The high-quality intrinsic a-Si layer between the c-Si wafer and the doped a-Si layer helps to achieve very good surface passivation which is crucial in thin wafer-based solar cells. For contacts, transparent conductive oxide (TCO) layers and metal grid electrodes are fabricated on both sides.

The trend of fabricating cost-effective and efficient cell indicates that the next generation solar cells are going to be fabricated on much thinner (50–100 µm) wafers. In such case, rear surface passivation and light-trapping structure would be

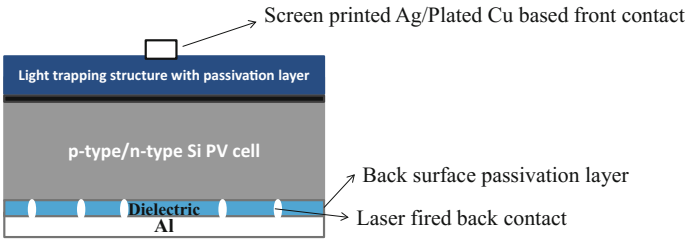

Fig. 2.20 Schematic of a typical next generation thin c-Si solar cell

playing important role in manufacturing efficient and cost-effective solar cells. The next generation cell would have typical device structure as shown in Fig. 2.20. The back surface passivation would be essential part of the cell and laser firing-based contact (LFC) would be preferable option for back contact formation (Schneiderlochner et al. 2002; Sánchez-Aniorte et al. 2010; Petermann et al. 2012; Wang et al. 2014). Front contact can be screen printed Ag/Al or plated Cu based contacts.

The front surface would have light-trapping structure with antireflection coating. Advanced light-trapping structure would replace texturing-based light-trapping structure since texturing of surface increases surface recombination which is more crucial when thinner wafer are being aimed. Texturing-based light-trapping structures also consume material and also results in reduction in absorption in active material. Traditional light-trapping structure as well as advanced alternative light-trapping structures favorable for next-generation thin c-Si solar cells has been explored in this book in greater detail in subsequent chapters.

2.8 Questions and Problems

1. Discuss the role of wafer prices on solar cell manufacturing cost over the years?
2. Classify the different c-Si-based solar cell technology in detail?
3. Mono c-Si solar cells generally perform better than multi c-Si solar cells. Why?
4. Discuss the evolution of c-Si solar cell technology?
5. How modification in c-Si solar cell design and processes impacted the cell performance over the years?
6. What are the main factors which drove the c-Si solar cell cost down over the years?
7. What do you understand by HIT cell? How is different from mono and multi c-Si solar cell technology?
8. Discuss the fabrication steps involved in solar cell manufacturing of a typical c-Si solar cell?
9. What do you understand by photovoltaic effect in c-Si solar cell?
10. Discuss the performance parameters of a solar cell. How are they interrelated?
11. The short circuit current of a c-Si solar cell at room temperature is 36 mA/cm^2 and the reverse saturation current is 10^{-8} mA/cm^2. Calculate the maximum output power and efficiency of the cell under AM1.5G radiation. Consider that the device ideality factor is 1 and the fill factor is 76%.
12. What do understand by ITRPV? How does it play role in c-Si solar cell technology development?
13. Discuss the next generation c-Si solar cells and the role of light-trapping structures?

References

Altermatt PP, Heiser G, Aberle AG et al (1996) Spatially resolved analysis and minimization of resistive losses in high-efficiency Si solar cells. Prog Photovolt Res Appl 4:399–414. doi:10.1002/(sici)1099-159x(199611/12)4:6<399:aid-pip148>3.0.co;2-4

Blakers AW, Zhao J, Milne AM et al (1990) Characterization of 23-percent efficient silicon solar. Technology 37:331–336

Dongre G, Zaware S, Dabade U, Joshi SS (2015) Multi-objective optimization for silicon wafer slicing using wire-EDM process. Mater Sci Semicond Process 39:793–806. doi:10.1016/j.mssp.2015.06.050

Goetzberger A, Knobloch J, Voss B (1998) Crystalline silicon solar cells. Wiley (1998)

Green MA (2009) The path to 25% silicon solar cell efficiency: history of silicon cell evolution. Prog Photovolt Res Appl 17:183–189. doi:10.1002/pip.892

Green MA (2002) Photovoltaic principles. Phys E Low-Dimensional Syst Nanostruct 14:11–17. doi:10.1016/S1386-9477(02)00354-5

Green MA, Emery K, Hishikawa Y et al (2015) Solar cell efficiency tables (version 46). Prog Photovolt Res Appl 23:805–812. doi:10.1002/pip.2637

Green MA, Zhao J, Wang A, Wenham SR (1999) Very high efficiency silicon solar cells-science and technology. IEEE Trans Electron Devices 46:1940–1947. doi:10.1109/16.791982

Green MA, Keevers MJ (1995) Optical properties of intrinsic silicon at 300 K. Prog Photovolt Res Appl 3:189–192. doi:10.1002/pip.4670030303

Haynos J, Allison J, Arndt R, Meulenberg A (1974) The COMSAT nonreflective silicon solar cell: a second generation improved cell. In: International conference on photovoltaic power generation, p 18

International technology roadmap for photovoltaic (ITRPV) 2013 results (2014) www.itrpv.net/Reports/Downloads/2014/

ITRPV (2015) International technology roadmap for photovoltaic (ITRPV) 2014 results

NREL (2016) Best research cell efficiencies. http://www.nrel.gov/ncpv/images/efficiency_chart.jpg

Pankove JI (1971) Optical processes in semiconductors. Dover

Petermann JH, Zielke D, Schmidt J et al (2012) 19%-efficient and 43 μm-thick crystalline Si solar cell from layer transfer using porous silicon. Prog Photovolt Res Appl 20:1–5. doi:10.1002/pip.1129

Pysch D, Mette A, Glunz SW (2007) A review and comparison of different methods to determine the series resistance of solar cells. Sol Energy Mater Sol Cells 91:1698–1706. doi:10.1016/j.solmat.2007.05.026

Sánchez-Aniorte I, Colina M, Perales F, Molpeceres C (2010) Optimization of laser fired contact processes in c-Si solar cells. Phys Procedia 5:285–292. doi:10.1016/j.phpro.2010.08.148

Schneiderlochner E, Preu R, Ludemann R, Glunz SW (2002) Laser-fired rear contacts for crystalline silicon solar cells. Prog Photovolt Res Appl 10:29–34. doi:10.1002/pip.422

Sze SM, Ng KK (2006) Physics of semiconductor devices, 3rd edn. Wiley, Hoboken

Taguchi M, Yano A, Tohoda S et al (2014) 24.7% record efficiency HIT solar cell on thin silicon wafer. IEEE J Photovolt 4:96–99. doi:10.1109/JPHOTOV.2013.2282737

Tanaka N (2010) Technology roadmap: solar photovoltaic energy. OECD Publishing

Treble F (1998) Milestones in the development of crystalline silicon solar cells. Renew Energy 15:473–478. doi:10.1016/S0960-1481(98)00207-9

Wang L, Lochtefeld A, Han J et al (2014) Development of a 16.8% efficient 18-μm silicon solar cell on steel. IEEE J Photovolt 4:1397–1404. doi:10.1109/JPHOTOV.2014.2344769

Wolf M, Rauschenbach H (1963) Series resistance effects on solar cell measurements. Adv Energy Convers 3:455–479. doi:10.1016/0365-1789(63)90063-8

Yablonovitch E (1982) Statistical ray optics. J Opt Soc Am 72:899–907. doi:10.1364/JOSA.72.000899

Yablonovitch E, Cody GD (1982) Intensity enhancement in textured optical sheets for solar cells. IEEE Trans Electron Devices 29:300–305. doi:10.1109/T-ED.1982.20700

Zhao J, Wang A, Altermatt P et al (1996) 24% efficient perl silicon solar cell: recent improvements in high efficiency silicon cell research. Sol Energy Mater Sol Cells 41–42:87–99. doi:10.1016/0927-0248(95)00117-4

Chapter 3
Principle of Dielectric-Based Anti-reflection and Light Trapping

This chapter explores the interference-based anti-reflection and light trapping methodologies for solar cell applications. When two monochromatic coherent waves having constant phase difference meet, the interference phenomena is observed. Detailed analysis of interference-based anti-reflection and principle behind the observed phenomenon has been covered. Starting from simple reflection and interference of the reflected light from single dielectric coating, the phenomenon of anti-reflection has been covered and extended to multilayer anti-reflection coating applications. The thickness and refractive index of a dielectric layers are the two most important parameters of concerns for their use as anti-reflection coatings. Correlation with reflectance minima with wavelength and dielectric layer parameters has been presented. Experimental measurements of reflectance for various suitable anti-reflection coatings have also been presented and compared with the theoretical results. At the end, benefits and limitations of dielectric-based reflectance have been discussed in context of c-Si solar cells.

3.1 Reflection, Refraction, and Transmission from Dielectric Interfaces

When light (electromagnetic wave/radiation) incident and interact at the interface of two different dielectric materials having different refractive indices (RI's), phenomenon of reflection, refraction, and transmission is observed.

3.1.1 Reflection, Refraction, and Transmission

The phenomenon where some fraction of light is reflected is called reflection and this fraction is quantized and termed as reflection coefficient or reflection amplitude.

© Springer Nature Singapore Pte Ltd. 2017

C.S. Solanki and H.K. Singh, *Anti-reflection and Light Trapping in c-Si Solar Cells*, Green Energy and Technology,
DOI 10.1007/978-981-10-4771-8_3

The term reflectance (R) is used to represent the proportion of light getting reflected back at the interface with respect to incident light/radiation. Further; the phenomenon of light deflection from its path while entering in other medium from interface is called refraction. The light deflection from its path is governed by the refractive index (RI) of the material. The light entering into the medium at interface of two dielectric medium either gets absorbed or transmitted depending upon the absorption coefficient of the material/medium as discussed in Sect. 1.7. The term absorbance (A) is used to represent the proportion of light getting absorbed within the medium with respect to incident light/radiation. Also, the phenomenon where some fraction of light gets through the second medium without getting absorbed within the medium is called transmission and the term transmittance (T) is used to represent the proportion of light getting transmitted through the medium at the interface with respect to incident light/radiation. At any given point and time, the reflectance (R), transmittance, (T) and absorbance (A) are related as in Eq. (3.1).

$$R + A + T = 1 \tag{3.1}$$

Reflection, refraction, and transmission phenomenon at an interface of two different dielectric medium having refractive index n_1 and n_2 respectively can be seen in Fig. 3.1. The radiation having amplitude r_i incident at interface of two different dielectrics at an incident angle θ_i from normal gets reflected at an angle θ_r from normal with amplitude r_r and refracted/transmitted at an angle θ_t from normal with amplitude r_t. The plane which contains the incident ray/radiation and the normal is known as plane of incidence. Experimental observations have shown that the phenomenon of light reflection, refraction, and absorption follows certain laws.

At an interface of two dielectric medium, the reflected radiation (r_r) lies in the same plane as incident radiation (r_i) and angle of reflection is same as angle of incidence, i.e., $\theta_i = \theta_r$. This is known as law of reflection. Also, the refracted/transmitted radiation (r_t) from interface lies in the same plane and the

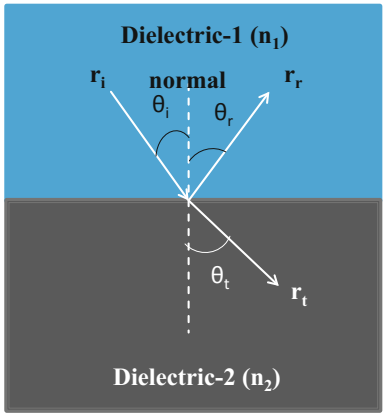

Fig. 3.1 Schematic of electromagnetic (light) reflection, refraction and transmission at an interface between two dielectric medium having refractive index n_1 and n_2 respectively. Subscript "i" stands for incident radiation, "r" for reflected radiation and "t" for refracted or transmitted radiation

angle of refraction is related with angle of incidence as per Eq. (3.2). This relation is known as law of refraction or Snell's law.

$$n_2 \sin\theta_t = n_1 \sin\theta_i \tag{3.2}$$

It indicates that the propagation of light in denser medium (high refractive index) is closer to surface normal. Note that all the laws as mentioned above fall under ray optics, required for understanding of the light propagation, reflection, and refraction. However, it does not describe the diffraction, polarization, and interference phenomenon observed when the electromagnetic waves/light interact with each other. These concepts are well treated in wave optics.

3.1.2 *Wave Optics Based Interaction of Light with Dielectric Medium and Interfaces*

Diffraction, polarization, and interference phenomenon which are the key to explain the observed reflection, absorption, and transmission accurately through dielectric medium and interfaces are explored under wave optics which follows Huygen's principle and describes optical phenomenon based on electromagnetic theory following Maxwell's Eqs. (3.3)–(3.6).

$$\vec{\nabla}.\vec{E} = \frac{\rho_f}{\varepsilon} \tag{3.3}$$

$$\vec{\nabla}.\vec{B} = 0 \tag{3.4}$$

$$\vec{\nabla} \times \vec{E} = -\frac{\partial \vec{B}}{\partial t} \tag{3.5}$$

$$\vec{\nabla} \times \vec{B} = \mu\sigma\vec{E} + \mu\varepsilon\frac{\partial \vec{E}}{\partial t}, \tag{3.6}$$

where $\vec{E}$ is electric field and $\vec{B}$ is magnetic field component of the electromagnetic wave/light usually expressed as Eqs. (3.7) and (3.8) (Griffiths 1999).

$$\vec{E}(\vec{r}, t) = \bar{E}_0 e^{i(\vec{k}.\vec{r}-\omega t)}\hat{n} \tag{3.7}$$

$$\vec{B}(\vec{r}, t) = \bar{B}_0 e^{i(\vec{k}.\vec{r}-\omega t)}(\hat{k} \times \hat{n}) \tag{3.8}$$

Here,ρ_f is free charge density. ε is permittivity which is indicator of dielectric medium ability to generate electric field per unit charge available in the medium. μ is permeability which is indicator of dielectric medium ability to get magnetized within itself when influenced by an applied magnetic field $\vec{B}$.σ is conductivity of the

dielectric. $\hat{n}$ is polarization vector, and $\vec{k}$ is propagation vector whose magnitude k is known as wave number represented by $\sqrt{\varepsilon}\frac{\omega}{c}$, where ω is angular frequency of electromagnetic wave/light and c is velocity of light.

At interface of the two dielectric medium, the incident (i), reflected (r), and transmitted (t) light would be continuous and would satisfy the following boundary conditions for electric and magnetic fields as mentioned in Eqs. (3.9) and (3.10).

$$\vec{E}^{(i)}(\vec{r},t) + \vec{E}^{(r)}(\vec{r},t) = \vec{E}^{(t)}(\vec{r},t) \tag{3.9}$$

$$\vec{H}^{(i)}(\vec{r},t) + \vec{H}^{(r)}(\vec{r},t) = \vec{H}^{(t)}(\vec{r},t) \tag{3.10}$$

The above two equations are the key to solve the electromagnetic equations for the case when light or any electromagnetic wave interact with matter at any interface having different refractive indices.

3.1.3 Fresnel Equations for Reflection and Transmission

Fresnel equations are solution of electromagnetic equations for light interaction at interface having different refractive indices. It accounts for the reflection and transmission of light from a dielectric interface and is helpful in estimating the faction of light/electromagnetic radiation that would be reflected or transmitted from the interface. In derivation of Fresnel equations, it is assumed that the surface/interface is flat and dielectric medium is homogenous. In Fresnel equations, the light is treated as plane wave. The light from sun coming to earth are randomly polarized or unpolarized. However, the mathematical treatment of unpolarized light is complicated. For mathematical analysis, the unpolarized light is assumed as superposition of two polarized waves whose plane of oscillation is perpendicular to each other. Here plane of oscillation is defined as plane containing electric field vectors. Figure 3.2a shows the representation of an unpolarized light consisting waves with randomly directed electric fields. Figure 3.2b shows the representation of unpolarized light in the form of superposition of two polarized waves having plane of oscillation perpendicular to each other. This is to represent the difference in physical behavior of s-polarized and p-polarized light which in combination can be used to represent the unpolarized light. Since, mathematically we can not do calculations representing the unpolarized light, the mathematical calculations are done for s-polarized and p-polarized light and results of these calculations are combined to draw conclusion for unpolarized light.

Here s-polarized light is defined as the light whose electric field vectors are perpendicular to the plane of incidence. The plane of incidence is defined as plane containing the incident, reflected, and refracted electromagnetic radiation/ray (yz plane in Fig. 3.3). Also, p-polarized light is defined as the light whose electric field vectors are parallel to the plane of incidence.

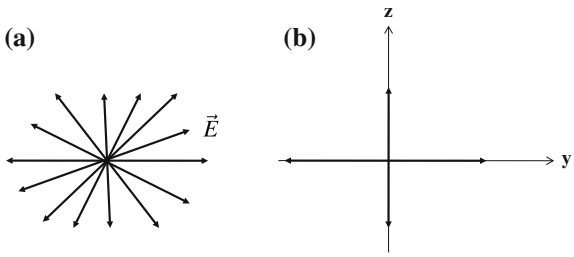

Fig. 3.2 **a** Unpolarized light consisting waves with randomly oriented electric fields; **b** representation of unpolarized light in form of superposition of two polarized waves having plane of oscillation perpendicular to each other

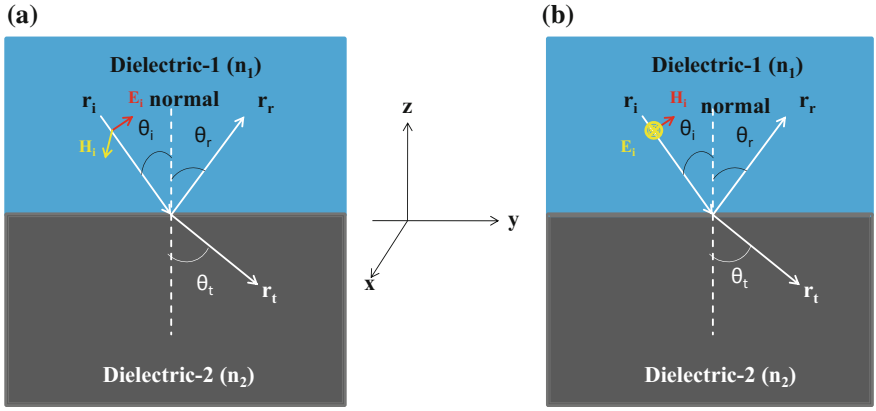

Fig. 3.3 Schematic for incident, reflection, refraction plane and light interaction at dielectric interface for the case of **a** incident electromagnetic wave (light) parallel to the plane of incident (p-polarized light); **b** incident electromagnetic wave (light) perpendicular to the plane of incident (s-polarized light)

Solving the Maxwell electromagnetic equations with boundary conditions (Eqs. 3.9 and 3.10) gives the Fresnel equations for normalized reflected (r_r) and transmitted (r_t) electromagnetic radiation/light amplitudes for the case p-polarized light and s-polarized light. These equations are given as Eqs. (3.11)–(3.14), where the dielectric medium has been assumed to be nonmagnetic which is true for most of the optical materials.

$$r_r^p = \frac{n_2 \cos\theta_i - n_1 \cos\theta_t}{n_2 \cos\theta_i + n_1 \cos\theta_t} \tag{3.11}$$

$$r_r^s = \frac{n_1 \cos\theta_i - n_2 \cos\theta_t}{n_1 \cos\theta_i + n_2 \cos\theta_t} \tag{3.12}$$

$$r_t^p = \frac{2n_1 \cos\theta_i}{n_2 \cos\theta_i + n_1 \cos\theta_t} \tag{3.13}$$

$$r_t^s = \frac{2n_1 \cos\theta_i}{n_1 \cos\theta_i + n_2 \cos\theta_t} \tag{3.14}$$

Here, r_r^p and r_r^s represent the normalized amplitudes of the reflected light for p-polarized and s-polarized case, respectively. Also, r_t^p and r_t^s represent the normalized amplitudes of the transmitted/refracted light for p-polarized and s-polarized case, respectively. n_1 is the refractive index of the first medium and n_2 is the refractive index of second medium (see Fig. 3.3). θ_i and-θ_t are angle of incidence and refraction respectively from normal.

The reflectance (R) for the p-polarized and s-polarized light is defined as square of normalized reflected (r_r) light amplitude. The reflectance of the p-polarized light and s-polarized light is given by Eq. (3.15) and Eq. (3.16), respectively.

$$R^p = (r_r^p)^2 = \frac{(n_2 \cos\theta_i - n_1 \cos\theta_t)^2}{(n_2 \cos\theta_i + n_1 \cos\theta_t)^2} \tag{3.15}$$

$$R^s = (r_r^s)^2 = \frac{(n_1 \cos\theta_i - n_2 \cos\theta_t)^2}{(n_1 \cos\theta_i + n_2 \cos\theta_t)^2} \tag{3.16}$$

Further, assuming that there is no loss of energy at boundary/interface, the transmittance (T) can be given by Eq. (3.17) and Eq. (3.18) for p-polarized light and s-polarized light, respectively.

$$T^p = 1 - R^p = \frac{4n_1 n_2 \cos^2\theta_i}{(n_2 \cos\theta_i + n_1 \cos\theta_t)^2} \tag{3.17}$$

$$T^s = 1 - R^s = \frac{4n_1 n_2 \cos^2\theta_i}{(n_1 \cos\theta_i + n_2 \cos\theta_t)^2} \tag{3.18}$$

For unpolarized light, the reflectance and transmittance is calculated as average of reflectance (R) for the p-polarized and s-polarized light as shown in Eq. (3.19) and Eq. (3.20), respectively.

$$R = \frac{R^p + R^s}{2} \tag{3.19}$$

$$T = \frac{T^p + T^s}{2} \tag{3.20}$$

For solar cell application, it is important that the light reaches to active absorbing material, where photovoltaic effect takes place and hence the reflection from surface

should be minimum. In c-Si solar cell, reflection from air–Si interface is obvious as there is dielectric medium change where refractive index (RI) changes. The reflectance from interface for different wavelengths would be different as the refractive index of a material is wavelength dependent parameter. The reflection form air–Si interface can be minimized for selected wavelengths by introducing dielectric thin film layer at interface as discussed in next section.

3.2 Dielectric Thin Films and Their Role in Reflection Reduction

As discussed above when light falls on any interface of two different dielectrics, the phenomenon of reflection, refraction, and transmission is observed. In solar cell operation, there is need to minimize the reflection from the surface to allow maximum light to travel into the active absorber material and get absorbed. The reflection can be engineered by introducing a thin dielectric film at the top of absorber layer. Depending upon the thickness and refractive index of the introduced thin dielectric film, the reflection from surface can be tuned. The dielectric layer with refractive index n_2 introduced between two dielectric layers with refractive indices n_1 and n_3 results in creating another interface affecting the incident light as shown in Fig. 3.4a. The incident radiation/light now gets reflected from interface of dielectrics with RI's n_1 and n_2 as well as at interface of dielectrics with RI's n_2 and n_3.

In such case, the interference occurs between the rays reflected from the two interfaces. Depending upon the phase difference between the two reflected rays (ray or wave amplitudes r_{12} and r_{23}), constructive or destructive interference occur

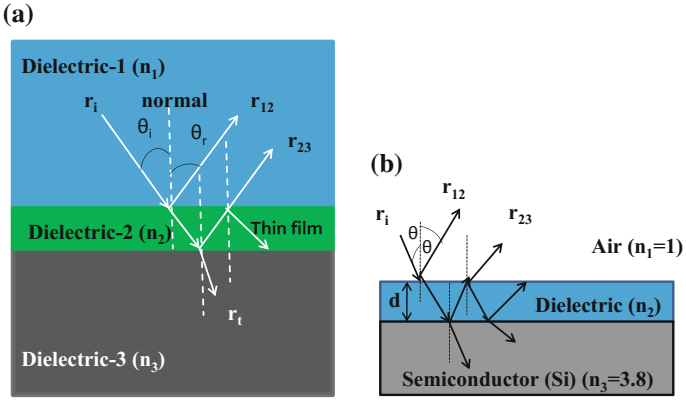

Fig. 3.4 Schematic for reflection, refraction of incident rays at thin dielectric film with refractive index n_2 introduced at interface of two dielectric medium with refractive indices n_1 and n_3, respectively; **b** dielectric film with thickness "d" and refractive index "n_2" introduced at interface air (refractive indices $n_1 = 1$) and Si (refractive indices $n_3 = 3.8$) respectively

which leads to high or low reflection from the interface. The phase difference ($\Delta\phi$) between the two reflected rays (r_{12} and r_{23}) is related with the path difference between the two rays (which is approximately equal to the double of the thin dielectric film thickness) as given in Eq. (3.21):

$$\Delta\phi = \frac{2\pi n}{\lambda} \times 2d, \tag{3.21}$$

where n is refractive index of medium in which path difference occur, λ is wavelength of light, and d is the thickness of the dielectric thin film. Hence, the phase difference between the two reflectance rays through the thin dielectric medium would be

$$\Delta\phi = \frac{2\pi n_2}{\lambda} \times 2d \tag{3.22}$$

The reflected rays would result in high resultant reflection from the interface for wavelength λ if the total phase difference is 0, 2π, 4π, 6π, etc., i.e., even multiple of π. It would result in a resultant reflection minimum if the total phase difference is 0, π, 3π, 5π, etc., i.e., odd multiple of π. Now to count the total phase difference, it is important to know that whenever light incident at interface from lighter dielectric medium (low refractive index) to denser dielectric medium (high refractive index), there would be always a phase change of π. However, no phase change occurs during refraction and for the case of light incident at interface from denser medium to lighter dielectric medium. The sum of interface-based phase shift and the phase shift introduced by path difference due to dielectric thin film gives total phase difference between the reflected rays. It means if $n_2 > n_1$ and $n_2 > n_3$(see Fig. 3.4a), the path difference between the two rays (2d) with $(m+1/2)\frac{\lambda}{n_2}$, where m is a whole number (m = 0, 1, 2, 3…) would result in high resultant reflection from the interface for wavelength λ as it would make total phase difference an even multiple of π since r_{12} would see a phase shift of π at dielectric-1–dielectric-2 interface ($n_2 > n_1$) and no phase shift for r_{23} at dielectric-2–dielectric-3 ($n_2 - n_3$) interface ($n_2 > n_3$). Also, a resultant reflection minimum would be observed if the path difference between the two rays (2d) is $(m)\frac{\lambda}{n_2}$ which would make total phase difference an odd multiple of π.

Here also by solving Maxwell electromagnetic equations with appropriate boundary conditions, Fresnel equations for normalized reflected (r_r) and transmitted (r_t) electromagnetic radiation amplitudes for the case p-polarized light and s-polarized light can be obtained which can be used to calculate the reflectance from the interface as discussed in above section. The Fresnel equation based reflectance in such case is given by Eq. (3.23):

$$R = \frac{r_{12}^2 + r_{23}^2 + 2r_{12}r_{23}\cos(\Delta\phi)}{1 + r_{12}r_{23} + 2r_{12}r_{23}\cos(\Delta\phi)}, \tag{3.23}$$

where r_{12} is the reflection amplitude between dielectric-1 to dielectric-2 interface and r_{23} is the reflection amplitude between dielectric-2 and dielectric-3 interface (see Fig. 3.4a) and this Eq. (3.23) is true for both p-polarized and s-polarized light independently which can be calculated similar to Eqs. (3.11)–(3.20). $\Delta\phi$ is phase difference between rays r_{12} and r_{23} calculated as per Eq. (3.22).

Experimentally measured total reflectance from c-Si wafer and c-Si wafer coated with dielectric anti-reflection layer (75 nm thick silicon nitride (SiN_x)) for near normal incident light is shown in Fig. 3.5. Notice that the reflection for c-Si is much higher than the c-Si coated with silicon nitride dielectric layer. Also, for the case of dielectric coated layer there is a clear reflection minima seen at around 580–590 nm.

This position of reflection minima at around 570–580 nm is due to fact that the condition destructive interference gets satisfied for these wavelengths. Wavelength for which the reflection minima would occur is given by Eq. (3.24):

$$\Delta\phi = \frac{2\pi n_2}{\lambda} \times 2d = 2\pi\left(m + \frac{1}{2}\right), \tag{3.24}$$

where m is whole number (m = 0, 1, 2, 3…). Here odd multiple of π is taken as refractive index of air ($n_1 = 1$) is less than the dielectric thin film refractive index (SiN_x; $n_2 = 1.95$); and refractive index of c-Si substrate ($n_3 = 3.8$) is greater than the dielectric thin film refractive index (SiN_x; $n_2 = 1.95$) ($n_2 > n_1$ and $n_3 > n_2$; see Fig. 3.4b). So to keep the total phase difference an odd multiple of π for reflection minima, the phase difference introduced by path length reference with the help of thin SiN_x dielectric film should be odd multiple of π as light incident at interface from lighter dielectric medium (low refractive index) to denser dielectric medium (high refractive index) at interface and both rays undergo an interface-based phase change of π. So here total 2π interface-based phase change which is different from the case as discussed above for case of $n_2 > n_1$ and $n_2 > n_3$, where total

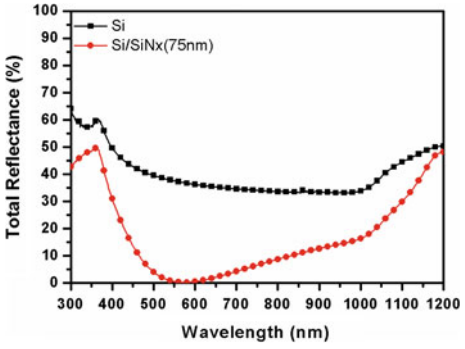

Fig. 3.5 Measured total reflectance from a c-Si wafer and a c-Si wafer coated with 80 nm silicon nitride (SiN_x) dielectric layer for near normal incident light

interface-based phase change is only π. So considering m = 0 in Eq. (3.24), the equation is modifies as:

$$\frac{2\pi n_2}{\lambda_{\min}} \times 2d = \pi \tag{3.25}$$

Therefore, wavelength at which the reflection minima would occur would be given by following equation

$$\lambda_{\min} = 4d.n_2 \tag{3.26}$$

In this case, n_2 is 1.95 and d = 75 nm and hence λ_{min} would theoretically be at around 585, which is also observed at similar wavelength range in experimentally measured data presented in Fig. 3.5.

3.3 Role of Refractive Index and Dielectric Medium

As discussed in above Sects. 3.1 and 3.2, when light falls on an interface of two dielectric materials of different refractive indices, reflection, refraction, and transmission would occur. The faction of light which would be reflected or transmitted at the interface is governed by the refractive index of the material or medium. Refractive index (also known as index of refraction) of a material/medium is expressed as the ratio of speed of light in vacuum (c) to the phase velocity of light in material/medium (v) as given in Eq. (3.27) and indicates the bending of light when it passes from one medium to other.

$$n = \frac{c}{v} \tag{3.27}$$

If refractive index of a material is 2, it indicates that the light travels two times slower in the material/medium compared to in vacuum. This speed difference comes from the bending of light from its original path during refraction. Refractive index of a material/medium is different for different wavelengths and is also a characteristic of a material or medium. For better light anti-reflection in solar cells, it is necessary to choose suitable dielectric material so that the reflection can be minimized from the interface. There are many dielectrics, e.g., silicon dioxide (SiO_2), silicon nitride (SiN_x), titanium oxide (TiO_2), aluminum oxide (Al_2O_3), magnesium fluoride (MgF_2), amorphous silicon (a-Si), silicon carbide (SiC), etc., which can be used as anti-reflection coating. The refractive index plot for some dielectric materials mostly used for anti-reflection effect in c-Si solar cells is shown in Fig. 3.6 for 300–1200 nm wavelength range.

Let us evaluate the impact of refractive index on reflection from interface of two dielectrics and for the case where the interface is coated with thin dielectric thin film for anti-reflection effect. For simplicity of calculations and understanding, assume

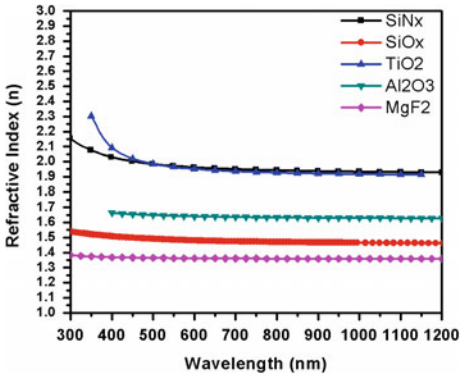

Fig. 3.6 Wavelength dependent refractive index for Silicon nitride (SiN_x) (Duttagupta et al. 2012), Silicon oxide (SiO_x) (McIntosh et al. 2014), Titanium oxide (TiO_2) (Richards 2003), Aluminum oxide (Al_2O_3) (Kumar et al. 2009), and magnesium fluoride (MgF_2) (Siqueiros et al. 1988)

that the normal incident of light at the interface, that means the ray incident at the interface at an angle $\theta_i = 0^o$(r_i in Fig. 3.3 and Fig. 3.4).

Case I: Consider the case of two dielectrics (dielectric-1 and dielectric-2) interface as shown in Fig. 3.3, where light falls from dielectric-1 and goes through interface to dielectric-2. For the case of normal incidence of light, θ_i would be 0°. And from Snell's law of refraction as given in Eq. (3.2), $\cos(\theta_t)$ would be given by Eq. (3.28):

$$\cos\theta_t = \sqrt{1 - (\frac{n_1}{n_2})^2 Sin^2\theta_i} \tag{3.28}$$

which results in $\cos(\theta_t) = 1$; and the reflectance and transmittance Eqs. (3.19)–(3.20) would be transformed into following form:

$$R = \frac{(n_1 - n_2)^2}{(n_1 + n_2)^2} \tag{3.29}$$

$$T = 1 - R = \frac{4n_1 n_2}{(n_1 + n_2)^2} \tag{3.30}$$

It is clear from Eq. (3.29) that the reflection would be minimum if the refractive index is same of both dielectrics. However, in c-Si solar cells, light comes from air (refractive index ~ 1) and falls on air–Si interface. The reflectance from Si surface for light of wavelength 680 nm (refractive index ~ 3.8 at 680 nm) in such case would be around 34–36% which is really high and would require minimization.

Case II: In case II, let us consider the case of two dielectrics (dielectric-1 and dielectric-2) interface where interface is coated with thin dielectric thin film for anti-reflection effect as shown in Fig. 3.4. Here again for the case of normal incidence of light, θ_i would be 0^o and $\cos(\theta_t) = 1$ as discussed above. The reflectance in this case would be resultant of $R_{12,}$ i.e., the reflectance between dielectric-1 to

dielectric-2 interface and $R_{23,}$ i.e., the reflectance between dielectric-2 to dielectric-3 interface (see Fig. 3.4a) as discussed in Sect. 3.2. Here since there are three dielectrics are involved, two more cases can arise:

Situation (II-a): $n_1 < n_2 < n_3$ or $n_1 > n_2 > n_3$
In such situation, interface-based phase shift would be same at both dielectric interface $n_1 - n_2$ and $n_2 - n_3$ (see Fig. 3.4a) and minimum reflection would be observed for path difference based phase shift $\Delta\phi = \frac{2\pi n_2}{\lambda} \times 2d = 2\pi(m + \frac{1}{2})$(where m = 0, 1, 2, 3…) which means if $\cos(\Delta\phi) = -1$, the Eq. (3.23) can be rewritten for minimum reflection as:

$$R_{\min} = \frac{r_{12}^2 + r_{23}^2 - 2r_{12}r_{23}}{1 + r_{12}r_{23} - 2r_{12}r_{23}} = \frac{(r_{12} - r_{23})^2}{(1 - r_{12}r_{23})^2} \tag{3.31}$$

For the case of normal incidence of light, θ_i would be 0^o and $\cos(\theta_t)$ at second interface would also be 1. And the minimum reflection equation would be as follows:

$$R_{\min} = (\frac{n_1 n_3 - n_2^2}{n_1 n_3 + n_2^2})^2 \tag{3.32}$$

Equation (3.32) indicates that to have minimum reflection (zero or nearly zero) using dielectric thin film coating, the refractive index of the thin film dielectric should be square root of the top and bottom dielectrics.

$$n_2 = \sqrt{n_1 n_3} \tag{3.33}$$

For Si substrate (see Fig. 3.4b), the thin dielectric coating refractive index (n_2) should be around 1.9–2 for minimum reflection in visible wavelength range. Dielectric layers like SiN_x and TiO_2 are the promising candidates for anti-reflection coating.

Situation (II-b): $n_1 < n_2 > n_3$ or $n_1 > n_2 < n_3$
In such situation, interface-based phase shift would be introduced at only one dielectric interface $n_1 - n_2$ or $n_2 - n_3$ (see Fig. 3.4a), where the light enters from low refractive index medium to high refractive index medium. And minimum reflection would be observed for path difference based phase shift $\Delta\phi = \frac{2\pi n_2}{\lambda} \times 2d = 2\pi m$ (where m = 0, 1, 2, 3…), i.e., if $\cos(\Delta\phi) = 1$. Therefore, the Eq. (3.23) can be rewritten for minimum reflection as:

$$R_{\min} = \frac{r_{12}^2 + r_{23}^2 + 2r_{12}r_{23}}{1 + r_{12}r_{23} + 2r_{12}r_{23}} = \frac{(r_{12} + r_{23})^2}{(1 + r_{12}r_{23})^2}$$

Again here, for the case of normal incidence of light, θ_i would be 0^o and $\cos(\theta_t) = 1$. And the equation for minimum reflection would be as follows:

$$R_{\min} = \left(\frac{n_1 - n_3}{n_1 + n_3}\right)^2 \tag{3.32}$$

This situation indicates that there is no role of thin dielectric film (n_2) in reflection minimization when intermediate dielectric film refractive index is either higher or lower than both top and bottom dielectrics ($n_1 < n_2 > n_3$ or $n_1 > n_2 < n_3$).

This analysis suggests that minimum reflection using dielectric thin film coating can be achieved only when the dielectrics are arranged in graded manner either in decreasing or increasing order of refractive indices ($n_1 < n_2 < n_3$ or $n_1 > n_2 > n_3$).

3.4 Multilayer Dielectric Thin Films for Reflection Reduction

We have seen the role of a thin dielectric film at the interface of two dielectric medium as how it can be utilized to reduce reflection from surface. Also, it is explained in the previous section that to get minimum reflection from interface using anti-reflection coating, the refractive index should be either in increasing or decreasing order. The suitable design is obtained when the dielectric material refractive index is in decreasing order from top to bottom.

It is observed that using single-layer dielectric layer reflection from the surface can be minimized only at one particular wavelength. However for c-Si solar cells, it is desirable to minimize the reflection across the useful wavelength range of solar spectrum ranging from 300 to 1200 nm. By using multiple dielectric films as anti-reflection coatings, one can achieve multiple reflection minima from the surface which results in overall reduction in reflection. A multilayer thin dielectric film coated system can be seen in Fig. 3.7a. The condition for better anti-reflection from multiple dielectric films would be same as that of single film, i.e., the refractive indices of the thin dielectric coatings on interface should be in increasing order from top to bottom.

In multilayer anti-reflection coating, the reflection and transmission from each interface is important and governs the resultant reflection from the entire device/system. The Snell's law for refraction/reflection angle in the multilayer system is expressed as follows (see Fig. 3.7a):

$$n_i \sin\theta_i = n_2 \sin\theta_2 = n_p \sin\theta_p = n_{m+1} \sin\theta_t \; (\mathrm{p} = 1, 2, 3, 4 \ldots \mathrm{m} + 1) \tag{3.33}$$

The use of multilayer thin film coatings for reflection reduction should not result in increased cost, which is always an important constraints in solar cell applications. Invariable due to addition processing cost, as the number of anti-reflection films increases the cost also increases. As a result, at most, two layers or double-layer

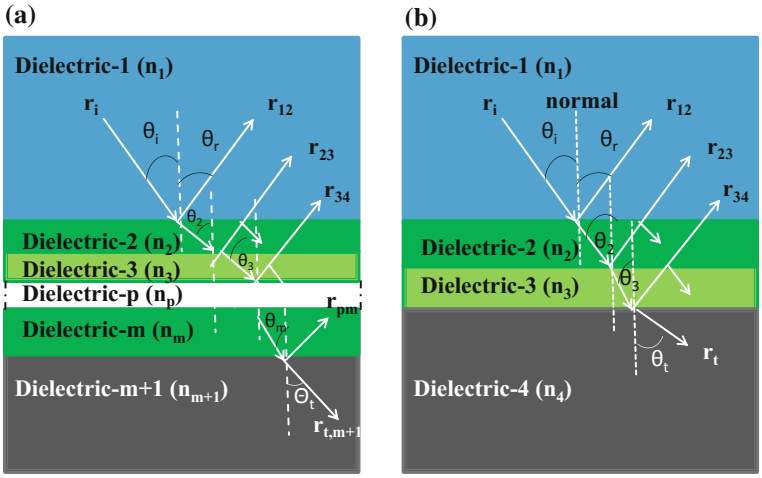

Fig. 3.7 Schematic of **a** a multilayer thin dielectric film coated interface of dielectric-1 and dielectric-(m+1); **b** double-layer thin dielectric film coated interface of dielectric-1 and dielectric-(4)

anti-reflection coatings are used in c-Si solar cells. Figure 3.7b shows a device schematic where two thin dielectric films has been introduced between the dielectric-1 and dielectric-4. In double-layer anti-reflection geometry, the Snell's law for refraction/reflection angle can be given as per Eq. (3.34):

$$n_1 \sin\theta_i = n_2 \sin\theta_2 = n_3 \sin\theta_3 = n_4 \sin\theta_t \tag{3.34}$$

$$\text{So, } \sin\theta_t = \frac{n_1}{n_4} \sin\theta_i \tag{3.35}$$

Solving Maxwell electromagnetic equations with appropriate boundary conditions, Fresnel equations for normalized reflected (r_r) and transmitted (r_t) electromagnetic radiation amplitudes for the case p-polarized light and s-polarized light can be obtained which can be used to calculate the reflectance from the interface as discussed in Sect. 3.1.

For multilayer anti-reflection coating, the Fresnel equation derivation is much more complex and is not being discussed here. The Fresnel equation for reflectance from double-layer anti-reflection coating as shown in Fig. 3.7b can be given by Eq. (3.36):

$$R = \frac{A + B + C + D + E}{F + G + H + I + J} \tag{3.36}$$

Here,

$$
\begin{aligned}
A &= r_{12}^2 + r_{23}^2 + r_{34}^2 + r_{12}^2 r_{23}^2 r_{34}^2 \\
B &= 2r_{12}r_{23}(1 + r_{34}^2)\cos(\Delta\phi_{12-23}) \\
C &= 2r_{23}r_{34}(1 + r_{12}^2)\cos(\Delta\phi_{23-34}) \\
D &= 2r_{12}r_{34}\cos(\Delta\phi_{12-23} + \Delta\phi_{23-34}) \\
E &= 2r_{12}r_{23}^2 r_{34}\cos(\Delta\phi_{12-23} - \Delta\phi_{23-34}) \\
F &= 1 + r_{12}^2 r_{23}^2 + r_{12}^2 r_{34}^2 + r_{23}^2 r_{34}^2 \\
G &= 2r_{12}r_{23}(1 + r_{34}^2)\cos(\Delta\phi_{12-23}) \\
H &= 2r_{23}r_{34}(1 + r_{12}^2)\cos(\Delta\phi_{23-34}) \\
I &= 2r_{12}r_{23}\cos(\Delta\phi_{12-23} + \Delta\phi_{23-34}) \\
J &= 2r_{12}r_{23}^2 r_{34}\cos(\Delta\phi_{12-23} - \Delta\phi_{23-34}),
\end{aligned}
$$

where r_{12} is the reflection amplitude between dielectric-1 to dielectric-2 interface, r_{23} is the reflection between dielectric-2 to dielectric-3 interface and r_{34} is the reflection between dielectric-3 to dielectric-4 interface (see Fig. 3.7b) and the Eq. (3.36) is true for both p-polarized and s-polarized light independently which can be calculated as per Eqs. (3.15), (3.16), and (3.19). The $\Delta\phi_{12-23}$ is phase difference between rays r_{12} and $r_{23}$and $\Delta\phi_{23-34}$ is phase difference between rays r_{23} and r_{34} calculated as per Eqs. (3.37) and (3.38):

$$\Delta\phi_{12-23} = \frac{2\pi n_2}{\lambda} \times 2d_2 \tag{3.37}$$

$$\Delta\phi_{23-34} = \frac{2\pi n_3}{\lambda} \times 2d_3, \tag{3.38}$$

where d_2 and d_3 is the thickness of thin dielectric films dielectric-2 and dielectric-3 respectively.It is clear from Eqs. (3.36), (3.37) and (3.38) that for better optimization of reflection from a double-layer anti-reflection coating, thickness of the two dielectric thin films and their refractive indices would play a crucial role.

Assuming the graded index pattern where $n_1 < n_2 < n_3 < n_4$ (see Fig. 3.7a), the minimum reflectance would be observed for path difference based phase shift $\Delta\phi_{12-23} = \frac{2\pi n_2}{\lambda} \times 2d_2 = 2\pi(m + \frac{1}{2})$ and $\Delta\phi_{23-34} = \frac{2\pi n_3}{\lambda} \times 2d_3 = 2\pi(m + \frac{1}{2})$ (where m = 0, 1, 2, 3…) which means if $\cos(\Delta\phi_{12-23})$ and $\cos(\Delta\phi_{23-34})$ is equal to −1, the interface-based phase shift would be same at all the dielectric interface $n_1 - n_2$, $n_2 - n_3$ and $n_3 - n_4$(see Fig. 3.7b) as the light travels from lighter to denser medium. In such case, $\cos(\Delta\phi_{12-23} + \Delta\phi_{23-34}) = 1$ and $\cos(\Delta\phi_{12-23} - \Delta\phi_{23-34}) = 1$ and the Eq. (3.36) can be rewritten for minimum reflection as:

$$R_{\min} = \frac{r_{12}^2 + r_{23}^2 + r_{34}^2 + r_{12}^2 r_{23}^2 r_{34}^2 - 2r_{12}r_{23}(1 + r_{34}^2) - 2r_{23}r_{34}(1 + r_{12}^2) + 2r_{12}r_{34} + 2r_{12}r_{23}^2 r_{34}}{1 + r_{12}^2 r_{23}^2 + r_{12}^2 r_{34}^2 + r_{23}^2 r_{34}^2 - 2r_{12}r_{23}(1 + r_{34}^2) - 2r_{23}r_{34}(1 + r_{12}^2) + 2r_{12}r_{23} + 2r_{12}r_{23}^2 r_{34}} \tag{3.39}$$

Equation (3.39) is true for both p-polarized and s-polarized light independently which can be calculated similar to Eqs. (3.11)–(3.20). For better anti-reflection using double anti-reflection coating, thickness of coatings and refractive index require proper optimization. The dielectric material and its thickness as an effective anti-reflection coating is decided by targeted wavelength range, where we want to minimize reflection. For c-Si solar cells, the wavelengths of our interest are 300–1200 nm, where we would need broadband anti-reflection effect for this whole wavelength range. Open source software's like OPAL2 (PVlighthouse; Mcintosh and Baker-finch 2012) and PC1D (PC1D 5.9) can be used for calculations and for better understanding for reflectance profile from multilayer dielectric thin films.

In c-Si-based solar cells for double anti-reflection coating (DLARC) based reflection minimization, mostly SiO_x and SiN_x dielectric or TiO_2 and MgF_2dielectric combination is used. In Fig. 3.8a, an example of simulated reflectance from Si substrate using 80 nm thin magnesium fluoride (MgF_2), 80 nm thin silicon nitride (SiN_x) and SiN_x (60 nm)-MgF_2 (40 nm) optimum combination is shown. Impact of DLARC over single-layer anti-reflection coating (ARC) and role of refractive index material on reflection reduction can be noticed. For single-layer ARC, silicon nitride (SiN_x) with refractive index about 2 is better choice than magnesium fluoride (MgF_2) with refractive index about 1.3 as it leads to relatively better anti-reflection effect as shown in Fig. 3.8a. Also, further improvement in anti-reflectance is expected for certain wavelengths when optimum combination of SiN_x (60 nm)-MgF_2 (40 nm) DLARC is used. For example, relatively better anti-reflection below 550 nm can be seen in Fig. 3.8a with combination of SiN_x (60 nm)-MgF_2 (40 nm) DLARC compared to 80 nm SiN_x ARC.

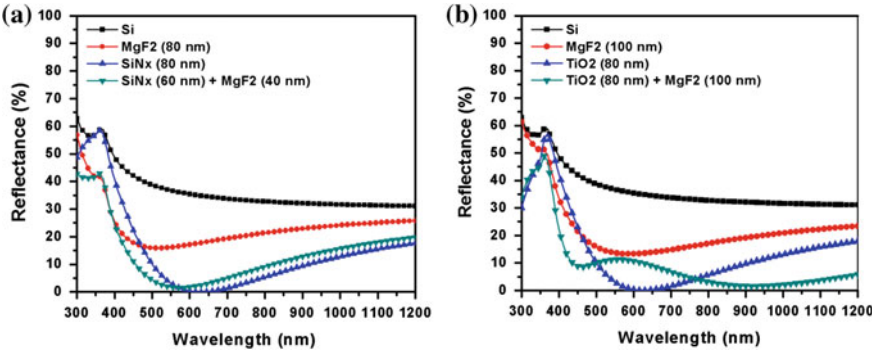

Fig. 3.8 Simulated reflectance from **a** Si substrate using 80 nm thin magnesium fluoride (MgF_2), 80 nm thin silicon nitride (SiN_x) and SiN_x (60 nm)-MgF_2 (40 nm) optimum combination; **b** Si substrate using 80 nm thin titanium oxide (TiO_2), 100 nm thin magnesium fluoride (MgF_2) and TiO_2 (80 nm)-MgF_2 (100 nm) optimum combination

Similarly, in Fig. 3.8b, an example of simulated reflectance from Si substrate using 80 nm thin titanium oxide (TiO_2), 100 nm thin magnesium fluoride (MgF_2), and TiO_2 (80 nm)-MgF_2 (100 nm) optimum combination is shown. Here again, impact of DLARC over single-layer anti-reflection coating (ARC) and role of refractive index material on reflection reduction can be noticed. Improvement in anti-reflectance for certain wavelengths is as expected when optimum combination of TiO_2 (80 nm)-MgF_2 (100 nm) DLARC is used. For example, relatively better anti-reflection below 500 nm and above 800 nm can be seen in Fig. 3.8b with combination of TiO_2 (80 nm)-MgF_2 (100 nm) DLARC compared to 80 nm TiO_2 ARC. Also, for combination of TiO_2 (80 nm)-MgF_2 (100 nm) DLARC, two reflection minima can be noticed at around 450 nm and 900 nm instead of single minima at around 600 nm as for 80 nm TiO_2. This is due to the condition met for destructive interference of light reflected from the dielectric interfaces at two different wavelengths in 300–1200 nm wavelength range. As discussed in Sect. 3.3 for reflection minimum, it is required that the phase shift ($\Delta\phi = \frac{2\pi n_2}{\lambda} \times 2d$) be integral multiple of π. For different combination of dielectric film thicknesses and refractive indices, reflection minima can be achieved for two or more wavelengths in 300–1200 nm wavelength range.

3.5 Additional Functionality of Dielectric Anti-reflection Layers

As discussed in above sections for reflection minimization using dielectric thin films, refractive index and thickness of dielectric thin film should be optimized such that it would be in accordance with targeted wavelength range for which the reflection is to be minimized. However, the suitability of dielectric material is not only decided by its reflection minimization property. In c-Si solar cells, these dielectric thin films also serves the purpose of surface passivation and this should be also taken care of while choosing the dielectric material.

c-Si surface sees abrupt discontinuity of crystal structure which leads to unsaturated valance bonds of Si atoms in the crystal, also known as dangling bonds (see Fig. 3.9a). These dangling bonds act as recombination center and reduce the minority carrier life time in the Si material (Goetzberger et al. 1998; Aberle 2001; Rahman 2012; Choi et al. 2012). To avoid such recombination at surface, surface passivation is done either by chemical passivation or by field passivation methods. In chemical passivation, thin dielectric films helps to passivate the dangling bonds present at c-Si surface and result in reduction of interface defects which would had acted as recombination center instead. In field passivation method, the concentration of electron or hole is significantly reduced at the surface/interface by means of built in electric field. The recombination process happens when both electron and

holes are present and recombination at interface would be maximum when electron and holes are available in equal magnitude (Rahman and Khan 2012). The magnitude of electrons or holes at interface can be altered by means of providing electrostatic field at interface which repels a particular type of charge carrier (electron/hole). This is done either by engineering the doping profile below the interface or by fixed insulator charges at the interface. The term "surface recombination velocity (SRV)" is used to quantify the passivation quality. The surface recombination velocity indicates the rate of recombination between electron and hole at surface/interface. For well-passivated surface, the SRV should be as low as possible within cost constraints. A dielectric thin films would act as good passivation layer if it suitably passivates the dangling bonds chemically at Si surface and also provide sufficient fixed insulator charges (see Fig. 3.9b).

Now, it should be clear that how the passivation ability of a particular dielectric thin film is also crucial apart from the refractive index and appropriate thickness of the dielectric thin film used as anti-reflector. In p-type c-Si solar cells, mostly SiN_x-based dielectric thin film is used as anti-reflector which also offers better passivation of emitter due to fixed positive insulator charges at SiNx/Si interface (Aberle 2001). In n-type c-Si solar cells, mostly Al_2O_3-based dielectric thin film is used as anti-reflector which also offers better passivation of emitter due to fixed negative insulator charges (in the range of 10^{12}–10^{13}/cm^2) at Al_2O_3/Si interface (Rahman and Khan 2012). In some high-efficiency solar cells, double-layer anti-reflector is used such as stack of SiN_x/SiO_2, SiN_x/Al_2O_3, TiO_x/SiN_{x-}, TiO_x/Al_2O_3 (Aberle 2001; Rahman and Khan 2012; Davis et al. 2015) which offers better surface passivation along with desired anti-reflection property.

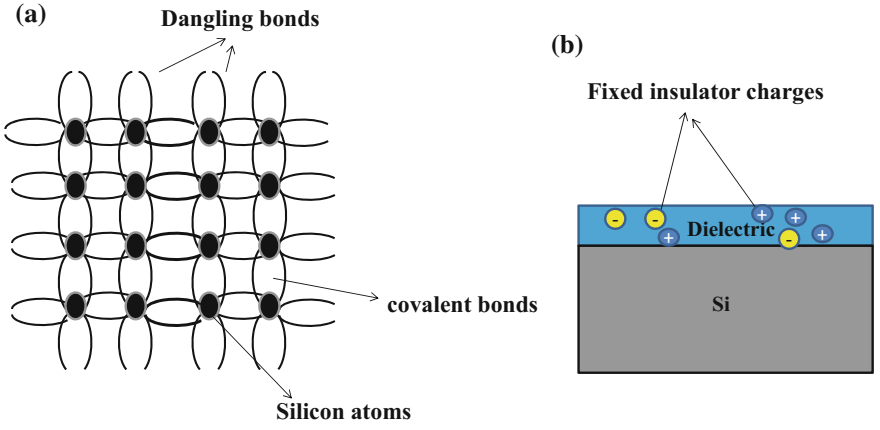

Fig. 3.9 Schematic of **a** Si crystal structure and unsaturated covalent bonds (dangling bonds); **b** Fixed insulator charges in dielectric thin film and dielectric-Si interface

3.6 Limitation of Dielectric-Based Anti-reflection Structure

As it is seen in above sections for reflection minimization, optimization of dielectric thin film thickness and refractive index is important. Additionally the dielectric layer also has to play the role of surface passivation. The minimization of reflection for broad wavelength range (300–1200 nm) using interference-based technique, as presented in this chapter, has its own limitations. It has been seen in Eq. 3.26, for a given thickness and refractive index the reflection can be minimized but only for certain wavelengths. The same is demonstrated in Fig. 3.10b for measured reflectance from a Si substrate coated with SiN_x dielectric thin film of different thickness and refractive index in the range of 1.92–1.96. As the thickness of SiN_x dielectric thin film increases, the reflection is reduced and a reflection minima is seen for particular wavelength, where condition of phase shift for destructive interference, between incident and reflected light, is met as discussed in Sect. 3.3.

More than one minima can be seen when increasing the dielectric thin film/anti-reflector layer thickness as for 160 nm SiN_x film coated substrate in Fig. 3.10b. This is due to reflection minima condition met for different combination of dielectric film thicknesses and refractive indices in 300–1200 nm wavelength range as discussed in above Sect. 3.4. However, increasing thickness does not result in broadband reflection minimization though significant reflection reduction is achieved for certain wavelengths of light as already seen from Eq. (3.26) as discussed in Sect. 3.2.

A technical term "weighted reflectance (WR)" is used to quantify and compare the reflectance from various samples. Weighted reflectance is weighted average of reflectance weighted with incident radiation falling on earth surface in

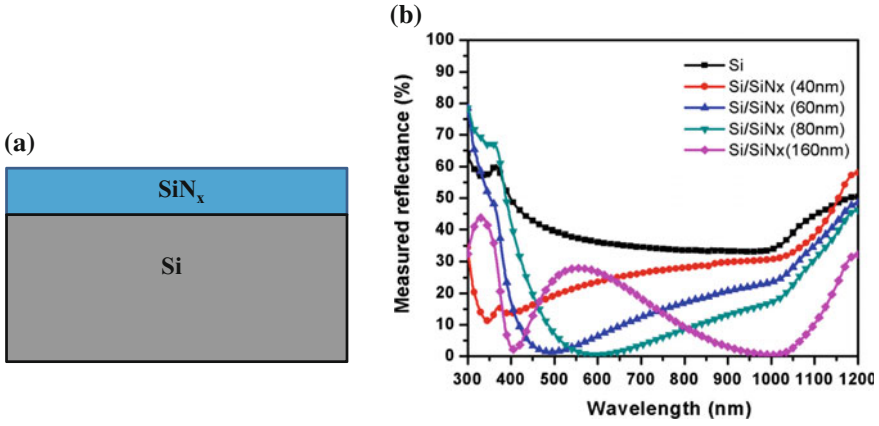

Fig. 3.10 **a** Schematic of a c-Si substrate coated with silicon nitride (SiN_x) thin film; **b** measured total reflectance from c-Si substrate and substrates coated with SiN_x of different thickness (40, 60, 80 and 160 nm)

AM 1.5G condition. The calculation of weighted reflectance can be done using Eq. (3.40) (Singh et al. 2016).

$$WR = \frac{\sum_{\lambda_1}^{\lambda_2} (R_{Total}(\lambda) \times I_{1.5G}(\lambda))d\lambda}{\sum_{\lambda} I_{1.5G}(\lambda)d\lambda}\% \tag{3.40}$$

In Eq. (3.40), $R_{total}(\lambda)$ represents the measured total reflectance from the sample for wavelength λ; $I_{1.5G}(\lambda)$ represents the spectral irradiance in $W/m^2/nm$ for AM 1.5G at wavelength λ as per IEC 60904-3 (Standard IEC 60904-3 2008). The $d\lambda$ is wavelength interval for sampled data used for calculation which can be 1 nm or 5 nm as per availability of the data. λ_1–λ_2 is the wavelength range for which WR is to be calculated. For c-Si-based solar cell, λ_1 is usually 300 nm and λ_2 is 1200 nm. It should be noted that the total reflectance accounts for reflectance from surface, not only in particular direction obeying Snell's law but also all other directions too. For smooth flat surface, the total reflectance is generally equal to specular reflectance which follows the Snell's law. However, if there is any roughness which may lead to scattering of light, total reflectance from surface becomes important.

Following Eq. (3.40), the weighted reflectance calculated from reflectances of the samples, shown in Fig. 3.10b, has been given in Table 3.1. The data indicated that WR for Si is about 38.5% and is brought down to 13.8% using 80 nm SiN_x anti-reflection layer.

Working on refractive index and thickness of SiN_x anti-reflection layer, the weighted reflectance can be brought down to 12–13% but still it is significant and should be further minimized. For doing this, other approaches are used and many other are being explored. One approach is to randomized light and enhances the light trapping in silicon solar cells further using surface texturization. More details of surface texturization based light trapping technology has been covered in next chapter.

Table 3.1 Calculated weighted reflectance for samples for which the measured reflectance is presented in Fig. 3.10b

Sample	Weighted reflectance (%) (for 300–1200 nm)
Si	38.5
Si/SiN_x (40 nm)	25.1
Si/SiN_x (60 nm)	14.8
Si/SiN_x (80 nm)	13.8
Si/SiN_x (160 nm)	16.3

3.7 Questions and Problems

1. What do you understand from reflection, refraction, and transmission through dielectric interfaces?
2. Discuss the laws of reflection and refraction.
3. What do you understand from the terms "ray optics" and "wave optics"? Which one is more suitable to explain the interference, diffraction, and polarization phenomenon?
4. Discuss the boundary conditions which are the key to theoretically explain the observed reflection and transmission from dielectric interfaces?
5. What do you mean by Fresnel equations? Discuss the reflection and transmission through dielectric interfaces using Fresnel Eqs.
6. How dielectric thin films help in reflection reduction from any surface/interface? Discuss the appropriate Fresnel equations which can be used to predict the reflection behavior from a dielectric surface/interface?
7. What do you understand from interface-based phase shift and path length based phase shift? How refractive index of a dielectric material plays role in phase shifting in case of electromagnetic ray/wave interacting with the dielectric material?
8. What would be the condition for reflection minimization if the light incident on a dielectric surface coated with thin dielectric materials having refractive indices n_1, n_2, n_3 from top to bottom such that $n_1 < n_2 < n_3$? Assume that the dielectric material used as substrate has highest refractive index.
9. List the commonly used dielectric materials used for anti-reflection effect in c-Si solar cells?
10. What are the parameters which are to be considered when deciding the choice of dielectric material for anti-reflection purpose in solar cells?
11. If you are asked to design an anti-reflector which can minimize the reflection at 600 nm wavelength light from Si surface, what would be your choice as anti-refection material? How much thickness of the anti-refection material would be needed to achieve the goal?
12. What are the limiting factors which hold dielectric thin film based anti-reflection technology implementation as sole technology for light trapping purpose in c-Si solar cells?
13. A Si substrate has been coated with a dielectric material having refractive index 2.5. The coating thickness of the dielectric material is 60 nm. For which wavelengths of light you expect the reflection from coated substrate would be minimum? Assume that Si substrate has refractive index 3.8

References

Aberle AG (2001) Overview on SiN surface passivation of crystalline silicon solar cells. Sol Energy Mater Sol Cells 65:239–248. doi:10.1016/S0927-0248(00)00099-4

Choi P-H, Kim H-J, Baek D-H, Choi B-D (2012) A study on the electrical characteristic analysis of c-Si solar cell diodes. JSTS J Semicond Technol Sci 12:59–65. doi:10.5573/JSTS.2012.12.1.59

Davis KO, Jiang K, Habermann D, Schoenfeld WV (2015) Tailoring the optical properties of APCVD titanium oxide films for all-oxide multilayer antireflection coatings. IEEE J Photovolt 5:1265–1270. doi:10.1109/JPHOTOV.2015.2437272

Duttagupta S, Ma F, Hoex B et al (2012) Optimised antireflection coatings using silicon nitride on textured silicon surfaces based on measurements and multidimensional modelling. In: Energy procedia, pp 78–83

Goetzberger A, Knobloch J, Voss B (1998) Crystalline silicon solar cells. Wiley

Griffiths DJ (1999) Introduction to electrodynamics, 3rd edn.

Kumar P, Wiedmann MK, Winter CH, Avrutsky I (2009) Optical properties of Al2O3 thin films grown by atomic layer deposition. Appl Opt 48:5407. doi:10.1364/AO.48.005407

Mcintosh KR, Baker-finch SC (2012) OPAL 2.0: rapid optical simulation of practical silicon solar cells. In: 38th IEEE PVSC 265. doi:10.1109/PVSC.2012.6317616

McIntosh KR, Kho TC, Fong KC et al (2014) Quantifying the optical losses in back-contact solar cells. In: 2014 IEEE 40th Photovoltaic Specialist Conference (PVSC). IEEE, pp 0115–0123

PC1D 5.9 PC1D (ver 5.9) Software for modelling a solar cell

PVlighthouse OPAL2: Optical simulator. https://www2.pvlighthouse.com.au/calculators/OPAL2/OPAL2.aspx

Rahman MZ (2012) Modeling minority carrier' s recombination lifetime of p-Si Solar Cell

Rahman MZ, Khan SI (2012) Advances in surface passivation of c-Si solar cells. Mater Renew Sustain Energy 1:1. doi:10.1007/s40243-012-0001-y

Richards BS (2003) Single-material TiO2 double-layer antireflection coatings. Sol Energy Mater Sol Cells 79:369–390. doi:10.1016/S0927-0248(02)00473-7

Singh HK, Arunachalam B, Kumbhar S et al (2016) Opto-electrical performance improvement of mono c-Si solar cells using dielectric–metal–dielectric (D-M-D) sandwiched structure-based plasmonic anti-reflector. Plasmonics 11:323–336. doi:10.1007/s11468-015-0049-5

Siqueiros JM, Machorro R, Regalado LE (1988) Determination of the optical constants of MgF2 and ZnS from spectrophotometric measurements and the classical oscillator method. Appl Opt 27:2549. doi:10.1364/AO.27.002549

Standard IEC 60904-3 (2008) Measurement principles for terrestrial PV solar devices with reference spectral irradiance data

Chapter 4
Principle of Texturization for Enhanced Light Trapping

In this chapter, exploration on methodologies of texturization for light trapping has been presented. Starting from impact of surface morphology on light trapping, detailed analysis and principle behind the observed phenomenon from textured surfaces has been discussed. For any real solar cell application, the decision for choosing the light trapping structure depends on its cost effectiveness and potential for generating higher current from the solar cells under given solar spectrum. Analytical analysis on current generation potential based on optical path length enhancement capability for different light trapping structures appropriate for c-Si solar cells has been covered. Also, light trapping structures for both mono as well as multi c-Si wafer based cells has been discussed along with, benefits and limitations of different surface morphology based light trapping structures.

4.1 Surface Morphology and Its Impact on Light Reflection, Refraction and Transmission

As we have seen in previous chapter, when the light incident on any planer surface, the phenomenon of reflection, refraction and transmission occurs. In planer surface, the reflected light lies in the same plane as incident light and angle of reflection is same as angle of incidence, i.e., $\theta_i = \theta_r$ as per law of reflection. The refracted/transmitted light from interface lies in the same plane and the angle of refraction is related with angle of incidence, as per Eq. (3.2) which is known as law of refraction. A typical schematic light reflection, refraction and transmission can be seen in Fig. 4.1a for planer surface case of an absorbing material.

When the surface is rough, light interaction on material's surface gets changed. The reflected light is not observed in the same plane and the angle of incident light and the angle of reflection is not necessarily in the same as the angle of incidence, i.e., $\theta_i \neq \theta_r$. Note that the laws of reflection and refraction are always valid for given

© Springer Nature Singapore Pte Ltd. 2017

C.S. Solanki and H.K. Singh, *Anti-reflection and Light Trapping in c-Si Solar Cells*, Green Energy and Technology,
DOI 10.1007/978-981-10-4771-8_4

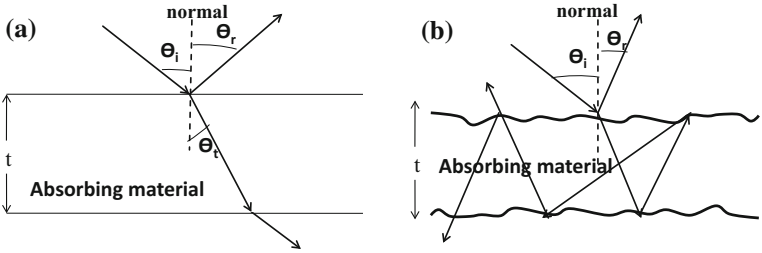

Fig. 4.1 Schematic of light reflection, refraction and transmission on **a** planer surface ($\theta_i = \theta_r$); **b** rough surface ($\theta_i \neq \theta_r$)

point and time, however, in rough surface case, the surface orientation changes at the adjacent points and light go through multiple interaction at rough surface before it is observed to the observer as reflected light. As a result, the final observed angle of reflection is different from angle of incidence in most of the cases (see Fig. 4.1b).

When parallel rays of light falls on planer/smooth surface, reflected light rays are observed as per law of reflection where angle of reflection is same as angle of incidence. Such reflection phenomenon is known as specular reflection as shown in Fig. 4.2a. In such case specular reflectance is measured by placing the detector at an angle same as angle of incidence to quantify the reflection phenomenon. However, when similar parallel rays of light falls on rough surface, reflection in random direction is observed. In such case the observed angle of reflection is not same as angle of incidence. Such reflection is known as diffused reflection (see Fig. 4.2b) and the term 'diffused reflectance' is used to quantify the reflection phenomenon. For solar cells, the total reflectance (specular + diffused) is to be minimized. Hence to characterize the reflection from surface, total reflectance is measured using integrating sphere where light reflected in all directions are collected and measured by the detector.

Roughening of the surface not only randomize the angle of reflection, it also impact the angle of refraction and results in optical path enhancement of light as light travel longer distance in absorbing material (see Fig. 4.1b).The reflection from

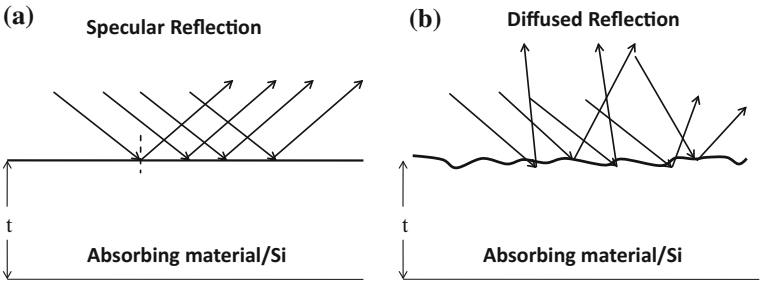

Fig. 4.2 Schematic for reflection of parallel rays of light from **a** planer surface; **b** rough surface

rough surface which randomize the incident light into random direction is also known as Lambertian reflection. Surface roughening helps in tuning the angle of incidence and achieving the required condition leading to total internal reflection. By understanding the total internal reflection and role of angle of incidence tuning with the help of surface roughening, the reason for enhanced optical path and light trapping in rough surface based absorbing material can be understood. The total internal reflection is observed when light incident on any interface from denser medium (higher refractive index) to less denser medium (lesser refractive index) at angle larger than critical angle (θ_c). The critical angle (θ_c) is defined by Snell's law using the condition where light is reflected in same medium, i.e., when θ_t is 90°or greater. For the case of absorbing material (refractive index: n) to air (refractive index: 1) interface as shown in Fig. 4.3a, the Snell's law would be written as per Eq. (4.1) and therefore the critical angle (θ_c) would be given by Eq. (4.2).

$$n\sin\theta_c = \sin(90^\circ) \tag{4.1}$$

$$\theta_c = \sin^{-1}\left(\frac{1}{n}\right) \tag{4.2}$$

Any light falling on absorbing material-air interface after internal reflection would escape from surface if the incident angle is less than the critical angle (θ_c) as ray-1 shown in Fig. 4.3a. If light incident at angle larger than the critical angle (θ_c), the phenomenon of total internal reflection would occur and light again return in the same absorbing material/medium as ray-2 shown in Fig. 4.3a. In such case, light stays in the same medium and would travel at least one more time in the absorbing material and hence optical path length enhancement is observed. The light would escape from absorbing materials only if it falls on front interface after internal reflection from the bottom surface within an angle of θ_c. Such light escape would be addition to the primary reflection from front surface and can be noticed in reflectance measurements. For c-Si absorbing materials, n is in the range of 3.5–3.8 for wavelength range of 300–1200 nm and hence Θ_c is in the range of 15°–17°.

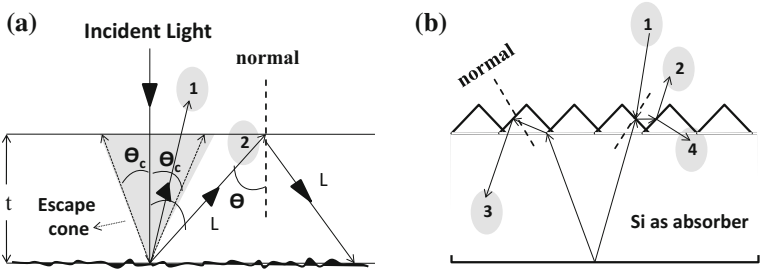

Fig. 4.3 **a** Schematic of (**a**) internal reflection of light within absorbing material/medium and representation of critical angle; **b** trapping of light by Si textured surface which have random pyramids on surface

Escape cone term is used to define the front escape, i.e., the light escape from front surface which adds up with the reflectance from front surface as discussed above. This escape cone is three dimension which accounts for light escape from front surface not only in particular direction, but from all direction at any angle within the cone. The fraction of light which would escape is the fraction of light within the escape cone (f_{esc}). Assuming the transmissivity at top surface as 100% and rear surface as perfect reflector (R = 1 or 100%), f_{esc} would be give by Eq. (4.3) (in spherical coordinates).

$$f_{esc} = \frac{\int_0^{\theta_c}\int_0^{2\pi} \cos\theta \sin\theta d\theta d\phi}{\int_0^{\pi/2}\int_0^{2\pi} \cos\theta \sin\theta d\theta d\phi} = \frac{1-\cos 2\theta_c}{2} = \frac{1}{n^2} \tag{4.3}$$

where θ_c is critical angle. It indicates the dependence of front escape on refractive index of the absorbing material.

Further, in case of Lambertian light trapping geometry, the average path length of light across the absorbing material between front and rear surface is at least twice of the absorbing material thickness (t) due to oblique propagation of light (Campbell and Green 1987).

The mean path length of weekly absorbed light for Lambertian top surface and reflective rear surface (with reflectance R) can be calculated by tracking the path length of escaping rays. The mean path length can be calculated as follows (Campbell and Green 1987):

$$\bar{P} = t[2(1-R) + 4fR + 6R(1-f)(1-R) + 8f(1-f)R^2 + \cdots] \tag{4.4}$$

Here f is fraction of light escaped/coupled out each time when light strikes the top surface and t is the thickness of absorbing material/substrate. The Eq. (4.4) can be expressed in power series form as (Campbell and Green 1987):

$$\bar{P} = 2t\left(\sum_{m=0}^{\infty}[(2m+1)(1-R) + (2m+2)fR][R(1-f)]^m\right) \tag{4.5}$$

Equation (4.5) can be further reduced to form as given in Eq. (4.6) as follows:

$$\bar{P} = \frac{2t(1+R)}{1-R(1-f)} \tag{4.6}$$

In limiting case where transmissivity at top surface is 100% and rear surface is perfect reflector (R = 1 or 100%), which would be an ideal condition for a solar cell, f would be $1/n^2$ as given in Eq. (4.3). In this scenario, mean path length would be $4tn^2$ where n is the refractive index of the absorbing material. This indicates a maximum possible path length enhancement of $4n^2$ for Lambertian light trapping geometry. Now if the rear surface is considered to be non-perfect reflector and also depends on total internal reflection then reflectance from rear surface (R) would be $(1 - f)$. In

such case the path length enhancement would come down to $2n^2$ (Campbell and Green 1987). For Si based solar cells in ideal condition with perfect back reflector, maximum possible path length enhancement for weekly absorbing light is about 46–50.

Also, the solid angle of escape cone (Ω_c) would be fraction of 4π and can be given by Eq. (4.7) (Yablonovitch 1982).

$$\Omega_c = \frac{4\pi}{2n^2} \tag{4.7}$$

Solid angle of escape cone (Ω_c) can be linked to probability for light escape in one scattering event and this probability would be $1/2n^2$ where n is the refractive index of absorbing material (Yablonovitch 1982).

In order to achieve enhanced light trapping in c-Si absorbing material, we need to ensure total internal reflection and probable angular randomization of light on subsequent reflections. If light is made to fall outside the escape cone, front escape of light would be minimized. For angular randomization and to make incident light fall at angle higher than the critical angle, surface texturing is done which results in random pyramids at Si surface as shown in Fig. 4.3b. When light incident on one surface (ray-1), it gets reflected and fall on another pyramid surface (ray-2 and ray-3 in Fig. 4.3b). Multiple interactions of light and interface increase the chances for inward coupling of light (ray-4). Also, after reflection from back surface, if it falls at angle larger than the critical angle (ray-3), total internal reflection would occur. Angle of incident can be tuned with the help of pyramid size, shape and angle of surface of each pyramid from base surface. Therefore by optimizing the surface morphology, the reflection from the front surface and front escape, i.e. light escape from front surface after getting reflected from back surface and reaching the front surface, can be minimized to a greater extent. As a result, enhanced light trapping can be achieved.

4.2 Textured Surfaces in c-Si Solar Cells

As discussed in above section, randomizing the surface can enhance the light trapping in absorbing materials used in solar cell applications. For Si solar cells, it is infra-red wavelengths for which weak absorption is seen and the front escape for such weakly absorbed wavelengths is to be minimized. The wavelengths for which the front escape is to be minimized depends on the thickness of the absorbing material, as the need of front escape minimization comes for those wavelengths which reaches to front after getting reflected from back and do not get transmitted from front surface or absorbed within the absorbing material.

The surface roughening can be of different types e.g. structures like regular pyramids, Lambertian (random surface roughness), random pyramids, inverted pyramids etc. In case of mono c-Si solar cells, random pyramids are used for light

trapping and in case of multi c-Si solar cells, honeycomb like structures are used for enhancing the light trapping. Figure 4.4a shows the schematic of a random pyramids like structured used in mono c-Si solar cells and Fig. 4.4b shows the schematic of honeycomb like structure useful for light trapping in multi c-Si wafer based cells.

In case of mono c-Si wafers, different crystal planes have different atomic density. Typical mono c-Si wafers used for solar cells have (100) orientation. For such wafers (100) and (111) planes have different density of atoms. In this situation, chemical etching results in different etching rate in different plane direction (anisotropic etching), which results in formation of random pyramid. However, in case of multi c-Si wafers, the crystal grains have different orientations and very few have the required (100) orientation which can be used for pyramid formation using etching process. This leads to non-uniform and higher reflectance across the wafer. For multi c-Si solar cells, uniform texturing is required, which should be isotropic and independent of crystal orientation. More detail about the process requirements for such structures have been discussed in next chapter.

The pyramid arrangement for light tapping in mono c-Si solar cells can be in regular pattern, random pattern or in brickwork arrangement. In regular pyramid layout, each pyramid size is same and the pyramids are at regular interval (see Fig. 4.5a). In random pyramid arrangement, the pyramids are of different sizes at random spatial locations (see Fig. 4.5b). In brickwork arrangement, each pyramid is shifted from base center from the neighboring pyramid (see Fig. 4.5c). The other arrangement is perpendicular slat as shown in Fig. 4.5d where the sides of groves are formed by anisotropic etching as done for pyramid structure fabrication (Campbell and Green 1987).

Based on geometrical analysis, it has been shown that 40% of rays striking the surface in regular pyramid arrangement and 44% in random pyramid arrangement do not escape even after getting reflected from reflective rear surface and passing through the absorbing material reaching the top having structured surface Campbell and Green (1987). In brickwork arrangement, 80% of rays striking the surface do not escape after passing through structured surface at top and reflective rear surface. Double side textured surface or perpendicular slat geometry perform much better than the single side structured surface at top and reflective rear surface based light trapping structures and their performance is closer to Lambertian light trapping

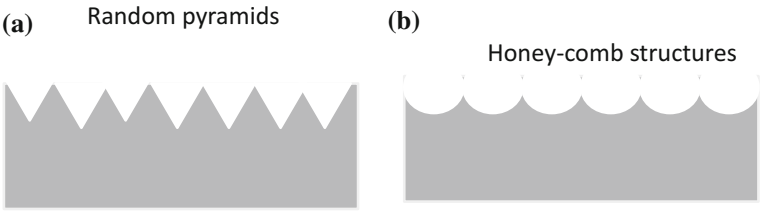

Fig. 4.4 Schematic of light trapping structures **a** random pyramid based structures used in mono c-Si solar cells; **b** honeycomb like structures used in multi c-Si solar cells

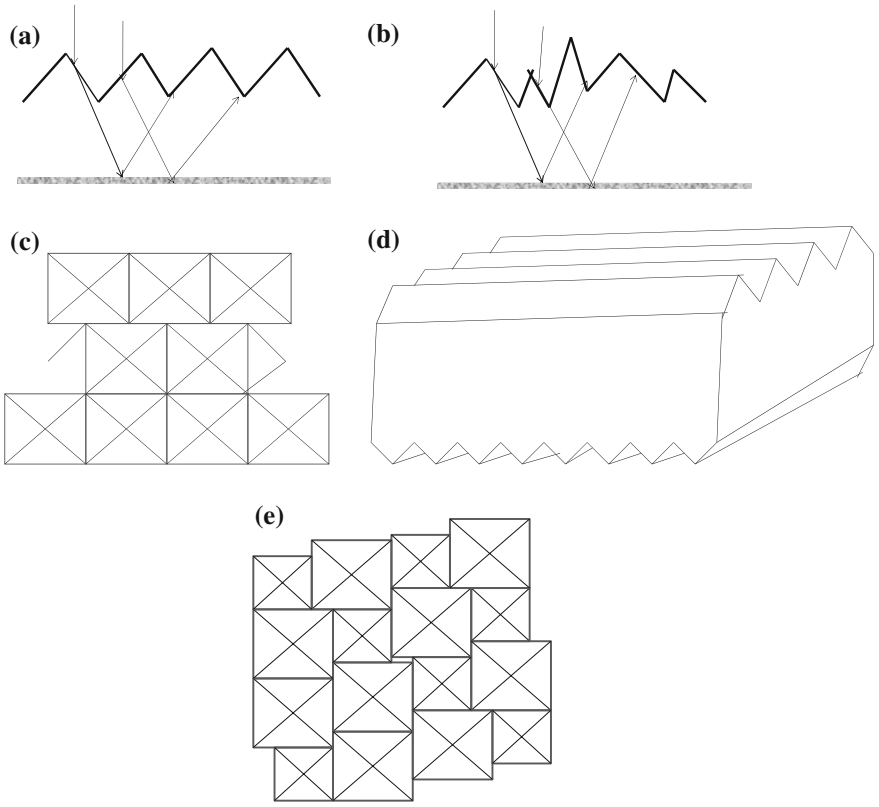

Fig. 4.5 Schematic of a **a** regular pyramid arrangement (*side view*); **b** random pyramid arrangement (*side view*); **c** brickwork arrangement (*top view*); **d** perpendicular slat based light trapping structure (after Ref. (Campbell and Green 1987)); **e** arrangement of random inverted pyramid (two sizes) (*top view*) (after Ref. (Green et al. 1999))

geometry. Random size inverted pyramids have also been shown to give better light trapping (Green et al. 1999) (see Fig. 4.5e). The best c-Si cell efficiency has been reported with inverted pyramid based light trapping structure (Green et al. 1999).

Theoretically, the best performance (light trapping) can be achieved for completely randomized surface (Lambertian surface) where almost 100% (theoretically) of rays striking the surface would not escape even after getting reflected from reflective rear surface and passing through the absorbing material reaching the top surface (Campbell and Green 1987). However, such ideal structure is far from reality. Therefore, for enhanced light trapping in mono c-Si solar cells mostly random pyramids (see Fig. 4.6a) are used and for multi c-Si solar cells honeycomb like structures (see Fig. 4.6b) are used.

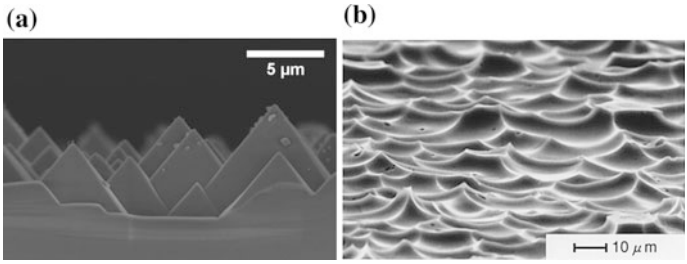

Fig. 4.6 SEM image of **a** a mono c-Si wafer with random pyramids at surface (from Ref. (Singh 2016) (cross-sectional view), reproduced with permission); **b** a multi c-Si wafer with honeycomb like structure on surface (from Ref. (Nishimoto 1999), Reproduced by permission of The Electrochemical Society.)

4.3 Role of Texture Size and Shape in Light Trapping and Reflection Reduction

As we discussed in above section, there are many light trapping structures which can be used to enhance the absorption. However, the potential of amount of light trapping is very much depends on the shape and the size of the light trapping structure. The pyramids, most widely used structure for light trapping in c-Si solar cells, are defined by four (111) planes and one (100) base plane in mono c-Si wafer whose surface is terminated at (100) crystal orientation. The pyramid can be upright or inverted as shown in Fig. 4.7. Angle between (100) base and (111) plane, also known as characteristic angle (θ), is about 54.7° for the case of mono c-Si wafers. The height (h) or depth (d) (in case of inverted pyramid) of pyramid can be calculated from base dimension using Eq. (4.8) where l is the length of the base. The height/depth of the pyramid is also known as pyramid size.

$$h = \tan\theta \times \frac{l}{2} \tag{4.8}$$

In mono c-Si solar cells, regular/random pyramids are used and the size of pyramid may vary from 1–10 μm. Pyramid structure sizes in the range of 5–10 μm is most widely used.

Based on computer modeling (Campbell and Green 1987) calculated the fraction of light rays that remains trapped as function of number of passes made through the absorbing material where the *top* surface has different light trapping geometries and rear surface is considered reflective. The calculated histogram plot is shown in Fig. 4.8. It can be clearly seen that the Lambertian light trapping geometry is best among all, as the fraction of light that remains trapped is maximum for this type of light trapping geometry and the hence the fraction of light rays that would escape and adds up to the reflection from the surface (for weekly absorbing light) would be minimum. The brickwork pattern based light trapping geometry (Fig. 4.5d) is also

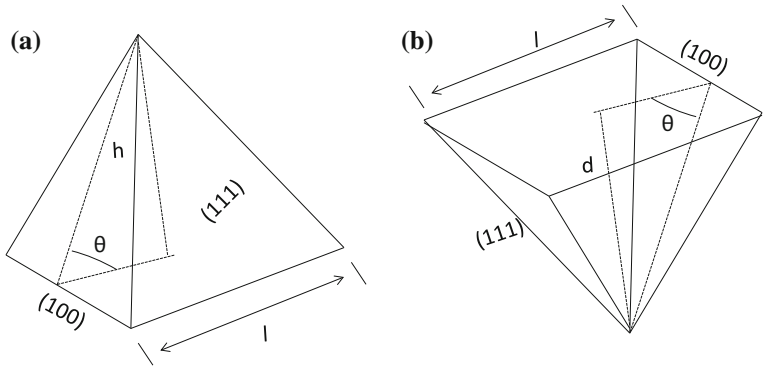

Fig. 4.7 Schematic of **a** upright pyramid with height **h** and characteristic angle θ between planes (111) and base (100); **b** inverted pyramid with depth **d** and characteristic angle θ between planes (111) and base (100) for case of mono c-Si wafers

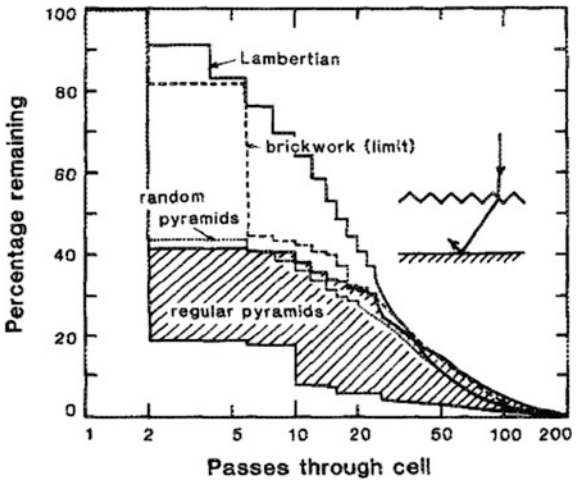

Fig. 4.8 Fraction of light rays that remains trapped as function of number passes made through the absorbing material where the top surface has different light trapping geometries and rear surface is considered reflective (Reproduced from (Campbell and Green 1987), with permission of AIP Publishing)

competitive. In pyramid based light trapping geometry, random pyramid geometry is shown to give better performance than the regular pyramids.

In case of multi c-Si based absorbing material, honeycomb like textures, usually achieved by isotropic etching of the surface, are used for light trapping as discussed in previous section. The reflection in such multi c-Si based absorbing material is governed by width (W) and depth (d) of the texture as shown in Fig. 4.9.

The honeycomb structure can be assumed to part of an imaginary sphere with radius r and the width (W), depth (d) and radius can be related as:

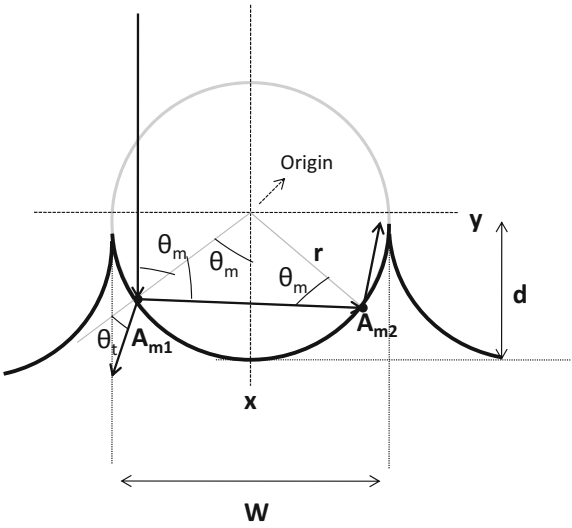

Fig. 4.9 Schematic of a texture design used for reflection reduction in multi c-Si based absorbing material (after Ref. (Nishimoto 1999))

$$W^2 = 8rd - 4d^2 \tag{4.9}$$

The reflectance from such structures can be calculated as (Nishimoto 1999):

$$R = \sum_{m=0}^{k+1} \frac{R_{m,1} \times dS_m}{S} \tag{4.10}$$

where $R_{m,1}$ represents the reflectance from individual points ($A_{m,1}(x_{m,1},y_{m,1})$, for m = 0, 1, 2, 3…k) which divides the half texture into k parts and dS_m and S is given as per Eqs. (4.11) and (4.12) respectively.

$$dS_m = \pi(y_{m,1}^2 - y_{m+1,1}^2) \tag{4.11}$$

$$S = \pi \times (\frac{W}{2})^2 \tag{4.12}$$

where $x_{m,1} = m \times \frac{W}{2k}$ and $y_{m,1} = \sqrt{r^2 - x_{m,1}^2}$ are point co-ordinates for m = 0, 1, 2,…k.

Above equations indicate the dependency of reflectance on width (W) and depth (d) of the texture. For small value of d/W, the change in reflectance is not significant. However for lager value of d/W, reflectance reduction is observed (Nishimoto 1999). It means textures with larger value of d/W ratio would be required for better reflection reduction. As an example, d/W value of about 0.5 result in minimum reflection for a 600 nm wavelength of light as per calculation done by Nishimoto (1999).

The above discussions clearly show the sensitivity to light trapping geometry/shape and size on light trapping potential. Type of surface structure as well as optimum size and shape is necessary for efficient light trapping and reflection reduction.

4.4 Single Side Texturing Versus Both Side Texturing

As discussed above in pyramid based light trapping geometry for the case of single side textured surfaces, maximum light is escaped after just two passes and only 40–44% remains trapped (see Fig. 4.8). This was the case where light was escaping after getting reflected from reflective rear surface and passing through the absorbing material reaching the top having textured surface. However, this light escape can be further minimized by texturing both side of Si (absorbing material/substrate) which can enhance the light trapping further. Pyramidal textured surface at both side of the Si substrate greatly reduces the front escape due to more randomization of light rays hitting the bottom surface. The fraction of light rays that remains trapped as function of number passes made through the absorbing material as calculated by Campbell and Green (1987) based on computer modeling, where the top and bottom surface has same kind of light trapping geometry and rear surface has been considered reflective, is shown in Fig. 4.10.

It can be clearly noticed from Fig. 4.10 that double side pyramidal texture based light trapping structure (see Fig. 4.11b) performs much better than single side pyramidal texture based light trapping structure (see Fig. 4.11a).

Also, double side random pyramidal texture based light trapping structure in this case also have better light trapping potential than regular pyramidal texture based light trapping structure. Random double side pyramidal texture based light trapping

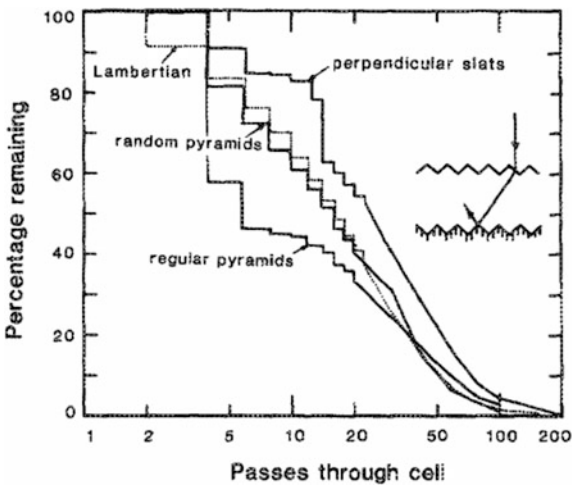

Fig. 4.10 Fraction of light rays that remains trapped as function of number passes made through the absorbing material where the *top* and *bottom* surface has same kind of light trapping geometry and rear surface has been considered reflective (Reproduced from (Campbell and Green 1987), with permission of AIP Publishing)

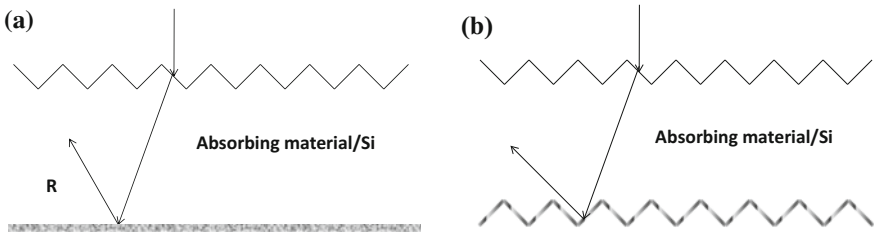

Fig. 4.11 Schematic of Si substrate (absorbing material) with **a** single side (*top*) pyramidal textured surface and reflecting bottom surface; **b** double side (*top* and *bottom*) pyramidal textured surface and reflecting *bottom* surface

structure is even indicating the light trapping potential closer to Lambertian light trapping scheme for the initial passes of light. The other arrangement, perpendicular slat, (as in Fig. 4.5d), which has sides of groves formed at both sides of Si, is also competitive to Lambertian light trapping geometry. For case of Lambertian light trapping geometry, there is not much difference between single side and both side roughening based light trapping structure (see Fig. 4.8 and Fig. 4.10).

In case of commercial mono c-Si solar cells, it is required to use cost effective and easily implementable structure. Random pyramids can be formed by anisotropic etching which is cost effective and more practical structure for mono c-Si based solar cells. Therefore, while fabricating mono c-Si solar cells, pyramidal textures are formed at both sides of the Si substrate, is used as shown in Fig. 4.11b. This light trapping structure provides higher current generation from the cell compared to single side pyramidal textures based light trapping geometry.

4.5 Most Suitable Textured Surface for Better Light Trapping

As discussed above, there are many structure/geometry which can be used for enhancing the light trapping in c-Si based solar cells. The discussions till now were based on how much path length enhancement can be achieved and how much light can be trapped. However, for real solar cell application one has to decide on which light trapping structure should be used for higher current generation from the solar cells under given solar spectrum, depending on its cost effectiveness. The current generation from solar cell would depend on optical properties of the active absorbing material as well as light trapping scheme. For terrestrial application, the evaluation of current generation potential for different light trapping structures should be based on AM 1.5G radiation spectrum (Standard IEC 60904-3 2008). Based on computer program, (Campbell and Green 1987) presented the current contribution from different light trapping structures on different thicknesses of silicon solar cells. The graph plot has been shown in Fig. 4.12. Figure 4.12 analysis

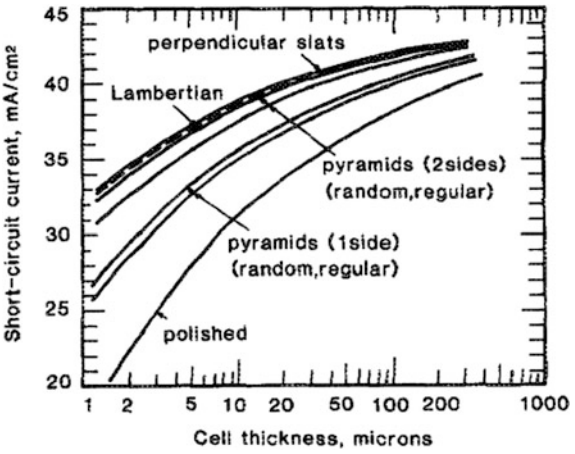

Fig. 4.12 Maximum current generation potential (short circuit current) for different thicknesses of c-Si solar cells with different light trapping structures under AM 1.5G spectrum with integrated intensity of 97 mW/cm^2 (Reproduced from (Campbell and Green 1987), with permission of AIP Publishing)

indicate that the best light trapping structure would be perpendicular slat which is competitive with the Lambertian light trapping structure. Also, the random pyramid on both side of the cell has similar kind of current generation potential.

The single side pyramidal texture either regular or random has lower current generation potential than the both side pyramidal texture based light trapping geometry. Random pyramidal texture at both side surface (front and back) is more suitable light trapping structure from cost and implementation point of view and is widely used scheme in c-Si solar cell manufacturing.

The above analysis is based on assumption that there is 100% transmissivity from top surface to the Si absorbing material for incident light at any angle. However in case of rear surface, there will always be some reflection from the front which may vary for different angle of incidence and would result in relatively lower current generation. The current generation potential for different light trapping geometry can be calculated using following Eq. (4.13) (Davis et al. 2015):

$$J_G = q.\int \phi_{ph}(\lambda).T_f(\lambda).e^{-\alpha(\lambda).Z(\lambda).t}.d\lambda \tag{4.13}$$

where q is electron charge, $\phi_{ph}(\lambda)$ is photon flux of spectrum under consideration e.g. AM 1.5G, $T_f(\lambda)$ is transmission into the cell from air-Si interface at front, $\alpha(\lambda)$ is absorption co-efficient of Si at wavelength λ. Z(λ) is optical path length enhancement of the cell for wavelength λ and t is cell (absorbing material) thickness.

The maximum optical path length enhancement (Z(λ)) is $4n(\lambda)^2$ where n(λ) is refractive index of Si at wavelength λ as discussed in Sect. 4.1. There are some more expressions/models are available for Z(λ) as given below(PV-Lighthouse):

$$Z(\lambda) = \frac{\ln(1 + 4n(\lambda)^2.\alpha(\lambda).t)}{\alpha(\lambda).t} \tag{4.14}$$

$$Z = 4 + \frac{\ln[n^2(\lambda) + (1 - n^2(\lambda)).e^{-4.\alpha(\lambda).t}]}{\alpha(\lambda).t} \tag{4.15}$$

Z(λ) given in Eqs. (4.14) and (4.15) leads to $4n(\lambda)^2$ as $\alpha(\lambda).t$ tends to zero, which is limiting case. Equation (4.13) shows the maximum current achievable from the cell. However, there are reflection losses from front and other parasitic absorption losses can lead to lesser current generation potential. The losses in form of reflection or parasitic absorption can be represented in current loss form as given in following Equations:

$$J_R = q. \int \phi_{ph}(\lambda).R_f(\lambda).e^{-\alpha(\lambda).Z(\lambda).t}.d\lambda \tag{4.16}$$

$$J_A = q. \int \phi_{ph}(\lambda).A_f(\lambda).e^{-\alpha(\lambda).Z(\lambda).t}.d\lambda \tag{4.17}$$

where $R_f(\lambda)$ represent reflection from front surface and $A_f(\lambda)$ represent parasitic absorption at front interface which is not transmitted nor reflected from the interface. Open source simulation software are available e.g. ray tracer from PV-light house (PV-Lighthouse) which can be used to calculate the optical path length enhancement in Si material at different wavelengths for different light trapping structure. Also, it calculates the equivalent current generation potential and current losses associated reflection and parasitic absorption.

The pyramidal texture is more suitable light trapping structure and widely used scheme in c-Si solar cell manufacturing as discussed above. Further, there are two possible types of pyramids which can be used are upright pyramid and inverted pyramid respectively. Performance comparison of such structures (upright and inverted pyramid) using ray tracer can be done. Monte Carlo ray tracing method is used in ray tracing (PV-Lighthouse)following the laws of geometrical optics. Figure 4.13a shows path length enhancement for weekly absorbing light in Si as calculated by wafer ray tracer (PV-Lighthouse) in case upright pyramidal light trapping geometry with mean pyramid size of 5 μm in 200 μm c-Si wafers. Figure 4.13b shows path length enhancement for inverted pyramidal light trapping geometry with similar geometrical features. In both cases, the AM1.5G light spectrum is used and simulated light has been allowed to fall on surface at 0° from normal. The back surface has been assumed to be perfectly reflecting (R = 1).

It can be seen from Fig. 4.13a, b that in both cases random pyramids at front and rear result in highest path length enhancement for the weekly absorbing light compared to all other light trapping schemes. Hence for c-Si solar cells, both side texturization would be the best choice. Now for choice between inverted and upright pyramid structure, current generation potential can be estimated.

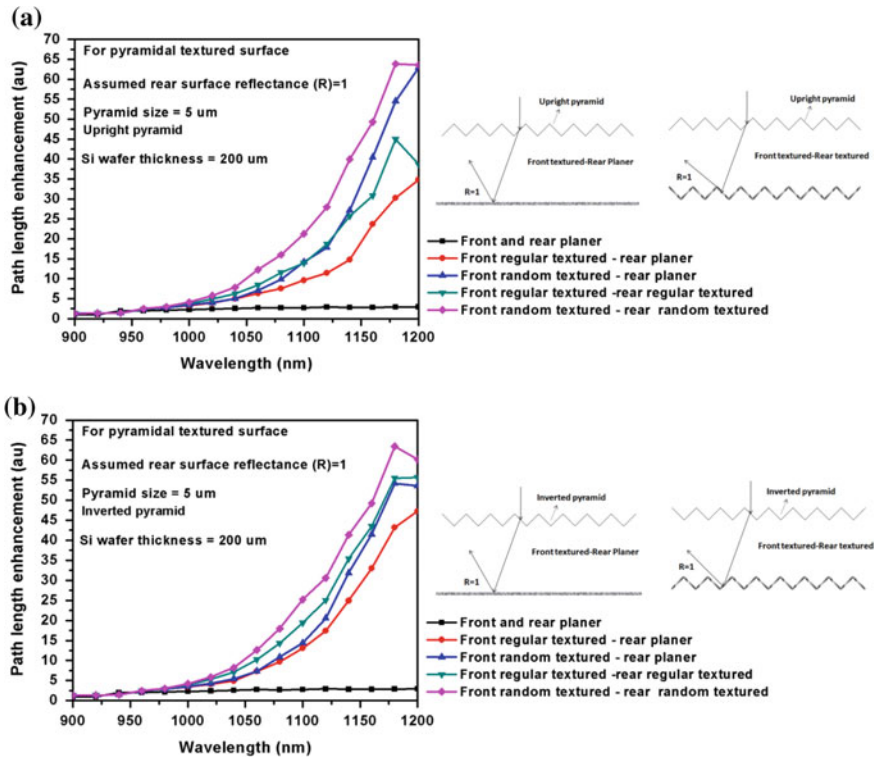

Fig. 4.13 Path length enhancement for weekly absorbing light in Si as calculated by ray tracer (PV-Lighthouse) in case pyramidal light trapping geometry with mean pyramid size of 5 μm in 200 μm c-Si wafers for (a) upright pyramid case; (b) inverted pyramid case

An example can be seen in Fig. 4.14 for four different light trapping schemes. It shows maximum possible photogeneration for above disused case of 200 μm cell with mean pyramid size of 5 μm.

This analysis based on current generation potential evaluation for the four different light trapping schemes in two cases, i.e., upright pyramids and inverted pyramid case, indicate that inverted pyramid based light trapping structure is better than upright pyramid based light trapping structure. And randomness of the pyramid at both surface also leads to more current generation. In summary, we can say that the random inverted pyramid at both side of solar cell surface would be the best choice as light trapping structure. Here note that the above discussed analysis is for normal incidence light assuming the rear is perfect reflector. However, there can be parasitic absorption at front and rear surface and the rear surface may not be perfect reflector in practical situations in solar cells which may impact the total current generation potential of the said light trapping structures. Readers can perform their

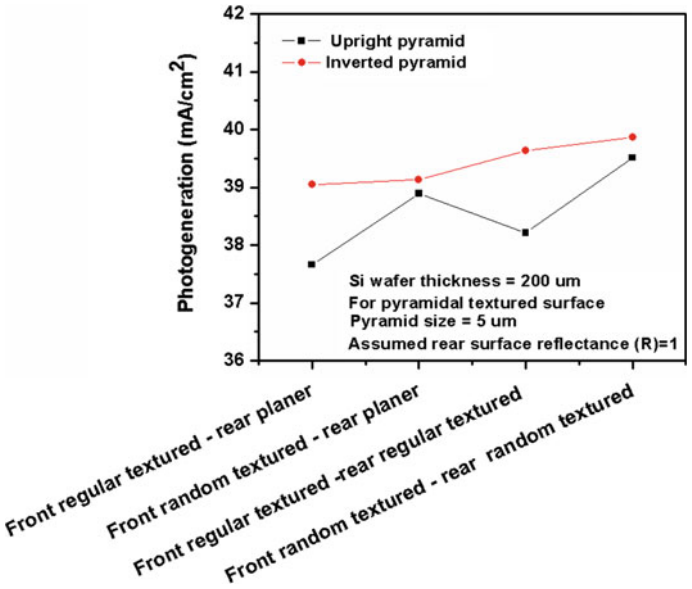

Fig. 4.14 Current generation potential for a 200 μm cell with mean pyramid size of 5 μm in case of upright pyramid structure and inverted pyramid structure with different light trapping schemes

own simulations of different light schemes in different conditions using open source wafer ray tracer simulation software available at PV light house (PV-Lighthouse).

4.6 Implication of Texturing Based Light Trapping Structure

All the discussions made in this chapter were for texture/surface roughening based light trapping. By texturing/roughening of the surface, the reflection from Si can be minimized from 40–42 to 12–15% (total reflectance) as shown in Fig. 4.15. It shows measured total reflectance from c-Si wafer having polished surface and both side chemically textured surface respectively. Reflectance in the range of 12–15% for texture surface based light trapping scheme is still considered high and should be further minimized.

Texturing or surface roughening of Si creates many recombination centers at surface and results in creation of unsaturated dangling bonds as discussed in Sect. 3.5 of the previous chapter. In case of pyramidal texture based light trapping geometry, the texture surface have more area covered by (111) planes which has relatively more defect states. It would lead to more surface recombination probability compared to planer (100) surface in c-Si wafer based cells and would result in poor cell performance (Fesquet et al. 2009; McIntosh and Johnson 2009). For

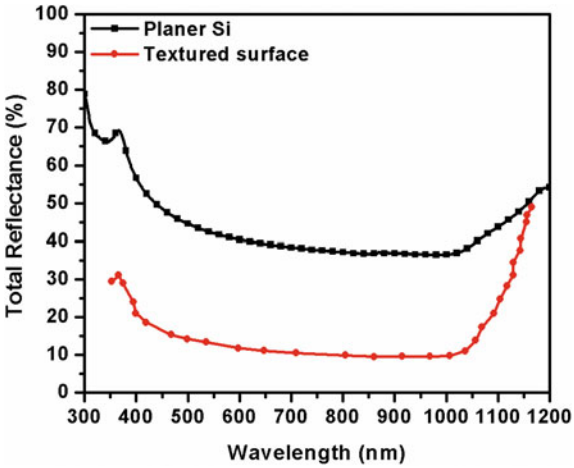

Fig. 4.15 Measured total reflectance from c-Si wafer having polished surface and chemically textured surface

addressing the surface recombination issue due to roughening of surface, dielectric based surface passivation is done as discussed in previous chapter (Sect. 3.5). This dielectric passivation layer with optimized thickness and refractive index also act as anti-reflection layer on textured surface based light trapping structure. It helps in reducing the reflection from surface further and enhances the light trapping in solar cells which leads to better solar cell performance. More about combination of dielectric thin film and textured surface based light trapping structure and relative impact on solar cell performance has been discussed in Chap. 6.

4.7 Questions and Problems

1. Discuss the influence of surface morphology on reflection from surface of an absorbing material?
2. What do you understand from total reflectance, diffused reflectance and specular reflectance? How are they inter-related?
3. What do you understand from front escape and escape cone? How is it relevant in explaining the light trapping phenomenon in active absorbing materials used for solar cells?
4. Discuss on different type of texture surfaces useful for light trapping in c-Si solar cell? Which structure has best light trapping potential?
5. What do you mean by Lambertain light trapping structure?
6. Discuss the role of depth and height in a honeycomb structure on reflection reduction in multi c-Si solar cells?
7. Why double side textured surfaces are preferred for light trapping in c-Si solar cells?

8. What do you mean by path length enhancement? How is it important for enhancing the current generation in c-Si solar cells?
9. Explore light trapping potential of a pyramidal texture surface with mean pyramid size of 2 μm and 8 μm. Consider the incident light flux as per AM 1.5G spectrum and assume that the light incidence angle is 40°. Also assume that the wafer thickness is 100 μm and rear surface is perfectly reflecting. [Hint: Use wafer ray tracer simulation software available at www.pvlighthouse.com.au]
10. Discuss the implication associated with textured surface based structure being used as sole light trapping scheme in c-Si solar cells? What should be done to make such light trapping structures more effective for solar cell applications?

References

Campbell P, Green MA (1987) Light trapping properties of pyramidally textured surfaces. J Appl Phys 62:243. doi:10.1063/1.339189

Davis KO, Jiang K, Habermann D, Schoenfeld WV (2015) Tailoring the optical properties of APCVD titanium oxide films for all-oxide multilayer antireflection coatings. IEEE J Photovolt 5:1265–1270. doi:10.1109/JPHOTOV.2015.2437272

Fesquet L, Olibet S, Damon-Lacoste J, et al (2009) Modification of textured silicon wafer surface morphology for fabrication of heterojunction solar cell with open circuit voltage over 700 mV. Conf Rec IEEE Photovolt Spec Conf 000754–000758. doi:10.1109/PVSC.2009.5411173

Green MA, Jianhua Zhao, Wang A, Wenham SR (1999) Very high efficiency silicon solar cells-Science and Technology. IEEE Trans Electron Devices 46:1940–1947. doi:10.1109/16.791982

McIntosh KR, Johnson LP (2009) Recombination at textured silicon surfaces passivated with silicon dioxide. J Appl Phys 105:124520. doi:10.1063/1.3153979

Nishimoto Y (1999) Investigation of acidic texturization for multicrystalline silicon solar cells. J Electrochem Soc 146:457. doi:10.1149/1.1391628

PV-Lighthouse www.pvlighthouse.com.au. http://www.pvlighthouse.com.au. Accessed 4 May 2016

Singh HK (2016) Plasmonics based light-trapping structures for c-si solar cell applications. IIT Bombay, Powai, Mumbai

Standard IEC 60904-3 (2008) Measurement Principles for Terrestrial PV Solar Devices with Reference Spectral Irradiance Data

Yablonovitch E (1982) Statistical ray optics. J Opt Soc Am 72:899. doi:10.1364/JOSA.72.000899

Chapter 5
Texturing Process of c-Si Wafers

This chapter focuses on process technology for making texture surface in c-Si solar cells. Starting with c-Si crystal structure and role of crystal planes, wafer type and orientation in deciding the chemical process chemistry for texturing has been covered. Also, chemical processes used for achieving different shape of textures on surface in mono- as well as multi c-Si wafers has been discussed along with the principle behind the process, which makes texturization possible. At the end, practical implications involved in chemical texturing based technology has been discussed in context of manufacturing of the c-Si solar cells.

5.1 Si Crystal Structure

The spatial arrangements of atoms or ions are characterized by crystal structures. In crystalline material, periodicity in atoms or group of atoms arranged in particular sequence are observed for long atomic distances. Atoms or ions/molecules are bound in a repetitive three-dimensional pattern with its nearest neighboring atoms or ions/molecules. Different type of crystal structures leads to different types of physical properties of materials. There are many types of crystal structure exists in nature. The atoms or ions/molecules are considered as solid sphere with well-defined diameters when the crystal structure is represented for understanding the material system and properties. The term "lattice" is used where it represent three-dimensional array of points coinciding with atom positions (Callister and Rethwisch 2007). The repetitive arrangements of a group of atoms or ions/molecules, also called "unit cell", is mostly used to represent the crystal structure of solid materials.

The unit cell represents the symmetry of crystal structure and by translation of the unit cell with integral distances, in the three-dimensional space along its edges; the whole crystal can be generated. In such case, the unit cell act as basic structure or building block of a crystalline material (see Fig. 5.1). There may exist more than

© Springer Nature Singapore Pte Ltd. 2017

C.S. Solanki and H.K. Singh, *Anti-reflection and Light Trapping in c-Si Solar Cells*, Green Energy and Technology,
DOI 10.1007/978-981-10-4771-8_5

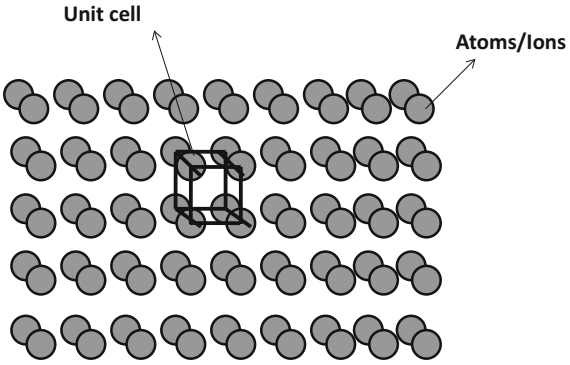

Fig. 5.1 Symbolic representation of a crystal structure with periodic atoms/ions. The *rectangular* shape having representative atoms at its corners represents a unit cell

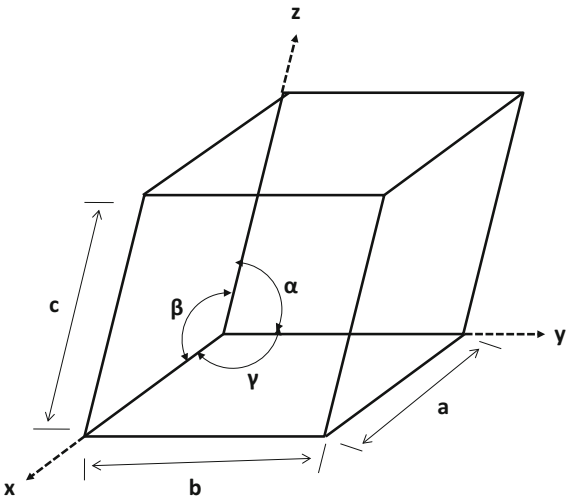

Fig. 5.2 Schematic of a unit cell having edge lengths a, b and c along x, y and z directions and interaxial angles α, β and γ. (after Ref. (Callister and Rethwisch 2007))

on unit cell in a crystal. However, unit cell having highest level of geometrical symmetry is considered (Callister and Rethwisch 2007).

There are many types of crystal structure and are divided in groups based on unit cell arrangement or atomic arrangements. The unit cell is usually defined by six parameters where the unit cell is considered as parallelepiped with origin at one corner and edges in x, y, z direction with edge lengths a, b, and c and inter-axial angles α, β, and γ as shown in Fig. 5.2. The values of a, b, and c are termed as lattice parameters. There are total seven different combinations if a, b, and c with α, β, and γ are defined which collectively represents the crystal system namely cubic, hexagonal, rhombohedral, orthorhombic, tetragonal, monoclinic, and triclinic.

c-Si material falls into cubic crystal system where $a = b = c$ and $\alpha = \beta = \gamma = 90^{\circ}$. The cubic crystal system is further subdivided into three categories, i.e., simple cubic (SCC), body-centered cubic (BCC), and face-centered cubic (FCC), based on the location of lattice points (atoms) in the unit cell. In SCC structure,

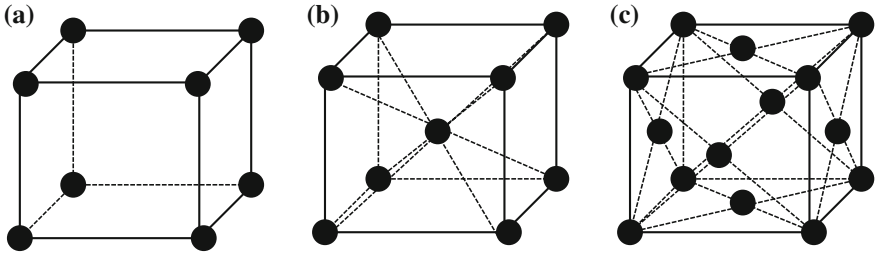

Fig. 5.3 Schematic of **a** simple cubic structure (SCC); **b** body centered cubic structure (BCC); **c** face centered cubic structure (FCC)

there exist one lattice point at each corner of the cube and each atom at the lattice point is shared by adjacent cubes equally (see Fig. 5.3a). In SCC structure, each unit cell will have one effective atom as each lattice point would have eight adjacent possible cubes sharing the atom on lattice point equally. So eight corners of cube contributing one-eighth of the atom in the cell leads to $8 \times 1/8 = 1$ atom per unit cell.

In BCC structure, there exists one lattice point at the center of unit cell along with eight lattice points at the corner (see Fig. 5.3b). This additional atom at central lattice point increases the share of atoms per unit cell to 2. In FCC crystal structure, there exists one lattice point at each face of the cube in addition to lattice points at the corners (see Fig. 5.3c). The atoms at lattice points on faces are shared by neighboring cube face and effective share of atom of this face to the unit cell is ½. There are total six faces in cube leading effective eight atoms from faces and one from corners and total share of atoms per unit cell is increased to 4.

Silicon material has diamond cubic lattice structure which is visualized as two merged face-centered cubic (FCC) lattices where the origin of second lattice originates from the first by a/4 (a is lattice constant of Si) in each direction. The unit cell representation of diamond crystal structure is shown in Fig. 5.4.

In diamond crystal structure, there are total eight atoms per unit cell (one equivalent atom from corners, three equivalent atoms from faces of cube, and four

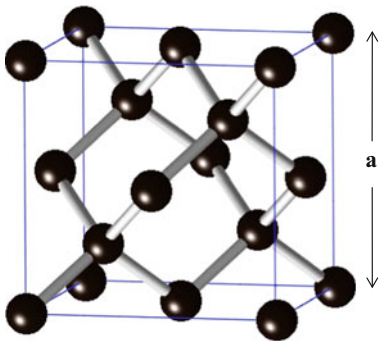

Fig. 5.4 Schematic of a unit cell of diamond cubic crystal structure (crystal structure found in Si material)

from inside of cell). The lattice constant (a) for Si is 0.543 nm. The density of Si atoms is given by numbers of atoms per unit cell volume which is about 5×10^{22} atoms/cm^3.

In mono c-Si materials, unit cell/atom periodicity occurs for longer range/distances, across the dimensions of the wafer. However, there are possibilities where unit cell or atom arrangement/periodicity may occur for short or very short distance. Such structure would exhibit polycrystalline structures or microcrystalline structure. Monocrystalline and polycrystalline structure based Si wafers used in c-Si solar cell manufacturing has already been discussed in Sect. 2.2 of Chap. 2. In the following section, we would discuss the crystal orientation of wafer preferred for solar cell manufacturing.

5.2 Wafer Type and Orientation for c-Si Solar Cell Fabrication

Orientation of planes for a crystal structure is represented by Miller indices (hkl). Note that the h, k, and l values, i.e., Miller indices are evaluated from inverse of side edge lengths of the crystal structure unit cell. It means if x-intercept of plane in the unit cell is a, then h would be 1/a. Similarly, if y and z-intercept of planes are b and c, respectively, then k and l would be 1/b and 1/c, respectively. So, (hkl) would have fractional intercepts as 1/a, 1/b, 1/c. The fractional intercepts are multiplied or divided by a common number in order to simplify them. For example, if the fraction intercepts are 1/3, 1/2, 1/4; then the miller indices would be written as (463).

Further, parallel planes are equivalent and represented by identical indices. For example, a crystal plane is represented by (hkl) where h is inverse of x-intercept of plane, k is inverse of y-intercept of plane, and l is inverse of z-intercept of plane as discussed above. Also, the equivalent planes are represented by {hkl} and the crystal direction is represented by [hkl]. The equivalent crystal directions are represented by <hkl>.

In Si-based semiconductor device manufacturing, (100) and (111) are the two principal silicon crystal orientations which are widely used (Plummer et al. 2000). Wafer having orientations like (100) or (111) indicates that the Si crystal terminates at the wafer surface on [100] or [111]. Figure 5.5 shows some important cubical crystal miller indices. In the figure, you can see the intercepts of plane on the axis. In the extreme left figure, the shaded region represent the (100) plane. Similarly, middle and extreme right figures show the (110) and (111) planes respectively. The h, k or l value equals to zero (0) means the axial intercept along x, y, or z axis is infinite (∞). This means it is parallel to that particular axis.

The <100>, <110> and <111> direction view of diamond cubic crystal structure and atomic arrangements would look different which can be seen in Fig. 5.6. Also, the (100), (110) and (111) plane of a Si crystal can be seen in Fig. 5.7.

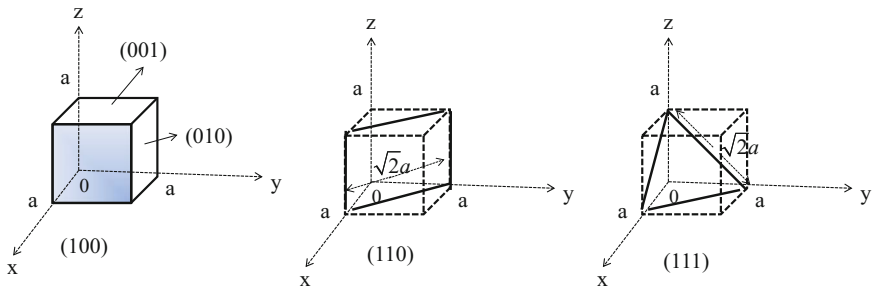

Fig. 5.5 Schematic of some important cubical crystal miller indices (after Ref. (Sze and Ng 2006))

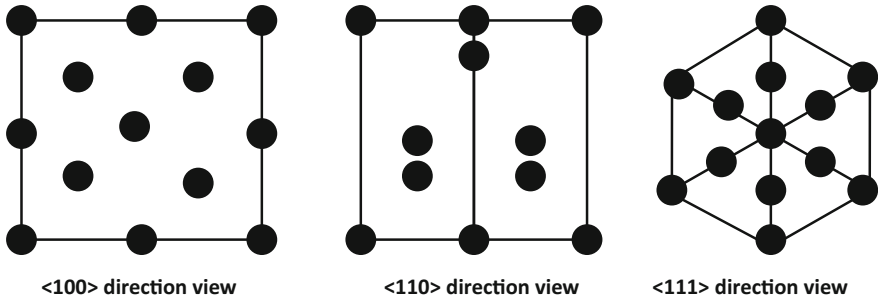

Fig. 5.6 Si crystal structure (diamond crystal structure) unit cell view in <100>, <110> and <111> directions

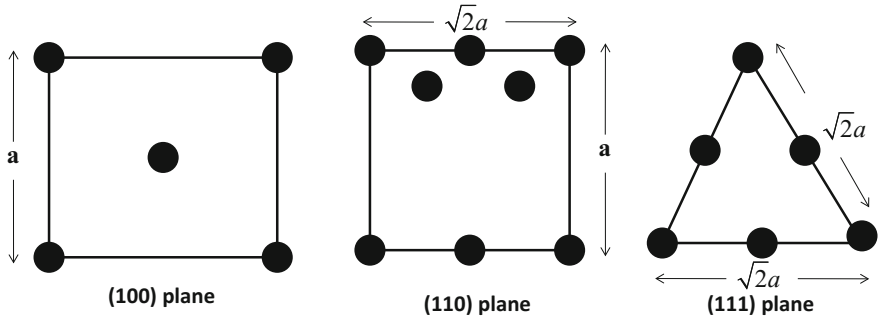

Fig. 5.7 Atoms in (100), (110) and (111) plane of c-Si cubic crystal structure

In c-Si solar cell, for etching the surface and to form pyramidal structure, anisotropic etching is required. The rate of etching depends on the number of atoms in given direction. In such scenario, it becomes important to know the number of atoms in given direction/plane. To calculate number of atoms per unit area for a

given plane, we need to know the area of each plane and number of effective atoms in that plane. If "a" is the lattice constant for Si(which is 0.543 nm), then, one can calculate the value of each side for given plane as shown in Fig. 5.7. And accordingly, the area of each plane can be calculated as follows:

$$\text{Area of } (100) \text{ plane would be } A_{100} = a \times a = a^2 = 0.295 \times 10^{-14}\text{cm}^2$$

$$\text{Area of } (110) \text{ plane would be } A_{110} = a \times \sqrt{2}a = \sqrt{2}a^2 = 0.417 \times 10^{-14}\text{cm}^2$$

$$\text{Area of } (111) \text{ plane would be } A_{111} = \frac{1}{2} \times \sqrt{2}a \times \frac{\sqrt{3}}{\sqrt{2}}a = \frac{\sqrt{3}}{2}a^2 = 0.255 \times 10^{-14}\text{cm}^2$$

Now, for (100) plane, there would be four atoms at the corner leading to effective 4 × 1/4 = 1 atoms and 1 atom in the middle entirely for plane. So total effective atoms in (100) plane (N_{100}) would be 1 + 1 = 2. For (110) plane, again there would be four atoms at the corner leading to effective 4 × 1/4 = 1 atoms and two atoms in the middle entirely for plane. Also, two more atoms at the side shared by neighboring cells leading to total effective atoms in (110) plane (N_{110}) to (4 × 1/4) + 2 + (2 × 1/2) = 4. Similarly, for (111) plane, there would be three atoms at the corner shared by five more neighboring cells, which leads to effective 3 × 1/6 = 1/2 atoms. Also, three atoms shared between two unit cells contribute 3 × 1/2 effective atoms to this plane. Hence total effective atom in (111) plane (N_{111}) would be 3/2 + 1/2 = 2. So, the density of atoms for given plane can be calculated as follows:

$$\text{Density of atoms in } (100) \text{ plane} = N_{100}/A_{100} = 2/a^2 = 6.78 \times 10^{14}\text{atoms/cm}^2$$

$$\text{Density of atoms in } (110) \text{ plane} = N_{110}/A_{110} = 4/\sqrt{2}a^2 = 9.59 \times 10^{14}\text{atoms/cm}^2$$

$$\text{Density of atoms in } (111) \text{ plane} = N_{111}/A_{111} = 2/\left(\sqrt{3}/2\right)a^2 = 7.84 \times 10^{14}\text{atoms/cm}^2$$

As discussed above that (111) and (100) are the two principal silicon crystal orientations which are widely used. Now to decide which one is better for c-Si solar cells, the above analysis of atom density can be used to decide. It can be clearly seen that the (111) planes in Si crystal has more number of silicon atoms/cm^2 and (100) plane has lowest atoms/cm^2. It means (111) plane-based c-Si wafers would have higher densities of electrical defects (interface states) and unsaturated bonds which may result in increased surface recombination compared to (100) plane based c-Si wafers. So, the (100) surface would have better electrical properties than (111) surface. This makes (100) plane-based c-Si wafers more useful and is used in majority in c-Si based solar cell industry. And also, the difference in atomic density along different planes makes it possible to get different etching rate in different crystal plane direction by choosing the appropriate chemistry. The anisotropic etching is important in achieving the pyramidal textures in mono c-Si wafer based solar cells.

5.3 Chemical Process for Texturing

As discussed in previous chapter, for enhanced light trapping in wafer based c-Si solar cells, random surface roughening is required. Fabrication of random pyramids or honeycomb-like structures on Si wafer surface would be able to provide desired surface roughening and enhanced light trapping. For achieving such surface roughening, chemical etching is the most widely used method. Since (100) c-Si wafers are preferably used in mono c-Si wafer based solar cells, anisotropic etching based on alkaline chemical solution (sodium hydroxide (NaOH) or potassium hydroxide (KOH) based) is the best selection for achieving random pyramids on Si wafer surface. Anisotropic etching method utilizes the different etching rate in different crystal direction due to different atomic density as discussed in above section. Chemical etching rate in (111) direction is less compared to (100) direction and this result in pyramid structure formation which has base (100) and four faces of pyramid with (111) plane as shown in Fig. 5.8a and b.

In multi c-Si wafers, isotropic etching is required as it contains crystal grains having different orientation of crystal planes. Since grains having (100) crystal plane, required for pyramidal structure formation, may be relatively very less and effective texturization would not be achieved with alkaline chemical solution. Therefore alkaline chemical solution based anisotropic etching does not work well in multi c-Si wafers and leads to nonuniform reflection from surface. Those regions on wafer surface which have grains with (100) plane are well textured and results in lower reflections; and those regions that do not have preferred crystal plane are not textured properly and lead to relatively high reflection from surface. For texturing of the multi c-Si wafers, acidic solution (hydrofluoric acid (HF) and nitric acid (HNO_3)) are typically used which leads to isotropic etching of the surface and is

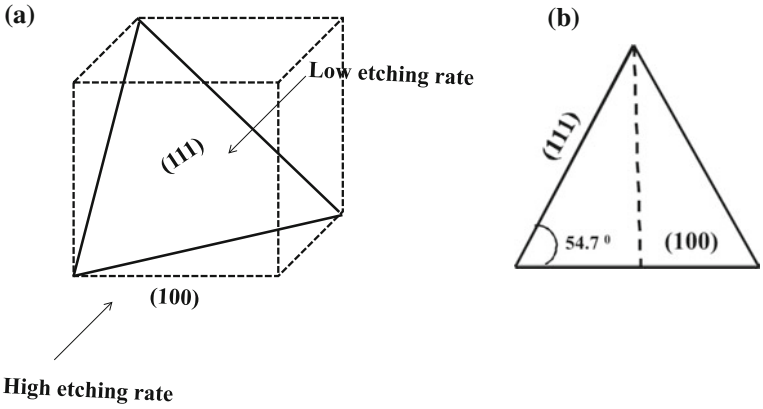

Fig. 5.8 **a** Schematic for 3D view of (100) and (111) plane having different etching rate; **b** two dimensional schematic of a pyramid structure having base with (100) plane and pyramid faces (111) plane

independent of crystal orientation. The alkaline and acidic chemical processes for mono and multi c-Si wafer texturing as been discussed below:

a) Alkaline Chemical Process for Mono c-Si Wafer Texturing

In alkaline solution based surface texturing, sodium hydroxide (NaOH) or potassium hydroxide (KOH) and de-ionized water (DI) are used along with organic agents like isopropyl alcohol (IPA). Optimization is done for volume ratios of these chemicals as per process requirements. In such chemical solutions, etching rate of Si in (100) plane is highest and is lowest in (111) plane as already shown in Fig. 5.8a. For texturing the Si wafers, the wafers are submerged vertically in the solution of KOH/NaOH, IPA, and DI with optimized volume ratios. This chemical solution, also referred as chemical bath, is kept around 80 °C temperature. The chemical reaction mechanism involved in the process is as follows:

KOH or NaOH provide hydroxyl ions (OH^-) which reacts with silicon and forms $Si(OH)_4$. $Si(OH)_4$ further reacts with hydroxyl ions and forms negative $SiO_2(OH)_2$ and water molecule. The chemical reaction is given below

$$\mathrm{NaOH/KOH + H_2O \rightarrow Na^+/K^+ + OH^-}$$
$$\mathrm{Si + 2OH^- + 2H_2O \rightarrow Si(OH)_4 + H_2}$$
$$\mathrm{Si(OH)_4 + 2OH^- \rightarrow SiO_2(OH)_2^- + 2H_2O}$$

In this reaction, the role of IPA is to control the etching rate of Si and it does not participate in the chemical reaction directly. It helps to achieve good Si surface wettability and hence pyramidal structure uniformity across the wafer.

Note that this chemical process result in upright pyramid structure as shown in Fig. 5.9a. Inverted pyramids can also be fabricated with slight modification in process sequence. For fabricating inverted pyramid, usually photolithography

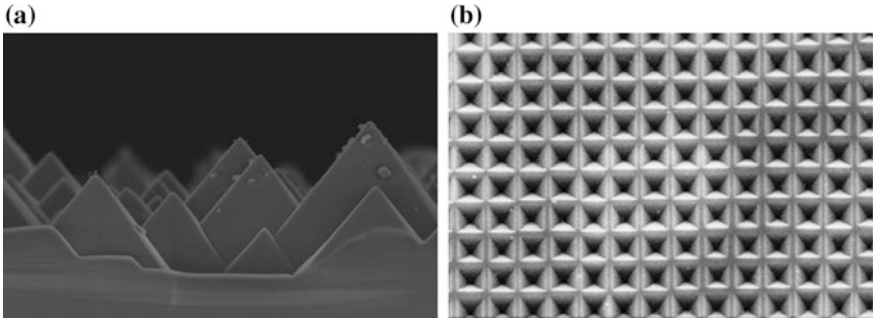

Fig. 5.9 SEM image of **a** textured mono c-Si surface (*side view*) having upright pyramid (from Ref. (Singh 2016), reproduced with permission); **b** textured mono c-Si surface (*top view*) having inverted pyramids ((Sivasubramaniam and Alkaisi 2014), Reprinted from Microelectron Eng, 119, Sivasubramaniam S, Alkaisi MM, Inverted nanopyramid texturing for silicon solar cells using interference lithography, 146–150, 2014, with permission from Elsevier)

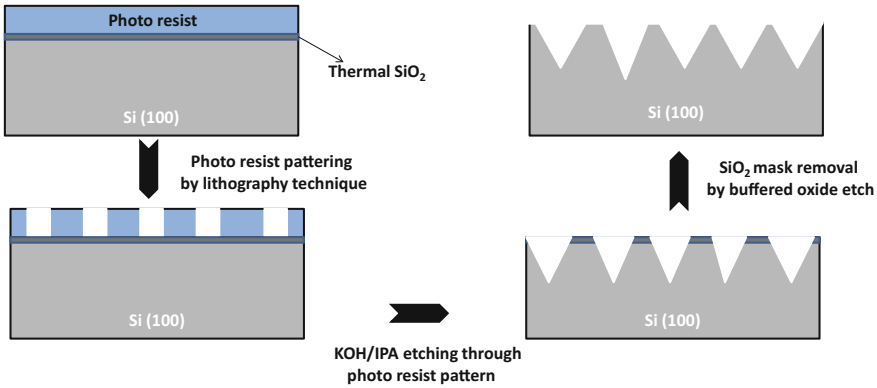

Fig. 5.10 Typical process sequence for fabricating inverted pyramid based light trapping structure (after Ref. (Sivasubramaniam and Alkaisi 2014))

technique is used. A typical SEM image of inverted pyramid based light trapping structure on c-Si wafer is shown in Fig. 5.9b. In photolithography process, a photoresist is deposited on Si wafer coated with thermal oxide. A typical schematic of process steps involved in photolithography based inverted pyramid fabrication is shown in Fig. 5.10. After photoresist deposition, interference lithography is done for opening holes through photoresist which is latter exposed to dry etching (usually plasma etching) to transfer photoresist pattern to thermal oxide.

After pattern transfer to thermal oxide, the wafer under process is exposed in KOH/NaOH + IPA + DI water chemical solution for surface etching as discussed above. This forms the inverted pyramid on the surface. After inverted pyramid formation, thermal oxide mask is removed using buffer oxide etchant.

b) Acidic Chemical Process for Multi c-Si Wafer Texturing

In acidic solution based surface texturing, hydrofluoric acid (HF), nitric acid (HNO_3) and de-ionized water (DI) is used which etches silicon isotropically. Different volume ratios of these chemicals are used and optimized as per process requirements. In the etching process, HNO_3 oxidizes Si surface and forms silicon oxide (SiO_2). The formed SiO_2 on Si surface are removed by HF. A water soluble complex (H_2SiF_6) gets formed by reacting with SiO_2 layer. The chemical reaction equations are as follows (Cheng et al. 2011):

$$3Si + 4HNO_3 \rightarrow 3SiO_2 + 2H_2O + 4NO \uparrow$$
$$SiO_2 + 6HF \rightarrow H_2SiF_6 + 2H_2O$$

The etching rate for such solution is independent of crystal orientation and can be controlled by controlling the volume ratio of HF:HNO_3:DI water. Acetic acid (CH_3COOH) or phosphoric acid (H_3PO_4) is also used to moderate the etching rate (Nishimoto 1999). CH_3COOH or H_3PO_4 has lower dielectric constant than water

and help in controlling the dissociation of HNO_3 and result in higher oxidation power of etching solution. Also, CH_3COOH or H_3PO_4 help in achieving proper wetting of Si wafer surface which is hydrophobic in nature. The acidic solution based texturing works better when surface is rough and hence as-cut wafers are preferred. Also, it requires temperature controlled environment (usually bath temperature <8 °C) as these solutions result in exothermic reactions (Einhaus et al. 1997). A typical isotropic etching based textured Si surface SEM is shown in Fig. 5.11. Also, to form honeycomb-like structure with control over depth and width of the targeted texture shape using chemical process, laser assisted surface texturing is done. In this process (see Fig. 5.12), first the full area is of wafer surface is coated with dielectric masking layer (usually silicon nitride) for masking purpose which is partially opened using lasers.

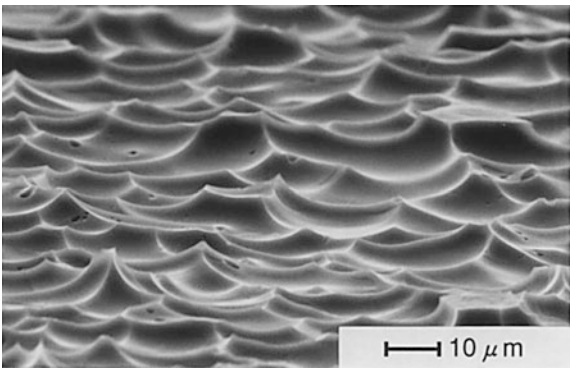

Fig. 5.11 SEM image of a multi c-Si wafer with isotropic etching based surface (from Ref. (Nishimoto 1999), reproduced by permission of The Electrochemical Society)

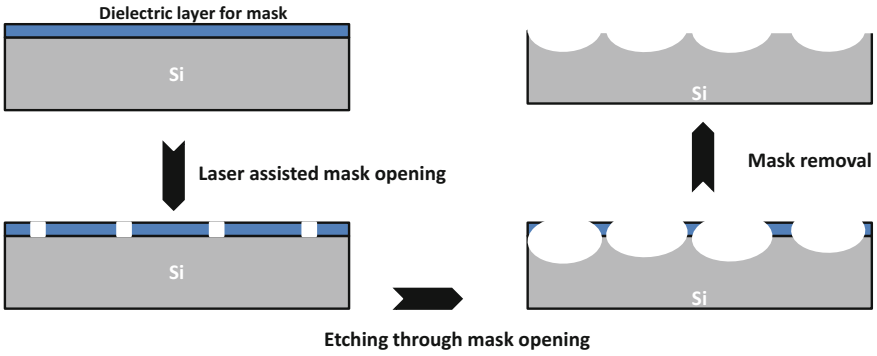

Fig. 5.12 Typical process sequence for fabricating honeycomb like textured surface (after Ref. (Volk et al. 2013))

After opening the masked layer with laser, the partially opened masked layer is exposed to HNO_3/HF chemical as discussed above for isotropic etching of Si surface. After removal of top dielectric masking layer, usually by buffered HF solution, honeycomb-like structure on multi c-Si wafer surface becomes visible. In this process, use of laser processing helps in producing homogenous hexagonal pattern and more control for adjusting the process and honeycomb structure based surface morphology (Volk et al. 2013).

5.4 Process Control for Texture Pyramids Size and Shape Distribution

Rate of etching and the shape of structures formed on the surface are important parameters of texturing process. In anisotropic etching using KOH/NaOH + IPA + DI water solution and isotropic etching using HNO_3 + HF + DI water solution, the volume ratio of chemical used in texturing process decides the etching rate. For example, in KOH:IPA:DI-based chemical solution used in pyramidal texturing of c-Si wafers, IPA concentration plays a major role in etching rate of Si surface and uniformity of pyramidal surface. If the IPA is not present in chemical solution, the etching rate would be very high (Quiebras 2013) and pyramidal shape formation on texture surface would be least probable. Also, size of the pyramidal texture would depend on the time duration for which the wafer surface is subjected into etching solution. When the wafer surface is kept for longer time in etching solution, it would result in etching of higher thickness of Si surface, which leads to the formation of pyramids of larger size. This happens when etching rate is moderate and etching rate along different crystallographic planes are distinguishable. Etching of the Si surface for different times leads to different sizes of pyramids as size and size distribution of pyramid would depend on the total etched depth as well as efficiency of the chemical residue removal during etching for given process chemistry. Different size pyramids achieved with different etching times influences the reflectance from the surface which can be seen from Fig. 5.13. The duration of etching affects the distribution of pyramid shapes and their sizes. As the pyramid size and shape distribution changes, the reflectance from surface also changes. Also, there exist optimum size and shape for which minimum reflection would occur, hence the etching time should be properly optimized. Larger pyramid size or longer etching time does not mean more reflection reduction from the surface as can be seen in Fig. 5.13. It shows that the Si wafer surface etched for 40 min result in high reflection compared to 30 min etched surfaces. The minimum reflection can be noticed for an optimum etching time of 30 min in this case. Chemical bath temperature is also crucial which govern the chemical reaction and hence the etching rate. Generally, better etching and surface texturing is achieved at chemical bath temperature of 70–80 °C. So, to control the size and shape of texture surface in KOH + IPA + DI based chemical process, KOH and IPA concentration in DI

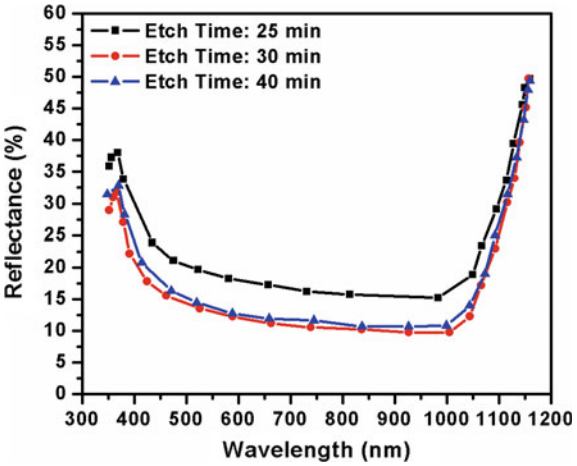

Fig. 5.13 Reflectance from etched Si wafers surface, etched for different times (25, 30, and 40 min). (after Ref. (Quiebras 2013))

water, bath temperature as well as the etching duration must be optimized for getting minimum reflection from Si surface.

Similarly, in HNO_3 + HF + DI water chemical solution based isotropic etching process, the volume ratio of HNO_3, HF, and etch rate controlling catalytic agent like CH_3COOH/H_3PO_4 is important. The etch rate for Si using such chemical solution can be varied by varying the ratio of HNO_3 and HF in DI water. Usually the chemical solution which is HNO_3 rich, etches the surface uniformly and surface texture may not be visible. For texturing the multi c-Si wafers to get texture surface, HF rich chemical solution is required (Nishimoto 1999). However, a HF rich chemical solution leads to very high etching rate and may reduce the thickness of wafer significantly which in result would reduce the wafer mechanical strength. To moderate the etching rate, catalytic agents like CH_3COOH/H_3PO_4 comes into picture. Increasing proportion of CH_3COOH/H_3PO_4 in HNO_3 + HF + DI based chemical solution can decrease the etching rate by 5–10 times and would help in achieving better texture surface leading to minimum reflection for surface.

5.5 Industrial Processes Used for Surface Texturing

In solar industry, thousands of wafers are processed every hour and hundreds of wafers are processed together in a batch for manufacturing c-Si solar cells. Usually as-cut wafers are used which are first subjected to saw damage removal before texturing process using high etch rate solution having KOH/NaOH + DI water. This etches the wafers from both sides and then the batches of these wafers are moved to dilute chemical solutions having catalytic agent mixed in it which provides better surface wettability and etching rate control as discussed above. For texturing mono c-Si wafers, hot KOH + IPA based chemical solutions are widely

used. For multi c-Si wafers, HNO_3 + HF + DI water based chemical solution optimized for isotropic etching is widely used.

For saw damage removal and texturing process, the wafers are kept in wafer cassettes (usually made of Teflon) vertically. The cassettes are loaded in holders which are automated and moves through the production unit passing in sequence for different unit processes involved in solar cell manufacturing. During texturing, the wafers are merged in chemical bath for optimized duration. During texturing process, gas bubbles, usually using hydrogen, are created to remove the residues from surface during texturing. Proper arrangements are made to avoid the wafer lifting and wafer breakage during chemical processing. Also, possible chemical spillage should be avoided. After texturing process, the wafers are rinsed several times in fresh DI water. An acid rinse is also given which neutralizes the residues of Na/K on Si wafer surface, if any. The neutralization of Na/K from Si wafer surface is important as its presence leads to impact the surface passivation of the cell and degrades its performance. After texturization, neutralization and final rinse step, the wafers are dried in spinner and are moved for further processing for solar cell fabrication.

5.6 Practical Implications of Chemical Texturing Processes

In surface texturing process of c-Si wafers, various alkaline or acidic chemical are used. At industry level, where thousands of cells are produced every day, chemical requirements are also huge. Huge requirement of chemicals poses problems of storing and managing the waste after use. During texturing process, large amount of water is also used for rinsing and texturing purpose which is also a matter of concern. The chemicals like KOH, NaOH, HF, and HNO_3 are hazardous and pose serious threat to human body if not handled properly. So, for all the chemical-related processes and experiments, proper chemical uses practice is required. Hence, these chemicals should be handled in expert supervision; otherwise, it can lead to severe injury and even death. Also, storing and managing the waste require proper knowledge and expertise. The requirement of such chemicals and disposal of waste products after use, add up to the cost of solar cell manufacturing besides negatively impacting the environment. Additionally, chemical processes influence the throughput and yield of solar cell manufacturing. If an alternative technique can be developed which can provide the cost effective solution for texturing or light trapping, without chemical processes, would be advantageous not only from cost and logistic point of view but also from environmental point of view. Several light trapping alternatives are being researched worldwide. Some important and relevant light trapping structures have been discussed in the subsequent chapters.

5.7 Questions and Problems

1. Discuss the diamond crystal structure of c-Si material. Also, calculate the atomic density and number of atoms per unit cell in Si crystal structure.
2. Why Si wafers with (100) orientation is preferred in c-Si based solar cell manufacturing?
3. Why alkaline chemical solution based surface texturing is preferred in mono c-Si wafer based solar cell manufacturing?
4. Which kind of chemical solution is preferred for surface texturing in multi c-Si solar cell manufacturing and why?
5. What are the additional processes required for making inverted pyramids on Si wafer surface using chemical method?
6. What are the roles of catalytic agents like CH_3COOH, H_3PO_4, IPA etc. in chemical texturing process?
7. Chemical composition, chemical bath temperature, catalytic agent proportion and etching time plays crucial role in texturing the Si surface and related texture size and shape. How?
8. Discuss the industrial chemical processes of texturing the c-Si wafers for solar cell manufacturing.

References

Callister W, Rethwisch D (2007) Materials science and engineering: an introduction, 7'th edn. Wiley

Cheng Y-T, Ho J-J, Tsai S-Y et al (2011) Efficiency improved by acid texturization for multi-crystalline silicon solar cells. Sol Energy 85:87–94. doi:10.1016/j.solener.2010.10.020

Einhaus R, Vazsonyi E, Szlufcik J et al (1997) Isotropic texturing of multicrystalline silicon wafers with acidic texturing solutions. In: Twenty sixth IEEE photovoltaic specialists conference—1997. IEEE, pp 167–170

Nishimoto Y (1999) Investigation of acidic texturization for multicrystalline silicon solar cells. J Electrochem Soc 146:457. doi:10.1149/1.1391628

Plummer JD, Deal MD, Griffin PB (2000) Silicon VLSI technology: fundamentals, practice and modeling

Quiebras JNX (2013) Wet chemical textures for crystalline silicon solar cells. University of Konstanz

Singh HK (2016) Plasmonics based light-trapping structures for c-Si solar cell applications. IIT Bombay, Powai, Mumbai

Sivasubramaniam S, Alkaisi MM (2014) Inverted nanopyramid texturing for silicon solar cells using interference lithography. Microelectron Eng 119:146–150. doi:10.1016/j.mee.2014.04.004

Sze SM, Ng KK (2006) Physics of semiconductor devices, 3rd edn. Wiley, Hoboken, NJ, USA

Volk A-K, Gutscher S, Brand A, et al (2013) Laser assisted honeycomb-texturing on multicrystalline silicon for industrial applications. In: 28th European PV solar energy conference and exhibition, pp 1024–1028

Chapter 6
Anti-reflection Coatings with Textured Surface for c-Si Solar Cells

In this chapter, focus is on comparative study of dielectric layer based, textured based, and combination of the both light trapping structures on the solar cell performances. Also, implications and solutions have been discussed in context of next generation c-Si solar cells. Solar cell performance comparisons for different light trapping combinations shown in this chapter are based on simulated results. Material/semiconductor properties used in simulations for getting the cell electrical performance are based on most relevant c-Si solar cell device. Also, the anti-reflection properties of the considered device used in simulations are mostly based on actual measured values.

6.1 Primary Benefit of Textured Surface in Combination with Anti-reflection Layer

As we have seen in pervious chapters that only use of anti-reflection layer on c-Si wafer or texturization of wafer surface cannot be the optimum solution for reflection reduction as in each case the reflection does not reduce below 12–15%. For better anti-reflection and light trapping, combination of both texturing as well as anti-reflection coating, would be required which brings down the reflection from c-Si wafer to 3–4% which is honorable. Figure 6.1 shows reflection from a 180 μm c-Si wafer having 80 nm silicon nitride (SiN_x) based anti-reflection coating (ARC) on non-textured surface and on textured surface having 5–8 μm upright pyramids. Clear reduction in reflectance for the combination of ARC and texturing can be seen for broad wavelength range. This is main/primary benefit of using ARC in combination of texture-based light trapping structure.

The other benefit of using dielectric-based ARC is reduction in surface recombination arising due to surface roughening as discussed in Sect. 3.5 of Chap. 3 and Sect. 4.6 of Chap. 4. Now let us see the relative gain in terms of solar cell

© Springer Nature Singapore Pte Ltd. 2017

C.S. Solanki and H.K. Singh, *Anti-reflection and Light Trapping in c-Si Solar Cells*, Green Energy and Technology,
DOI 10.1007/978-981-10-4771-8_6

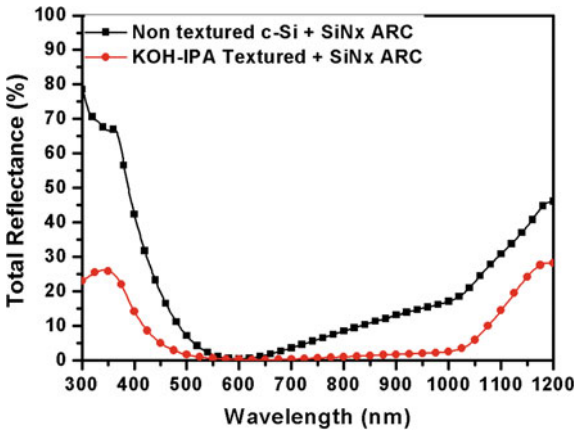

Fig. 6.1 Reflectance from surface of a 180 μm c-Si wafer having silicon nitride (SiN_x) based anti-reflection coating on non-textured surface and textured surface

performance due to improvement in anti-reflection from surface. The best way to compare the solar cell performance is simulation of cell assuming all parameters same except reflection. PC1D-based simulation (PC1D 5.9) is a simple yet effective tool for such comparison where actual reflectance data can be used in simulating the cell parameters. For comparisons, let us assume two scenarios, i.e., best cell condition and typical cell condition. In both case, let us assume the cell thickness is 180 μm and cell active area is 100 cm^2. Considering base wafer as p-type having resistivity 1 Ω-cm and diffused n-type emitter with sheet resistance 50 Ω/sq having erfc diffusion profile. Let us assume the junction depth of about 400 nm. The light source for simulation would be AM 1.5G spectrum with intensity 100 mW/cm^2 which is meant for cell performance targeting terrestrial application. The simulation parameters for simulation of solar cell with actual reflectance profile has been given in Table 6.1.

In best cell and typical cell scenario, the cell parameters which are taken different are bulk minority carrier lifetime, front and back surface recombination velocity, series resistance, and shunt resistance as tabulated in Table 6.1. The typical conditions assumed are closer to what we get in normal routine of cell fabrication. In the given table, the actual reflectance means actual measured reflectance from light trapping structures with samples having 80 nm silicon nitride (SiN_x) based anti-reflection coating (ARC) on non-textured surface and on textured surface having 5–8 μm upright pyramids as shown in Fig. 6.1. The schematic of device under consideration can be seen from Fig. 6.2 for case of anti-reflection coating (ARC) on non-textured surface and on textured surface where both side surfaces are assumed textured. The simulated data in the two cases, i.e., ARC on non-textured surface case and textured surface case, would help in understanding the role of anti-reflection layer on cell performance enhancement. Also, cell's other relevant parameters and their contribution can be tracked which might be contributing in the cell performance improvement when simulated electrical performance comparison is done for a typical and a best device having similar reflection profile. Here, typical

Table 6.1 Simulation parameters for PC1D simulation in best cell scenario and typical cell scenario

Solar cell parameters	Best cell scenario	Typical cell scenario
Cell/Wafer thickness	180 µm	180 µm
Cell active area	100 cm^2	100 cm^2
P-type base wafer resistivity	1 Ω-cm	1 Ω-cm
Emitter sheet resistance (after doping)	50 Ω/sq (Diffusion profile: erfc)	50 Ω/sq (Diffusion profile: erfc)
Junction depth	400 nm	400 nm
Bulk recombination lifetime	400 µs	40 µs
Front surface recombination velocity	100 cm/s	10^4 cm/s
Back surface recombination velocity	100 cm/s	1000 cm/s
Temperature	300 °K	300 °K
Series resistance	1 mili-Ω	5 mili-Ω
Shunt resistance	1000 Ω	100 Ω
Reflectance profile	Actual reflectance	Actual reflectance
Light source	One Sun, AM 1.5G spectrum	One Sun, AM 1.5G spectrum
Light intensity	100 mW/cm^2	100 mW/cm^2

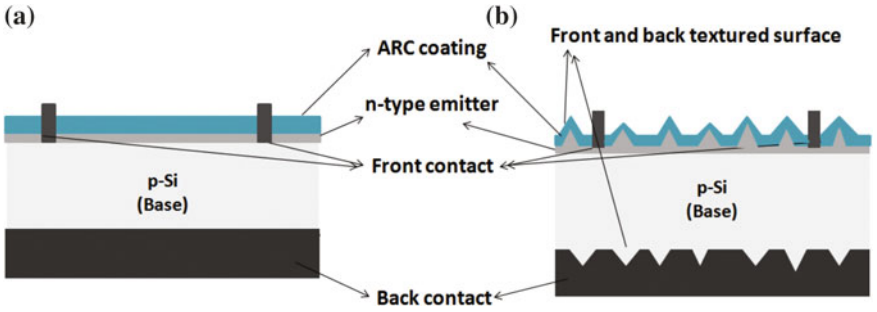

Fig. 6.2 Schematic of solar cell **a** having anti-reflection coating (ARC) on non-textured surface and **b** ARC coating on textured surface (both side textured) (Texture size and individual layer thicknesses are for representation purpose and not to scale)

and best device term is used to distinguish the material/semiconductor parameters difference in the simulation.

The simulated I–V characteristics can be seen from Fig. 6.3 which clearly indicate the improvement for combination of both light trapping structures, i.e., textured surface coated with dielectric ARC layer. Also to notice that the cell with "best cell scenario" parameters generate more current compared to "typical cell

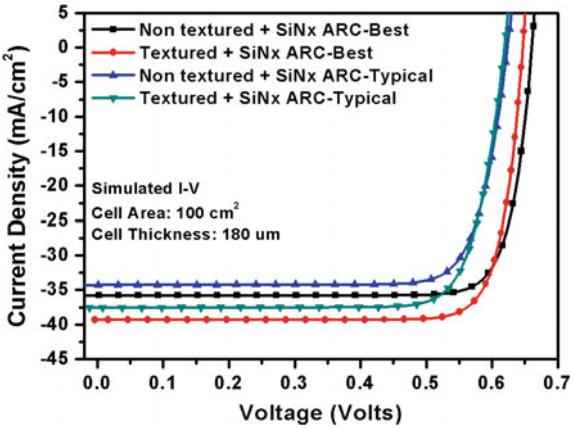

Fig. 6.3 Simulated I–V characteristics of solar cell device having ARC coating on non-textured surface and textured surface for "best cell scenario" and "typical cell scenario" parameters

scenario" parameters though the reflection profile is same. Note that in the simulation, no parasitic absorption has been assumed. Also, for textured surface and non-textured surface based cell performance comparison in each scenario, similar surface recombination velocity has been assumed for particular case though the textured surface would generally lead high recombination velocity compared to planner surface. This shows the comparison of the cell performance improvements due to anti-reflection and light trapping improvement in cell solely, as all other parameters were kept constant.

Table 6.2 gives PC1D-simulated cell performance parameters for textured and non-textured surface with ARC for both "best cell scenario" and "typical cell scenario". The data indicates that there is gain in short circuit current (J_{sc}) of up to 3.2–3.5 mA/cm^2 for the case of ARC on textured surface as compared to the case of ARC on non-textured surface.

You can also notice from Table 6.2 that there is major improvement in open circuit voltage (V_{oc}) when device parameters are selected for "best cell scenario", however, impact on J_{sc} is relatively less. Also, the textured surface lead to lower V_{oc}

Table 6.2 Cell performance parameters as per PC1D simulation

Cell	Open circuit voltage (V_{oc}) (mV)	Short circuit current (J_{sc}) (mA)	Efficiency (η) (%)
Non-textured + SiN_x ARC (Best cell scenario)	660.4	35.8	19.7
Textured + SiN_x ARC (Best cell scenario)	646.6	39.3	21.1
Non-textured + SiN_x ARC (Typical cell scenario)	623.4	34.3	17.2
Textured + SiN_x ARC (Typical cell scenario)	618.8	37.5	18.6

due to increased defect states on surface because of increased (111) crystal plane area as discussed in Sect. 5.2 of previous chapter. It is worth mentioning that the defect states increment due to texturing and exposure of more (111) plane on the surface is well accounted in PC1D during simulation and the impact can be seen in the simulated results.

6.2 Analysis on Cell Performance Having Textured Surface but Without and with Anti-reflection Layer

In the above section, we saw the impact on solar cell performance for ARC layer in combination of texture surface and ARC layer in combination of non-texture surface. Now let us see what would be expected gain in solar cell performance when it is compared for light trapping structure having textured surface in combination of ARC layer and texture surface alone. The schematic of device can be seen from Fig. 6.4a for case of textured surface as sole light trapping structure and Fig. 6.4b for anti-reflection coating (ARC) in combination of textured surface. From Fig. 6.5, which shows the reflection from a 180 μm c-Si wafer having 80 nm silicon nitride (SiN_x) based anti-reflection coating (ARC) on textured surface and from textured wafer surface, significant reduction in reflectance for broad wavelength range can be noticed. Now, if this reflectance data is used for PC1D simulation, we would get to know how much relative improvement we are expecting in solar cell performance when adding anti-reflection layer (ARC) to a textured surface. For comparisons, let us again assume two scenarios, i.e., "best cell scenario" and "typical cell scenario" as assumed in above section. In both cases, let us assume the 180 μm cell thickness of cell and 100 cm^2cell active area.

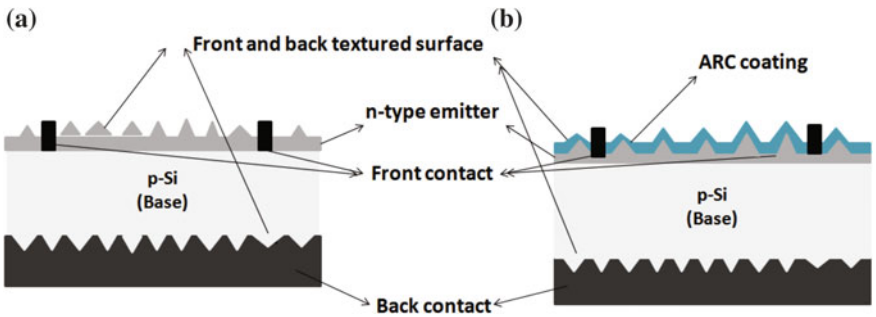

Fig. 6.4 Schematic of solar cell **a** having textured surface as sole light trapping structure; **b** having combination of anti-reflection coating (ARC) and textured surface for light trapping (Texture size and individual layer thicknesses are for representation purpose and not to scale)

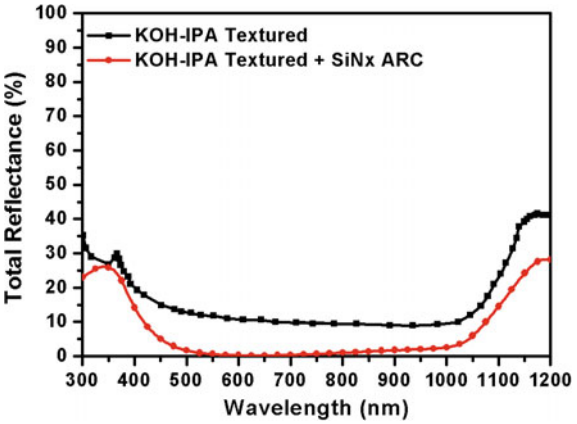

Fig. 6.5 Reflectance from surface of a 180 μm c-Si wafer having KOH-IPA based textured surface and KOH-IPA based textured surface coated with silicon nitride (SiN_x) based anti-reflection coating

Further, base wafer as p-type having resistivity 1 Ω-cm and diffused n-type emitter with sheet resistance 50 Ω/sq having erfc diffusion profile is assumed. Also, it is assumed that the junction depth is 400 nm. AM 1.5G spectrum with intensity 100 mW/cm^2 is taken for I–V simulation. Simulation parameters used to obtain Fig. 6.5 are summarized in Table 6.1. Figure 6.6 shows the simulated I–V characteristics which indicate the significant improvement for combination of both light trapping structures, i.e., textured surface coated with dielectric ARC layer.

Again, notice that in the cell with "best cell scenario" parameters more current gets generated as compared to "typical cell scenario" though the same reflection profile is assumed in both cases. Cell performance parameters as per PC1D simulation has been tabulated in Table 6.3. The data analysis indicates that there is expectation of gain in short circuit current (J_{sc}) of up to 3.4–3.6 mA/cm^2 for textured based surface in combination to ARC when compared with non-ARC coated textured surface. You can also notice from Table 6.3 that there is slight improvement in open circuit voltage (V_{oc}) which is due to improved J_{sc}.

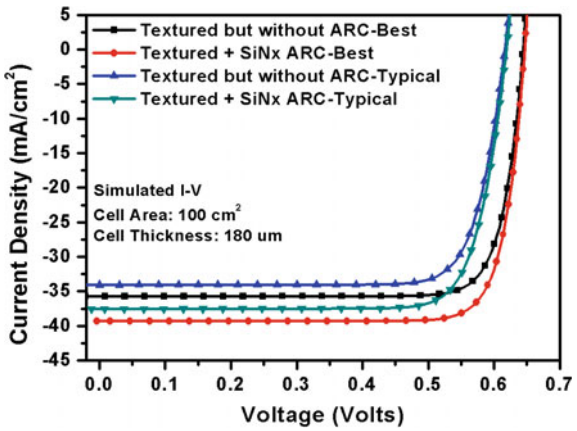

Fig. 6.6 Simulated I–V characteristics of solar cell device with and without ARC coating on textured surface in two cell conditions (Best and Typical)

Table 6.3 Cell performance parameters as per PC1D simulation

Cell	Open circuit voltage (V_{oc}) (mV)	Short circuit current (J_{sc}) (mA)	Efficiency (η) (%)
Textured but without ARC —(Best)	644.1	35.7	19.1
Textured + SiN_xARC—(Best)	646.6	39.3	21.1
Textured but without ARC —(Typical)	616.3	34.1	16.9
Textured + SiN_xARC—(Typical)	618.8	37.5	18.6

Note that here we talked about the sole expected gain due to anti-reflection improvement. The assumption for particular cell scenario, in a given case, the surface recombination velocities (SRV) are same and dielectric ARC coating does not influence the surface passivation, is hypothetical. However, in actual case there is always improvement in SRV which adds up to the relative performance positively for case of texture surface coated with dielectric ARC. The improvement in SRV due to dielectric ARC coating reflects the dual role of dielectric ARC's, i.e., improved anti-reflection and improved surface passivation. Analysis and discussion on dual role of dielectric ARC's and solar cell performance is done in next section.

6.3 Dual Role of Anti-reflection Layers in c-Si Solar Cells

Till now we discussed about how improving the anti-reflection enhances the solar cell performance, especially short circuit current. Dielectric layer/anti-reflection coating (ARC) in combination with textured surface gives best performance mostly due to much better light trapping. Also, the ARC improves the passivation from the surface as it helps in saturating the dangling bonds present on c-Si wafer surface due to abrupt termination of atoms as discussed in Sect. 3.5 of Chap. 3.

For comparison of current enhancement in above sections, the surface recombination velocities (SRV's) were assumed same in each scenario for cells with and without ARC-coated textured surfaces. However, if the textured surface is not coated with dielectric passivation layer, the front surface recombination velocity (FSRV) would be in the range of 10^6–10^7 cm/s. Using well-optimized dielectric layer on such texture surface may improve the FSRV to 100–1000 cm/s. Let us see how improvement in FSRV due to dielectric passivation layer impacts the cell performance. For this, let us again assume the cell thickness and cell active area same as assumed in Sect. 6.2. Also, the same kind of base wafer, i.e., p-type having resistivity 1 Ω-cm and diffused n-type emitter with sheet resistance 50 Ω/sq having erfc diffusion profile with the junction depth of about 400 nm. The light source as per AM 1.5G spectrum with intensity 100 mW/cm^2. For IQE, let us assume the

Table 6.4 Simulation parameters for PC1D simulation in textured without ARC and textured with ARC based solar cell cases

Solar cell parameters	Cell with textured surface and No ARC	Cell with textured surface and with ARC
Cell/Wafer thickness	180 μm	180 μm
Cell active area	100 cm^2	100 cm^2
P-type base wafer resistivity	1 Ω-cm	1 Ω-cm
Emitter sheet resistance (after doping)	50 Ω/sq (Diffusion profile: erfc)	50 Ω/sq (Diffusion profile: erfc)
Junction depth	400 nm	400 nm
Bulk recombination lifetime	40 μs	40 μs
Front surface recombination velocity	10^6 cm/s	1000 cm/s
Back surface recombination velocity	1000 cm/s	1000 cm/s
Temperature	300 °K	300 °K
Series resistance	5 mili-Ω	5 mili-Ω
Shunt resistance	100 Ω	100 Ω
Reflectance profile	Actual reflectance	Actual reflectance
Light source	One Sun, AM 1.5G spectrum	One Sun, AM 1.5G spectrum
Light intensity	100 mW/cm^2	100 mW/cm^2
Light intensity for EQE and IQE simulation	1 mW/cm^2	1 mW/cm^2

light intensity for simulation is 1 mW/cm^2. The required simulation parameters for simulating solar cell performance and IQE with actual reflectance profile (see Fig. 6.5) has been tabulated in Table 6.4. For comparative analysis, let us assume that the dielectric ARC coating improves the FSRV from 10^6 to 1000 cm/s.

The improved FSRV specially influences the collection of charge carriers generated due to short wavelengths. As the FSRV improves, internal quantum efficiency (IQE) improves at shorter wavelength range as you can see in Fig. 6.7 which shows the simulated IQE for the two cases. Clear improvement can be seen in short wavelength range (300–500 nm) for cell with better FSRV. The cell performance parameters tabulated in Table 6.5 also indicate the difference of improved FSRV which mainly influences the open-circuit voltage (V_{oc}) of the cell.

The short-circuit current gain is mainly due to improved anti-reflection when textured surface is coated with dielectric layer.

So, the dual role of such dielectric layer which improves anti-reflection leading to improved short circuit current, and improving surface passivation and hence FSRV leading to improved open circuit voltage, can be understood from this analysis. Improved charge carrier collection especially in short wavelength region adds up to the current collection from the solar cell device leading to overall performance improvement.

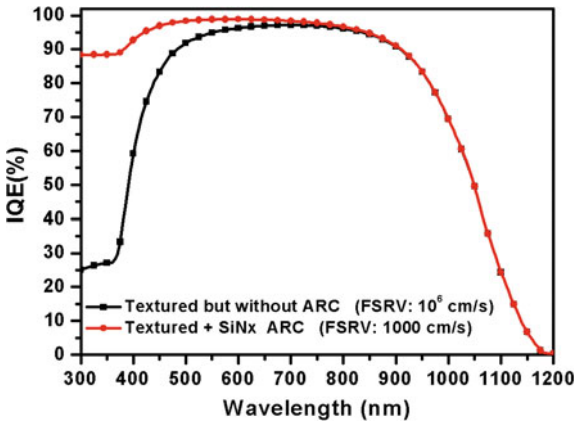

Fig. 6.7 Simulated IQE characteristics of solar cell device with and without ARC coating on textured surface

Table 6.5 Cell performance parameters as per PC1D simulation

Cell	Open circuit voltage (V_{oc}) (mV)	Short circuit current (J_{sc}) (mA)	Efficiency (η) (%)
Cell with textured surface and No ARC	598.9	32.6	15.6
Cell with textured surface and with ARC	619.7	37.6	18.7

6.4 Most Suitable Light Trapping Geometry

As we have seen in above discussions that textured surfaces with anti-reflection coating in c-Si solar cells lead to better cell performance. In those discussed cases, improved light trapping contribution is seen mainly in enhancing the current generation potential of the cell. Also, improved surface passivation by dielectric coating improves current collection and open-circuit voltage from the cell. We also have seen in Chap. 4 that there are many types of texture-based light trapping structures which with combination of appropriate ARC can lead to better performance. But, cost effectiveness is the deciding factor in implementation and adoption of these light trapping structures for large-scale solar cell production. The upright pyramid based light trapping structure in combination with optimized dielectric coating is simpler and scalable to industrial production level and is a widely preferred light trapping technology. However, the inverted pyramids based light trapping would be better compared to upright pyramids based light trapping structure as discussed in Sect. 4.5 of Chap. 4. Best reported cell in mono c-Si solar category had inverted pyramid based light trapping structure coated with double dielectric layer (Zhao et al. 1996). But to form inverted pyramid structure,

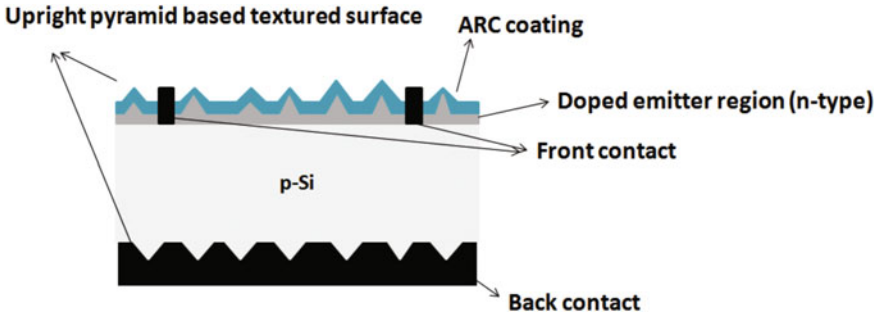

Fig. 6.8 Schematic of widely preferred p-type mono c-Si solar cell having textured surface in combination with anti-reflection coating (ARC) (Texture size and individual layer thicknesses are for representation purpose and not to scale)

lithography technique is required as discussed in Sect. 5.3 of Chap. 5. So, though the inverted pyramid based light trapping structure may provide comparatively better light trapping, due to cost effectiveness as well as comparative implementation simplicity, chemical texturing based upright pyramidal light trapping structure is preferred in mono c-Si wafer based solar cell manufacturing line. A typical cell schematic which is well-preferred device structure for p-type mono c-Si solar cell is shown in Fig. 6.8.

The shown p-type mono c-Si solar cell in the figure has upright pyramid based textured surface at both front and back surface and front surface is coated with dielectric layer which acts as surface passivation layer as well as anti-reflection coating. The back surface is passivated by back surface field (BSF) formed during contact firing of the cell where highly doped region are formed at metal (back contact)-Si interface as discussed in Chap. 2.

In multi c-Si solar cells, where the upright pyramid structures are not possible for large area processing and is not preferred as suitable texture structure, honeycomb structures are used which are fabricated by chemical isotropic etching as discussed in Chap. 5. A typical cell schematic which is well-preferred device geometry for

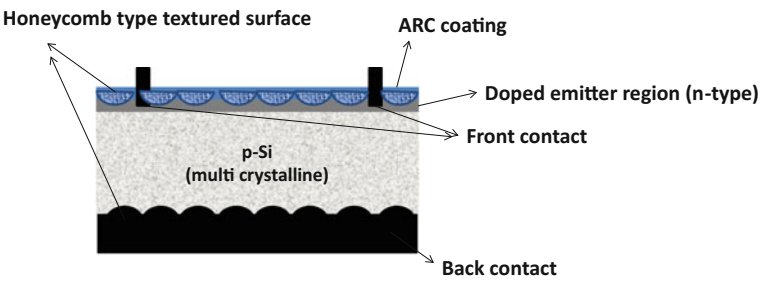

Fig. 6.9 Schematic of widely preferred p-type multi c-Si solar cell having textured surface in combination with anti-reflection coating (ARC) (Texture size and individual layer thicknesses are for representation purpose and not to scale)

p-type multi c-Si solar cell is shown in Fig. 6.9. The cell geometries remain the same as mono c-Si solar cell except the substrate wafer which is multi-crystalline instead of (100) mono crystalline.

6.5 Implication of Existing Light Trapping Geometry for Next Generation Solar Cells

All the discussions are made for different light trapping structures until now indicated that having combination of texture and ARC-coated surfaces would result in better performing cells. All these analysis are true and well appreciated considering the fact that still we are using commonly available wafer thickness of 180–200 μm. However, when we talk about further cost reduction in solar cell manufacturing, wafer thickness used in solar cell fabrication should decrease to bring down the uses of Si material to reduce cost proportion shared by wafer in cell price as discussed in Chap. 2. Thinner wafer based solar cell would be preferred in near future and lots of efforts are being put to manufacture cost effective thinner c-Si wafers at industrial scale.

When the current c-Si solar cell technology would be shifting towards thin (<100 μm) wafer based technology, light trapping using textured and ARC combination based technology would be a concern and may not be favorable. Such light trapping geometry in thinner wafer based cells would result in relatively more surface recombination due to roughening of the surface. The surface roughening result in relative increment of (111) plane based surface compared to planner surface having (100) plane considering pyramidal textures. A study presented by McIntosh et al. (McIntosh and Johnson 2009) indicates that when (100) Si wafer is textured, surface area covered with (111) planes on surface increases and the surface area increase is about 1.73 times or more when compared with planner (100) wafer surface. This increased surfaces area with more (111) planes have more dangling bonds and trap states which would lead to more recombination events at the surface. McIntosh et al. (McIntosh and Johnson 2009) did comparative study for recombination increment between Si wafers having planner surface and textured surface. They used a 400 μm thick and (100) float-zoned n-type silicon wafers with resistivity ≥ 100 Ω-cm. After texturing, their sample had 1.5–2 μm random pyramids. Their planner and textured surface based samples had been subjected to light $POCl_3$ diffusion (both sides) with post-processing sheet resistance of 130–160 Ω/sq and passivated using thermally grown oxide. The measured effective lifetime using photo conductance method for the two cases and the observed results are shown in Fig. 6.10.

The effective lifetime for random textured silicon wafer sample show significantly shorter lifetime compared to planner (100) Si sample. Increased recombination, up to 10–12 times for random textured surface when compared with planner (100) surface, is indicated. Also, for non-diffused Si with textured surface and passivated with PECVD SiN_x, many researcher have shown up to 35 times

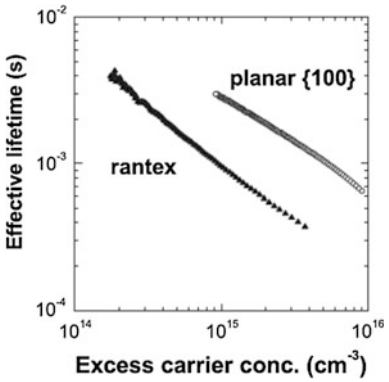

Fig. 6.10 Effective lifetime as a function of excess carrier concentration for rantex (random textured) and planar (100) wafer based samples (Reproduced from (McIntosh and Johnson 2009), with permission of AIP Publishing)

increment in recombination when compared to planner Si surface processed under same condition. Such increment in surface recombination which impacts the minority carrier life time (τ) adversely is matter of concern, especially when our target is thin c-Si wafer based cells. Minority carrier lifetime (τ) is most important parameter for cell electrical performance point of view and larger value τ is preferred for fabricating an efficient solar cell. Relative reduction in minority carrier lifetime due to increased recombination at surface is the major downside of the traditional texturization based light trapping structure. Impact on minority carrier lifetime becomes much more critical as the thickness of wafer is reduced further. The high recombination probability in small thickness wafers, where more charge carrier generation happen in relatively smaller volume, the surface recombination effect becomes much more prominent. The texturization process leading to relatively higher surface recombination would require extremely good surface passivation as the wafer thickness reduces. Let us point out here that c-Si solar cells with good efficiency has also been reported using thinner c-Si wafer having textured surface, e.g., heterojunction with intrinsic thin-layer (HIT) cells as discussed in Sect. 2.7 of Chap. 2. However, there is no comparison that exists at present for relative performance improvement if the same cells are fabricated avoiding texturization step. Also, if some light trapping structure comes as alternative to texturization with similar light trapping potential, these cells may even perform better due to relatively improved minority carrier lifetime.

6.6 Suitable Light Trapping Structure for Next Generation Solar Cells

Next generation c-Si solar cells would be based on thinner wafers and light management in such low thickness wafer based cells would be challenging. The main implication of textured surface based light trapping structure in combination of suitable anti-reflection coating (ARC) is increase in surface recombination which

adversely impacts the solar cell performance. Also, texturing process requires etching of Si material and usually 5–10 μm texture surface requires about 5–10 μm etching of Si wafer from each side, which is really significant for next generation thin c-Si solar cell technology where target wafer thickness is ≤ 100 μm for solar cell manufacturing. In such scenario, the requirement of better light trapping arrangement becomes essential so that we can target better light trapping as well as lower loss of active absorbing material. The suitability of alternative light trapping structure would be decided by its potential to increase the cell performance in competence with texture and ARC combination based light trapping structures. As discussed in Sect. 6.1, for ARC on textures surface when compared with ARC on planner surface, there is scope of 3.2–3.5 mA/cm^2 current enhancement (see Table 6.2). Whereas reduction in open circuit voltage due to increased recombination (SRV) at surface because of surface roughening is evident. The analysis made in Sect. 6.1 was for 180–200 μm thick c-Si wafer based cells. However, more suitable light trapping structure for next generation c-Si solar cells would be one for which we could make similar enhancement in current even if the thickness of wafer used for the cell fabrication is reduced to ≤ 100 μm. If somehow the light trapping structure does not take part in active device (i.e., where the actual light absorption and the charge carrier generation and recombination happens) and do not influence the surface passivation adversely as textured structure, degradation in V_{oc-} can also be avoided and overall enhancements in cell performance can be expected. Also, it is worth mentioning here that as the thickness of wafer reduces, the enhancement in V_{oc} can be expected provided the surface recombination velocity tends to zero, i.e., if excellent surface passivation could be achieved. The thickness of solar cell and open circuit voltage are related as per following given Eq. (6.1) provided the wafer thickness (W) $\leq$ minority carrier diffusion length (L) (Brendel and Queisser 1993).

$$\frac{dV_{oc}}{dW} = -\frac{kT}{q} \times \frac{1}{W}, \tag{6.1}$$

where k is Boltzmann constant, q is charge of electron, T is temperature of the cell. So, for moving towards next generation c-Si solar cells, we would need such light trapping structure which should not be the part of active device, i.e., no surface modification for light trapping should be associated with active absorbing material which might lead to increased recombination. And yet it should provide competitive light trapping when compared to ARC-coated textured surface based light trapping structure. Schematic of solar cells with current and indicative next generation light trapping structure, which indicates the expected shift in device architecture design, is shown in Fig. 6.11. Figure 6.11a shows schematic of a c-Si solar cell architecture currently in use having ARC coated textured surface at front and have both side surface textured. Also, a probable next generation thinner c-Si wafer based solar cell schematic is shown in Fig. 6.11b which has an indicative alternative light trapping structure as replacement of texturization-based light trapping geometry and where both front and back surfaces are planner. It indicates

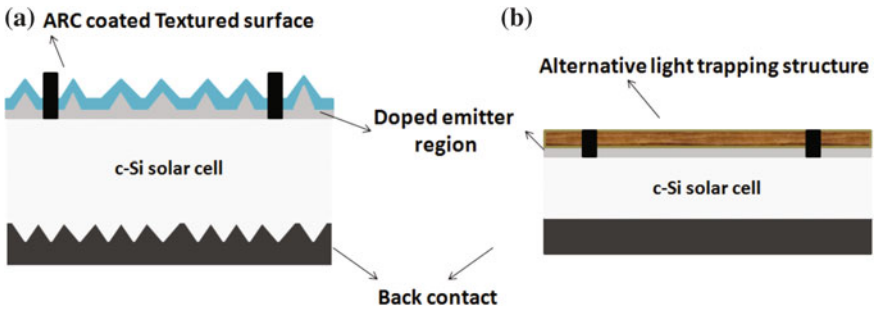

Fig. 6.11 Schematic of c-Si solar cell architecture **a** currently in use having ARC coated textured surface; **b** for next generation thinner c-Si wafer based solar cells having indicative alternative light trapping structure

no surface modification for light trapping to avoid increment in surface recombination.

Here discussion on alternative light trapping structure has been made as replacement of textured surface. However, it is worth pointing out here that thinner c-Si solar cells with textured surface coated with ARC has also been reported. For example, 18 μm thin c-Si solar cell on steel substrate (Wang et al. 2014) and 47 μm thin c-Si solar cell with PERL structure (Wang and Zhao 1996) by Wang et al. Also, 43 μm thin c-Si solar cell by Petermann et al. (2012). All these cells were reported to give short circuit current in the range of 34–37.8 mA/cm^2 with optimized structures. But, comparison to relative performance improvement for the same cells fabricated avoiding texturization step does not exist and the impact of texturization and relative gain or loss in V_{oc} and J_{sc} of the cell cannot be commented for such thin c-Si wafer based cells.

Alternative light trapping structures with similar light trapping potential may lead to better cell performance due to relatively lower recombination at surface. Some advancement in alternative light trapping geometries as alterative to texturization-based light trapping structures has been discussed in subsequent chapters.

6.7 Questions and Problems

1. Discuss on the performance improvement of a c-Si solar cell when an anti-reflection layer is added on textured surface?
2. How solar cell performance is influenced by incorporating texture surface in addition to anti-reflection coating on planner surface for case of 180–200 μm thick wafer based c-Si solar cells?

3. Compare the performance of c-Si solar cells for the two scenarios using PC1D where (i) cell is with ARC coating (thickness 80 nm and RI: 2.0) on planner surface and (ii) cell is having textured surface (texture pyramid size of 5 μm) only. Consider the following parameters for computation.

Solar cell parameters	Parameters values
Cell/Wafer thickness	200 μm
Cell active area	100 cm^2
P-type base wafer resistivity	1 Ω-cm
Emitter sheet resistance (after doping)	50 Ω/sq (Diffusion profile: erfc)
Junction depth	400 nm
Bulk recombination lifetime	200 μs
Front surface recombination velocity	1000 cm/s
Back surface recombination velocity	1000 cm/s
Temperature	300 °K
Series resistance	5 mili-Ω
Shunt resistance	800 Ω
Light source	One Sun, AM 1.5G spectrum
Light intensity	100 mW/cm^2

4. Why open-circuit voltage of the cell decreases while short circuit current increases when ARC coated planner surface of the cell is replaced with ARC coated textured surface?
5. How much increment in short circuit current can be expected when ARC-coated planner surface of the cell is replaced with ARC-coated textured surface in typical cell condition and best cell condition? What influences the difference in current gain in these two scenarios?
6. How is the internal quantum efficiency (IQE) influenced by ARC. What does it indicate? Is it an indicator of passivation quality of surface or light trapping? Discuss.
7. What do you mean by most suitable light trapping geometry?
8. Discuss the implications of texturing-based light trapping structures and impact on solar cell performance?
9. What do you mean by next generation c-Si solar cells? What would be the implications of using textured and ARC combination based light trapping structures in thinner wafer based c-Si solar cells?
10. What should be the focus of light trapping structure development for next generation c-Si solar cells?
11. Calculate the gain in open circuit voltage if the cell thickness is reduced from 200 μm to 80 μm? Assume that the cell is at room temperature and minority carrier diffusion length is 400 μm. Also, the cell surface passivation quality is excellent.

12. Compare the performance of c-Si solar cells having thicknesses (i) 200 μm and (ii) 50 μm for the two scenarios using PC1D where (a) cell is with ARC coating (thickness 80 nm and RI: 2.0) on planner surface and (b) cell is having ARC-based textured surface with fixed reflectance of 3%. Consider the following parameters for computation.

Solar cell parameters	Parameters values
Cell active area	100 cm^2
P-type base wafer resistivity	1 Ω-cm
Emitter sheet resistance (after doping)	50 Ω/sq (Diffusion profile: erfc)
Junction depth	300 nm
Bulk recombination lifetime	200 μs
Front surface recombination velocity	100 cm/s
Back surface recombination velocity	1000 cm/s
Temperature	300 °K
Series resistance	1 mili-Ω
Shunt resistance	1000 Ω
Light source	One Sun, AM 1.5G spectrum
Light intensity	100 mW/cm^2

References

Brendel R, Queisser HJ (1993) On the thickness dependence of open circuit voltages of p-n junction solar cells. Sol Energy Mater Sol Cells 29:397–401. doi:10.1016/0927-0248(93)90098-N

McIntosh KR, Johnson LP (2009) Recombination at textured silicon surfaces passivated with silicon dioxide. J Appl Phys 105:124520. doi:10.1063/1.3153979

PC1D 5.9 PC1D (ver 5.9) Software for modelling a solar cell

Petermann JH, Zielke D, Schmidt J, et al (2012) 19%-efficient and 43 μm-thick crystalline Si solar cell from layer transfer using porous silicon. Prog Photovolt Res Appl 20:1–5. doi:10.1002/pip.1129

Wang A, Zhao J (1996) 21.5% efficient thin silicon solar cell. Sol Energy 4:55–58

Wang L, Lochtefeld A, Han J et al (2014) Development of a 16.8% efficient 18-μm silicon solar cell on steel. IEEE J Photovolt 4:1397–1404. doi:10.1109/JPHOTOV.2014.2344769

Zhao J, Wang A, Altermatt P et al (1996) 24% efficient perl silicon solar cell: Recent improvements in high efficiency silicon cell research. Sol Energy Mater Sol Cells 41–42:87–99. doi:10.1016/0927-0248(95)00117-4

Chapter 7
Advancements in Traditional Light Trapping Structures

This chapter focuses on latest developments in traditional light trapping structures. In this chapter, the discussion have been made mainly on the advancement in traditional light trapping e.g. development and techniques for nano-sized textures, back reflectors and the cell designs incorporating the latest developments. Interference lithography technique for nano-sized inverted pyramids based in c-Si solar cell has been discussed. Also, brief introduction to nanoparticles based back reflectors as well as plasmonics based light director and related developments and scopes has been discussed.

7.1 Traditional Light-Trapping Structures

Traditional light-trapping structure means the light-trapping structure which is widely in use currently for manufacturing c-Si solar cells where c-Si wafers of thickness in the range of 180–200 μm is used. The widely used light trapping structure in c-Si solar cells is pyramidal texture in combination with anti-reflection coating.

In pyramidal texture-based light trapping, upright pyramids at both the surfaces of the cell, as shown in Fig. 7.1a, is the most widely used. In such design, the front texture is coated with anti-reflection coating, usually with silicon nitride (SiN_x) thin film, for enhanced forward coupling of light and better cell performance as discussed in pervious chapter. Also, the front surface has fingers and bus bars for contact. For the back contact, the complete surface at back is covered with metal which also provides better back reflection from the surface.

The other light trapping geometry is inverted pyramid texture in combination with anti-reflection coating as shown in Fig. 7.1b. In such design, all other layers, like front contact, back contact, and anti-reflection coating thickness, remains the same expect the texture shape at both sides of the cell. As discussed in the previous chapter, cells having such inverted pyramidal textures on surface, gives better cell performance compared to upright pyramidal textures.

© Springer Nature Singapore Pte Ltd. 2017

C.S. Solanki and H.K. Singh, *Anti-reflection and Light Trapping in c-Si Solar Cells*, Green Energy and Technology,
DOI 10.1007/978-981-10-4771-8_7

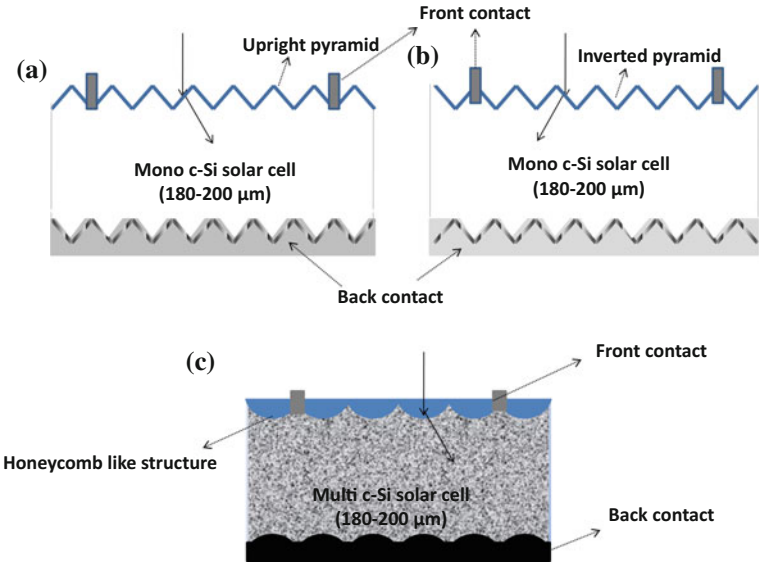

Fig. 7.1 Schematic of mono c-Si wafer-based solar cell having **a** upright pyramid-based texture at both side and anti-reflection coating on front; **b** inverted pyramid-based texture at both side and anti-reflection coating on front; **c** multi c-Si wafer-based solar cell having honeycomb-like texture at both side and anti-reflection coating at front

In multi-c-Si solar cells, since pyramidal texture is not possible due to different grain sizes having different orientations of crystal plane, isotropic etching-based honeycomb-like structures in combination of anti-reflection coating are used as shown in Fig. 7.1c. In this case also, other layers, like front contact, back contact, and anti-reflection coating thickness, are similar as in pyramidal texture based mono c-Si solar cells expect the texture shape at both side. In all the above-mentioned cases of traditional light-trapping structures, where 180–200 µm c-Si wafers are used, the texture dimension lies in the range of 5–10 µm. In order to achieve the texture dimension of 5–10 µm, usually the loss of thickness from each side is in order of 10–15 µm.

In efforts to reduce the cell manufacturing cost, ways for manufacturing thinner c-Si wafers are being explored. Now, if the thickness of wafer would reduce, 5–10 µm texture dimension currently used for light trapping may not be favorable as it would lead to increased surface to volume ratio and higher surface recombination. A representative schematic of texture surface proportion and its dominance in surface to volume ratio can be visualized from Fig. 7.2. Figure 7.2a represents a 180–200 µm wafer with larger size dimension and Fig. 7.2b represents ≤ 100 µm wafer with larger size dimension. Here, larger size dimension refers to 5–10 µm pyramid shape textures. You can clearly distinguish the relative proportion of texture surface in representative thinner wafer. Processing such 5–10 µm texture surface in ≤ 100 µm wafers would not only lead to more surface recombination as

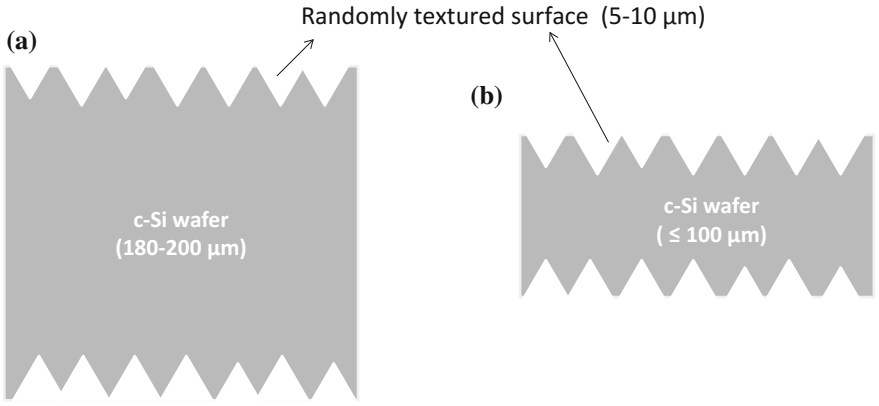

Fig. 7.2 Schematics of textures shapes on surface **a** having larger size textures (say 5–10 µm size) on 180–200 µm wafer; **b** having larger size (say 5–10 µm size) textures on ≤ 100 µm wafer

discussed in previous chapter, but also would increase the comparative material loss proportion in texturing. For example, assume that for making 5–10 µm texture surfaces, the texturization process etches the wafer by 15 µm from each size. It would mean a total of 30 µm of wafer material loss. For 200 µm wafer, it would account approximately 15% material loss. However, when you do the calculation for 100 µm thick wafer, this proportional loss would become about 30%, which is significant.

One solution may be use of smaller dimension (few nanometer to ≤ 1 µm) based texture surfaces for obtaining good light trapping in thinner c-Si-based solar cells and many researchers are also exploring in this direction. There has been recent developments where alternative processing techniques are explored to fabricate nano-texture shapes (≤ 1 µm) which may be suitable for thin c-Si wafers-based cells (Mavrokefalos et al. 2012; Sivasubramaniam and Alkaisi 2014; Liu et al. 2015). Such nano-sized texture shapes on thinner c-Si wafers, as represented in Fig. 7.3, with good light-trapping capability would help in lowering

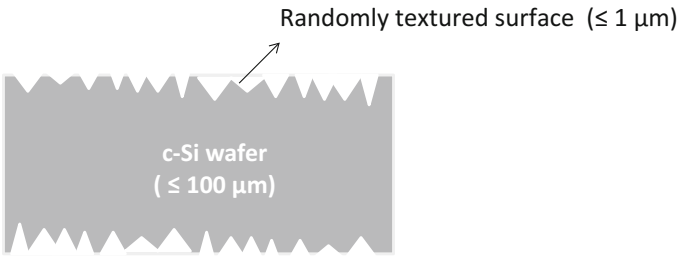

Fig. 7.3 Schematics of textures shapes on surface having smaller size texture on ≤ 100 µm wafer

the surface recombination as well as in minimization of the material loss in etching process. More about developments in fabrication of nano-sized pyramidal textures on c-Si surfaces has been covered in the following section.

7.2 Inverted Pyramid-Based Light Trapping for Thin Wafer-Based Cells

In pyramidal texture-based light-trapping scheme, inverted pyramids are better as compared to upright pyramid-based light-trapping structure. As discussed in the above section, for thinner c-Si solar cells, it is necessary to avoid large size textures as well as material losses. With technology development, now it is possible to fabricate inverted pyramids of nano sizes with good light trapping potential. As discussed in Sect. 5.3 of Chap. 5, using interference lithography with anisotropic etching method, inverted pyramids on c-Si wafer can be fabricated. This technique allows us to fabricate nanoscale-inverted pyramids for light trapping provided the lithography system has high resolution and capability to form interference pattern on photoresist at nanoscale dimension. For example, Mavrokefalos et al. (2012) fabricated scalable nano-sized-inverted pyramids on SOI (Si on insulator) wafers using interference lithography with the help of negative photoresist and subsequent KOH-based anisotropic etching. The inverted pyramids of sizes smaller than 1 μm with spacing between successive inverted pyramids of about 100 ± 10 nm has been demonstrated. The SEM image of the fabricated sample is given in Fig. 7.4.

In recent development, Liu et al. (2015) presented Cesium Chloride (CsCl)-based self-assembled lithography for nanoscale-inverted pyramid fabrication on c-Si wafers. In this technique, first CsCl thin film is deposited on c-Si wafer and annealed to form CsCl nano island as shown in Fig. 7.5. After CsCl nano island

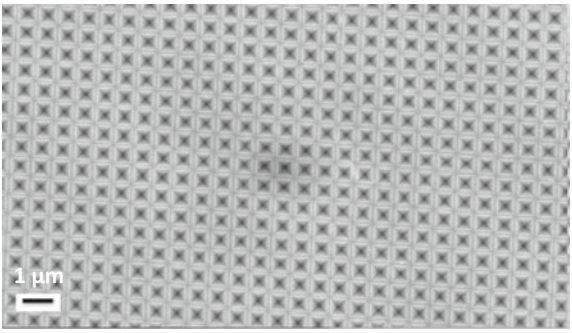

Fig. 7.4 SEM image (*top view*) of nano-sized inverted pyramids fabricated on SOI wafers using interference lithography (Reprinted with permission from Nano Lett, 12, Mavrokefalos A, Han SE, Yerci S, et al., Efficient Light Trapping in Inverted Nanopyramid Thin Crystalline Silicon Membranes for Solar Cell Applications, 2792–2796, 2012, American Chemical Society)

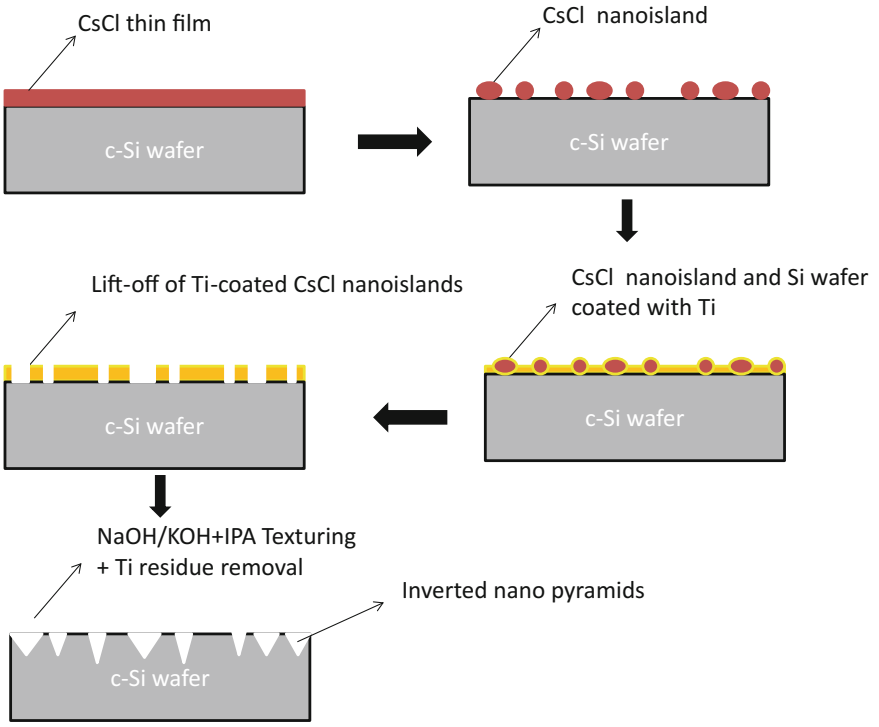

Fig. 7.5 Process flow of Cesium Chloride (CsCl) based self-assembled lithography for nanoscale-inverted pyramid fabrication on c-Si wafers (after Ref. Liu et al. 2015)

formation, Titanium (Ti) thin film is deposited on the substrate and latter the substrate is agitated with help of ultrasonication technique in deionized (DI) water for lift-off of Ti-coated CsCl islands. This process leaves only Ti on Si wafer with nanoporous Si surface.

After ultrasonication step, when CsCl islands coated with Ti is lifted-off, the sample is subjected to NaOH/KOH + IPA-based anisotropic etching process as discussed in Chap. 5. At the end the process, sample is cleaned in HF and DI water solution for completely removing the Ti from Si surface and the samples are dried for further cell processing. Pyramid of size below 1 μm is possible with this technique. The SEM image of nanoscale-inverted pyramid using this technique by Liu et al. (2015) is shown in Fig. 7.6. The size and morphology of inverted pyramid in this method is governed by diameter of fabricated CsCl islands and etching time of the sample in alkaline solution. Liu et al. (2015) achieved less than 10% reflectance from Si wafer for 400–1000 nm wavelength range with nanoscale-inverted pyramid structure using this technique.

Here, it would be worth mentioning that the fabrication and implementation of such nano-sized inverted pyramids in thin c-Si wafer-based cell technology seems easy but it is not that easy. When we talk about solar cells, each additional process

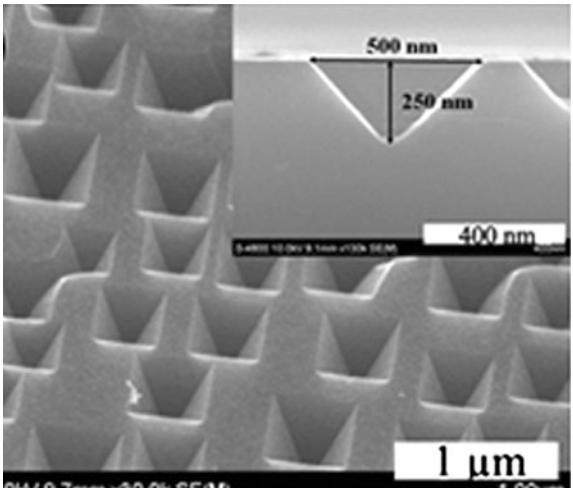

Fig. 7.6 SEM image of nanoscale-inverted pyramid fabricated using CsCl based self-assembled lithography technique (Reprinted from Mater Sci Semicond Process, 40, Liu J, Zhang X, Sun G, et al., Fabrication of inverted pyramid structure by Cesium Chloride self-assembly lithography for silicon solar cell, 44–49, 2015, with permission from Elsevier)

would add to the cost of manufacturing of the cell. Especially, a process involving lithography has not been seen as cost effective process. So, one should also keep in mind while developing such effective technique for fabrication of light trapping structures that how such processes could be made less complicated and could be scaled up for implementation in the existing manufacturing line.

7.3 Back Reflectors for Enhanced Light Trapping

In c-Si solar cells, the back surface is completely covered with metal which acts as back contact. Usually Aluminum (Al)/Silver (Ag) is used for back contact in c-Si solar cells which also acts as back reflector. Remember the discussion made in Chap. 4 about path length enhancement using different light trapping structures. Theoretically maximum path length enhancement would be $4n^2$ for case of Lambertian surface, if the back surface is perfectly reflecting. If the back surface is not perfectly reflecting, the path length enhancement would come down to $2n^2$, i.e., the light-trapping potential of light-trapping structure would be reduced by half. This establishes the significance of back reflector in light trapping and cell performance.

The back contact material used for c-Si solar cell should be such that it should make ohmic contact with Si material and at the same time it should be a perfect reflector, as it is clear that for better light trapping, both sides of the wafer should be textured while fabricating the cell. The back contact completely covers the textured surface at the back as it has been shown in Fig. 7.1. The textured surface helps in reflecting the weekly absorbing light from back surface at angle larger than critical angle and minimizes the escape of weekly absorbing light from front surface.

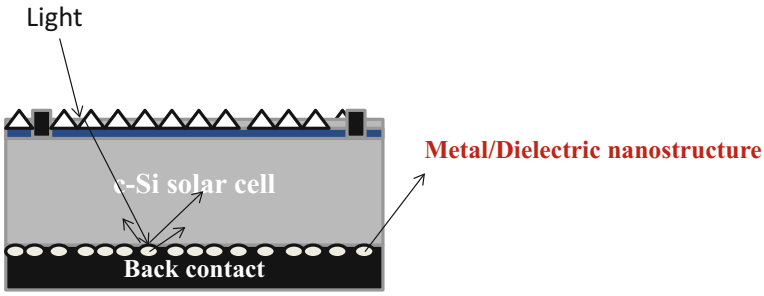

Fig. 7.7 Schematic of nanostructures-based back scattering of light in combination with back contact based back reflector

However, as we talk about cell fabrication using thinner wafers and avoiding roughening of the surface, we must have some alternate way to reflect the light back at larger angle. This can be done using nanostructures at surface as shown in Fig. 7.7 where nanoparticles of metals or dielectrics can be used between Si and back contact interface at back surface. In such scenario, enhanced light trapping can be expected without texturing the back surface, i.e., only one side of surface texturing would be required.

In this direction, there have been some recent developments where researchers have tried to use nanostructure made of metals or dielectrics at back side of the cell and have reported some positive results. For example, Eisenlohr et al. (2015) explored the light-trapping enhancement in c-Si solar cell using silicon oxide (SiO_2)-based dielectric spheres at back as shown in Fig. 7.8a. A thin tunnel passivating layer is also used to electrically separate the dielectric spheres from cell's base. Such structure by Eisenlohr et al. (2015) indicated better absorption of light for wavelengths above 1050 nm. The enhancement in absorption was equivalent to 0.4 mA/cm^2 current. Please note that in this case the device was having front surface textured and rear surface planer in combination with dielectric spheres having diameter approximately 1000 nm. This enhancement was in comparison to device having front surface textured and rear surface planer, without dielectric spheres. The relative enhancement in absorption is shown in Fig. 7.8b. Also, for the case where the device was having front surface planer and rear surface planer in combination with dielectric spheres, showed absorption enhancement equivalent to 1.6 mA/cm^2, when compared with device having front and rear both surfaces planer.

Similar approach has also been explored by Yang et al. (2012) where silver nanoparticles were tested at back surface for enhancing the trapping of weakly absorbed infrared light in PERT (Passivated Emitter and Rear Totally Diffused) cell configuration. Rear structure corresponding to a standard PERT cell with silver nanoparticle combination is shown in Fig. 7.9. In Fig. 7.9b, SiO_2 layer not only

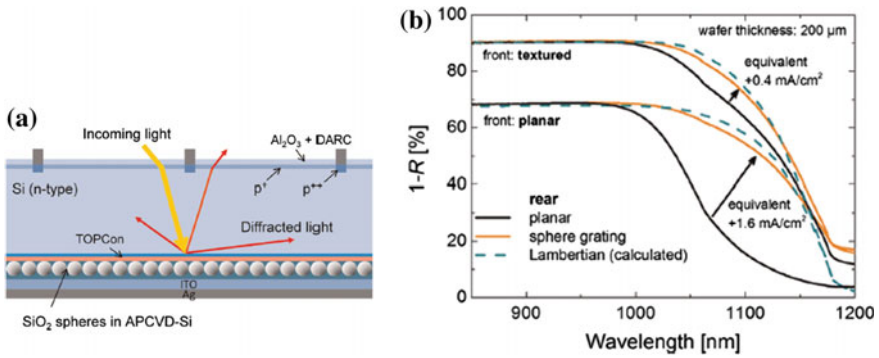

Fig. 7.8 **a** Schematic of c-Si solar cell which uses silicon oxide (SiO_2)-based dielectric spheres at back for enhancing the trapping of weakly absorbing light; **b** Absorbance (1-Reflectance) curves for samples having planar or textured (random pyramids) surface at front and planer or silicon oxide (SiO_2)-based dielectric spheres combined with planar surface at back (Reprinted from Sol Energy Mater Sol Cells, 142, Eisenlohr J, Lee BG, Benick J, et al., Rear side sphere gratings for improved light trapping in crystalline silicon single junction and silicon-based tandem solar cells, 60–65, 2015, with permission from Elsevier)

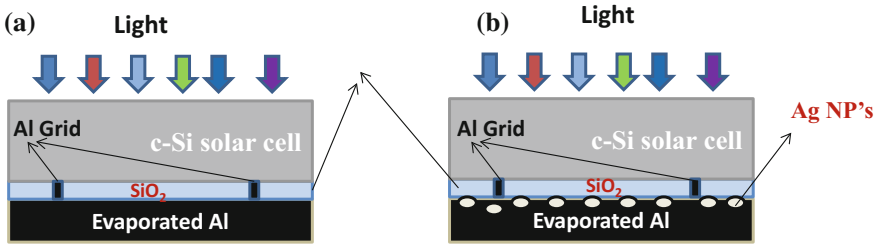

Fig. 7.9 Schematic of **a** rear structure corresponding to a standard PERT cell; **b** rear structure corresponding to a PERT cell in combination of silver nanoparticles at back (after Ref. Yang et al. 2012)

passivates the rear surface but also provide isolation to silver nanoparticles from the cell.

Yang et al. (2012) showed optical path length enhancement (Z) of about 10.05 ± 3.9 for light having wavelength 1200 nm using silver nanoparticles in zinc sulfide (ZnS) and magnesium fluoride (MgF_2) matrix at back with evaporated Al-based back contact for cells having PERT structure. Metal or dielectric nanostructures which provide backscattering of light similar to texture surface at back utilizes Mie scattering effect. The backscattering capability of Mie scattering is governed by nanostructure dimension, spacer layer thickness, nanostructure and medium dielectric constants, etc. More about Mie scattering and back reflection from nanostructures is covered in next chapter.

7.4 Advanced Light-Trapping Structures for Next-Generation c-Si Solar Cells

c-Si solar cell technology has evolved since 1950s and the wafer thickness used for the cell fabrication have gone down from ≥ 500 μm to currently 180–200 μm. There is projection that the next-generation c-Si solar cells would be fabricated using much thinner wafers (≤ 100 μm). The light-trapping methodologies discussed till now were focused on surface roughening of the wafer which was introduced by Haynos et al. (1974) in 1974. Since then it has been main stream light-trapping technology for c-Si solar cells. Now, when moving ahead and progressing toward the use of thinner wafer for the cell fabrication, texturization process of surface, which leads to increased surface recombination and absorbing material loss as discussed in above sections, would be not a favorable option. In view of this, nano-sized-inverted pyramid textures have been introduced which might result relatively lesser surface recombination and lower material loss during etching process. However, such technique still roughens the surface and there is probability that it would still impact the minority carrier life time in thinner c-Si wafers. Also, fabrication of nano-sized-inverted pyramidal textures, as discussed in above section, uses lithographic technique which is additional process and its processing cost adds up in the cost of the cell fabrication. Therefore there is need to introduce alternative light trapping scheme, which is not based on texturization or surface roughening but provides light trapping similar to texturization-based technology, which is needed for next-generation thin c-Si solar technology. Such requirement brings in the concept of light directors. Light directors can be high refractive index-based nanostructures which can forward scatter or couple the incident light toward active absorbing material as shown in Fig. 7.10.

Such designs, if implemented on the surface of c-Si solar cells, would help in avoiding surface roughening process for light trapping. And hence, it would help in lowering the surface recombination and would allow us to minimize material loss which happens during etching process. Such light directors in combination with optimized anti-reflectors at planner surface can substitute the texturization step in

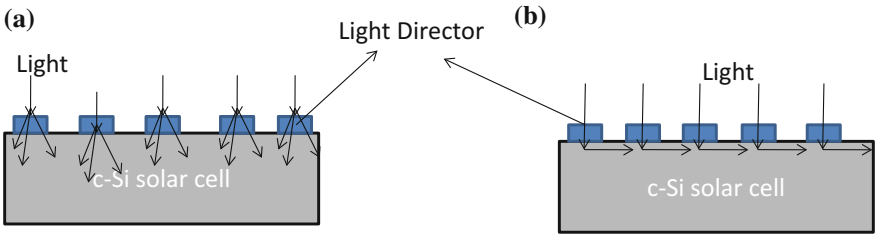

Fig. 7.10 Schematic of **a** scattering-based light directors which scatter the incident light toward the active absorbing material of c-Si solar cell at larger angle; **b** forward coupling-based light directors which couple the incident light into the active absorbing material of c-Si solar cell

c-Si solar cell fabrication. There has been many developments in this direction recently where researchers have tried to explore metal nanoparticles (Pillai and Green 2010; Green and Pillai 2012), dielectric gratings (Zhou et al. 2010; Brongersma et al. 2014), combination of metal and dielectric nanostructures (Singh et al. 2016) for enhanced light trapping in solar cells. The target for such light-trapping structure development is to achieve broadband reflection minimization, in the wavelength range of 300–1200 nm, which is most suitable for c-Si solar cells. For wide acceptance of such trapping structures, it should be cost effective and easy to implement in thin c-Si wafer-based solar cell fabrication technology. Light directors based on nanostructure of metal/dielectric materials utilize plasmonics technology or Mie scattering phenomenon during light–matter interaction and provide capability to control light propagation at nanoscale. More about Mie scattering and plasmonic-based light–matter interaction for enhanced light trapping in c-Si solar cells is covered in subsequent chapters.

7.5 Questions and Problems

1. Summarize your understanding about texturization-based light-trapping structures in c-Si solar cells?
2. What do understand from next-generation c-Si solar cell technology? Discuss about complexity involved in using texturing-based light trapping in next-generation c-Si solar cells?
3. How nano-sized pyramidal textures can be useful in next-generation thin c-Si solar cell technology?
4. How would you fabricate nano-sized inverted pyramids using noninterference-based lithography technique?
5. What is the role of back reflectors in c-Si solar cells? How does it influence the light trapping?
6. What should be the qualities in a good back reflector for c-Si solar cell applications?
7. How metal/dielectric-based nanostructures can be used for better light trapping in combination with flat back reflectors?
8. What do you understand from light directors? When can it be considered better compared to texturization-based light-trapping technique?
9. What should be the qualities of light directors which could be suitable for next generation thin c-Si solar cell applications?
10. How much Si material (in %) would be lost during texturing process for fabricating pyramids of size 5 μm at both sides of the wafer if the starting wafer is having thickness: (a) 200 μm, (b) 150 μm, (c) 100 μm, (d) 50 μm. Assume that you etched about 12 μm thickness of the wafer from each side during fabrication of the pyramids.

References

Brongersma ML, Cui Y, Fan S (2014) Light management for photovoltaics using high-index nanostructures. Nat Mater 13:451–460. doi:10.1038/nmat3921

Eisenlohr J, Lee BG, Benick J et al (2015) Rear side sphere gratings for improved light trapping in crystalline silicon single junction and silicon-based tandem solar cells. Sol Energy Mater Sol Cells 142:60–65. doi:10.1016/j.solmat.2015.05.043

Green MA, Pillai S (2012) Harnessing plasmonics for solar cells. Nat Photonics 6:130–132. doi:10.1038/nphoton.2012.30

Haynos J, Allison J, Arndt R, Meulenberg A (1974) The COMSAT nonreflective silicon solar cell: a second generation improved cell. In: International conference on photovoltaic power generation, p 18

Liu J, Zhang X, Sun G et al (2015) Fabrication of inverted pyramid structure by Cesium Chloride self-assembly lithography for silicon solar cell. Mater Sci Semicond Process 40:44–49. doi:10.1016/j.mssp.2015.05.048

Mavrokefalos A, Han SE, Yerci S et al (2012) Efficient light trapping in inverted nanopyramid thin crystalline silicon membranes for solar cell applications. Nano Lett 12:2792–2796. doi:10.1021/nl2045777

Pillai S, Green MA (2010) Plasmonics for photovoltaic applications. Sol Energy Mater Sol Cells 94:1481–1486. doi:10.1016/j.solmat.2010.02.046

Singh HK, Arunachalam B, Kumbhar S et al (2016) Opto-electrical performance improvement of mono c-Si solar cells using Dielectric–Metal–Dielectric (D-M-D) sandwiched structure-based plasmonic anti-reflector. Plasmonics 11:323–336. doi:10.1007/s11468-015-0049-5

Sivasubramaniam S, Alkaisi MM (2014) Inverted nanopyramid texturing for silicon solar cells using interference lithography. Microelectron Eng 119:146–150. doi:10.1016/j.mee.2014.04.004

Yang Y, Pillai S, Mehrvarz H et al (2012) Enhanced light trapping for high efficiency crystalline solar cells by the application of rear surface plasmons. Sol Energy Mater Sol Cells 101:217–226. doi:10.1016/j.solmat.2012.02.009

Zhou L, Huang C, Wu S et al (2010) Enhanced optical transmission through metal-dielectric multilayer gratings. Appl Phys Lett 97:011905. doi:10.1063/1.3458702

Chapter 8
Plasmonic-Based Advanced Anti-reflection and Light Trapping: Principles and Technology

In this chapter, the principle and technology of plasmonics has been explored for an alternate light-trapping method. Historical developments in the area of plasmonics and the review on applicability of plasmonic-based light-trapping technology in solar cells have been presented. Also, a broad overview on physics of light trapping using plasmonic-based nanostructures has been covered. Relevant light-trapping techniques such as scattering, local field enhancement, and surface plasmon polariton (SPP) has been discussed along with the associated mechanism involved for efficient light trapping. Also, widely used Mie scattering theory and the mathematical solutions to calculate Mie efficiencies for different size, shape, dielectric medium-based nanostructures has been covered. Towards the end of the chapter, discussion on better metal/material choice for plasmonic-based light-trapping applications has been done.

8.1 Plasmonics: Historical Development

Plasmonics is a field of study where photon-electron cloud-based electromagnetic interaction is studied. It enables us to understand the interaction of light and free electrons in matter, especially in metals. It has been subject of interest since many years due to its applicability and usefulness in different applications.

8.1.1 Plasmon and Surface Plasmon Effect

Plasmon term was first introduced by David Pines in 1956 (Hubenthal 2011) which was meant for collective oscillation of the free electron gas density. This term was adopted for surface plasmon resonance in later years. As the conduction electrons in metal nanoparticles/nanostructures do the movement due to excitation by incident

© Springer Nature Singapore Pte Ltd. 2017

C.S. Solanki and H.K. Singh, *Anti-reflection and Light Trapping in c-Si Solar Cells*, Green Energy and Technology,
DOI 10.1007/978-981-10-4771-8_8

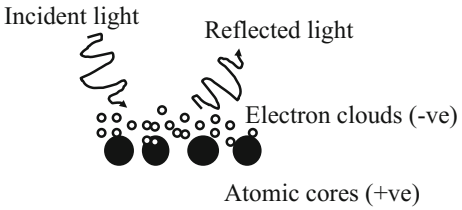

Fig. 8.1 Schematic of polarization effect due to movement of conduction electrons by incident light excitation where atomic cores are positively charged and conduction electrons at particle surface behave like electron cloud which are negatively charged

radiation, they behave like electron gas and lead to build up of polarization charges on the particle surface as shown in Fig. 8.1. These polarization charges are the result of particles/nanostructure electrons displacement from equilibrium due to incident electromagnetic (EM) radiation electric field.

The conduction electron acceleration by the incident radiation's electric field induces the polarization in both, the particle and surrounding medium. The restoring force due to polarization charges leads to confinement of the electrons to dimensions smaller than the wavelength of light which is responsible for surface plasmon effect, i.e., oscillatory motion of the electrons with a characteristic frequency (Evanoff and Chumanov 2005). Such restoring forces, which results in oscillatory motion of the electrons with a characteristic frequency, lead to the concept of surface plasmons, where the characteristic frequency is known as surface plasmons frequency. Note that the polarization is induced in the surrounding medium because the oscillating electrons are in opposite direction. This in return reduces the restoring force for the electrons and leads to shifting of the surface plasmon frequency to a lower frequency (Evanoff and Chumanov 2005). Thus frequency corresponding to the plasmon resonance can be fine-tuned to desired frequency by controlling the dielectric constant of the surrounding medium. This kind of control and light–matter interaction at nanoscale dimension opens up avenues for its application in various fields.

8.1.2 Historical Presence and Development

Plasmonic-based technology is currently an area of interest in different application-oriented developments like biomedical sensors, metamaterials, LED's, drug delivery, cancer diagnosis, etc. It has also been actively explored and exploited in past, either knowingly or unknowingly, in different areas and applications like medicine, architecture, painting, biotechnology, etc. In early days, the development and application-oriented possibilities of plasmonic-based technology were dependent on the ability to synthesize/fabricate nanostructures of various materials with different sizes and shapes.

First example of plasmonic-based technology is Roman Lycurgus Cup, which dates to the fourth century AD (Evanoff and Chumanov 2005; Garcia 2011). It is a bronze cup lined with colored glass. As per Evanoff and Chumanov (2005), the glass scatters a dull green light and transmits red light. The glass contains 70 nm particles, which are an alloy of silver (70%) and gold (30%) as per study commissioned by the British Museum. In fourth century AD, it would have not been known that why such shift in scattered light wavelength occurs. The explanation to such beautiful scattering and light–nanostructure interaction came in twentieth century, when Gustav Mie published his work in 1908 on the extinction of light by metal spheres. Now, it is well known that such silver nanoparticles of this sizes scatters green light and transmit orange and how gold (Au) presence shifts the absorption band to longer wavelengths. This explains the observation made for Lycurgus Cup as why it scatters dull green light and transmits red light.

In the past, small nanoparticles have been used to create stained glass with help of ruby red Au and lemon-yellow Ag nanoparticles. In 1850s, Michael Faraday conducted the first notable scientific study of the optical properties of metal nanoparticles colloidal suspensions and ultra-thin metal films (Evanoff and Chumanov 2005). He noticed the ability of extremely thin Au leaf to transmit green light and speculated that if a material is capable of strong interaction with light then it can also do strong interaction even if dimensions is smaller than visible wavelengths.

The scattering phenomenon and optical responses of Au suspensions were explained by Gustav Mie, who studied the extinction of light by metal spheres. In his paper published in 1908, Mie had mathematically described the optical responses of Au suspensions (Evanoff and Chumanov 2005). Starting from the macroscopic Maxwell equations, Mie calculated the extinction, scattering, and absorption cross-sections of Au nanoparticles and showed how the spectra of the suspensions evolve as a function of particle size. The origin of the optical properties of metallic nanoparticles (NP's) was understood after Mie's work in the early twentieth century. However, further exploitation was limited by the capabilities to synthesize and manipulate the nanoparticles in a controlled way (Garcia 2011). Surface plasmons and related application-oriented possibilities spread quickly in many fields toward the end of twentieth century when the era of nanotechnology started.

8.2 Plasmonics in Solar Cells

Plasmonic-based light trapping has been explored in recent years for different types of solar cell technologies to improve the cell performance. Westphalen et al. (2000) explored this technology for photovoltaic conversion efficiency enhancement of an organic solar cell by incorporation of small metal clusters as shown in Fig. 8.2a. Nahm et al. (2011) explored such technology to show efficiency enhancement in die-sensitized solar cell where they used Au nanoparticles for improving light trapping in the cell as shown in Fig. 8.2b.

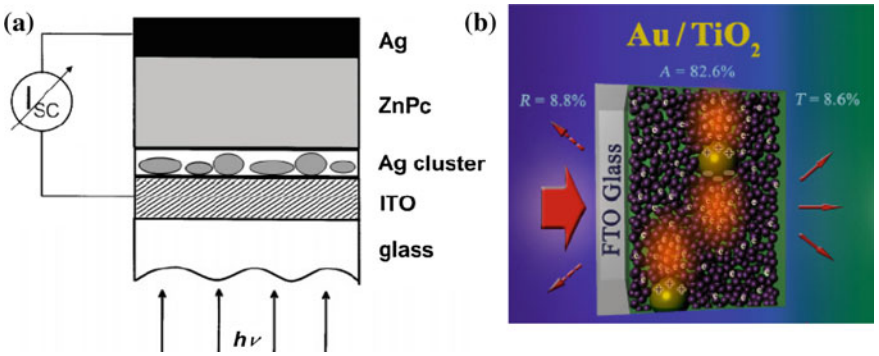

Fig. 8.2 **a** Schematic of an organic solar cell structure where small metal clusters have been incorporated (Reprinted from Sol Energy Mater Sol Cells, 61, Westphalen M, Kreibig U, Rostalski J, et al., Metal cluster enhanced organic solar cells, 97–105, 2000, with permission from Elsevier); **b** Schematic of TiO_2-based dye-sensitized solar cells (DSSCs), where Au nanoparticles are incorporated into TiO_2 nanoparticles which helps to trap more light (Reproduced from [Nahm C, Choi H, Kim J, et al. (2011), The effects of 100 nm-diameter Au nanoparticles on dye-sensitized solar cells, Appl Phys Lett 99:253107], with permission of AIP Publishing.)

Silver nanoparticles on front surface for Si-based solar cells (see Fig. 8.3) has also been explored for light-trapping enhancement where enhancement in light trapping and current generation potential of the cell near its active absorbing material (i.e., Si) band gap has been demonstrated (Pillai et al. 2007).

There are various ways where metal nanoparticles can be used for enhancement in light-trapping capability of the cell and its performance. In a nice review paper, Atwater and Polman (2010) have discussed about different possible ways that plasmonic-based technology using metal nanostructures can be implemented for enhanced light trapping in active absorbing material of the solar cells. This include scattering, local field enhancement, and surface plasmon polariton-based light-trapping technologies. Let us have a look on these techniques.

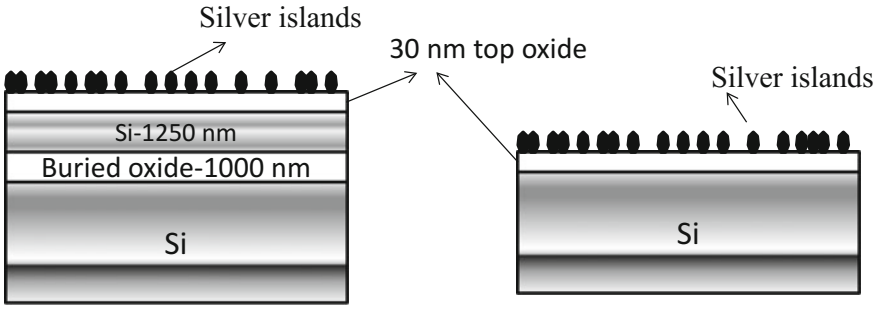

Fig. 8.3 Schematic of Si-based cell structure where nanoparticles at front surface has been explored for light-trapping enhancement (after Ref. Pillai et al. 2007)

8.2.1 Enhanced Light Trapping by Light Scattering Based on Particle Plasmons

Using metallic nanoparticles as subwavelength scattering elements, light trapping can be enhanced. Metallic nanoparticles help in coupling the freely propagating electromagnetic radiation/light into an active absorbing material (Fig. 8.4a). In such technique, multiple and high-angle scattering result in trapping of light into the active absorbing material of the solar cell. In this method, high-angle scattering results in an increased effective optical path length in the absorbing material. Such technique, where the particles can be incorporated and implemented at the final stage of device processing, is encouraging if it works for broad wavelength range. This light scattering-based technique would be more appropriate for implementation in solar cells, where nanoparticles can be incorporated on surface without adversely impacting the other important parameters required for efficient cell. c-Si wafer-based solar cell technology would be a good candidate for wavelength scattering-based light-trapping structure.

8.2.2 Enhanced Light Trapping by Particle Plasmons-Based Light Concentration

In case of particle plasmons-based light concentration for enhanced light trapping, metallic nanoparticles/nanostructures are used with appropriate dimensions such that they act as subwavelength antennas. When light interacts with the metallic nanostructures, the plasmonic near-field is coupled and in return it increases its effective absorption cross-section into the active absorbing material immediate to the nanostructure (Fig. 8.4b). The excited metallic structure near-field helps in more light absorption and the creation of electron–hole (e–h) pairs in the absorbing material. Such light concentration-based arrangement works well but only with small metallic nanoparticles (5–20 nm diameter) for which the albedo (scattering cross-section over sum of scattering and absorption cross-sections) is low. This

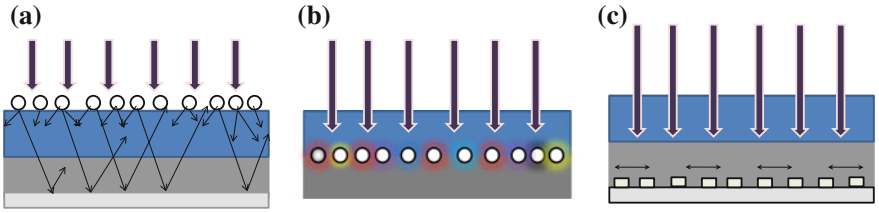

Fig. 8.4 Plasmonic light-trapping geometries for enhanced light trapping **a** light scattering based on particle plasmons, **b** particle plasmons-based light concentration, **c** surface plasmon polariton (SPP)-based light trapping (after Ref. Atwater and Polman 2010)

technique would be useful in materials, where the carrier diffusion length is small. One important requirement of such arrangement is that the photo carriers must, thus, be generated close to the collection junction area.

For metallic nanostructure-based antennas to have efficient energy conversion effects, the absorption rate in the absorbing material must be larger than the reciprocal of the typical plasmon decay time (lifetime 10–50 fs) (Atwater and Polman 2010). If such conditions are not achieved, the absorbed energy would be dissipated into ohmic damping in the metal. If absorbing material is in close contact to the field, absorption would be enhanced due to the high density of states of the photons. This effect can be further enhanced by decreasing the spacing and size/shape of the particles (Pillai and Green 2010; Hubenthal 2011). This type of technique has been shown to be useful in many organic and direct-band gap inorganic semiconductors, where the nanoparticles can be put inside the active absorbing layer rather than on the front or rear of the material surface. Light concentration-based light-trapping arrangement is more suitable and beneficial in case of organic solar cells (Westphalen et al. 2000; Lee et al. 2009; Zhu et al. 2011; Gan et al. 2013).

8.2.3 *Enhanced Light Trapping by Surface Plasmon Polariton (SPP)*

A corrugated metallic film on the back surface of a thin photovoltaic absorber layer helps in exciting surface plasmon polariton (SPP). At the metal/semiconductor interface, in-coupling of the sunlight into SPP mode occurs. The light coupled in SPP mode at metal back surface propagates in the plane of the semiconductor layer, where the light is absorbed and converted into photo carriers (Fig. 8.4c). Such SPP coupling mechanism would be beneficial for efficient light absorption and trapping only if absorption of the SPPs in the semiconductor is stronger than in the metal. In such case, the incident light is generally turned by 90° and is absorbed along the lateral direction of the solar cell absorbing material. For such structures to be useful, the lateral dimensions of the semiconductor should be orders of magnitude larger than the optical absorption length.

Now, if we look at its application for c-Si solar cells, which is the main focus of this book, out of these three different techniques, most suitable light-trapping geometry would be one which does not influence the other performance parameters of solar cells. Since the presence of metal directly inside semiconductor or direct contact with active absorbing material of the solar cell would lead to various recombinations and would result in loss of solar cell efficiency. So, the best plasmonic-based light-trapping nanostructure would be the one which is not part of active device. Hence, for c-Si-based solar cells, light concentration using particle plasmons would not be a feasible option. However, light scattering using particle plasmons and light trapping using surface plasmon polariton (SPP) can be

feasible provided the metal nanostructures are separated from active absorbing material, i.e., c-Si slab/wafer by means of some dielectric spacer. In this chapter, the focus have been given on these two methods of light trapping, i.e., light scattering based on particle plasmons and surface plasmon polariton (SPP) in subsequent sections.

8.3 Light–Matter Interaction and Plasmonics

As discussed earlier, plasmons are collective oscillations of free or conduction electrons and oscillatory motion of the electrons with a characteristic frequency lead to concept of surface plasmons. The surface plasmons are of two types. One is localized surface plasmons (LSP) which is non-propagating in nature and excited in thin films or metal nanoparticles/nanostructures by swift electrons. When light interact with the metal nanostructures, depending upon the size, shape, and surrounding medium, light–matter interaction takes place and result in scattering, absorption, and other plasmonic effects. Light is an electromagnetic wave and electromagnetic waves exhibit scattering property when they interact with matter. Electromagnetic scattering is distinguished and named as per their convention and are of two types which are known as (i) elastic scattering and (ii) inelastic scattering. Elastic light scattering involves negligible energy loss/transfer. The good examples of elastic scattering are Rayleigh scattering and Mie scattering. In the other type of scattering, i.e., inelastic scattering, there exists energy loss/transfer. Some examples includes Brillion scattering, Raman scattering, inelastic X-ray scattering, Compton scattering etc. (Bohren and Huffman 1983; Roqué et al. 2006).

Light scattering are categorized into three different domains based on a dimensionless quantity known as size parameter x, which is defined as per below Eq. (8.1).

$$x = \frac{2\pi \cdot a \cdot n_m}{\lambda} \tag{8.1}$$

Here 'a' represents the particle radius, 'λ' represents the wavelength of incident radiation, and 'n_m' represents refractive index of medium. Based on the value of x, the domains are categorized as below (Bohren and Huffman 1983):

if $x \ll 1$: Rayleigh scattering (small particle compared to wavelength of light)
if $x \simeq 1$: Mie scattering (particle about the same size as wavelength of light)
if $x \gg 1$: Geometric scattering (particle much larger than wavelength of light)

When electromagnetic wave/light is scattered by a very small nanoparticle, it is called Rayleigh scattering. Rayleigh's model applies when the sphere is smaller in diameter than the wavelength (λ) of the scattered wave. Typically, for Rayleigh scattering, the upper limit for particle diameter is taken to be about one-tenth of the

wavelength. In this size regime, the exact shape of the scattering center is not very significant.

For larger diameter spherical particles, i.e., spheres larger than the Rayleigh range, scattering phenomenon is known as Mie scattering. This type of scattering is named after Gustav Mie, who solved the puzzle of scattering from particles of such dimensions. In Mie regime, the shape of the scattering center becomes much more significant and the theory applies to sphere shape nanoparticles. Also, it is applicable to spheroid and ellipsoid but after certain modifications (Kreibig and Vollmer 1995). Both Mie and Rayleigh scattering are elastic scattering in which the energy (also wavelength or frequency) of the light is not changed significantly. However, Mie scattering and Rayleigh scattering are different from each other in many aspects. Rayleigh scattering occurs symmetrically (Fig. 8.5). On the other hand, Mie scattering shows asymmetrical nature of scattering. It is larger in the forward direction than in the reverse direction. The greater the particle size, the more of the light is scattered in the forward direction (Fig. 8.5).

For very small nanoparticles (much smaller than the wavelength of the incident light), strong absorption and weak scattering of the light is observed. However, as the nanoparticle size increases, the contribution of higher order modes due to excitation of multipoles along with dipoles, which are responsible for reradiation of electromagnetic wave from the particle, becomes larger as the field across the particle becomes non uniform (RAR Tricker 1970). Scattering by particles similar to or larger than the wavelength of light is typically treated by the Mie theory or the discrete dipole approximation.

For particle diameter to wavelength ratio more than 10, laws of geometrical optics are mostly used to describe the interaction of light with the particle.

Further, Mie theory, also called Lorenz–Mie theory or Lorenz–Mie–Debye theory, is an analytical solution of Maxwell's equations for the scattering of

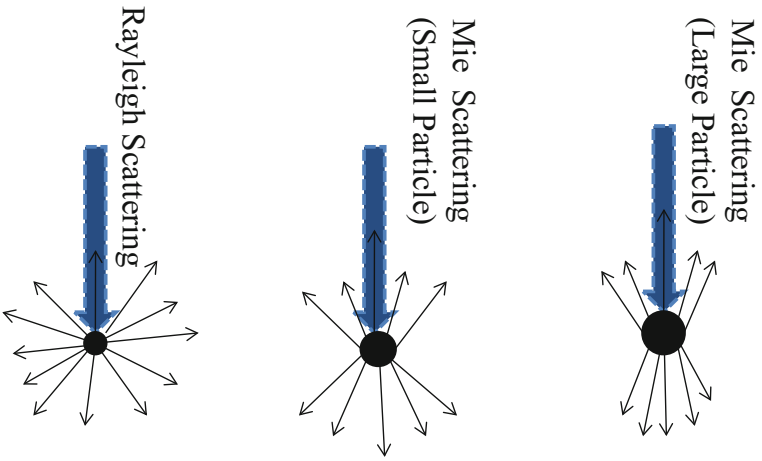

Fig. 8.5 Schematic for Rayleigh scattering and Mie scattering

electromagnetic radiation by spherical particles (also called Mie scattering as discussed above) (Bohren and Huffman 1983). Note that "Mie theory" is not an independent physical theory or law. This is the solution of Maxwell equations and therefore the phrase "Mie solution", which means solution to Maxwell equations, is considered more appropriate and widely used to address the Mie scattering effect. Mie solutions allow us to calculate the electric and magnetic fields inside and outside a spherical object. It is generally used to calculate the proportion of light that is scattered; optical cross-sections, etc. In irregularly shaped particles, where both Rayleigh and Mie models do not apply, other numerical methods, e.g., finite element method (FEM), finite-difference time-domain method (FDTD), etc., come into picture to explain the observed scattering phenomenon.

Now, the other type of light–matter interaction results in surface plasmon polariton (SPP) which is of propagating nature. SPP is an electromagnetic excitation which exists on metal–dielectric interface and the electromagnetic (EM) field amplitude decays exponentially with distance from the interface/surface in either direction/medium (Zayats et al. 2005). In case of SPP, the interaction of incident electromagnetic light and excitation of surface plasmons greatly depends upon the surface/interface conditions. The electromagnetic field of surface plasmon polariton on a metal–dielectric interface is usually obtained by solving Maxwell's equations with suitable boundary conditions. In 1941, Fano introduced the concept of propagating wave at the interface between dielectric and metal. He explained the low reflectivity regions observed in wavelength-dependent reflectivity measurement on ruled metal gratings by woods (Murray 2005).

Different kinds of SPP behavior, e.g., scattering, reflection, interference, backscattering and localization etc., can be seen depending upon the surface/interface conditions. The impact on radiation, when it interacts with dielectric–metal interface, is governed by abrupt discontinuity in material properties at the interface. For nonmagnetic materials, the dielectric permittivity (ε) of the material plays a major role (Murray 2005) in the light–mater interaction at the interface. More about SPP-based light–matter interaction and light trapping have been discussed in Sect. 8.6.

8.4 Mie Efficiencies

When light interacts with nanostructure/nanoparticle, it results in scattering event as well as local field enhancements. Nanostructures/nanoparticles have hundreds of atoms/molecules. The resultant interaction of light with the nanostructure depends on how the nanostructure/nanoparticle or atoms/molecules respond to the incident light collectively (see Fig. 8.6). The individual atom/molecule in nanostructure may interact differently and scattered field may have different phases. However, the observed scattering in given direction would be resultant of all the scattered fields. When the nanostructure/nanoparticles are small enough, the scattered field may be in phase and observed resultant scattering field would not have much dependence

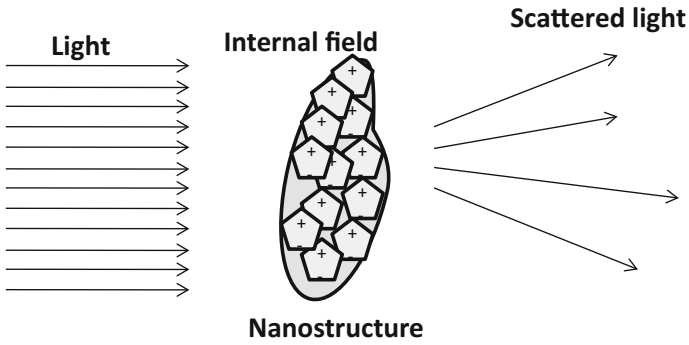

Fig. 8.6 Schematic of light–nanostructure interaction and scattering event (after Ref. Bohren and Huffman 1983)

on scattering direction. However, if the particle size increases, it would increase the probability of phase variation in scattered fields which will lead to strong dependence on the scattering direction. In such case, geometrical factors like particle shape, size play crucial role. Now to build up concept, the individual atoms/molecules in nanostructure can be conceptualized as dipole/multipoles which scatter the light/electromagnetic field.

8.4.1 Scattering and Absorption Efficiencies

In 1908, Mie presented metal nanoparticles interaction with light and solved Maxwell Equation for appropriate conditions (Luk'yanchuk et al. 2007; Luk'yanchuk et al. 2010; Garcia2012). The solution to Maxwell equations, also known as Mie solutions, as discussed above, presented an exact solution for spherical nanoparticles (NP's) with an assumption that the NP's are noninteracting. It means the distance between the NPs are large enough. It implies that the electric field created by an NP does not affect the rest of them. The analytically solved Maxwell equation solutions for the scattering, extinction (extinction means scattering + absorption), and absorption cross-sections are given as in Eqs. (8.2), (8.3), and (8.4) (Bohren and Huffman 1983):

$$Q_{sca} = \frac{2}{x^2}\sum_{n=1}^{\infty}(2n+1)(|a_n|^2+|b_n|^2) \tag{8.2}$$

$$Q_{ext} = \frac{2}{x^2}\sum_{n=1}^{\infty}(2n+1)\mathrm{Re}(a_n+b_n) \tag{8.3}$$

$$Q_{abs} = Q_{ext} - Q_{sca} \tag{8.4}$$

where a_n and b_n are given by Eqs. (8.5) and (8.6):

$$a_n = \frac{m^2 j_n(mx)[xj_n(x)]' - \mu_1 j_n(x)[mxj_n(mx)]'}{m^2 j_n(mx)[xh_n^1(x)]' - \mu_1 h_n^1(x)[(mxj_n(mx)]'} \tag{8.5}$$

$$b_n = \frac{\mu_1 j_n(mx)[xj_n(x)]' - j_n(x)[mxj_n(mx)]'}{\mu_1 j_n(mx)[xh_n^1(x)]' - h_n^1(x)[(mxj_n(mx)]'} \tag{8.6}$$

here,

$$z = mx \tag{8.7}$$

$$m = \left(\frac{\varepsilon_p \mu_p}{\varepsilon_m \mu_m}\right)^{1/2} \tag{8.8}$$

$$x = \frac{2\pi a}{\lambda} n_{medium} \tag{8.9}$$

'x' is size parameter as discussed in the above section. ε_p and μ_p are permittivity and permeability of the nanoparticle, respectively and ε_m and μ_m are permittivity and permeability of the medium, respectively. Q_{ext} and Q_{sca} are extinction and scattering efficiency by the nanoparticles which is normalized value of extinction and scattering cross-section with the particle projected area. Q_{abs} denotes the absorption efficiency of the nanoparticle. a_n and b_n are calculated parameters from Maxwell equation to compute the amplitudes of the scattered field. m is complex quantity given by $m = \varepsilon_r + i\varepsilon_k$. 'a' represents the radius of the particle. μ_1 is the ratio of the magnetic permeability of the particle to the magnetic permeability of the ambient medium. $j_n(z)$ and $h_n^1(z)$ are spherical Bessel functions of order n (n = 1, 2, …) and of the given arguments, $z = x/m$ x respectively. Here, primes mean derivatives with respect to the argument. For the calculation to be practical, all infinite series (see Eqs. (8.2) and (8.3)) must be truncated after n_{max} terms. For n_{max}, Bohren and Huffman (Bohren and Huffman 1983) proposed a value which is given as in Eq. (8.10).

$$n_{max} = x + 4x^{1/3} + 2 \tag{8.10}$$

Further, dipolar approximation also offers simple equations to calculate light absorption of metallic NP, if the NP size is smaller than the light wavelength (Garcia 2011). Mathematically, this approximation can be achieved assuming that x is very very small and hence considering the first term n = 1 in Eq. (8.3). In such case, the

nanoparticle acts as Hertzian dipole (Hubenthal 2011). Such quasi-static approximation is valid for a <0.06λ (Hubenthal 2011). The quasi-static approximation can also be applicable for nonspherical nanopartilces, nanoparticles in inhomogeneous medium, and can also account for inter-band transition in metals. But, it would require certain modification where polarizability should be treated as tensor quantity for nonspherical shape and permittivity to be modified to take inter-band transition into consideration (Hubenthal 2011). This makes the calculations much more complex and tedious. For a >0.06λ, and spherical shape particles, Mie solutions would be more appropriate (Hubenthal 2011). For point dipole model, the solved scattering (C_{sca}) and absorption (C_{abs}) cross-sections are given by the following Eqs. (8.11) and (8.12) (Bohren and Huffman 1983; Garcia 2012):

$$C_{scat} = \frac{1}{6\pi}\left(\frac{2\pi}{\lambda}\right)^4 |\alpha|^2 \tag{8.11}$$

$$C_{abs} = \frac{2\pi}{\lambda}\mathrm{Im}[\alpha] \tag{8.12}$$

where, α is polarizability as given by Eq. (8.13):

$$\alpha = 3V\left[\frac{\varepsilon_p/\varepsilon_m - 1}{\varepsilon_p/\varepsilon_m + 2}\right] \tag{8.13}$$

Here V is the particle volume, ε_p is the dielectric function of the particle, and ε_m is the dielectric function of the embedding medium. It is clear from the Eq. (8.13) that when $\varepsilon_p = -2\varepsilon_m$, the particle polarizability would be very very large. Such condition would be the resonance condition.

For calculating the optical properties of metallic NPs, the heterogeneous system formed by the NPs and the surrounding media may be replaced by a homogeneous medium with an effective dielectric function $\varepsilon_{eff1} + i\varepsilon_{eff2}$ (Garcia 2012). Such method is known as effective medium theory. The effective medium theory for effective dielectric function is considered to be more suitable for the case of nanoparticle on substrate. For such case, dielectric constant of environment around nanoparticle is estimated from both environments with which the nanoparticle is in contact (Hubenthal 2011). For case of embedded nanoparticles in inhomogeneous medium, Newton defined an effective dielectric function as an average of the NPs and medium dielectric function weighted by their volume (Garcia 2012). Also, Maxwell–Garnett proposed to replace the NP's dielectric medium system by a homogeneous material which can exhibit the same dielectric polarization upon light illumination. This Maxwell–Garnett's approach is considered as the best approach within the framework of effective medium theories (Hubenthal 2011; Garcia 2012) and is more appropriate to take interparticle interactions or the presence of non-spherical NPs into account.

8.4.2 *Parameters Influencing the Scattering/Mie Efficiencies*

There are many factors which influence the scattering of light from nanostructures. It depends upon nanostructure size; nanostructure shape; metal property; dielectric constant of surrounding medium; interparticle spacing; etc.

(i) **Nanostructure size**

As you can see from Eqs. (8.2), (8.3), and (8.4), Q_{sca} and Q_{abs} depends on a_n and b_n which is function of size parameter x. Now x depends on size of the particle 'a', hence the scattering efficiency is function of nanostructure size (see Eq. (8.9)). With the increase in size of the particle, the scattering efficiency increases and becomes broader, i.e., wide range of wavelengths are scattered (see Fig. 8.7a). Also, the absorption efficiency of smaller particles is more (see Fig. 8.7b). It means small particles absorb more light and big particle scatter more light. Also, there is red shift in peak scattering efficiency of the particles with increasing size.

This indicates the tunability of scattering for different wavelengths by choosing appropriate particle size. In solar cells, if the nanoparticles are being used for scattering purpose, larger size of particles would be preferable. Also, as you can see in Fig. 8.7b, which shows the absorption efficiency for the silver-based nanoparticles, absorption by silver particles lies in UV wavelength region. Such absorption within nanoparticles would not be favorable when light is expected to be absorbed in active absorbing material of the cell.

(ii) **Nanostructure shape**

Nanostructure shape also plays an important role in the effective utilization of scattering property. Larger size particles deposited on a substrate tend to lose their spherical property and looks more like ellipsoids/spheroids. Such shape deformation causes red shifting in the resonance frequency (Pillai et al. 2007). Disks and other similar particle shapes, that have a large fraction of their volume close to the semiconductor, can lead to a very high fraction of light scattered into the substrate

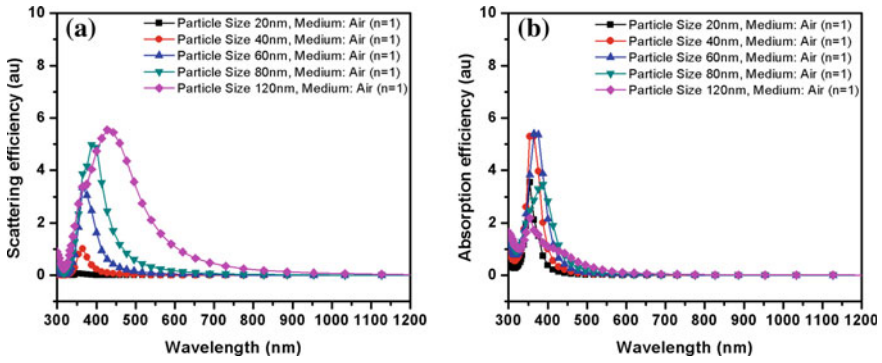

Fig. 8.7 **a** Scattering and **b** absorption efficiencies for silver nanoparticles of different sizes

and may enhance the absorption of light within the active absorbing materials of the cell. For the cylinder and hemisphere shape particles, the fraction of light scattered into the substrate is much higher than that for a spheres shape particle (Catchpole and Polman 2008a).

(iii) **Metal property**

Since a_n and b_n as given in Eqs. (8.5) and (8.6) are the function of permittivity (ε) of nanostructure (see Eq. (8.8)), and so the scattering and absorption efficiencies. Plasmon resonance, at which the scattering or absorption efficiencies are maximum, vary and is different for different metal nanostructures. Silver (Ag) exhibits surface plasmon resonance in ultra-violet wavelength region (Catchpole and Polman 2008b). However, for gold (Au) and copper (Cu), surface plasmon resonances lie in the visible wavelength region. Also, the resonance frequency can be tuned by varying the dielectric constant of the embedding medium. More about metal and associated plasmonics properties is discussed in Sect. 8.7.

(iv) **Dielectric constant of surrounding medium**

The scattering and absorption efficiency of the nanoparticles/nanostructures is very much influenced by the surrounding medium. The medium permittivity (ε_m) or the effective medium permittivity (ε_{eff}) can be an influencing parameter and may govern the scattering and absorption. When metal nanoparticles are placed on semiconductor substrate, an effective medium permittivity (ε_{eff}) is considered as discussed in Sect. 8.4.1. With the increase in dielectric constant/permittivity, the scattering efficiency increases and becomes broader, i.e., wide range of wavelengths are scattered (see Fig. 8.8a). Also, the absorption efficiency of smaller particles is relatively high (see Fig. 8.8b). It indicates that smaller particles absorb more light and bigger particle scatter more light as the effective dielectric constant of medium increases. Also, red shift in peak scattering efficiency of the particles is observed as the surrounding medium effective dielectric constant increases.

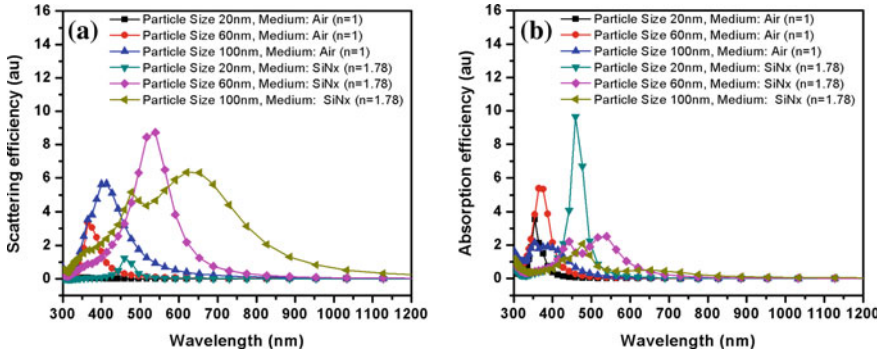

Fig. 8.8 Scattering and absorption efficiencies for silver nanoparticles **a** for different sizes in air (n = 1) and **b** in air (n = 1) and at silicon nitride (SiN_x)/Air interface having effective dielectric function (n) of 1.78

Sharp peaks at lower wavelengths are observed as particle size increases which are due to multipole effect. The multipole effect is due to variation of charge distribution in nanostructures as particle size increases. As the particle size increases, quadruple, octapole etc., oscillations also comes into picture which influence the scattering and absorption capability of metal nanoparticles. Such control by changing the dielectric medium gives us freedom to adjust and tune the scattering and absorption from/within nanostructures.

(v) **Interparticle spacing**

Mie solutions do not account for interparticle spacing and their influence on each other. However, recent experimental observations have shown that these interactions show the influence on scattering property of the nanostructures/nanoparticles. The scattering of waves involves propagation along different paths and results in interference phenomena. Constructive interference corresponds to resonant enhancement and destructive interference results in resonant suppression.

Resonance is usually introduced by the means of a harmonic oscillator with periodic forcing (Miroshnichenko et al. 2010). If the frequency of the driving force is close to the Eigen frequency of the oscillator, the amplitude of the other oscillator grows toward its maximal value. Miroschnichenko et al. (2010) suggests that many physical systems exhibit the opposite phenomenon when their response is suppressed and some resonance condition is met. Such resonant destructive interference is known as Fano resonance.

Coherent oscillations of conduction band electrons, i.e., plasmons, govern the optical properties of metals. Also, the charge density oscillations dominate the interaction between light and metallic nanoparticles on the closed surfaces which is known as localized surface plasmon (LSP). Miroschnichenko et al. (2010) suggests that plasmonic nanostructures can be considered as a physical realization of coupled oscillator systems at the nanoscale and indication of Fano resonance presence is observed whenever a resonant suppression of forward scattering (or transmission) is observed. The resonant suppression of forward scattering (i.e., Fano resonance) observed in nanoparticle aggregates where particles are very close to each other (Malynych and Chumanov 2003; Lassiter et al. 2010; Luk'yanchuk et al. 2010). Also, a red shift and broadening in surface plasmon resonance is observed when two nanoparticles are closer to each other and dipole–dipole interaction occur among them (Hubenthal 2011).

8.5 Backscattering Effect in Nanostructures

Scattering efficiency tells us about the scattering of light in all directions. However, the scattering can be divided into forward scattering and backward scattering (see Fig. 8.9). Depending upon the application, the particular scattering property from the nanostructure can be utilized.

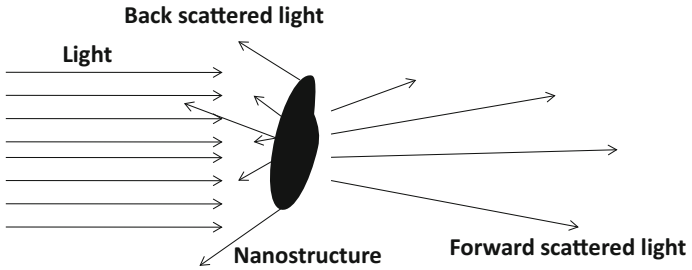

Fig. 8.9 Schematic for forward and backward scattering of light

Following the Mie scattering, backscattering efficiency from the nanostructures/nanoparticles can also be calculated using following Eq. (8.14) (Bohren and Huffman 1983). It indicates the relative scattering in backward direction.

$$Q_b = \frac{1}{x^2}\left|\sum_{n=1}^{\infty}(2n+1)(-1)^n(a_n - b_n)\right|^2 \tag{8.14}$$

Here Q_b (backscattering efficiency) is also known as the radar backscattering efficiency where again, x is size parameter, and a_n and b_n, calculated from Maxwell equations, are to compute the amplitudes of the scattered field as per Eqs. (8.5) and (8.6) as discussed above. The backscattering efficiency is also very much influenced by particle size and dielectric constant of the surrounding medium. For example, you can see the calculated back-scattering efficiency for different sizes of silver nanoparticle in Fig. 8.10a. Increasing the particle size increases the backscattering effect. Also, backscattering occurs for broader wavelength range and red shift is observed in backscattering efficiency as the particle size increases. It means more

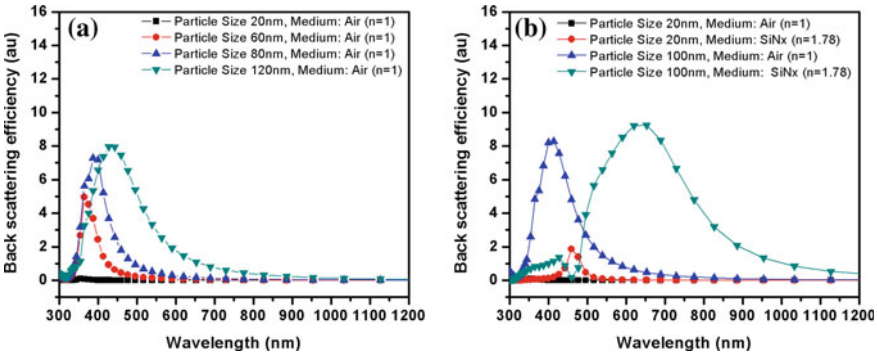

Fig. 8.10 Back-scattering efficiencies for silver nanoparticles **a** for different sizes in air and **b** in air and at silicon nitride (SiN_x)/Air interface having effective permittivity of 1.78

light of relatively longer wavelengths are scattered due to increase in interaction of light with relatively larger particles.

Further, as the surrounding medium changes and effective refractive index is increased for the nanostructure, backscattering efficiency for the same particle size is also increased. The impact of surrounding medium with increased effective refractive index/dielectric constant is large if the particle size is large as it can be seen in Fig. 8.10b. Also, red shifting in back-scattering efficiency peak occur along with the broadening in wavelength range that can be backscattered. This means by tuning the particle size and surrounding medium, the backscattering effect from nanostructures can be tuned as per requirement. In c-Si solar cells, the backscattering effect of nanostructures/nanoparticles can be efficiently utilized by keeping them at back surface. More about backscattering application in c-Si solar cell has been discussed in the next chapter.

8.6 Extraordinary Transmission Through Metal–Dielectric Extended Layers

As discussed in Sect. 8.3, light–matter interaction may also result in surface plasmon polariton (SPP) which has propagating nature. The electromagnetic excitation at metal–dielectric interface results in SPP mode excitation where the electromagnetic (EM) field amplitude decays exponentially with distance from the interface/surface in either direction/medium (Zayats et al. 2005). Abrupt discontinuity in material properties at the interface governs the light propagation through such structures. For nonmagnetic materials, dielectric permittivity (ε) of the material plays major role in light–matter interaction and propagation. With proper selection of dielectric and metal interface, and corresponding thickness can enable us to allow or block certain range of wavelengths through the interface. Also, such SPP-based structures provide ability to transmit light where classically it would have been impossible. Such extraordinary ability to tune the light propagation at nanoscale has been recent interest of international scientific community, especially for solar cell application.

For light–matter interaction, excitation of SPP's at metal–dielectric interface is crucial. Wave-vector associated with SPP (k_{spp}) at planar dielectric–metal interface is usually greater than the wave-vector of incident light ($k_{light} = \sqrt{\varepsilon}(\omega/c)$) (Murray 2005; Zayats et al. 2005). To excite SPP mode, it is important that the associated momentum ($\hbar k$) of the wave-vectors match. This can be achieved by some surface and interface modification, which leads to appropriate SPP mode excitation. 'Propagation length' and 'Penetration depth' are two important parameters to explain the light propagation along the interface or through the interface. Let us have a look about these parameters which have been discussed below.

8.6.1 Penetration Depth and Propagation Length

The spatial extent of electromagnetic field amplitude in SPP bounding media is called penetration depth. On the other hand, propagation of SPP mode along the interface before it decays is called propagation length. SPP mode has both longitudinal and transverse components of the electromagnetic field. Let us consider a metal–dielectric interface where metal, having thickness d and permittivity $\varepsilon(\omega)$, is on a dielectric layer having permittivity ε_s as shown in Fig. 8.11. Also, consider that the light falls on the metal at air–metal interface and the region $z \geq d$ represents air, $0 < z < d$ is metal region, and $z < 0$ is dielectric region. In this case, the SPP mode would be excited on air–metal interface and metal–dielectric interface. For very small thickness of metal, there would be interaction between these two SPPs excited at air–metal interface and metal–dielectric interface; and these would influence the propagation of each other along the surface. The SPP mode which would have less extent of electric field inside the metal would show longer propagation length since it would interact with the dissipating medium weakly (Zayats et al. 2005).

So, the propagation length of the SPP mode is the length traveled by the electromagnetic field associated with SPP mode along the interface till it decayed to 1/e of its initial value and represented by L_{spp}. It depends on imaginary component of the complex wave-vector k^i_{spp}. Since, amplitude decay with distance as $L_{spp} = \exp(-k^i_{spp}x)$, the intensity, which is square of amplitude, would decay as $L_{spp} = \exp(-2k^i_{spp}x)$ (Murray 2005). So, the propagation length would be given by following Eq. (8.15):

$$L_{spp} = \frac{1}{2k^i_{spp}} \tag{8.15}$$

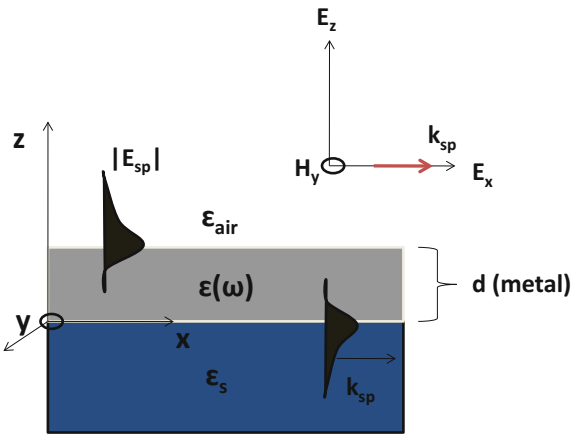

Fig. 8.11 Schematic showing surface plasmon on metal–dielectric interface (after Ref. Zayats et al. 2005)

Propagation length may vary from few nanometers to more than 100 μm for different wavelengths of light. For corrugated surfaces having periodicity less than propagation length, Bragg scattering may occur for the SPP mode. Such scattering would lead to radiative nature of SPP mode rather than localized nature as localized surface plasmon (LSP).

Further, penetration depth is the distance normal to the interface where the electric field amplitude is decreased by 1/e from its maximum value at interface. The decay of the field occurs as $\exp(-k_z^i z)$, where k_z^i is imaginary component of the propagation vector (k) in z-direction. So the penetration depth, represented by L_z, can be written as following Eq. (8.16):

$$L_z = \frac{1}{|k_z^i|} \tag{8.16}$$

For much lesser metal thicknesses, i.e., less than the penetration depth, electromagnetic field may interact with both the surfaces (see Fig. 8.11). In such scenario, there is strong possibility that light would couple in forward direction and may result in enhanced transmission of light through the metal–dielectric interface which would not have been possible otherwise (Economou 1969).

In case of metals, the penetration depth is also known as skin depth and is represented by δ. It can be co-related with permittivity of the metal. For the metals, the refractive index ($\tilde{n}$), permittivity ($\tilde{\varepsilon}$) as well as propagation wave-vector ($\tilde{k}$) are complex quantities. The complex wave-vector ($\tilde{k} = \mathrm{k^r} + \mathrm{ik^i}$) is co-related with complex refractive index ($\tilde{n} = \mathrm{n} + \mathrm{ik}$) as per Eq. (8.17). Also, the complex refractive index is co-related with permittivity ($\tilde{\varepsilon} = \varepsilon_r + \mathrm{i}\varepsilon_k$) as in Eq. (8.18):

$$\tilde{k} = k^i + ik^r = \tilde{n}\frac{\omega}{c} \tag{8.17}$$

$$\tilde{n} = n + ik = \sqrt{\tilde{\varepsilon}} = \sqrt{\varepsilon_r + i\varepsilon_k} \tag{8.18}$$

So, the skin depth, δ, can be given as in Eq. (8.19):

$$\delta = \frac{1}{k^i} = \frac{c}{\omega k} = \frac{c}{\omega\sqrt{-\frac{\varepsilon_r}{2} + \frac{1}{2}\left(\sqrt{\varepsilon_r^2 + \varepsilon_k^2}\right)}} \tag{8.19}$$

The lesser value of skin depth is useful, especially when the skin depth (δ) < mean free path (l). This is because it leads to nonlocal anomalous skin effect (Bohren and Huffman 1983). For silver (Ag), bulk mean free path is 52 nm and the skin depth lies in the range of 24–29 nm for 300–1200 nm wavelength photons (see Table 8.1). Similarly for aluminum (Al), the bulk mean free path is 16 nm whereas the skin depth is 13 nm for these wavelengths. Also, for copper (Cu) and gold (Au), the bulk mean free path is 42 nm and skin depth is in the range of 30–37 nm (see Table 8.1) (Bohren and Huffman 1983). Since the metal thickness is less than skin

Table 8.1 Bulk mean free path and skin depth for different metals for 300–1200 nm wavelength photons (after Ref. Bohren and Huffman 1983)

Metal	Bulk mean free path (nm)	Skin depth (nm)
Ag	52	24–29
Al	16	16
Cu	42	30–37
Au	42	30–37

depth, forward coupling and enhanced transmission through dielectric–metal interface can be expected because for such case, mean free path of electron is larger than the classical skin depth of the metal. So, the SPP mode exited at the metal surface on each side at the metal–dielectric interface would be influenced by each other and there is possibility that it would lead to extraordinary transmission effects (Dai and Jiang 2009).

The penetration depth/skin depth tuning and optimized thickness for different plasmonics materials for utilizing the anomalous skin effects can be useful for different applications. For example, silver thin films in sandwiched structures have been used for plasma display technology in the past for electromagnetic interference shielding. Suitable metal (Ag) and dielectric multi-stack structure designs have been shown to act as band-pass filter in visible wavelength range (400–700 nm) (Sawada et al. 2001; Tachibana et al. 2003). Also, anomalous skin effect-based light–matter interaction and light propagation control for solar cell applications has been explored by many researchers. For example, metal thin film multilayers, like aluminum (Al)-doped zinc oxide (ZnO) and silver (Ag), have been explored for transparent conduction layer applications. The multilayer stack of Al:ZnO/Ag/Al:ZnO have been shown to give better conductivity with more light transmission through it (Sahu et al. 2007; Sahu and Huang 2009). Such structures have been proposed as better electrodes/transparent conducting oxides (TCO) for organic/die-sensitized solar cells. Zinc sulfide (ZnS) and silver (Ag) multilayer (ZnS/Ag/ZnS) have also been shown to give transparent conducting layers having comparatively better transparency as well as sheet resistance (Leftheriotis 2000). TiO_2/Ag/SiO_2-based dielectric–metal–dielectric sandwiched structure for transparent electrode with better conductivity has been reported recently by Chiu et al. (2014). Also, Zhou et al. (2010) have studied multilayered stack of SiO_2 (thickness 60 nm) and Ag (thickness 85 nm) which was milled by focused ion beam to form grating like structures. They have shown promising tunability of transmission for different wavelengths which depends on number of multilayers and grating pitch.

8.6.2 Metal–Dielectric Extended Layers and Propagation of Light

At planner metal–dielectric interface, wave-vector associated with SPP mode is larger than the wave-vector associated with light in the neighboring medium as discussed above. So, to excite SPP mode, special arrangements are done such as

surface modification using diffraction grating. Other methods include total internal reflection geometry-based photon tunneling methods.

In case of diffraction grating geometry (see Fig. 8.12), components of diffracted light, for which the wave-vector matches with SPP mode wave-vector, is coupled in SPP mode. Light coupling in such configuration is very sensitive to grating structure, grating period, incident wavelength etc. (Murray 2005; Zayats et al. 2005; Sun and Zuo 2011; Fan et al. 2013).

In case of total internal reflection geometry, there are two important SPP excitation configurations which result in enhanced light coupling:

(i) **Kretschmann geometry**

In this geometry, metal film is illuminated through dielectric prism with light at an incident angle greater than critical angle for total internal reflection as shown in Fig. 8.13. Under resonance condition, a sharp reflection minimum is observed from

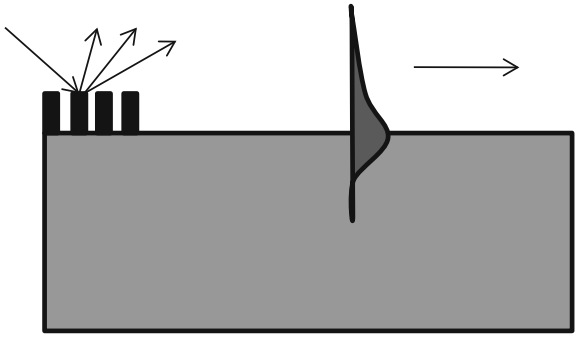

Fig. 8.12 Schematic for SPP excitation in diffraction grating method (after Refs. Murray 2005; Zayats et al. 2005)

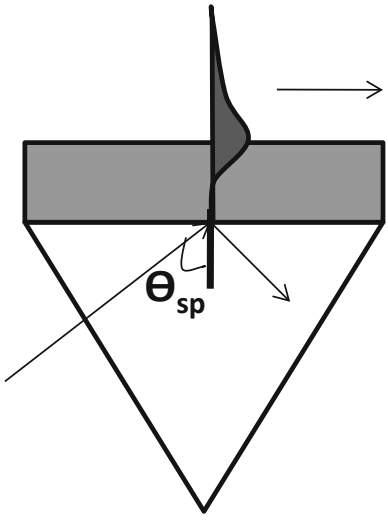

Fig. 8.13 Schematic for SPP excitation and light coupling in Kretschmann geometry (after Refs. Murray 2005; Zayats et al. 2005)

metal prism interface and light couple perfectly in SPP mode. In such geometry, metal thickness should be small. If the thickness is large, the SPP excitation would be less.

(ii) **Otto geometry**

In this geometry the conditions are analogous to Kretschmann geometry, except the prism. In this case, the prism is placed close to the metal surface and photon tunneling occurs through air gap between prism and surface (see Fig. 8.14). Otto geometry is more appropriate for thick metal films, where Kretschmann geometry is not suitable (Zayats et al. 2005). For such geometry, best light coupling occur if the spacer thickness is of the order of wavelength (Murray 2005).

All these discussed configurations are mostly used to explain the enhanced transmission or longitudinal propagation of lights on metal–dielectric interfaces. Mostly the structures in such configurations have metal films of thickness, typically, 35–40 nm or more (but <100 nm). These structures are also useful in making plasmonic waveguides due to less high propagation lengths (Stegeman et al. 1983; Park et al. 2010; Hu et al. 2013).

In summary, metal–dielectric extended layers have endless scope of applications. Solar photovoltaic technology has also been benefited from development of such structures. Applicability of such structures in solar cells can be maximized by exploiting the penetration depth or propagation length information and suitably optimizing the light-trapping structures. This provides us flexibility for tuning the light propagation in matter/active absorbing materials and enabling us to control the light transmission and absorption in the solar photovoltaic devices.

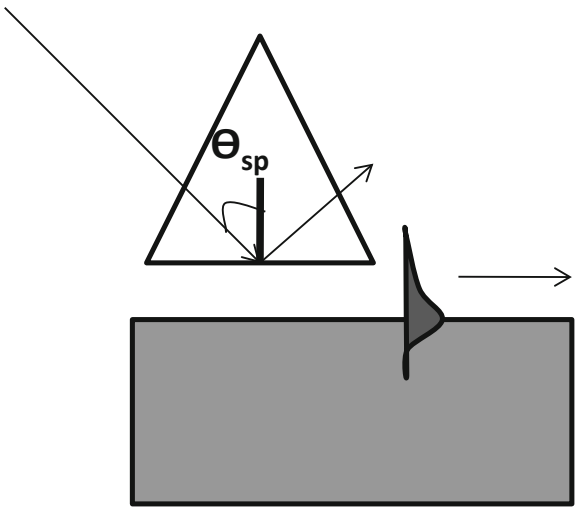

Fig. 8.14 Schematic for SPP excitation and light coupling in Otto geometry (after Refs. Murray 2005; Zayats et al. 2005)

8.7 Choice of Metal for Plasmonics Applications

When we talk about plasmonics, it means we talk about collective oscillations of free or conduction electrons. The free and conduction electrons are found in metals and hence the plasmonics is mostly studied for metals. There are many types of metals available in nature and they are unique in their properties. For plasmonics applications, the choice of metal depends on the application we seek. For solar cell application, our target is to trap light in the active absorbing material of the cell. Hence, the metal nanostructure should be such that its plasmonic property should be useful. It means it should help in enhancing the light absorption/coupling in active absorbing material in the desired wavelength range for which the solar cell has probability for efficient performance. For c-Si solar cell, the desired wavelength range is 300–1200 nm. This means the choice of metal for plasmonic-based light trapping would depend on the metal plasmonics property such that it helps the cell to utilize maximum of the wavelengths for electricity generation, and there should not be parasitic absorption within the metal. It means low inter-band absorption is desired in metals, especially where the cell has high absorption capability.

In case of metal nanoparticles, having spherical shape and in free space, there exist a plasmon resonance frequency which depends on density of free electrons (N) in the metal, effective mass, m (also called optical mass (Kreibig and Vollmer 1995)) of electron in the metal and free-space dielectric constant, ε_0. The bulk plasmon resonance frequency (ω_p) for such metal particle is given by the following Eq. (8.20):

$$\omega_p^2 = \frac{2Ne^2}{m\varepsilon_0} \tag{8.20}$$

Equation (8.20) indicates the dependence of resonance frequency on the density of free electrons in the particle and optical mass. The density of free electrons for some metals is given in Table 8.2. Also, various parameters/constants for these metals have been tabulated from various references (Brust 1970; Johnson and Christy 1972).

Table 8.2 Parameters governing plasmonic properties of various metals

Metal	Atomic number	Electronic configuration	Electron density[a] (per m^3)	Optical mass
Silver (Ag)	47	[Kr] $4d^{10}$ $5s^1$	5.86×10^{28}	0.96 me
Aluminum (Al)	13	[Ne] $3s^2$ $3p^1$	6.03×10^{28}	1.45 me
Copper (Cu)	29	[Ar] $3d^{10}$ $4s^1$	8.49×10^{28}	1.49 me
Gold (Au)	79	[Xe] $4f^{14}$ $5d^{10}$ $6s^1$	5.9×10^{28}	0.99 me

[a]Electron Density = $\frac{\rho N_a}{A}$ where N_a is Avogadro's constant, ρ is density of metal, A is atomic weight

Table 8.3 Inter-band absorption threshold in various metals (after Ref. Kreibig and Vollmer 1995)

Metal	Threshold energy (eV)	Threshold energy wavelength equivalent (nm)
Silver (Ag)	3.87	320.4
Aluminum (Al)	1.5	826.7
Copper (Cu)	2.1	590.5
Gold (Au)	2.38	521

Also, threshold for inter-band absorption in these metals is given in Table 8.3 (Kreibig and Vollmer 1995). The threshold values for inter-band absorption depend on core electrons of the metals.

In nanostructures, surface plasmon resonance (ω_{sp}) is of more interest as it governs the light–matter interaction and it is co-related with bulk plasmon resonance (ω_p). For spherical nanoparticles, for the surface plasmon resonance $\omega_{sp} = \sqrt{3}\omega_p$. For Au, Cu, and Al, surface plasmon resonance lies in the visible wavelength region. For Ag, surface plasmon resonance occurs in ultra-violet wavelength region. The resonance frequency can be tuned by varying the dielectric constant of the embedding medium as discussed in the above section as higher index leads to a red shift in the resonance frequency. Beyond 700 nm, the dielectric functions of Au and Ag are very similar (Catchpole and Polman 2008a). Due to lower absorption in visible wavelength region and lower cost, Ag is considered as better choice than Au. However, Ag must be well encapsulated to avoid oxidation effects which are not the case for Au. Further, Cu is cheaper but absorbs more than Au. In the case for Au and Cu, inter-band transitions leads to decreased efficiency of plasmon excitation due to significant overlap between the inter-band absorption edge and the plasmon resonance. For Ag, the absorption edge is in the UV (320 nm) and show little impact on the plasmon resonance since it appears at wavelengths larger than 370 nm. Al easily forms oxide very rapidly under atmospheric conditions with thickness of about 2–3 nm, which impacts its plasmonic property (West et al. 2010). Overall, the excitation of the plasmon resonance in Ag particles is more efficient than Au, Cu, and Al particles (Garcia 2011). So, Ag is the preferred choice as plasmonics material in solar cell applications.

Further, the inter-band transition in metal nanoparticle/nanostructure is also dependent on the particle size. Gharibshahi et al. (2010) suggest that the quantum confinement effect of the conduction bands is stronger for silver and gold nanoparticles for the diameter less than 20 nm. Such nanostructures/nanoparticles, of size in the range of 1–100 nm, contains about 10^2–10^8 atoms and demonstrate different physical and chemical properties from their bulk and atomic counterparts. A typical schematic of the band structure of a metal nanoparticle can be seen in Fig. 8.15. When light interacts with particle/nanostructure, the occupied ground-state conduction electron absorbs photon energy and excite to the unoccupied higher energy state of the conduction band.

An increase in the number of atoms produces larger particle sizes. Increased particle size increases the nuclear potential energy of the system and decrease in the

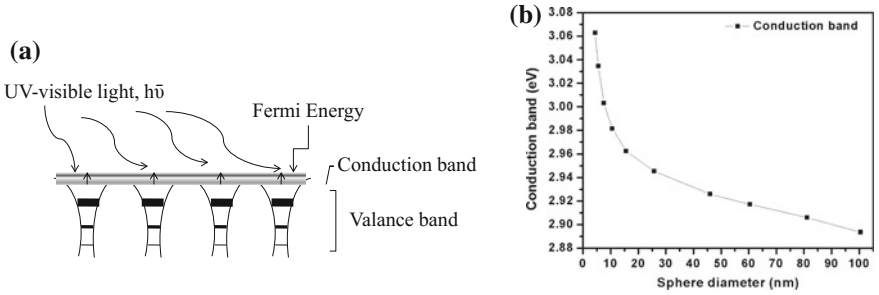

Fig. 8.15 **a** Schematic for energy band structure of four Ag atoms-based nanoparticle; **b** conduction band energy for Ag nanoparticles as a function of diameter (assuming spherical shape) (after Ref. Gharibshahi 2010)

conduction band energy is observed (conduction band $\sim 1/d$, d represents size). The conduction band energy of the Ag nanoparticles as a function of diameter can be seen from Fig. 8.15b, as estimated by Gharibshahi et al. (2010). One can see as the particle diameter increases from 4 to 100 nm, the conduction band decreases from 3.065 to 2.895 eV (Gharibshahi 2010). This change in conduction band is more significant for the smaller particle sizes than the larger particle sizes. This is the result of strong quantum confinement effects for the smaller Ag particles (sizes ≤ 20 nm). So, for scattering purpose, larger particle size would be more preferable where parasitic absorption within the metals can be minimized.

In summary, silver is the best material for plasmonic-based light-trapping application, especially for solar cells as it results in relatively low parasitic absorption in visible and NIR wavelength range. However, it has one issue that it degrades in atmospheric ambiance and it requires proper protection or encapsulation to avoid such atmospheric reactions.

8.8 Questions and Problems

1. What do you mean by plasmonics? Put some light on historical developments and its applicability in solar cells.
2. What are the different ways which can be explored using metal nanostructures for enhanced light trapping in solar cells?
3. Discuss on implementing plasmonic-based light trapping in a solar cell of any type as per your interest. Defend on the most suitable way of implementation?
4. What do you understand from Mie scattering? How is it different from Rayleigh scattering and geometrical scattering?
5. What do you mean by size parameter? How is it important for scattering effect from the nanostructures?

6. A nanoparticle of diameter 2 nm in air scatters the light. What kind of scattering do you expect from this nanoparticle if the wavelength of light is (a). 300 nm (b). 1200 nm. What would happen if the particle size is increased to 200 nm and 1 μm respectively?
7. What do you understand from Mie efficiencies? How are they dependent on particle size, shape, and medium refractive index?
8. Discuss on absorption and scattering efficiencies and their dependence on particle size and refractive index of the medium?
9. Consider light interaction with a metal nanoparticle which only excites dipole oscillations. Find out the ratio of scattering to absorption cross-section for (a). 20 nm particle, (b). 60 nm particle, (c). 150 nm particle where incident light wavelength is 400 nm and 620 nm. Assume that the medium is air and complex permittivity of metal nanoparticle at 400 nm is −3.78 + 0.67i and at 620 nm is −15.04 + 1.02i.
10. Find out the ratio of scattering cross-sections for 60 nm particle when incident light wavelength is 400 nm and 620 nm. Assume that the medium is air and complex permittivity of metal nanoparticle at 400 nm is −3.78 + 0.67i and at 620 nm is −15.04 + 1.02i. Also, assume that the light interaction with metal nanoparticle excite dipole oscillations.
11. Calculate the extinction (sum of scattering and absorption cross section) for a 100 nm particle when incident wavelength of light is 620 nm. Assume that the medium is having refractive index (RI) of 2 and permittivity of metal nanoparticle at 620 nm is −15.04 + 1.02i. (Hint: Permittivity = sqrt (RI)).
12. List all the metals from periodic table which has one electron in its outermost orbital and find out electron density of the corresponding metal.
13. What do you understand by absorption in metal? Is it good or bad? Discuss in detail considering all application scenarios like in organic solar cell, inorganic solar cell, die-sensitized solar cells, etc.?
14. You are given different particles of sizes 20, 40, 60, 80, and 100 nm. Which size of the particle will give highest scattering efficiency and which one will give highest absorption efficiency? Consider the medium is air and incident light wavelength is 1100 nm.
15. How does interparticle spacing influence the scattering properties from nanoparticles?
16. What do you understand by backscattering efficiency of metal nanostructures? How is it different from Mie scattering efficiency?
17. How light would interact at metal–dielectric interface if the metal is thin and continuous?
18. What do you understand from penetration depth and propagation length? Which one is important to identify the transmission capability of the structure?
19. Discuss the difference between Kretschmann geometry and Otto geometry?
20. What do you understand by plasmon resonance? What is the difference between bulk and surface plasmon resonance?

21. What are the parameters which guide the choice for metal to be used for light trapping in solar cells?
22. Calculate ω_{sp} and λ_{sp} for Cu, Ag, Au, Al nanoparticles.
23. What do you understand from inter-band absorption in metal nanostructures? How are they dependent on nanostructure size?

References

Atwater HA, Polman A (2010) Plasmonics for improved photovoltaic devices. Nat Mater 9:205–213. doi:10.1038/nmat2629

Bohren CF, Huffman DR (1983) Absorption and scattering of light by small particles. Wiley-VCH Verlag GmbH & Co, KGaA

Brust D (1970) Band structure and optical properties of aluminum. Solid State Commun 8:413–416. doi:10.1016/0038-1098(67)90128-7

Catchpole KR, Polman A (2008a) Design principles for particle plasmon enhanced solar cells. Appl Phys Lett 93:191113. doi:10.1063/1.3021072

Catchpole KR, Polman A (2008b) Plasmonic solar cells. Opt Express 16:21793. doi:10.1364/OE.16.021793

Chiu P-K, Lee C-T, Chiang D et al (2014) Conductive and transparent multilayer films for low-temperature TiO2/Ag/SiO2 electrodes by E-beam evaporation with IAD. Nanoscale Res Lett 9:35. doi:10.1186/1556-276X-9-35

Dai L, Jiang C (2009) Anomalous near-perfect extraordinary optical absorption on subwavelength thin metal film grating. Opt Express 17:20502. doi:10.1364/OE.17.020502

Economou EN (1969) Surface Plasmons in Thin Films. Phys Rev 182:539–554. doi:10.1103/PhysRev.182.539

Evanoff DD, Chumanov G (2005) Synthesis and Optical Properties of Silver Nanoparticles and Arrays. ChemPhysChem 6:1221–1231. doi:10.1002/cphc.200500113

Fan R-H, Zhu L-H, Peng R-W et al (2013) Broadband antireflection and light-trapping enhancement of plasmonic solar cells. Phys Rev B 87:195444. doi:10.1103/PhysRevB.87.195444

Gan Q, Bartoli FJ, Kafafi ZH (2013) Plasmonic-enhanced organic photovoltaics: Breaking the 10% efficiency barrier. Adv Mater 25:2385–2396. doi:10.1002/adma.201203323

Garcia MA (2012) Surface plasmons in metallic nanoparticles: fundamentals and applications. J Phys D Appl Phys 45:389501. doi:10.1088/0022-3727/45/38/389501

Garcia MA (2011) Surface plasmons in metallic nanoparticles: fundamentals and applications. J Phys D Appl Phys 44:283001. doi:10.1088/0022-3727/44/28/283001

Gharibshahi (2010) Quantum Mechanical Calculation of the Optical Absorption of Silver and Gold Nanoparticles by Density Functional Theory. Phys Int 1:57–64. doi:10.3844/pisp.2010.57.64

Hu H, Ji D, Zeng X et al (2013) Rainbow trapping in hyperbolic metamaterial waveguide. Sci Rep 3:1249. doi:10.1038/srep01249

Hubenthal F (2011) Noble Metal Nanoparticles: Synthesis and Optical Properties. In: Comprehensive Nanoscience and Technology edited by David L. Andrews, Gregory D. Scholes, and Gary P. Wiederrecht. pp 375–435

Johnson PB, Christy RW (1972) Optical Constants of the Noble Metals. Phys Rev B 6:4370–4379. doi:10.1103/PhysRevB.6.4370

Kreibig U, Vollmer M (1995) Optical Properties of Metal Clusters. Springer Series in Material Science vol 25; Berlin: Springer

Lassiter JB, Sobhani H, Fan JA et al (2010) Fano Resonances in Plasmonic Nanoclusters: Geometrical and Chemical Tunability. Nano Lett 10:3184–3189. doi:10.1021/nl102108u

Lee JH, Park JH, Kim JS et al (2009) High efficiency polymer solar cells with wet deposited plasmonic gold nanodots. Org Electron 10:416–420. doi:10.1016/j.orgel.2009.01.004

Leftheriotis G (2000) Development of multilayer transparent conductive coatings. Solid State Ionics 136–137:655–661. doi:10.1016/S0167-2738(00)00328-3

Luk'yanchuk BS, Tribelsky MI, Ternovsky V et al (2007) Peculiarities of light scattering by nanoparticles and nanowires near plasmon resonance frequencies in weakly dissipating materials. J Opt A Pure Appl Opt 9:S294–S300. doi:10.1088/1464-4258/9/9/S03

Luk'yanchuk B, Zheludev NI, Maier SA et al (2010) The Fano resonance in plasmonic nanostructures and metamaterials. Nat Mater 9:707–15. doi:10.1038/nmat2810

Malynych S, Chumanov G (2003) Light-induced coherent interactions between silver nanoparticles in two-dimensional arrays. J Am Chem Soc 125:2896–2898. doi:10.1021/ja029453p

Miroshnichenko AE, Flach S, Kivshar YS (2010) Fano resonances in nanoscale structures. Rev Mod Phys 82:2257–2298. doi:10.1103/RevModPhys.82.2257

Murray WA (2005) Optical properties of nanoscale silver structures fabricated by nanosphere lithography. Physics (College Park Md) 230:U240–U240

Nahm C, Choi H, Kim J et al (2011) The effects of 100 nm-diameter Au nanoparticles on dye-sensitized solar cells. Appl Phys Lett 99:253107. doi:10.1063/1.3671087

Park J, Kim K-Y, Lee I-M et al (2010) Trapping light in plasmonic waveguides. Opt Express 18:598. doi:10.1364/OE.18.000598

Pillai S, Catchpole KR, Trupke T, Green MA (2007) Surface plasmon enhanced silicon solar cells. J Appl Phys 101:093105. doi:10.1063/1.2734885

Pillai S, Green MA (2010) Plasmonics for photovoltaic applications. Sol Energy Mater Sol Cells 94:1481–1486. doi:10.1016/j.solmat.2010.02.046

Tricker RAR (1970) Introduction to meteorological optics. American Elsevier Publishing, New York

Roqué J, Molera J, Sciau P et al (2006) Copper and silver nanocrystals in lustre lead glazes: Development and optical properties. J Eur Ceram Soc 26:3813–3824. doi:10.1016/j.jeurceramsoc.2005.12.024

Sahu DR, Huang JL (2009) Development of ZnO-based transparent conductive coatings. Sol Energy Mater Sol Cells 93:1923–1927. doi:10.1016/j.solmat.2009.07.004

Sahu DR, Lin S-Y, Huang J-L (2007) Deposition of Ag-based Al-doped ZnO multilayer coatings for the transparent conductive electrodes by electron beam evaporation. Sol Energy Mater Sol Cells 91:851–855. doi:10.1016/j.solmat.2007.02.003

Sawada M, Higuchi M, Kondo S, Saka H (2001) Characteristics of indium-tin-oxide/silver/indium-tin-oxide sandwich films and their application to simple-matrix liquid-crystal displays. Jpn J Appl Phys 40:3332–3336. doi:10.1143/JJAP.40.3332

Stegeman GI, Burke JJ, Hall DG (1983) Surface-polaritonlike waves guided by thin, lossy metal films. Opt Lett 8:383. doi:10.1364/OL.8.000383

Sun Z, Zuo X (2011) Tunable absorption of light via localized plasmon resonances on a metal surface with interspaced ultra-thin metal gratings. Plasmonics 6:83–89. doi:10.1007/s11468-010-9172-5

Tachibana Y, Kusunoki K, Watanabe T et al (2003) Optical properties of multilayers composed of silver and dielectric materials. Thin Solid Films 442:212–216. doi:10.1016/S0040-6090(03)00984-2

West PR, Ishii S, Naik GV et al (2010) Searching for better plasmonic materials. Laser Photon Rev 4:795–808. doi:10.1002/lpor.200900055

Westphalen M, Kreibig U, Rostalski J et al (2000) Metal cluster enhanced organic solar cells. Sol Energy Mater Sol Cells 61:97–105. doi:10.1016/S0927-0248(99)00100-2

Zayats AV, Smolyaninov II, Maradudin AA (2005) Nano-optics of surface plasmon polaritons. Phys Rep 408:131–314. doi:10.1016/j.physrep.2004.11.001

Zhou L, Huang C, Wu S et al (2010) Enhanced optical transmission through metal-dielectric multilayer gratings. Appl Phys Lett 97:011905. doi:10.1063/1.3458702

Zhu J, Xue M, Shen H et al (2011) Plasmonic effects for light concentration in organic photovoltaic thin films induced by hexagonal periodic metallic nanospheres. Appl Phys Lett 98:151110. doi:10.1063/1.3577611

Chapter 9
Plasmonic-Based Light Trapping for c-Si Solar Cell Applications

Exploration of plasmonic-based technology as discussed in previous chapter can be a good step forward for light trapping applications in c-Si solar cells. Avoiding surface texturing in such solar cells would help in getting better surface passivation as planner/flat surface are better and relatively easier to passivate compared to textured surface. *This chapter is focused on such plasmonic-based light trapping structure research and developments for c-Si solar cells. Need and applicability of such emerging plasmonic-based light trapping structures in context of c-Si solar cells have been discussed. Also, a broad overview on limitations and solutions has been presented.*

9.1 Need for Plasmonic-Based Anti-reflection Structure in c-Si Solar Cells

Si is indirect band gap semiconductor and the maximum current generation capability is very much dependent on light trapping geometry. As discussed in Chap. 1, with appropriate light trapping geometry, the current generation potential in Si wafer based cells can be greatly enhanced. Depending upon the perfectness of light trapping structure, wafer optical thickness can be enhancement ideally to a maximum 50 times ($\sim 4n^2$) of geometrical thickness. This can make a c-Si wafer based solar cell, having thickness 100–200 μm, capable enough to generate a current of about 43–43.5 mA/cm^2 (refer to Chap. 1, Sect. 1.7). Without any light trapping structure, the cell of the same thickness would be capable of generating current in the range of 37–38 mA/cm^2 only. However, 50 times optical path length enhancement is an ideal situation. In c-Si solar cell technology, surface texturing technique is used for enhanced light trapping, as we already have seen in Chap. 4 that textured surface at both sides of the wafer is required for better light trapping and the dimension of texture should be in the range of 5–10 μm. With such

© Springer Nature Singapore Pte Ltd. 2017

C.S. Solanki and H.K. Singh, *Anti-reflection and Light Trapping in c-Si Solar Cells*, Green Energy and Technology,
DOI 10.1007/978-981-10-4771-8_9

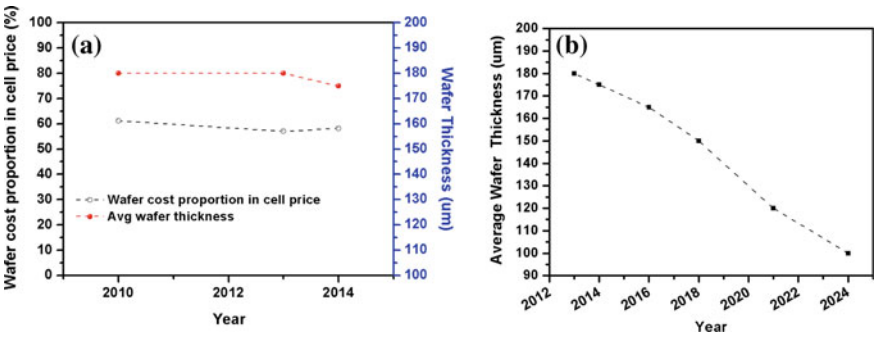

Fig. 9.1 **a** Available cell thickness and wafer cost share in cell price for last 5 years. **b** past, present, and future trend of average wafer thickness reduction with expected technology improvements (after Ref. http://www.itrpv.net/Reports/Downloads/2014/ 2014)

arrangement, the Si wafer-based cell would be capable of generating current in the range of 40–41 mA/cm^2 at its maximum capacity (refer to Chap. 4, Sect. 4.4).

In c-Si wafer based cell industry, the drive is toward reducing the cost and improving the cell performance. As per ITRPV analysis, the wafer cost proportion in cell manufacturing, using wafer thickness of 180–200 μm, is sustained at about 57%, which is significant (see Fig. 9.1a). For reducing the cost of the cell, wafer thickness reduction would be important as it would help in reducing the use of raw material for making the wafer and hence the wafer cost. Significant research is being done and techniques are being explored worldwide to make thinner wafer with lower kerf loss. ITRPV predicts that 100 μm or even lower thickness wafer would be in production by 2024 compared to currently used 180–200 μm (http://www.itrpv.net/Reports/Downloads/2014/ 2014). Figure 9.1b shows the expected trend for wafer thickness reduction in coming years.

Fabrication of c-Si-based solar cells using much lower thickness wafers would raise many challenges. Light trapping in such thin wafer based c-Si solar cells would be one of the many important challenges. The traditional way for light trapping in c-Si solar cell is surface texturing which would require 5–10 μm random pyramids on the wafer surface as discussed above. However, the problem with such textured surfaces in thin wafer based cells is that these would result in comparatively more surface defects. It would increase the probability of high minority carrier recombination in the surface and junction regions due to increased surface to volume ratio. In such scenario, an alternative way to enhance the light trapping would be necessary where we should be able to enhance the optical thickness of the wafer, i.e., enhanced light trapping within the wafer, without modifying/texturing the wafer surface. Exploration of plasmonic-based advanced light trapping structures may play a crucial role and may become a better solution for c-Si-based solar cell technology. Using such alternative light trapping geometry, where surface texturing can be avoided, would help in getting better surface passivation since planner/flat surface is better and relatively easier to passivate compared to the

textured surface. This would in result help us to get better electrical performance from the cell. Also, avoiding texturization of surface would have an additional benefit which is minimization of the loss in active absorbing material during texturing process. As a rough estimate, a 5 inch 180-μm-thick wafer weight is about 6.7 gm. In texturization process at both sides, which result in about 5 μm pyramids, roughly around 1.2 gm material is lost. It means about 18% active absorbing material by weight is lost considering wafer thickness of about 180 μm. If the wafer thickness would be 100 μm or less, the loss of active absorbing material due to texturization would be more significant, i.e., more than 36% by weight for getting same texture size. This makes plasmonic-based alternative light trapping technique more useful in getting better and enhanced current generation potential in thin wafer based cells. This can be possible because there is possibility of using such structures at planer surfaces and surface roughening/texturing required for light trapping can be avoided. Further, mechanical strength in the thin wafers can also be relatively maintained by avoiding absorbing substrate material loss which happens due to surface etching during surface texturing in traditional cell manufacturing process.

9.2 Expectation from Plasmonic-Based Anti-reflector or Light Trapping Structure

As discussed in above section, the main benefits of developing plasmonic-based alternative light trapping structure would be the replacement of traditional texturization-based light trapping structure. The need of such alternative light trapping is for next-generation thin c-Si solar cells where texturization of surface would not be favorable. If we want to have alternative light trapping structure, then it must be competitive to the existing texturization-based light trapping structure. The question is what and how much we should expect from plasmonic-based light trapping structure? Well, our aim is to get enhanced light trapping; that means enhancement in current generation. The next question would be how much? To answer this question, let us assume a 100 μm wafer based c-Si solar cell. To know the relative enhancement, let us consider the cell with silicon nitride (SiN_x) anti-reflection coating on planner surface as shown in Fig. 9.2a. Since the target is to replace texturization-based light trapping, let us consider hypothetically that there is a 100 μm wafer based c-Si solar cell which has textured surface (both side) and is coated with SiN_x anti-reflector coating as shown in Fig. 9.2b. Now, let us simulate the cell electrical performance of such thin c-Si solar cell and see how much relative gain we are expecting? Consider the simulation for two scenarios, i.e., best cell and typical cell scenario as we have already seen in Chap. 6. The simulation parameters used for simulating the electrical performance using PC1D (PC1D 5.9) can be seen in Table 9.1. Here, the main difference is that the assumed wafer thickness is 100 μm in both best cell and typical cell scenarios. Also, the bulk minority carrier

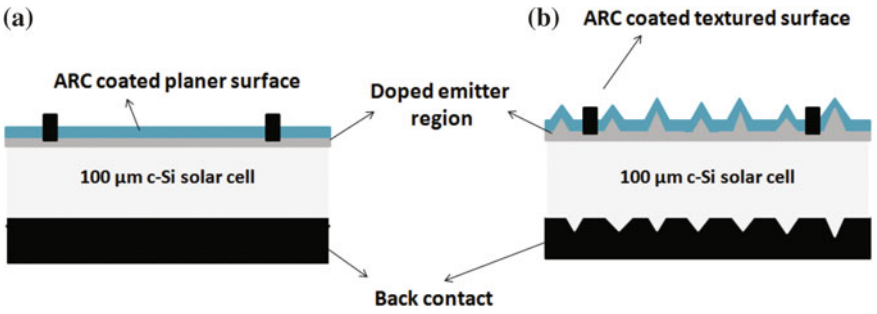

Fig. 9.2 Schematic of 100-µm-thin wafer-based c-Si solar cell with **a** silicon nitride (SiN_x) anti-reflection coating on planner surface; **b** silicon nitride (SiN_x) anti-reflection coating on textured surface

Table 9.1 Simulation parameters for PC1D simulation in best cell scenario and typical cell scenario

Solar cell parameters	Best cell scenario	Typical cell scenario
Cell/Wafer thickness	100 µm	100 µm
Cell active area	100 cm^2	100 cm^2
P-type base wafer resistivity	1 Ω cm	1 Ω cm
Emitter sheet resistance (after doping)	50 Ω/sq (Diffusion profile: erfc)	50 Ω/sq (Diffusion profile: erfc)
Junction depth	400 nm	400 nm
Bulk recombination lifetime	400 µs	40 µs
Front surface recombination velocity	100 cm/s	10^4 cm/s
Back surface recombination velocity	100 cm/s	1000 cm/s
Temperature	300 °K	300 °K
Series resistance	1 mili-Ω	5 mili-Ω
Shunt resistance	1000 Ω	100 Ω
Reflectance profile (simulated)	SiN_x^a and texture + SiN_x^b	SiN_x^a and texture + SiN_x^b
Light source	One Sun, AM 1.5G spectrum	One Sun, AM 1.5G spectrum
Light intensity	100 mW/cm^2	100 mW/cm^2

[a]SiN_x 75 nm with RI: 2.0 for planner
[b]Base reflectance 3% with texture height 5 µm (both side) for textured +ARC

lifetime, front and back surface recombination velocity has been slightly modified to see the impact on thin wafer based cells.

Silicon nitride (SiN_x) anti-reflection coating (ARC) with a thickness of 75 nm and refractive index of 2 has been considered for both planer and textured case. The

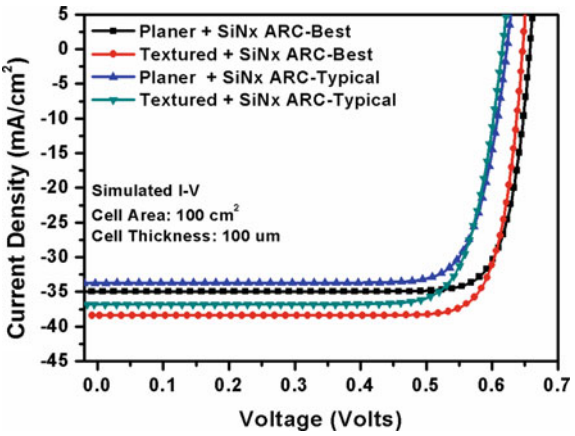

Fig. 9.3 Simulated I–V characteristics of 100 μm c-Si wafer-based solar cell having ARC coating on planer surface and on textured surface in two cell conditions

simulated I–V characteristics for the two scenarios can be seen in Fig. 9.3. Also, the comparative electrical performance can be seen as tabulated in Table 9.2.

Table 9.2 indicates 3.1–3.8 mA/cm^2 improvement in current generation for textured surface coated with SiN_x ARC layer depending upon the cell semiconductor parameters. Better cell parameters lead to more current generation compared to typical cell scenario. So, an alternative light trapping structure should be good enough to give relative current enhancement of the order of 3–3.8 mA/cm^2.

One more thing to notice from Table 9.2 is that there is reduction in open-circuit voltage (V_{oc}) when ARC coating is on textured surface. This is because of increased (111) planes for pyramidal textured surface which would have more defect states compared to planer (100) surface as discussed earlier also in Chaps. 5 and 6. The defect states increment due to texturing and exposure of more (111) plane on the surface is well accounted in PC1D simulation. So, there is improvement in current generation in textured surface based cell, but there is loss in open-circuit voltage. However, there is a gain in efficiency of around 1.3–1.5% absolute. Hence, for plasmonic-based light trapping structure, if implementable on planer surface, the target should be to achieve relative efficiency gain of 1.3–1.5%.

Table 9.2 Cell performance parameters as per PC1D simulation

Cell	Open-circuit voltage (V_{oc}) (mV)	Short-circuit current (J_{sc}) (mA)	Efficiency (η) (%)
Planer + SiN_x ARC—Best	657.5	34.9	19.1
Textured + SiN_x ARC—Best	646.6	38.4	20.6
Planer + SiN_x ARC—Typical	622.3	33.7	16.9
Textured + SiN_x ARC—Typical	615.4	36.8	18.2

In summary, when we talk about replacing texturing at lower thickness wafer based cell, the expectation should be a gain in both current and open-circuit voltage generation and it should be enough to translate the overall gain in efficiency of about 1–1.5% absolute. Also, it should be implementable with cost-effective manner with less/negligible influence on the existing cell manufacturing process.

9.3 Plasmonic-Based Anti-reflection Structure Suitable for c-Si Solar Cells

Various ways of using plasmonic-based light trapping structure for different kinds of solar cells have already been discussed in Chap. 8. We have discussed in Sect. 8.2 that there are three ways which can be exploited for enhanced light trapping in active absorbing material of the solar cells. Now, let us focus here on c-Si solar cells where we use c-Si wafers for cell fabrication. Incorporating metal nanostructures within wafer materials in controlled way would not be feasible because of the way wafers are produced. However, let us say it is possible, but it would not be favorable option as the presence of metals in absorbing material act as recombination centers and would degrade the wafer/cell electrical properties. The major impact would be on minority carrier lifetime which is one of the most important parameters of the c-Si wafer based solar cell. Hence, the remaining suitable way for using plasmonic-based light trapping structure would be either on the front surface or back surface of the cell active absorbing material as shown in Fig. 9.4a and b.

The next question is what kind of plasmonic-based light trapping structure would be beneficial for c-Si wafer based solar cell technology? As we know the

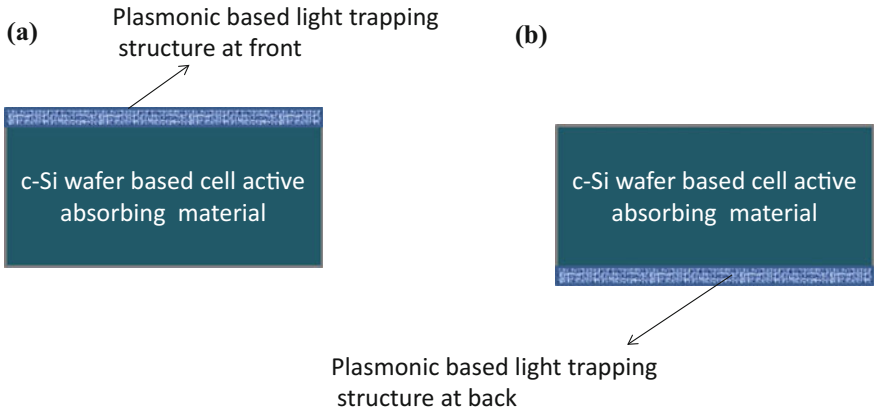

Fig. 9.4 Schematic for plasmonic-based light trapping structure for c-Si wafer-based technology where light trapping structure should be used at **a** front surface; **b** back surface

band gap of c-Si material is about 1.12 eV and it is capable of absorbing light of 300–1200 nm wavelengths, it means the light trapping structure should be such that it could provide broadband anti-reflection or efficiently scatter the light of these wavelengths into the c-Si material. Well, there has been lots of interest recently in the scientific community to exploit plasmonic-based different metal/dielectric nanostructures for achieving enhanced light trapping in the cell. Also, lots of exploration on appropriate design and their feasibility for c-Si solar cell applications are still in progress.

Further, there are many metal nanostructures or combination of metal and dielectric nanostructures which can be possible candidate for such applications, e.g., nano-holes/voids in metal films (Fig. 9.5a), metal grating based corrugated surface (Fig. 9.5b), metal–dielectric multilayer stacks (Fig. 9.5c), metal nanoparticles (Fig. 9.5d), etc.

Once we choose the structure, next thing to look at is its implementation in c-Si wafer based technology. The structure should be such that it provides less-complicated path for fabrication and should be a better substitute of traditional texturing-based light trapping structure.

Metal grating based corrugated surfaces are generally used for light coupling along the surface and mostly 30–50 nm or even more metal thicknesses are used. Further, nano-holes/voids in metals had been explored for better SPP coupling and enhanced transmission by many researchers in recent years. However, the enhanced transmission wavelength range is very narrow and very much sensitive to hole/void

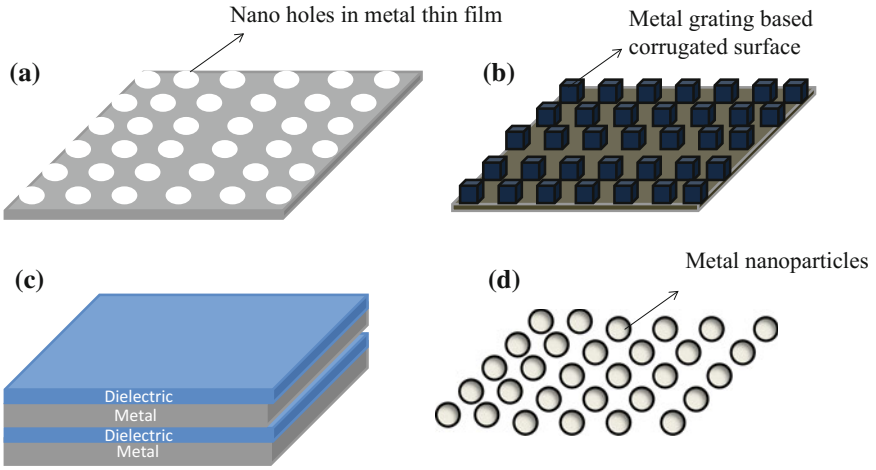

Fig. 9.5 Possible plasmonic-based light trapping structures **a** nano-holes/voids in metal films; **b** metal gratings based on corrugated surface; **c** metal–dielectric multilayer stack; **d** metal nanoparticles

diameter, pitch and metal thickness, etc. (Murray et al. 2004; Genet and Ebbesen 2007; Dunbar et al. 2012; Zeng et al. 2013; Callahan et al. 2013). Also, the complexities involved in such processes are high.

Other options which may be easier as well as cost effective are random nanoparticles or metal–dielectric multilayer stack. However, in such structures, the metals should be separated from active absorbing material via a spacer/dielectric layer. Appropriate combination of dielectric layer and metal nanostructure may result in better in-coupling of light. As discussed in Sects. 8.4 and 8.5 in the previous chapter, nanoparticles can be utilized in two ways. In one case, it can be used at front as shown in Fig. 9.6a and nanoparticle's forward scattering property can be utilized. In other case, nanoparticles can be used at bottom as shown in Fig. 9.6b, and its backscattering property can be exploited.

Also, dielectric–metal multilayer stack (see Fig. 9.6c) can be explored on c-Si wafer where the first layer is dielectric. In such case, one should look for optimized structure where minimum numbers of layers are required and it should be capable of providing better in-coupling of light for broader wavelength range.

The three probable light trapping structures as shown in Fig. 9.6 can be implementable without disrupting much the existing wafer-based cell fabrication process and would be favorable for thin c-Si wafer based solar cells. Note that the discussions made here are based on suitability and appropriateness accounting the c-Si solar cell design and requirement. However, such light trapping structures are still in research and development phase and a lot more research is required before such structures can be integrated into c-Si wafer based cell fabrication process. Advancement and recent developments in these light trapping structures appropriate for c-Si wafer based solar cells is covered in next section.

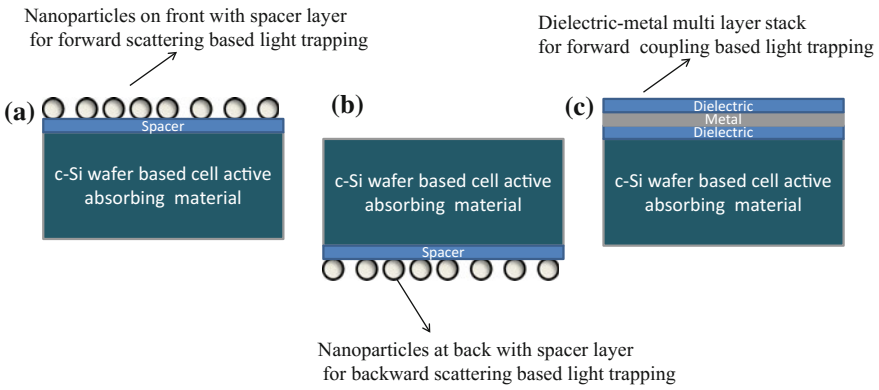

Fig. 9.6 Schematic of different light trapping structures, where **a** nanoparticles are placed at front using spacer/dielectric layer; **b** nanoparticles are placed at back using spacer/dielectric layer; and **c** dielectric–metal multilayer stack, on c-Si wafer-based cell active absorbing material

9.4 Recent Advancement in Plasmonic-Based Anti-reflector Development

Till now we have discussed different aspects of plasmonic-based light trapping structures. Now, let us see the recent advances in applications of plasmonics structures in the field for c-Si wafer based cell technology. As categorized above in three most appropriate designs, i.e., nanoparticles at front, nanoparticles at back, and dielectric–metal sandwiched structures, let us see the updates from the scientific community in this direction for each design.

9.4.1 Nanoparticles at Front

First of all, let us see the nanoparticles at front for enhanced light trapping in c-Si wafer based solar cells. As discussed in the previous chapter that nanoparticles scatter light and depending upon the dielectric environment, particle size, and shape, the scattering efficiency can be tuned. In 2007, a study on such nanoparticles at front-based light trapping structure, for 1.25 μm SOI (silicon on insulator) and double-sided polished 300 μm Si wafer based cells was presented by Pillai et al. (2007). In their study, they used silver nanoparticles deposited by thermal evaporation followed by annealing in nitrogen ambient at 200 °C for 50–60 min. For different sizes of particles, they deposited different mass thicknesses of silver thin films. The light trapping potential was studied by measuring the wavelength-dependent current from their devices for visible to IR wavelengths. They reported a relative increase in photocurrent for device with best optimized nanoparticle structure compared to without nanoparticle-based devices. For 1.25-μm-thick silicon-on-insulator based solar cells, close to 16-fold enhancement at around 1050 nm for particle sizes corresponding to 16 nm mass thickness of silver is shown. They showed 33% increment in current generation potential for cell having nanoparticles corresponding to 12 nm mass thickness, as compared to a similar cell having no nanoparticles. Also, for nanoparticles fabricated from 16 nm silver mass thickness, the cell showed 16% relative current enhancement. The current had been calculated from measured wavelength-dependent photocurrent and was averaged over the AM1.5G radiation. Their device architecture used for study and corresponding relative current enhancement result can be seen in Fig. 9.7a for SOI-based solar cell and in Fig. 9.7b for 300-μm double-side polished Si solar cell. For the 300 double-side polished Si solar cells, different particle sizes on 30 nm top oxide resulted in increase of 19%, 14%, and 2% in the photocurrent where the nanoparticles were fabricated from 12, 14, and 16 nm mass thickness of silver, respectively. Mostly, the enhancements were observed at longer wavelengths with larger particles. These enhancements were near band gap of Si where the potentials for enhancement are larger due to enhanced light trapping of weekly absorbed light.

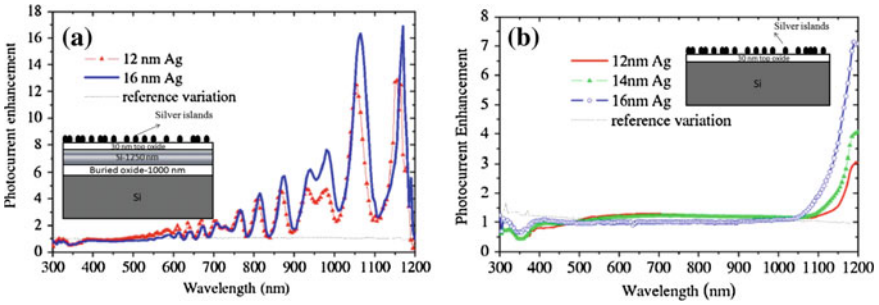

Fig. 9.7 Relative enhancement in photocurrent **a** for 1.25 μm SOI-based solar cell; and **b** for 300 μm double-side polished Si solar cell (Reproduced from [Pillai S, Catchpole K.R., Trupke T, Green M. A., Surface plasmon enhanced silicon solar cells. J Appl Phys 101:93105 (2007). doi:10.1063/1.2734885], with permission of AIP Publishing). Inset image is shown for indicating the sample geometry

The enhancement shown by Pillai et al. (2007) was encouraging; however, these were relative increment for solar cells which has 30 nm silicon oxide as spacer layer. Also, the enhancement was mostly for longer wavelengths and for shorter wavelength, reduction in photocurrent generation was observed. In c-Si solar cells, about 80–100-nm-thick silicon oxide/nitride is used for anti-reflection purpose for which reflection is very very low from top surface (less than 1%) in 550–600 nm wavelength range. The improvements shown by Pillai et al. (2007) may not be comparable with standard anti-reflection layer; however, it indicates nice light trapping behavior of nanoparticles used at front surface of the cell.

Toward exploring best optimized nanoparticles on front-based light trapping geometry, Spinelli et al. (2011) explored Ag nanoparticle arrays fabricated by means of electron beam lithography (EBL). Their test samples were 300 μm p-type single-side polished mono-crystalline Si wafers and had phosphorus-diffused emitter coated with a Si_3N_4 layer using plasma-enhanced chemical vapor deposition (PECVD). Ag nanoparticle arrays were fabricated on top of Si_3N_4 layer using EBL, silver evaporation, and lift-off processes. They studied nanoparticle array on front of the cell structure. The structure had dense-arrayed Ag particles with a surface coverage of 20%. Different Ag particle arrays in fields of 100 μm by 100 μm having different particle widths and array pitches along with different Si_3N_4 layer thicknesses for optimal light in-coupling were studied. For 180-nm-wide particles with a 450 nm array pitch, they reported their best anti-reflection structure. Measured specular reflection coefficients for different particle geometries where particle width/size, array pitch, and Si_3N_4 thickness on a Si substrate were varied, are shown in Fig. 9.8. Also, right-side SEM image in Fig. 9.8 shows the fabricated silver nanoparticle array by EBL. The specular reflection coefficients, which were weighted reflectance averaged for AM 1.5G spectrum in the wavelength range of 450–900 nm, were shown to be reduced from 5.7 to 1.4% with optimized particle array.

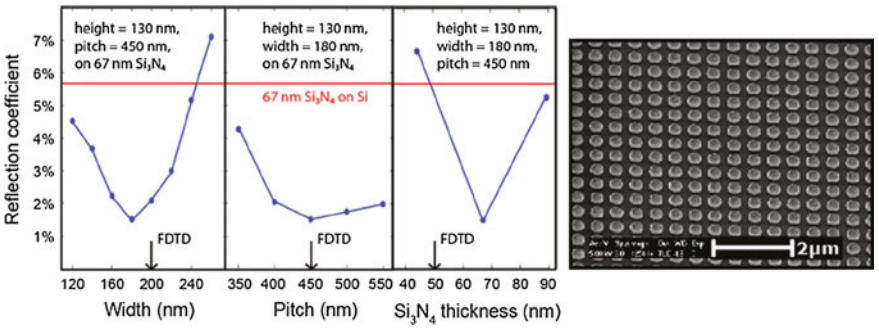

Fig. 9.8 Measured specular reflection coefficient for different particle geometries with varying particle width/size, array pitch, and Si_3N_4 thickness, on a Si substrate. Right-side SEM image shows fabricated silver nanoparticle array by EBL (Reprinted with permission from [Spinelli P, Hebbink M, de Waele R, et al., Optical Impedance Matching Using Coupled Plasmonic Nanoparticle Arrays. Nano Lett 11:1760–1765, (2011), doi:10.1021/nl200321u], (2011), American Chemical Society)

Figure 9.9 shows the measured reflectance for the samples with nanoparticles having optimal parameters on a 67-nm-thick Si_3N_4 spacer layer, for 300–1200 nm wavelength range.

Even with using most sophisticated method to fabricate well-controlled silver nanoparticles with optimized size and pitch, there was relatively high reflection in 600–800 nm (see Fig. 9.9). Here also the reflection reduction was mainly observed in infrared wavelength region.

In 2012, El Daif et al. (2012) presented a study where they had explored metal nanoparticles for thin c-Si solar cells toward utilizing the scattering property of nanostructures at front. Silver (Ag) nanodiscs on the surface of epitaxial cells grown on highly doped silicon substrates were investigated to exclusively see the effect of metal nanostructure (nanodiscs) on the front surface. For the nanodiscs, which were

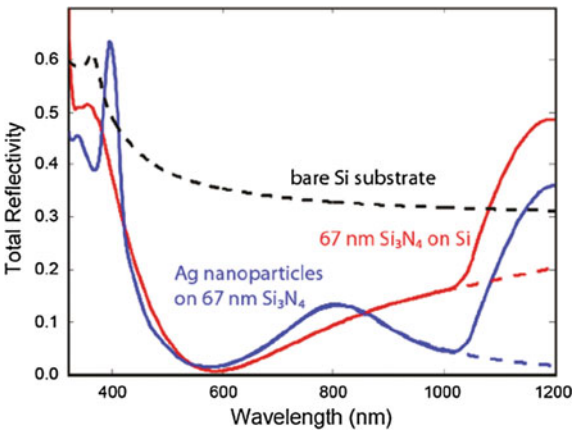

Fig. 9.9 Measured reflection profile from a 300 μm crystalline Si cell coated with 67 nm Si_3N_4 and with optimized Ag particle array on *top* (Reprinted with permission from [Spinelli P, Hebbink M, de Waele R, et al., Optical Impedance Matching Using Coupled Plasmonic Nanoparticle Arrays. Nano Lett 11:1760–1765, (2011), doi:10.1021/nl200321u], (2011), American Chemical Society)

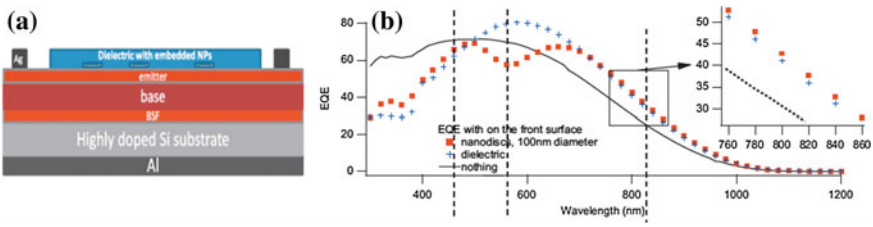

Fig. 9.10 **a** Schematic for epitaxial cell structure including Ag nanodiscs in the front dielectric coating; **b** EQE of three identical cells where front light trapping geometry in each cell is different and have either no anti-reflection coating, coated with standard anti-reflection coating or nanodiscs embedded in dielectric coating (Reprinted from Sol Energy Mater Sol Cells, 104, El Daif O, Tong L, Figeys B, et al., Front side plasmonic effect on thin silicon epitaxial solar cells, 58–63, 2012, with permission from Elsevier)

deposited through hole–mask colloidal lithography, increase in short-circuit current was reported compared to bare cells. However, when compared with cells having standard dielectric anti-reflection coating, relative decrease in efficiency was observed. Their test cell structure and the measured external quantum efficiency are shown in Fig. 9.10a and b, respectively.

The test cell structure had active layer thickness of 2–10 μm and the substrate thickness was more than 200 μm. The two cells had stack of Al/highly doped Si substrate (700 μm)/epi Si (10 μm)/SiO_2 (13 nm)/Ag nanodiscs (60 nm)/SiO_2 (95 nm) and Al/highly doped Si substrate (700 μm)/epi Si (10 μm)/SiO_2 (108 nm). An improved performance with respect to bare silicon-based cell, but barely any improvement with respect to the dielectric layer based light trapping structure, has been demonstrated in this study. The main reason for reduced performance with nanodisc-based light trapping structure was reduced photocurrent in visible wavelength region as you can see in Fig. 9.10b. However, there was relative improvement in EQE for longer wavelengths.

In nanoparticle-based structures, mostly backscattering effects are observed and that lies in visible range for 60–100 nm particles which result in high reflection in those wavelengths region and lower photocurrent generation. Singh et al. (2014) presented a study for silver nanoparticles on front surface of Si wafer having different spacer/dielectric thicknesses and compared the backscattering efficiencies from such structures. It has been showed that the high reflection regions in such structures are exactly in the same range as measured the total reflection from the samples. One such result of measured reflectance and compared backscattering efficiency can be seen in Fig. 9.11 where silver nanoparticles of about 60 nm size were fabricated on Si wafer coated with about 65 nm silicon nitride (SiN_x) spacer/dielectric layer.

In summary, metal nanoparticles/nanostructure at front surface-based light trapping and reflection reduction in broad wavelength range are still a major challenge and research and development activity in this direction in search of suitable design is still undergoing.

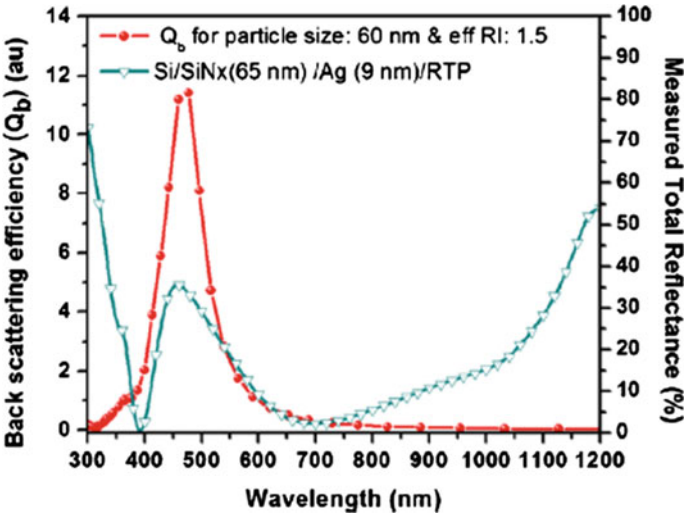

Fig. 9.11 Measured total reflectance and comparison with calculated backscattering efficiency for similar structure (from Plasmonics, Broadband reflection minimization using silver ultra-thin film sandwiched between silicon nitride layers for c-Si solar cell application, 9, 2014, 1409–1416, Singh H.K., Sharma P, Solanki C.S., Springer Science+Business Media New York 2014, with permission of Springer)

9.4.2 Nanoparticles at Back

The backscattering effect in metal nanostructures can be utilized for light trapping in c-Si solar cells using it at back surface. As discussed in Sect. 8.5 of previous chapter, the backscattering effect and backscattering efficiency of a nanostructure can be tuned. It depends on nanostructure/particle size and surrounding dielectric medium. However, using nanoparticles at back surface has limitation that it can interact only with those wavelengths which reach till back surface. For c-Si solar cells, when we talk about 80–100 μm wafer for cell fabrication, the expected wavelengths which would reach till bottom would be 850 nm or longer. It means the backscattering effect in the nanostructure should be optimized for IR wavelengths. For these wavelengths, the required particle size for better backscattering would be large, about 1 μm or more. For very thin wafers, lower size particle can also be beneficial.

Further, the dielectric spacer layer is also important as shown in Fig. 9.12 to avoid the direct contact with c-Si substrate which is active absorbing material. So, appropriate and effective ways to make back contact while using such light trapping structures should also be explored; for example, Al grids like contact as shown in Fig. 9.12.

Beck et al. (2010) did study to explore the use of nanoparticles at back and its impact on thin c-Si solar cell performance. The experiments were performed on

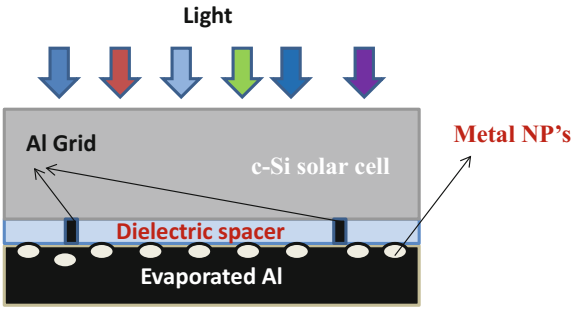

Fig. 9.12 Schematic of a typical c-Si solar cell where nanoparticles can be used at back surface and their backscattering properties can be exploited

22-μm-thin c-Si solar cells. The cell had a double-side dielectric layer structure with 10 nm of thermally grown SiO_2, 8 nm of Si_3N_4, and 82 nm of TiO_2 at front surface. At back surface, there was 10 nm of thermally grown SiO_2, 8 nm of Si_3N_4, and nanoparticles over-coated with 89 nm of TiO_2. Figure 9.13 shows the device geometry. For random Ag nanoparticles fabrication, 18 nm layers of Ag had been deposited by thermal evaporation which was annealed at 230 °C for 50 min in an atmosphere of N_2. The particles had equivalent diameters in the range of 50–204 nm and the average equivalent diameter was 131 nm. Also, surface coverage was 36% and had a flattened hemispherical shape with a height of ∼50 nm. The study showed relative photocurrent enhancements in such thin c-Si solar cells due to enhanced light trapping by self-assembled, random Ag nanoparticles at back surface. Note that the particles located at the rear of the cells had over-coating of TiO_2. With such geometry, relative increase in photocurrent of about 10% for the 22 μm Si cells due to increased light trapping was demonstrated. Also, it was observed that incorporation of a detached mirror behind the nanoparticles further increases the photocurrent and the relative enhancement goes up to 13%.

For thick (180–200 μm) wafer based c-Si solar cells, there is problem using nanoparticles at back as it requires bigger nanoparticles and fabrication of big

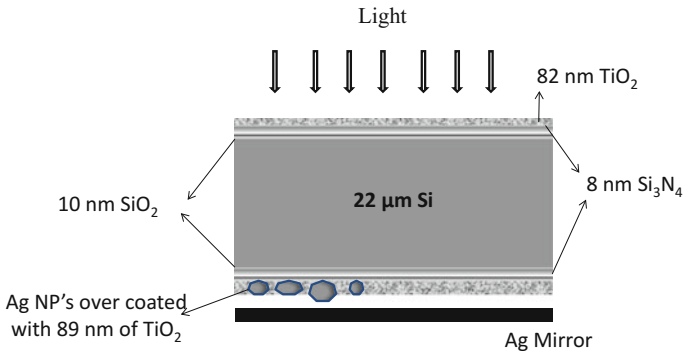

Fig. 9.13 Schematic of the experimental device geometry used by F. J. Beck et al. (Beck et al. 2010); (after Ref. Beck et al. 2010)

nanoparticles (≥ 1 μm) is very complicated. However, there have been reports of using dielectric-based nanospheres and utilizing the backscattering effects in such structures for cell performance enhancement. For example, Eisenlohr et al. (2015) explored the light trapping enhancement in 200-μm-thick c-Si solar cell using silicon oxide (SiO_2) based dielectric spheres at back as discussed in Sect. 7.3 of Chap. 7. The relative enhancement demonstrated was equivalent to 0.4 mA/cm^2 current enhancement where the device was having front surface textured and rear surface planer in combination with dielectric spheres (of size about 1 μm size). The comparison was made with a device having front surface textured and rear surface planer and without dielectric spheres. Also, for the device having front surface planer and rear surface planer in combination with dielectric spheres showed absorption enhancement equivalent to 1.6 mA/cm^2 current when compared with device having front and rear both surfaces planer.

For high-efficiency cells, nanoparticle-based structure at back surface is also being explored. For example, Yang et al. (2012) explored the use of the nanoparticles at back surface of the passivated emitter and rear totally diffused (PERT) solar cells. A total current enhancement of 18.4% for passivated emitter and rear totally diffused (PERT) cells, which were fabricated on 400 μm p-type FZ Si wafers, were demonstrated. These total current enhancements were calculated for wavelength range of 900–1200 nm only, which actually reaches till bottom surface of a 400-μm-thick cell. Silver nanoparticles had been used at back surface which were fabricated at optimized 19 nm SiO_2 spacer layer. With addition of detached metal mirror, they showed maximum current enhancement of 27% from such backscattering reflectors. The rear side schematics of the PERT solar cell used is shown in Fig. 9.14a. Also, the relative photocurrent enhancement curve for different arrangements of light trapping structure at back can be seen in Fig. 9.14b.

In summary, metal nanoparticles/nanostructure at back surface enhances the light trapping but mostly in IR wavelength region. And its advantage is that it does not influence the high energy photons which might have got reflected if it would

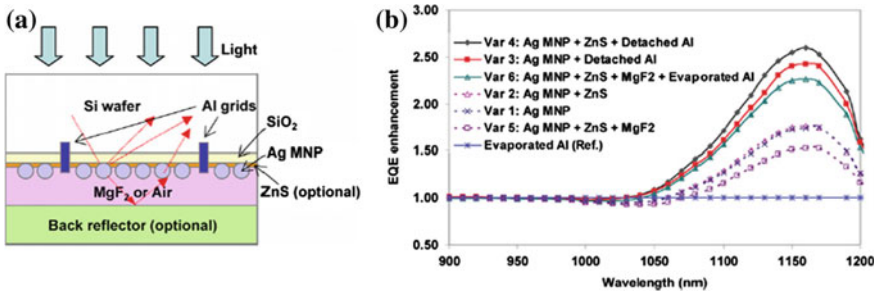

Fig. 9.14 **a** Schematics for rear side of PERT solar cell with Ag nanoparticles and detached Ag metal reflector; **b** relative photocurrent enhancement curve for different arrangements of light trapping structure at back (Reprinted from Sol Energy Mater Sol Cells, 101, Yang Y, Pillai S, Mehrvarz H, et al., Enhanced light trapping for high-efficiency crystalline solar cells by the application of rear surface plasmons, 217–226, 2012, with permission from Elsevier)

have been at front. However, when we talk about reflection reduction in broad wavelength range to replace texturization-based light trapping structure in thin c-Si wafer based cells, only nanoparticles at back could not be a sole solution. Further research and development for suitable design is needed.

9.4.3 *Dielectric–Metal Sandwiched Structure*

Now, let us see the updates about dielectric–metal sandwiched structure for enhanced light trapping in c-Si wafer based solar cells. As discussed in the previous chapter that using proper combination of metal and dielectric thin films, the reflection can be reduced from the surface and absorption in the cell active absorbing material can be enhanced. Suitable metal (Ag) and dielectric multi-stack structure designs have been shown to act as band pass filter in visible wavelength range (400–700 nm) (Sawada et al. 2001; Tachibana et al. 2003). Also, recent interest has been shown by scientific community for making transparent and better conducting electrodes for organic solar cells as pointed out in Sect. 8.6. However, for c-Si solar cell technology, there has been very little development in this type of light trapping structure. In a recent approach in exploiting such dielectric–metal sandwiched structure, Singh et al. (2016) has explored ultra-thin silver film sandwiched between silicon nitride dielectric layers for reflection reduction and enhanced light trapping for c-Si solar cell applications. Figure 9.15a shows the schematic for dielectric–metal–dielectric (D–M–D)-based light trapping structure for c-Si solar cell. Figure 9.15b shows the relative EQE enhancement for a c-Solar cell having D–M–D light trapping structure (PV-2) compared to a c-Si solar cell having standard anti-reflection coating (ARC) (PV-1). Using such D–M–D-based light trapping structure, Singh et al. (2016) reported reflection reduction for broad wavelength range (300–1200 nm). For broad wavelength range, the weighted reflectance (weighted for 300–1200 nm wavelengths with AM 1.5G solar spectrum) was demonstrated in the range of 8–9% with best optimized D–M–D light trapping structure. Also, for a 180 μm c-Si solar cell, external quantum efficiency (EQE) improvement showed a photocurrent enhancement equivalent to 0.5 mA/cm^2 with D–M–D sandwiched structure when compared to standard SiN_x anti-reflection coating (ARC) structure. EQE enhancement was reported for all wavelengths above 700 nm with maximum 25–26% enhancement at around 1125 nm, i.e., near band gap of c-Si material. In the D–M–D structure, the ultra-thin silver film had thickness of about 8 nm and SiN_x dielectric layers sandwiching it had about 80 nm thicknesses. Slight reduction in photocurrent is observed in visible region which was attributed to non-continuum silver film which leads to backscattering effect as seen in nanoparticles. Singh et al. (2016) had speculated that if silver ultra-thin film could be made continuous, the backscattering can be minimized and much better gain in cell performance would be achievable. The advantage of using such structure would be that it can be implemented at any thickness of wafer without disrupting much of the existing fabrication processes.

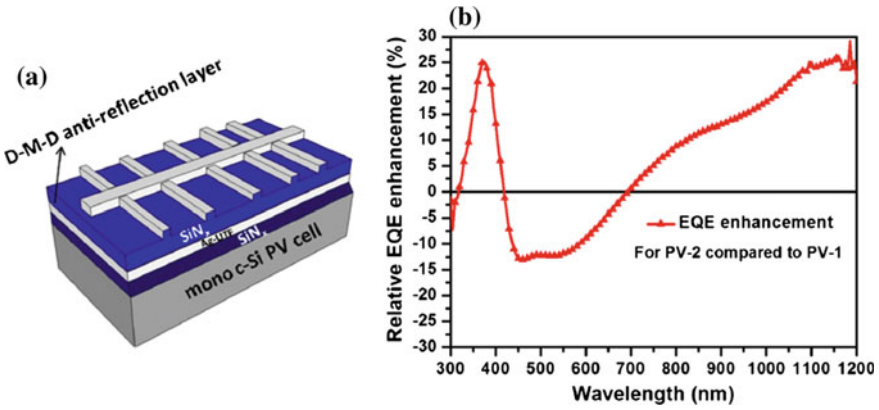

Fig. 9.15 **a** Schematic of dielectric–metal–dielectric (D–M–D)-based light trapping structure for c-Si solar cell; **b** relative EQE enhancement for PV-2 (c-Solar cell having D–M–D light trapping structure) compared to PV-1 (c-Solar cell having standard anti-reflection coating (ARC)) (from Plasmonics, Opto-electrical performance improvement of mono c-Si solar cells using dielectric–metal–dielectric (D–M–D)-sandwiched structure based plasmonic anti-reflector, 11, 2016, 323–336, Singh H.K., Arunachalam B., Kumbhar S., Sharma P, Solanki C.S., Springer Science +Business Media New York 2015, with permission of Springer)

However, this type of structure is still in research and development phase. Exploration of the easy fabrication method for ultra-thin Ag film with most continuum, angle-dependent reflection behavior of D–M–D anti-reflector and realization of best optimized D–M–D anti-reflection structure on thinner c-Si wafer based cells would be important and should be focus for future investigations (Singh 2016) before such structure can be a implementable solution and alternative to traditional texturization-based technology.

9.5 Present Limitations for Plasmonic-Based Anti-reflector Development and Implementations

As discussed, plasmonic-based anti-reflector or light trapping structure may replace the existing texturization-based light trapping structure, as such structures may not be favorable for next-generation thin c-Si solar cell technology. However, to reach the implementation target for such plasmonic-based light trapping structure, for next-generation thin wafer based c-Si solar cells, it has many hurdles. If we talk about nanoparticle at front-based light trapping structure, there is no evidence and demonstration available till date which can indicate broadband reflection minimization, especially in wavelength range of 300–1200 nm which is important for c-Si solar cells. Such structures with proper combination of dielectric spacer layer are able to give good anti-reflection behavior in infrared wavelength region but high

reflection in visible wavelength region due to backscattering effect overshadows this gain. Such backscattering effect in random nanoparticles is fundamental limitation of using it at front as suitable light trapping structure for specified 300–1200 nm wavelength range.

Further, putting backscattering effect of nanoparticles at good use by using them at back surface of the cell brings certain advantages like avoiding unnecessary back reflection of useful visible wavelengths. However, such structures are useful for enhancing the light trapping for those wavelengths which reaches till bottom surface of the cells, i.e., longer wavelengths above 850–900 nm. To scatter these wavelengths back efficiently, the particle size should be ≥ 1 μm. Fabricating these size metal nanoparticles would be a challenge when we target cost-effective and easier way. Also, such structures would not be beneficial for broad wavelength range where we target to replace texture-based light trapping technology. This is because it would not help in reflection reduction and forward in-coupling of light at front surface as it is placed at back surface.

Now, if we look at the design and suitability of dielectric–metal–dielectric-based sandwiched structure at front surface as discussed in above section, it seems promising. However, such structures are still in very early phase of development and lots of research and developments are needed. Singh et al. (2016) point out that such structure would require ultra-thin metal films having thickness less than 8 nm. However, at such lower thickness, it is very difficult to have continuous film which is necessary requirement to avoid any back reflection effect in visible wavelength regions. The aim for such light trapping structure development should be toward exploration for easy fabrication method for continuous ultra-thin metal films. This will help in minimization of reflection in broad wavelength range so that it becomes comparable to textured surface based light trapping structures. Also, the emphasis should be on fabrication for such D–M–D anti-reflection structure that it does not degrade the ultra-thin metal film during fabrication process. This is necessary to avoid tarnishing effects in metals which leads to parasitic absorption losses.

There are many metals with good plasmonic property which are to be explored for such applications, like gold, silver, aluminum, etc. However, the target should be to use metals having lower percolation threshold (<8 nm). Here, lower percolation threshold means ultra-thin metal films that can be fabricated with more continuums at lower thickness. Also, while choosing metal film and dielectric materials, negative impact from those should also be considered as it should not influence the minority carrier lifetime or passivation quality of the surface in c-Si solar cells negatively.

In summary, more detailed theoretical and experimental study for better understanding and to achieve better anti-reflection effects using such D–M–D-based sandwiched structures is needed. More in-depth insights would enable better understanding of the anti-reflection phenomenon and easy as well cost-effective implementation for such light trapping structures.

9.6 Questions and Problems

1. Discuss on need for development of alternative light trapping technique.
2. How plasmonic-based technology can play role in developing advanced alternative light trapping structures?
3. What would be the best possible way to implement plasmonic-based light trapping structure for the case of c-Si wafer based cells?
4. What would be your expectations from plasmonic-based light trapping structure if it is to be considered as alternative to traditional light trapping structure?
5. Discuss on merits and demerits of nanoparticle-based light trapping structure if it is used at (i) front surface or (ii) back surface of the c-Si solar cell.
6. What is your opinion about using plasmonics based light trapping structure as an alternative to traditional texturization-based light trapping structures in c-Si wafer based solar cell technology?
7. Calculate the expected particle size for which the backscattering efficiency would be maximum at (i) 954 nm; (ii) 1033; (iii) 1127; when the particle is at the interface of a dielectric layer with refractive index 2 and air having refractive index 1. Consider the particle material is silver and its complex refractive indices at 954 nm, 1033 nm, and 1127 nm are −41.3 +2.5i, −48.8 +3.2i, and −58.8 +3.9i, respectively.
8. What do you understand from D–M–D plasmonics anti-reflector? Discuss in brief.
9. What are the issues in D–M–D-based light trapping structure development and implementation?
10. Put some light on recent advances in plasmonic-based light trapping structure developments for the case of c-Si wafer based cells.
11. Discuss the limitations of plasmonic-based anti-reflector and implications associated with its implementation.

References

Beck FJ, Mokkapati S, Catchpole KR (2010) Plasmonic light-trapping for Si solar cells using self-assembled, Ag nanoparticles. Prog Photovolt Res Appl 18:500–504. doi:10.1002/pip.1006

Callahan DM, Horowitz KAW, Atwater HA (2013) Light trapping in ultrathin silicon photonic crystal superlattices with randomly-textured dielectric incouplers. Opt Express 21:30315. doi:10.1364/OE.21.030315

Dunbar RB, Hesse HC, Lembke DS, Schmidt-Mende L (2012) Light-trapping plasmonic nanovoid arrays. Phys Rev B 85:35301. doi:10.1103/PhysRevB.85.035301

Eisenlohr J, Lee BG, Benick J et al (2015) Rear side sphere gratings for improved light trapping in crystalline silicon single junction and silicon-based tandem solar cells. Sol Energy Mater Sol Cells 142:60–65. doi:10.1016/j.solmat.2015.05.043

El Daif O, Tong L, Figeys B et al (2012) Front side plasmonic effect on thin silicon epitaxial solar cells. Sol Energy Mater Sol Cells 104:58–63. doi:10.1016/j.solmat.2012.05.009

Genet C, Ebbesen TW (2007) Light in tiny holes. Nature 445:39–46. doi:10.1038/nature05350

International Technology Roadmap for Photovoltaic (ITRPV) 2013 Results. http://www.itrpv.net/Reports/Downloads/2014/ (2014)

Murray WA, Astilean S, Barnes WL (2004) Transition from localized surface plasmon resonance to extended surface plasmon-polariton as metallic nanoparticles merge to form a periodic hole array. Phys Rev B 69:165407. doi:10.1103/PhysRevB.69.165407

PC1D 5.9 PC1D (ver 5.9) Software for modelling a solar cell

Pillai S, Catchpole KR, Trupke T, Green MA (2007) Surface plasmon enhanced silicon solar cells. J Appl Phys 101:93105. doi:10.1063/1.2734885

Sawada M, Higuchi M, Kondo S, Saka H (2001) Characteristics of indium-tin-oxide/silver/indium-tin-oxide sandwich films and their application to simple-matrix liquid-crystal displays. Jpn J Appl Phys 40:3332–3336. doi:10.1143/JJAP.40.3332

Singh HK (2016) Plasmonics based light-trapping structures for c-Si solar cell applications. IIT Bombay, Powai, Mumbai

Singh HK, Arunachalam B, Kumbhar S et al (2016) Opto-Electrical performance improvement of mono c-Si solar cells using Dielectric–Metal–Dielectric (D–M–D) sandwiched structure-based plasmonic anti-reflector. Plasmonics 11:323–336. doi:10.1007/s11468-015-0049-5

Singh HK, Sharma P, Solanki CS (2014) Broadband reflection minimization using silver ultra thin film sandwiched between silicon nitride layers for c-Si solar cell application. Plasmonics 9:1409–1416. doi:10.1007/s11468-014-9757-5

Spinelli P, Hebbink M, de Waele R et al (2011) Optical impedance matching using coupled plasmonic nanoparticle arrays. Nano Lett 11:1760–1765. doi:10.1021/nl200321u

Tachibana Y, Kusunoki K, Watanabe T et al (2003) Optical properties of multilayers composed of silver and dielectric materials. Thin Solid Films 442:212–216. doi:10.1016/S0040-6090(03)00984-2

Yang Y, Pillai S, Mehrvarz H et al (2012) Enhanced light trapping for high efficiency crystalline solar cells by the application of rear surface plasmons. Sol Energy Mater Sol Cells 101:217–226. doi:10.1016/j.solmat.2012.02.009

Zeng B, Gao Y, Bartoli FJ (2013) Ultrathin nanostructured metals for highly transmissive plasmonic subtractive color filters. Sci Rep 3:1–9. doi:10.1038/srep02840

Chapter 10
Future Scope in Advanced Lighting Trapping Structure Development

This chapter focuses on the future scope and requirements for research for different light trapping technologies in context of c-Si solar cells. Discussion has been made mainly on the future advancement needed in light trapping structure development and a brief projection for certain areas which can be of immediate interest for research and development community.

10.1 Exploration of Metal–Dielectric Extended Layers

Dielectric–metal sandwiched structures have been explored for different applications by different research groups as discussed in the previous chapter. However, in the field of solar cells, there has seen recent interest in organic solar cells and c-Si solar cells. In organic solar cells, the aim has been to have highly transmitting and better conduction layer with dielectric–metal sandwiched structure (Sahu et al. 2007; Sahu and Huang 2009; Zhou et al. 2010; Chiu et al. 2014). The aim of such structures in c-Si solar cell technology is to replace texturization-based light trapping structure with the alternative which would show better anti-reflection for broad wavelength range (Singh et al. 2016). Such dielectric–metal sandwiched structure-based light trapping designs are still in very early phase of research and require lots of research and development in this area.

The very first requirement would be the fabrication method for ultra-thin metal film with utmost continuum. Better anti-reflection properties from dielectric–metal–dielectric (D–M–D) sandwiched structures have been demonstrated but for those metal films which has utmost continuous surface and much lesser thickness. It is one of the major challenges since different metals have different percolation thresholds. For example, silver has percolation threshold of 10–12 nm with physical vapor deposition technique (Sergeant et al. 2012). However, gold deposited by similar technique has percolation threshold of 7 nm or even lesser. It is worth mentioning that percolation threshold can be tuned. It depends on fabrication

© Springer Nature Singapore Pte Ltd. 2017

C.S. Solanki and H.K. Singh, *Anti-reflection and Light Trapping in c-Si Solar Cells*, Green Energy and Technology,
DOI 10.1007/978-981-10-4771-8_10

method and involved process condition like used substrate material, deposition rate, substrate temperature, etc. One can explore different methods and process conditions for controlling the percolation threshold, i.e., fabrication of continuous film at lower thicknesses. Also, one should look for such fabrication methods which do not degrade the metal film. For example, silver and aluminum are very sensitive to the exposure of air and form oxides. The oxide formation results in tarnishing effects which lead to parasitic absorption losses in such D–M–D structures as highlighted in previous chapter.

Another aspect of research can be exploration of different dielectric films with different sandwiched metals which may result in much better passivation of c-Si surface. Also, comparative study to observe and understand the role of ultra-thin metal films in improving the surface passivation quality can be done. It is well known that if the thickness of dielectric film is doubled, it would positively impact the surface passivation quality. So, D–M–D structure should also lead to better passivation of the surface. However, there has been no comparative experimental study yet and can be an area of interest for further in-depth study.

The next topic of interest can be angle-dependent reflection behavior of D–M–D anti-reflector. Since, in real application scenario, the cell faces sun at different angles from morning to evening. This leads to requirement of better broadband anti-reflection in wide angle range for the incident light. More about angle-dependent reflection reduction requirement has been discussed later in Sect. 10.3.

Finally, at the end, what matters most is the realization of best optimized D–M–D anti-reflection structure on thinner c-Si wafer based cells and the associated cost analysis. Study on stability of such structures in different environmental conditions would be an important area since the cell has to give stable performance and should last long. Stability of D–M–D anti-reflection structure would be important if it is to be adopted by any industry as alternative to traditional texturization-based technology. Also, for solar cells where cost is more important to make it available for masses, such light trapping structures must be cost effective and easy to implement. Figure 10.1 shows a most general device design with D–M–D-based light trapping structure. Note that there may be certain changes in device design when we move for thin c-Si wafer based cell application with such D–M–D light trapping structures. This may lead to many other challenges which may be crucial for future developments.

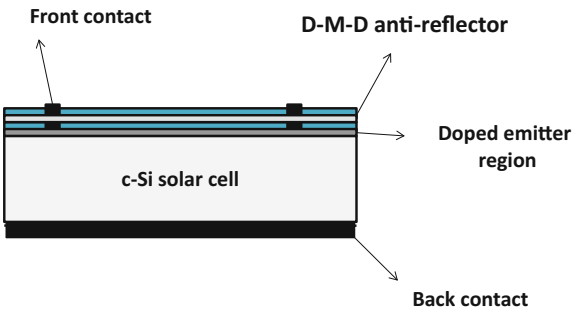

Fig. 10.1 Schematic of a most general c-Si wafer based cell design with D–M–D anti-reflection structure

In summary, there are lots of possibilities and opportunities for research and development in this type of plasmonic-based anti-reflector and there is long way to go before such technology can reach to industry application stage.

10.2 Nanoparticles at Back Surface of c-Si Solar Cells

Now, let us talk about future scope and further research and development for nanoparticles at back surface to enhance light trapping in c-Si solar cells. As we have already discussed in Sect. 9.4.2 that such structures utilize the backscattering property of the nanoparticles, such light trapping structures would be useful but only for longer wavelengths even if the used c-Si active absorbing material thickness is very low (as low as 22 μm (Beck et al. 2010)) as discussed in the previous chapter. Therefore, the main utilization of such light trapping structures would be for high-efficiency c-Si solar cells and cells where we can target to replace the back surface textures with nanoparticles as shown in Fig. 10.2.

Presently, in c-Si solar cell fabrication process, both sides are textured where the role of back side surface is to further randomize the direction of back-reflected light. In such scenario, if the back surface texturing is to be avoided while still texturing the front surface, nanoparticles at back can be a good option. Some positive results have already been reported by Eisenlohr et al. (2015) using dielectric spheres (silicon oxide) at back. From implementation point of view for such structures, further exploration can be on effective and cheaper way of fabricating larger size particles. And the ultimate goal should be their incorporation and test in real thin c-Si solar cells. Note that such structures cannot be expected to be full replacement of traditional texturization-based light trapping structure. However, more unique and advanced shape of nanoparticles can be explored with emphasis on cheaper and easier fabrication methods for further light trapping enhancements. Also, the

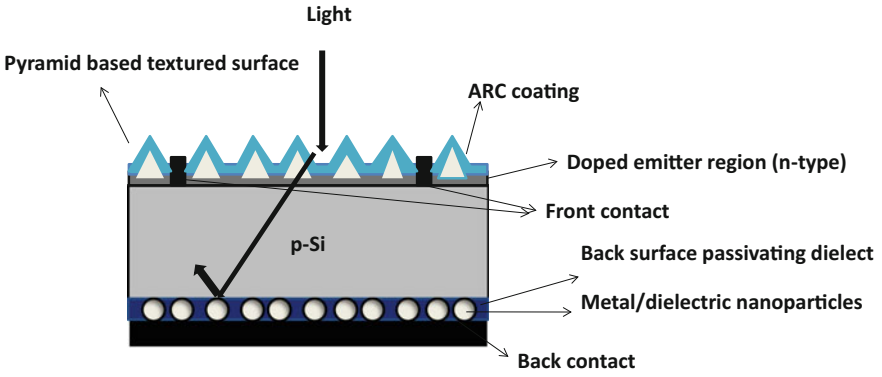

Fig. 10.2 Schematic of a c-Si solar cell having front surface textured and nanoparticles at back instead of texture surface and can be considered as partial replacement of texture surface

angle-dependent backscattering efficiency can be of interest to evaluate the light trapping potential of such structures. For finding the optimum arrangement of nanoparticles at back and corresponding evaluation of the cell performance, study can be done where incident light angle varies as the sun moves in the sky in real scenario.

10.3 Reflection Reduction Required for a Wide Range of Angle of Incidence and Compatibility of Different Light Tapping Structures

When we talk about solar cells, ultimately these would be used for making solar modules and later would be installed in the field where it would generate electricity from sunlight. Considering earth–sun geometry, for a person on earth, the sun moves from east to west and sunlight would fall on cells at different angles starting from sunrise in the east till sunset in the west. In relative motion, we can assume that the sun is moving around the earth. A spherical coordinate system may be used for sun's position with respect to earth as shown in Fig. 10.3. In different seasons, the distance between sun and earth varies. Also, the angular positions represented by Θ and ϕ would vary. Different positions of the sun in the sky in different seasons (e.g., winter, summer, etc.) may result in different angles of incidence and different intensities on the cell. So, for optimizing the cell light trapping structure, the cell design and the light trapping structure should be such that it provides best output from the cell, accounting the variation in angle of light incidence on cell surface also. In laboratory, usually the light trapping structure optimizations are done for

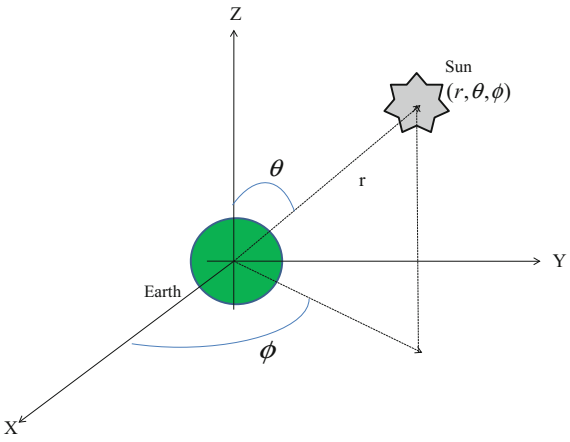

Fig. 10.3 Schematic of relative motion between sun and earth in spherical coordinate system

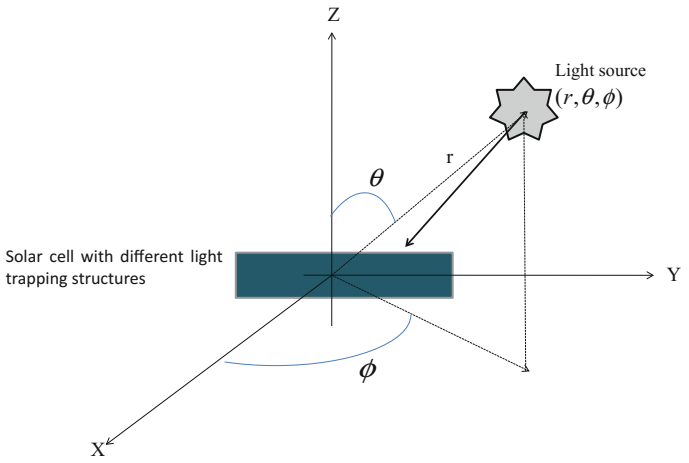

Fig. 10.4 Light incidence on test cell with variable angle of incidence (Θ and ϕ) proposed for light trapping structure capability and compatibility check for a wide range of angle of incidence

normal incidence of light. But, such optimized structure would not necessarily be an ideal one which may work for any angle of incidence of light. In this scenario, it becomes evident that we should explore light trapping structure which is optimized for best light trapping performance for a wide range of angle of incidence.

Considering the constant light intensity, one can explore the impact of angle of incidence on light trapping capability for different light trapping structures, especially, the plasmonic-based light trapping structures which have got recent attention and are in early phase of development. Research can be focused where cells can have different optimized light trapping structures. For comparison of different angles of light incidence (Θ and ϕ combinations, as shown in Fig. 10.4.) of optimized light trapping structure, cumulative power generation from the cell should be compared which accounts the overall cell performance for all angle of incidence as in real scenario as discussed above. Such study can be proved beneficial considering the importance of angle-dependent reflection behavior from cell surface and impact on cell performance.

Upcoming plasmonic-based advanced light trapping structures as well as the other existing light trapping structures compatibility for reflection reduction in a wide range of angle of incidence can be proposed. Some research and publications can be found in this direction. For example, Spinelli et al. (2012) had reported a study on angle-dependent specular reflectance from base silicon wafer, silicon coated with 60 nm silicon nitride anti-reflecting layer and silicon nanoparticles coated with 60 nm silicon nitride anti-reflecting layer. Figure 10.5 shows the measured specular reflectance for different angles of incidence for light of wavelength 632 nm.

In their study (Spinelli et al. 2012), the finding was that silicon nanoparticle arrays, coated with 60 nm silicon nitride anti-reflecting layer, show best

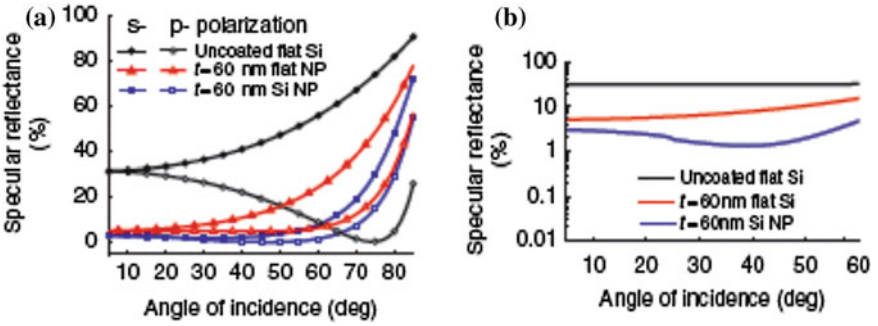

Fig. 10.5 Angle-dependent specular reflectivity measured for 632 nm light wavelength for bare Si, Si coated with 60 nm silicon nitride anti-reflecting layer, and Si nanoparticles coated with 60 nm silicon nitride. **a** for s-polarized (*solid symbols*) and p-polarized (*open symbols*) incident beam; **b** average of s-polarizations and p-polarizations, plotted on a logarithmic scale (Reprinted by permission from Macmillan Publishers Ltd: [NATURE COMMUNICATIONS] (Spinelli P., Verschuuren M.A., Polman A., Broadband omnidirectional anti-reflection coating based on subwavelength surface Mie resonators, 3:692. doi:10.1038/ncomms1691, (2012))

anti-reflection effect in a wide range of angle of incidence. Since there are very few such publications which show such study, there is a good scope for further research and development in this direction.

10.4 Efficient Light Directors

Nanoparticles at front surface of a c-Si solar cell are advantageous in terms of light trapping enhancement, but only for longer wavelengths. High reflection in visible wavelength region due to backscattering effect is the main cause of concern as discussed in Sect. 9.5. This can be the focus of future exploration of nanostructure design and development. Light directors, which can be high refractive index based nanostructures or combination of metal and dielectrics, can be explored which could enhance the forward scattering or couple the incident light to active absorbing material. A hypothetical light director from which the expectation could be scattering of the light in forward direction is shown in Fig. 10.6. In such case, the

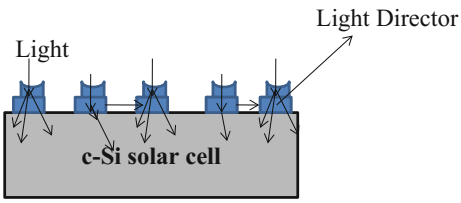

Fig. 10.6 Schematic of a hypothetical light director on c-Si solar cell

minimization of backscattering may be done by coupling the light along the surface which could be re-scattered in forward direction.

Such structure should show high forward scattering efficiency and negligible backscattering efficiency if it is to be considered as efficient light director. At this stage, such assumptions are hypothetical only, but one may think in this direction and can explore various shape and metal–dielectric nanostructure combinations for overcoming the backscattering effect as observed in nanoparticles at front case.

10.5 Combination of Multiple Light Trapping Technologies for Enhanced Cell Performance

Till now we have discussed many different light trapping structures, starting from dielectric-based anti-reflection coating in Chap. 3 and surface texturing with different shapes in Chaps. 4 and 5. Also, combination of dielectric coated textured surface has been discussed in Chap. 6 and the plasmonics and Mie scattering based light trapping have been discussed in Chaps. 7–9. All the designs and light trapping technology were discussed keeping c-Si wafer based solar cell in focus. Each light trapping structure has their advantages as well as disadvantages. However, combination of dielectric anti-reflection coating with surface texturing greatly influences the light trapping potential in c-Si solar cells as discussed in Chap. 6. Similarly, other light trapping structures can be combined and explored for next-generation thin c-Si wafer based cells where target is to fabricate efficient solar cells using 100 μm c-Si wafers. As an attempt to replace back surface texturing, as discussed in Sect. 10.2, Eisenlohr et al. (2015) used dielectric spheres (silicon oxide) at back in combination of dielectric coated textured front surface. A representative device schematic can be seen in Fig. 10.2. Similar research and development can be planned for combination of other Mie scatterer or plasmonic-based light trapping structures. Figure 10.7 shows some representative schematics as proposed combination of light trapping structures for c-Si solar cell applications.

The representative light trapping structure schematic is shown in Fig. 10.7a, where metal and/or dielectric nanoparticles at front and back may be used and can be explored for thinner c-Si solar cells. In this case, of course, the back reflection from front nanoparticles would create problem. However, different designs and shapes of nanostructures can be explored. Further, the representative light trapping structure schematic as shown in Fig. 10.7b, where D–M–D anti-reflection structures at front and metal and/or dielectric nanoparticles at back are shown, can be explored for broadband anti-reflection effects in thin c-Si wafer based cells.

Developments toward nano-pyramids/nano-textures fabrication and its relative impact on thin c-Si wafer based cell performance can also be explored. Use of nano-textures/nano-sized pyramids may give comparatively less surface recombination effects compared to traditionally used large-size texture pyramids (5–10 μm). However, a comparative study would be needed to confirm the relative

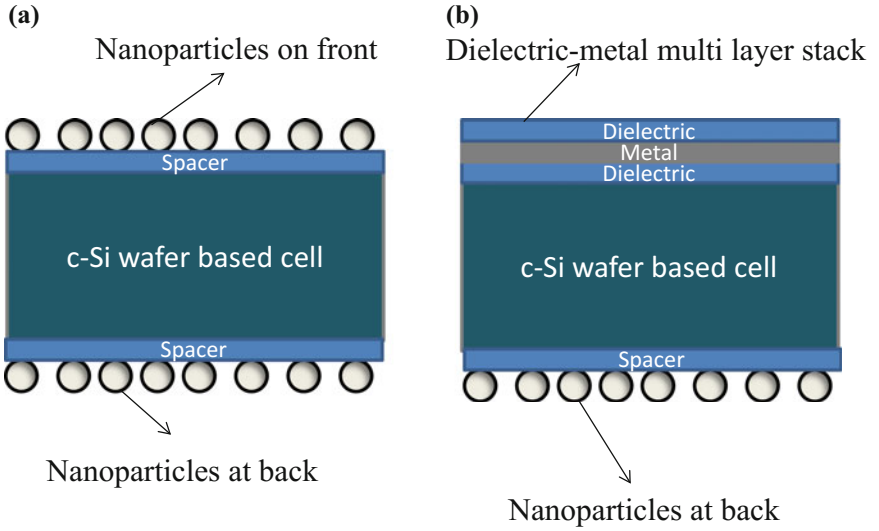

Fig. 10.7 Schematic for combination of light trapping structures for c-Si solar cell applications **a** metal and/or dielectric nanoparticles at front and back; **b** D–M–D anti-reflection structure at front and metal and/or dielectric nanoparticles at back

gain or loss for such nano-textures/nano-sized pyramids shapes. Also, combination of metal/dielectric nanostructures with such nano-textures surfaces can be evaluated in terms of electrical performance enhancement of the cell.

In summary, there are lots of scope for further research which can be done for individual light trapping structures and combination of different light trapping structures. It would be worthwhile to explore the impact of the combination of such light trapping structures on light trapping capability when exploring the discussed individual light trapping structures. At the end, the preferred structure would be one which would provide better light trapping and would involve relatively lesser cost for fabrication.

10.6 Advanced Light Trapping Structure Implementation in Next-Generation Solar Cells

Since the first c-Si solar cell made in 1941, there has been continuous effort to make the cell with better performance. There have been continuous efforts toward improving Si material quality, metal contacts, etc. as well as improvements in making cheaper and easy to use process technologies. In 1974, efforts toward improving the light trapping in Si-based cell came into light when COMSAT laboratories introduced surface texturing concept which we have already discussed in Chap. 2. Present c-Si wafer based cell technology reflects the success of research

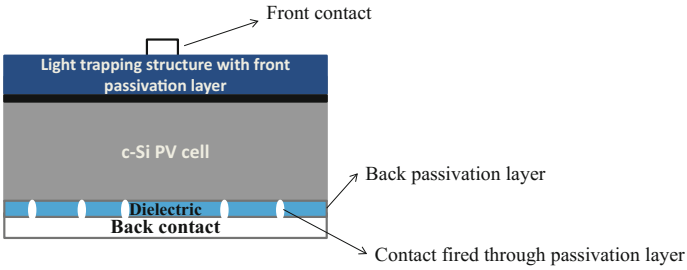

Fig. 10.8 Schematic of a representative basic back surface passivated thin c-Si solar cell

and development in the direction of surface texturing based light trapping technology and combination of such structure with dielectric anti-reflection coating. It has been emphasized many times in the book that the next-generation c-Si would require thinner c-Si wafer as substrate to maintain the cost reduction trend of the cell manufacturing. There have been many developments and a lot more to come in regards to manufacturing of thinner c-Si wafers. Both bottom-up and top-down approaches are being considered and being researched to make cheaper and cost-competitive cells (Martini et al. 2014; Terheiden et al. 2015; Teplin et al. 2015; Jain et al. 2015). Depending upon the wafer thickness, cell fabrication process may vary and many other challenges would appear. Now, as we move toward thinner c-Si wafer based cell technology, one requirement is for sure is the back surface passivation. When cell thickness reduces, the back surface recombination becomes critical and it greatly influences the open-circuit voltage (V_{oc}) and quantum efficiency (Q.E) of the cell at longer wavelengths. Figure 10.8 shows a representative image for a basic back surface passivated thin c-Si solar cell. Just addition of dielectric surface passivation layer at back would influence the process sequence and also the optimized condition for the appropriate light trapping structure. For example, the light reaching till back would not directly get reflected from Si–Al interface and the presence of dielectric would influence the front escape of the light. This is just an example as how this would change the optimization of the light trapping structure and a re-optimization of the existing light trapping structure may be required. There may be many other additional requirements. There is the possibility that the discussed noble and advanced light trapping structure prove to be more advantageous than what we predict today. However, all these would only be clear once the light trapping structures are optimized and then implemented in real solar cells and proper comparative study is done.

In summary, the aim of future research and development should be toward optimization of the individual light trapping structures and comparative study focusing on the cell electrical performance parameters and not just the reflection and absorption profile. Also, one should keep in mind the end device structure while doing the comparative light trapping performance study for a particular light trapping design. Note that such study would be of comparison for the two designs

and hence one should be very careful in designing the experiments and in analyzing the data. At the end, the choice of light trapping structure and design would depend on its easy to use the method and relative gain in cell performance in terms of power produced per unit cent spent in manufacturing the cell.

References

Beck FJ, Mokkapati S, Catchpole KR (2010) Plasmonic light-trapping for Si solar cells using self-assembled, Ag nanoparticles. Prog Photovoltaics Res Appl 18:500–504. doi:10.1002/pip.1006

Chiu P-K, Lee C-T, Chiang D et al (2014) Conductive and transparent multilayer films for low-temperature TiO2/Ag/SiO2 electrodes by E-beam evaporation with IAD. Nanoscale Res Lett 9:35. doi:10.1186/1556-276X-9-35

Eisenlohr J, Lee BG, Benick J et al (2015) Rear side sphere gratings for improved light trapping in crystalline silicon single junction and silicon-based tandem solar cells. Sol Energy Mater Sol Cells 142:60–65. doi:10.1016/j.solmat.2015.05.043

Jain S, Depauw V, Miljkovic VD et al (2015) Broadband absorption enhancement in ultra-thin crystalline Si solar cells by incorporating metallic and dielectric nanostructures in the back reflector. Prog Photovoltaics Res Appl 23:1144–1156. doi:10.1002/pip.2533

Martini R, Kepa J, Debucquoy M et al (2014) Thin silicon foils produced by epoxy-induced spalling of silicon for high efficiency solar cells. Appl Phys Lett 105:173906. doi:10.1063/1.4901026

Sahu DR, Huang JL (2009) Development of ZnO-based transparent conductive coatings. Sol Energy Mater Sol Cells 93:1923–1927. doi:10.1016/j.solmat.2009.07.004

Sahu DR, Lin S-Y, Huang J-L (2007) Deposition of Ag-based Al-doped ZnO multilayer coatings for the transparent conductive electrodes by electron beam evaporation. Sol Energy Mater Sol Cells 91:851–855. doi:10.1016/j.solmat.2007.02.003

Sergeant NP, Hadipour A, Niesen B et al (2012) Design of transparent anodes for resonant cavity enhanced light harvesting in organic solar cells. Adv Mater 24:728–732. doi:10.1002/adma.201104273

Singh HK, Arunachalam B, Kumbhar S et al (2016) Opto-electrical performance improvement of mono c-si solar cells using Dielectric–Metal–Dielectric (D-M-D) sandwiched structure-based plasmonic anti-reflector. Plasmonics 11:323–336. doi:10.1007/s11468-015-0049-5

Spinelli P, Verschuuren MA, Polman A (2012) Broadband omnidirectional antireflection coating based on subwavelength surface Mie resonators. Nat Commun 3:692. doi:10.1038/ncomms1691

Teplin CW, Grover S, Chitu A et al (2015) Comparison of thin epitaxial film silicon photovoltaics fabricated on monocrystalline and polycrystalline seed layers on glass. Prog Photovoltaics Res Appl 23:909–917. doi:10.1002/pip.2505

Terheiden B, Ballmann T, Horbelt R et al (2015) Manufacturing 100-µm-thick silicon solar cells with efficiencies greater than 20% in a pilot production line. Phys Status Solidi 212:13–24. doi:10.1002/pssa.201431241

Zhou L, Huang C, Wu S et al (2010) Enhanced optical transmission through metal-dielectric multilayer gratings. Appl Phys Lett 97:11905. doi:10.1063/1.3458702